Technical University of Denmark

DTU

Materials for Room Temperature Magnetic Refrigeration

Hansen, Britt Rosendahl

Publication date:
2010

Document Version
Publisher's PDF, also known as Version of record

Link back to DTU Orbit

Citation (APA):
Hansen, B. R. (2010). Materials for Room Temperature Magnetic Refrigeration. Roskilde: Danmarks Tekniske Universitet, Risø Nationallaboratoriet for Bæredygtig Energi. (Risø-PhD; No. 62(EN)).

DTU Library
Technical Information Center of Denmark

Materials for Room Temperature Magnetic Refrigeration

This thesis is submitted in partial fulfilment of the requirements for the Ph.D. degree at the Technical University of Denmark.

Abstract :
Magnetic refrigeration is a cooling method, which holds the promise of being cleaner and more efficient than conventional vapor-compression cooling. Much research has been done during the last two decades on various magnetic materials for this purpose and today a number of materials are considered candidates as they fulfill many of the requirements for a magnetic refrigerant. However, no one material stands out and the field is still active with improving the known materials and in the search for a better one. Magnetic cooling is based on the magnetocaloric effect, which causes a magnetic material to change its temperature when a magnetic field is applied or removed. For room temperature cooling, one utilizes that the magnetocaloric effect peaks near magnetic phase transitions and so the materials of interest all have a critical temperature within the range of 250 – 310 K. A magnetic refrigerant should fulfill a number of criteria, among these a large magnetic entropy change, a large adiabatic temperature change, preferably little to no thermal or magnetic hysteresis and the material should have the stability required for long term use. As the temperature range required for room temperature cooling is some 40 – 50 K, the magnetic refrigerant should also be able to cover this temperature span either by exhibiting a very broad peak in magnetocaloric effect or by providing the opportunity for creating a materials series with varying transition temperatures.

Ph.D. Thesis

Materials for Room Temperature Magnetic Refrigeration

Author:
Britt Rosendahl Hansen

Supervisors:
Dr. Luise Theil Kuhn
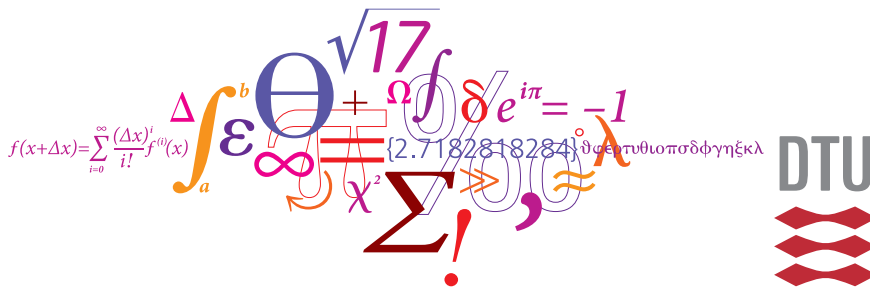Dr. Christian Bahl
Dr. Finn Willy Poulsen

July 2010

Abstract

Magnetic refrigeration is a cooling method, which holds the promise of being cleaner and more efficient than conventional vapor-compression cooling. Much research has been done during the last two decades on various magnetic materials for this purpose and today a number of materials are considered candidates as they fulfill many of the requirements for a magnetic refrigerant. However, no one material stands out and the field is still active with improving the known materials and in the search for a better one. Magnetic cooling is based on the magnetocaloric effect, which causes a magnetic material to change its temperature when a magnetic field is applied or removed. For room temperature cooling, one utilizes that the magnetocaloric effect peaks near magnetic phase transitions and so the materials of interest all have a critical temperature within the range of $250 - 310$ K. A magnetic refrigerant should fulfill a number of criteria, among these a large magnetic entropy change, a large adiabatic temperature change, preferably little to no thermal or magnetic hysteresis and the material should have the stability required for long term use. As the temperature range required for room temperature cooling is some $40 - 50$ K, the magnetic refrigerant should also be able to cover this temperature span either by exhibiting a very broad peak in magnetocaloric effect or by providing the opportunity for creating a materials series with varying transition temperatures.

To characterize magnetic refrigerants, magnetometry is a much used method as it allows one to determine hysteresis and magnetic entropy change. When recording the magnetization as a function of applied magnetic field, it is possible to sweep the field quite fast. It is demonstrated in this thesis that in the case of materials displaying a significant magnetocaloric effect, too high sweep-rates will cause a temperature change in the material during what should be isothermal measurements. The consequence is faulty magnetization measurements and the magnetic entropy change calculated from these measurements can vary significantly from the true value. Measurements demonstrating this issue of sweep-rates were conducted and are published.

Presented in this thesis is also the characterization of eight samples of the magnetocaloric material La(Fe,Co,Si)$_{13}$. One of the eight samples is a single plate with nominal stoichiometry La(Fe$_{0.851}$Co$_{0.066}$Si$_{0.083}$)$_{13}$, while the other seven samples, which were in the form of die-pressed blocks, constitute the material series La(Fe$_{1-x}$Co$_x$)$_{11.9}$Si$_{1.1}$ with $0.055 < x < 0.122$. By changing the ratio of Co to Fe, the Curie temperature of the ferromagnetic-to-paramagnetic

i

phase transition in the materials is adjusted to lie in the range of $255 - 345$ K. The La(Fe,Co,Si)$_{13}$ materials were manufactured by the company Vacuumschmelze GmbH using a novel powder metallurgy process by which industrial scale production is feasible. The characterization of the samples shows them to have many other favorable properties as magnetic refrigerants. A small non-quantitative corrosion study of one of the La(Fe,Co,Si)$_{13}$ samples is also presented.

Also presented is a brief study on the material Y$_6$(Fe$_{0.84}$Mn$_{0.16}$)$_{23}$. The Fe/Mn ratio in R$_6$(Fe,Mn)$_{23}$ materials can be chosen so that the critical temperature is near room temperature and the sample of Y$_6$(Fe,Mn)$_{23}$ was studied to determine its magnetocaloric properties. However, these properties are found to be very poor.

Finally, a study of a polycrystalline sample of Gd$_3$Fe$_5$O$_{12}$ is presented. This material has three magnetic sublattices which order antiferromagnetically in a complex manner. The total magnetic moment will align with an applied field and slowly decrease as the temperature increases. Near the compensation temperature of ~ 288 K the magnetic moments of the three sublattices cancel. Upon a further increase in temperature, the magnetic moments on the three sublattices will go through a spin reversal if a magnetic field is applied. Using Mössbauer spectroscopy this spin reversal can be seen directly from the hyperfine fields of the ^{57}Fe ions in the sample of Gd$_3$Fe$_5$O$_{12}$. Further, the magnetic properties, the magnetic entropy change and the heat capacity as a function of applied field were determined and are discussed.

Dansk resumé

Magnetisk køling er en kølemetode med attraktive muligheder; den spås at
være mere miljøvenlig og mere effektiv end konventionel gas-kompressionskøling.
Megen forskning i magnetiske materialer til dette formål er blevet udført gen-
nem de sidste to årtier og en række materialer anses i dag for at være kandi-
dater, da de opfylder mange af de krav, der stilles til en magnetisk køleenhed.
Dog er der ikke ét materiale, der skiller sig ud og således er forbedring af
de kendte materialer samt en søgen efter et bedre, aktive forskningsområder.
Magnetisk køling baserer sig på den magnetokaloriske effect, hvorved et mag-
netisk materiale ændrer sin temperatur, når et magnetfelt påtrykkes eller
fjernes. Køling ved stuetemperatur kræver udnyttelsen af, at den magne-
tokaloriske effekt topper ved magnetiske faseovergange og derfor har alle ma-
terialer af interesse en kritisk temperatur indenfor $250 - 310$ K. En magnetisk
køleenhed bør opfylde en række kriterier, bl.a. en høj magnetisk entropiæn-
dring, en høj adiabatisk temperaturændring, helst kun lidt eller ingen termisk
eller magnetisk hysterese og så bør materialet være stabilt efter lang tids
udnyttelse. Da det ønskede temperaturinterval ved stuetemperaturkøling er
$40 - 50$ K, bør den magnetiske køleenhed også kunne dække denne temper-
aturbredde. Dette kan opnås ved, at materialet enten har en meget bred top i
den magnetokaloriske effekt eller ved, at man har muligheden for at skabe en
materialeserie med forskellige overgangstemperaturer.

   Magnetometri er en ofte benyttet metode til karakterisering af magnetiske
køleenheder, da den giver mulighed for at bestemme både hysterese og den
magnetiske entropiændring. Ved måling af magnetiseringen som funktion af
påtrykt magnetfelt er det muligt at ændre feltet ganske hurtigt. Det demonstr-
eres i denne afhandling, hvorledes en for hurtig ændring af feltet ved måling
af materialer med en signifikant magnetokalorisk effekt vil føre til en tem-
peraturændring i materialet under målingen, der ellers burde være isotermisk.
Resultatet er ukorrekte magnetiseringsmålinger og den magnetiske entropiæn-
dring, der beregnes fra målingerne, kan variere betydeligt fra sin sande værdi.
Målinger, der demonstrerer problemet, er udført og publiceret.

   Præsenteret i denne afhandling er ligeledes karakteriseringen af otte prøver
af det magnetokaloriske materiale La(Fe,Co,Si)$_{13}$. Én af de otte prøver er en
plade med nominel støkiometri La(Fe$_{0.851}$Co$_{0.066}$Si$_{0.083}$)$_{13}$, mens de resterende
syv prøver, der var formet som blokke, udgør materialeserien La(Fe$_{1-x}$Co$_x$)$_{11.9}$Si$_{1.1}$
med $0.055 < x < 0.122$. Ved at ændre på forholdet mellem Co og Fe, æn-
dres Curie temperaturen for den paramagnetiske-til-ferromagnetiske faseover-

gang i materialerne, således at den ligger i temperaturområdet $255 - 345$ K. La(Fe,Co,Si)$_{13}$ materialerne er fremstillet af firmaet Vacuumschmelze GmbH, der har benyttet en ny pulver metallurgisk proces, hvorved produktion på industrielt niveau er muligt. Karakteriseringen af prøverne viser, at de har mange favorable egenskaber som magnetiske køleenheder. Et mindre ikke-kvantitativt korrosionsstudium foretaget på én af La(Fe,Co,Si)$_{13}$ prøverne præsenteres og diskuteres.

Ligeledes præsenteres et kort studium af materialet Y$_6$(Fe$_{0.84}$Mn$_{0.16}$)$_{23}$. Fe/Mn forholdet i R$_6$(Fe,Mn)$_{23}$ materialerne kan vælges således at den kritiske temperatur ligger nær stuetemperatur og Y$_6$(Fe,Mn)$_{23}$ prøven blev undersøgt for dens magnetokaloriske egenskaber. Imidlertid blev konklusionen at disse egenskaber er ringe.

Endeligt præsenteres et studium af en polykrystallinsk prøve af Gd$_3$Fe$_5$O$_{12}$. Dette materiale har tre magnetiske undergitre, der ordner antiferromagnetisk på en kompleks måde. Det totale magnetiske moment, der retter ind efter et påtrykt felt aftager langsomt med stigende temperatur. Nær 288 K udligner de magnetiske momenter i de tre undergitre hinande. Når temperaturen herefter øges, vil de magnetiske momenter i de tre undergitre gennemgå en spin-reversering, hvis et magnetfelt er påtrykket. Ved brug af Mössbauer spektroskopi kan denne spin-reversering ses direkte fra hyperfinfelterne af ^{57}Fe ionerne i Gd$_3$Fe$_5$O$_{12}$ prøven. De magnetiske egenskaber, den magnetiske entropiændring og varmekapaciteten som funktion af påtrykt felt er desuden bestemt og diskuteret.

Preface

This thesis is submitted in partial fulfillment of the requirements for obtaining the degree of Ph.D. at the Technical University of Denmark (DTU). The thesis work was carried out from April 2007 to July 2010 at Risø National Laboratory for Sustainable Energy, which is part of the Technical University of Denmark and finance was provided by a grant from the Programme Commission on Energy and Environment (EnMi) (Contract No. 2104-06-0032), which is part of the Danish Council for Strategic Research.

<div align="center">
Roskilde, July 2010
</div>

<div align="center">
Britt Rosendahl Hansen
</div>

Contributions

I. B. R. Hansen, M. Katter, L. Theil Kuhn, C. R. H. Bahl, A. Smith and C. Ancona-Torres, "Characterization Study of a Plate of the Magnetocaloric Material La(Fe,Co,Si)$_{13}$," Conference Proceedings of the 3rd International Conference on Magnetic Refrigeration at Room Temperature, 67-73 (2009).

II. B. R. Hansen, L. Theil Kuhn, C. R. H. Bahl, M. Lundberg, C. Ancona-Torres and M. Katter, "Properties of Magnetocaloric La(Fe,Co,Si)$_{13}$ Produced by Powder Metallurgy," *accepted for publication in J. Magn. Magn. Mater.* (2010).

III. B. R. Hansen, C. R. H. Bahl, L. Theil Kuhn, A. Smith, K. A. Gschneidner, Jr. and V. K. Pecharsky, "Consequences of the Magnetocaloric Effect on Magnetometry Measurements," *accepted for publication in J. Appl. Phys.* (2010).

IV. B. R. Hansen, C. Frandsen, S. Mørup, C. R. H. Bahl and L. Theil Kuhn, "Direct Measurement of the Spin Rotation in Gd$_3$Fe$_5$O$_{12}$ at the Compensation Point using Mössbauer Spectroscopy," *in preparation.*

Acknowledgements

My deepest gratitude is extended to my supervisors head of program Luise Theil Kuhn and senior scientist Christian Bahl. Their almost daily support and encouragement throughout my time as a Ph.D.-student has been invaluable and, at times, vital. Senior scientist Finn Willy Poulsen was as co-supervisor always most helpful when called upon and for this he is thanked. During the maternity leave of Luise Theil Kuhn, special advisor Anders Smith stepped in as co-supervisor, and I would like to express my gratitude for the guidance and suggestions he provided. Head of program Nini Pryds also deserves a special thanks. As my head of program and project manager, he has given me a lot of help, encouragement and, most importantly, some of his time, when needed. Those of us, who have attended his annual BBQ and Christmas gathering for his closest co-workers, have had an enjoyable time at these events.

Matthias Katter from Vacuumschmelze GmbH is thanked for not only providing the samples, which are the focus of chapter 5 and two papers, but also for his many answers to my questions and for helpful discussions. Professors Karl A. Gschneidner and Vitalij K. Pecharsky are likewise thanked for providing a sample of $Gd_5Si_2Ge_2$ for the study resulting in paper III and for their detailed feedback on the draft of that paper.

My time at Risø DTU was made all the more enjoyable by my colleagues, who have always been kind, helpful and a joy to be around. I would like to thank especially the remainder of the magnetic refrigeration group at Risø DTU, but also those from whom I have received help and answers and those with whom I have had useful or just enjoyable discussions. Mats Lundberg is thanked for his help with SEM measurements, for answering all the questions that followed and for being a lot of fun to work with.

The laboratory and research technicians at the Fuel Cells and Solid State Chemistry Division have shown that much appreciated combination of helpfulness and knowledge that has made it a joy to work with them. Research technician Jørgen Geyti deserves a special thanks for providing assistance with undertakings too numerous to mention, for always having an answer and for our small-talk. Our secretaries also deserve many thanks as they tend to our needs with efficiency and always with a smile. Secretary Lene Thorsted was, in particular, a great help during some of the administrative difficulties that arose during my time at Risø DTU and I would like to express my appreciation for this.

Contents

II   Papers

Paper I: Characterization Study of a Plate of the Magnetocaloric Material $La(Fe,Co,Si)_{13}$

Paper II: Properties of Magnetocaloric $La(Fe,Co,Si)_{13}$ Produced by Powder Metallurgy

Paper III: Consequences of the Magnetocaloric Effect on Magnetometry Measurements

Paper IV: Direct Measurement of the Spin Reversal in $Gd_3Fe_5O_{12}$ at the Compensation Point using Mössbauer Spectroscopy

Part I

Thesis

Chapter 1

Introduction

1.1 Motivation

Today, refrigeration in industry and homes is primarily achieved by the vapor-compression cycling of a gas. The gasses used in such refrigeration have often changed with time as they were either known to be toxic, *e.g.* ammonia, or later found to be harmful in some way to the atmosphere, *e.g.* CFCs[1]. In the vapor-compression cycle a gas is first compressed and therefore heats up. The heat is then allowed to dissipate, while the gas is still under pressure. The gas is then let through an expansion valve and the pressure of the gas drops, leading to a temperature drop. With the cold end in thermal contact with an object in need of cooling, *e.g.* the inside of a refrigerator, this cycle will remove heat from the object. Conventional compressor-based refrigeration has the advantage of being relatively inexpensive, but it is also a mature technology meaning that large breakthroughs are few. In addition, the problems with the environmental harmfulness of the refrigeration gasses and their safe containment are unresolved. As other types of refrigeration promise equal or higher efficiency and thereby the possibility of lower power consumption as well as less environmental impact, compressor-based refrigeration may see itself outmaneuvered in the coming years. The current focus on energy and sustainability has brought attention to alternatives such as magnetic refrigeration. At the heart of magnetic refrigeration lies the magnetocaloric effect, *i.e.* the heating or cooling of a magnetic material due to a change in applied magnetic field.

---

[1]As an interesting aside CFCs were developed for refrigeration in 1928 by the American engineer, Thomas Midgley Jr., who in 1921 had developed TEL (Tetra-ethyl lead) for use as an additive in gasoline. Midgley thus leaves behind a rather poor legacy as the negative environmental impacts of his research has become clear. It is perhaps fortunate that he died before any of this was widely recognized, though the manner of his death was somewhat tragic.

1.2   Outline of thesis

In chapter 2 the theory behind magnetic refrigeration is given. It is assumed that the reader has a basic understanding of magnetism and is familiar with various ways in which magnetic ordering can occur. As will be shown in chapter 2 the magnetocaloric effect can be described using thermodynamics and there we derive equations important for our understanding of the process. For years the magnetocaloric effect has been used for cooling to low temperatures by the process of adiabatic demagnetization in dilute paramagnetic materials. Temperatures in the picoKelvin range have been obtained this way, see *e.g.* [1]. We will delve momentarily into adiabatic demagnetization to understand how cooling can be achieved and why at temperatures higher than ~ 10 K a different type of magnetic materials is needed. In this "high temperature" region materials with a phase transition, which causes a large change in the magnetization, are required.

Several magnetic materials with a significant magnetocaloric effect near room temperature are candidates for the role of magnetic refrigerant within a magnetic refrigeration system. Some of the more studied of these materials are presented in chapter 3 and cover a range of material types: metals as well as ceramics displaying either 1st or 2nd order magnetic transitions. A great deal of research has been done on all these materials, but all have advantages and disadvantages in relation to magnetic refrigeration. No one material stands out at the moment and it may be that an as yet unknown material ends up as magnetic refrigerant if a commercial magnetic refrigeration system becomes a reality.

A large amount of experimental data has been collected on a number of samples using various equipment. Chapter 4 describes the experimental equipment, methods used and the subsequent analysis of the data. A Matlab$^{\circledR}$ program was written by this author to calculate the magnetic entropy change from a set of isothermal magnetization curves and create various plots of magnetization data. The function of this program is discussed and its source code supplied in appendix A.

Chapter 5 presents the results of the extensive work done by this author to characterize eight samples of $La(Fe,Co,Si)_{13}$. A large part of the research was published in two peer-reviewed papers, I and II. $La(Fe,Co,Si)_{13}$ is one of the promising materials for magnetic refrigeration and so is also discussed in chapter 3. The study on $La(Fe,Co,Si)_{13}$ shows that some of the disadvantages of the material have been remedied by the production and handling methods of the company Vacuumschmelze GmbH, which supplied the samples.

In the short chapter 6 the work done to characterize a sample of $Y_6(Fe,Mn)_{23}$

is presented. The $R_6(Fe,Mn)_{23}$ materials were thought interesting as a stoichiometry can be chosen so that the critical temperature is close to that of room temperature. The $Y_6(Fe,Mn)_{23}$ sample was characterized using x-ray diffraction and magnetometry. From the calculated magnetic entropy change it is clear that the magnetocaloric properties of the material are poor.

Another original contribution is presented in chapter 7, which deals with results obtained on the material $Gd_3Fe_5O_{12}$. The material was initially studied to learn about the magnetocaloric effect near the so-called compensation temperature, where the three magnetic sublattices in the material cancel. However, using Mössbauer spectroscopy an additional result was obtained as the spin rotation that takes place at the compensation temperature when a magnetic field is applied was directly observed.

Finally, conclusions and an outlook are presented in chapter 8.

1.3   Final Remarks on Thesis Structure

It is the hope of the author that sufficient information has been provided for the reader to appreciate this thesis. At the same time, it was important that not too much information be given so as not to confuse and obfuscate the central points. Clarity without cluttering is a difficult task and hopefully the reader will enjoy the results of the effort. The following quotation provided guidance in the effort:

> *Many a book would have been much clearer, if it had not been intended to be so very clear.*
> - The critique of pure reason, Immanuel Kant (translation: J. M. D. Meiklejohn)

Magnetic Cooling

The basis for magnetic refrigeration is the magnetocaloric effect. As the name implies, the effect causes a temperature change in magnetic materials, when a magnetic field is applied. As we will see below, the field must be applied adiabatically, *i.e.* without heat exchange with the surroundings. Using the magnetocaloric effect for cooling was an idea published in the 1920's by P. Debye [2] and W. Giauque [3], independently. Both authors suggest the use of gadolinium sulfate, $Gd_2(SO_4)_3 \cdot 8H_2O$, for refrigeration at temperatures well below 1 K.

"The data indicate that the demagnetization of gadolinium sulfate at the temperatures of liquid helium not only provides enough cooling effect to produce temperatures considerably below 1° absolute, but that in addition other substances may be cooled by gadolinium sulfate for investigation of their properties." - W.F. Giauque and C.W. Clark[4]

In the following, equations for two important quantities in magnetic cooling, the magnetic entropy change and the adiabatic temperature change, are derived. Then, it is shown how one can obtain very low temperatures using adiabatic demagnetization, which was the first usage of the magnetocaloric effect for cooling. This method has been used for many years in experimental setups to obtain millikelvin temperatures. The method of adiabatic demagnetization is, however, not useful for cooling at high temperatures for reasons made clear later. In 1976 Brown [5] demonstrated how the magnetocaloric effect can be utilized for cooling near a magnetic phase transition. The material used by Brown was Gd, which has a ferromagnetic-to-paramagnetic phase transition around 293 K and so he demonstrated magnetic cooling near room temperature.

2.1 Thermodynamics of the Magnetocaloric Effect

In this section we derive the equations of two important quantities, the isothermal entropy change, ΔS_M, and the adiabatic temperature change, ΔT_{ad}.

In order to describe the state of a thermodynamic system we need a set of parameters, such as *e.g.* temperature, pressure, density. To find the relevant parameters to describe our system we consider what happens if an amount of heat dQ is added to the system. First, this will result in an increase in internal energy dU, second the system may expand and do work on its environment, so that a term pdV must be added, and finally we may see a decrease in magnetization due to the added heat. The latter is represented by the term $-\mu_0 H dM$, so that the thermodynamic state is given by

$$dQ = dU + pdV - \mu_0 H dM. \tag{2.1}$$

If we are dealing with a *reversible process*, the second law of thermodynamics tells us that

$$dQ = TdS \tag{2.2}$$

and by rearranging the terms we see that the change in internal energy for a magnetic material under those conditions is given by

$$dU = TdS - pdV + \mu_0 H dM. \tag{2.3}$$

Note that the internal energy of a magnetic system increases when a field, $\mu_0 H$ is applied to the system. As the internal energy contains the term TdS and the entropy is a difficult parameters to control, we want to express the energy of the system in a form that reflects our control of the parameters T, p and H. For this reason, we define the Gibbs free energy as

$$G \equiv U + pV - TS - \mu_0 H M. \tag{2.4}$$

If we take the differential of Gibbs free energy and insert the internal energy, dU, from Eq. (2.3), we find

$$
\begin{aligned}
dG &= dU + pdV + Vdp - (TdS + SdT) - (\mu_0 H dM + \mu_0 M dH) \\
&= TdS - pdV + \mu_0 H dM + pdV + Vdp - (TdS + SdT) - (\mu_0 H dM + \mu_0 M dH) \\
&= -SdT + Vdp - \mu_0 M dH. \tag{2.5}
\end{aligned}
$$

From this differential of Gibbs free energy, we find that

$$S = -\left(\frac{\partial G}{\partial T}\right)_{p,H} \tag{2.6}$$

and

$$M = -\frac{1}{\mu_0}\left(\frac{\partial G}{\partial H}\right)_{p,T}. \tag{2.7}$$

We can now derive a Maxwell relation, which follows by noting that for a thermodynamic potential, such as Gibbs free energy, the order of differentiation of two variables is irrelevant, so that

$$
\begin{aligned}
\frac{1}{\mu_0}\left(\frac{\partial S}{\partial H}\right)_{p,T} &= -\frac{1}{\mu_0}\frac{\partial}{\partial H}\left(\frac{\partial G}{\partial T}\right)_{p,H} \\
&= -\frac{\partial}{\partial T}\left(\frac{1}{\mu_0}\frac{\partial G}{\partial H}\right)_{p} \\
&= \left(\frac{\partial M}{\partial T}\right)_{p,H}.
\end{aligned}
\tag{2.8}
$$

By rearranging the terms and integrating we find that the isothermal entropy change due to a change, $\Delta H = H_2 - H_1$, in the applied field is given by

$$
\Delta S_M(T, \Delta H) = \mu_0 \int_{H_1}^{H_2}\left(\frac{\partial M}{\partial T}\right)_{p,H} dH.
\tag{2.9}
$$

An 'M' has been subscripted the entropy change to reflect that it is the magnetic entropy of the system, which changes. In studies of the magnetocaloric effect, the total entropy, S, is often said to derive from three sources: the electronic entropy, S_e, the lattice entropy, S_l, and the magnetic entropy, S_M. Only the magnetic entropy is significantly altered by the application of a magnetic field.

We now derive the adiabatic temperature change, ΔT_{ad}, from the heat capacity and the differential entropy. The heat capacity, c_x, where x is the fixed parameter, is defined by

$$
c_x = \left(\frac{\partial Q}{\partial T}\right)_x.
\tag{2.10}
$$

We again assume a reversible process so that $dQ = TdS$, and we may rewrite the heat capacity as

$$
c_x = T\left(\frac{\partial S}{\partial T}\right)_x.
\tag{2.11}
$$

If the only thermodynamic variables we alter are T and H, a change in entropy can be written

$$
\begin{aligned}
dS &= \left(\frac{\partial S}{\partial T}\right)_{p,H} dT + \left(\frac{\partial S}{\partial H}\right)_{p,T} dH \\
&= \frac{c_{p,H}}{T} dT + \mu_0\left(\frac{\partial M}{\partial T}\right)_{p,H} dH
\end{aligned}
\tag{2.12}
$$

where we have used Eqs. (2.8) and (2.11). We assumed that the process was reversible so that $dQ = TdS$. If we now assume that the process is
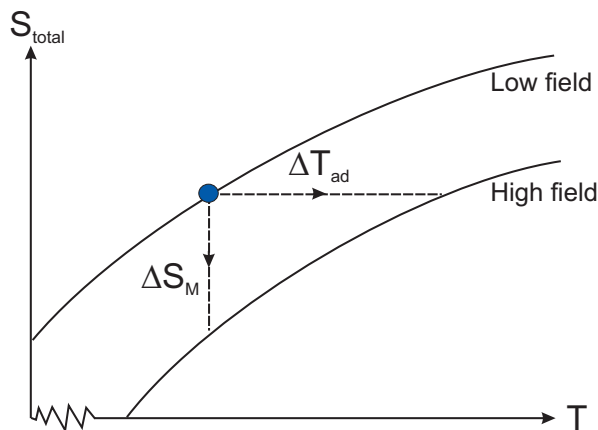
Figure 2.1: S,T-diagram visualizing the two quantities, ΔS_M and ΔT_{ad}, which form the theoretical basis of the magnetocaloric effect.

also adiabatic, *i.e.* without heat exchange with the surroundings, the process becomes isentropic in that $dQ = TdS = 0$. We rearrange the terms in Eq. (2.12) and integrate to find that the adiabatic temperature change due to a change ΔH in the applied field is given by

$$\Delta T_{ad}(T, \Delta H) = -\mu_0 \int_{H_1}^{H_2} \frac{T}{c_{p,H}} \left(\frac{\partial M}{\partial T} \right)_{p,H} dH. \qquad (2.13)$$

The two boxed equations, Eqs. (2.9) and (2.13), form the theoretical basis of the magnetocaloric effect and the quantities they describe can be visualized in an S,T-diagram, see Fig. 2.1.

2.2 Adiabatic Demagnetisation

The first use of the magnetocaloric effect for cooling was using adiabatic demagnetization of paramagnetic salts at very low temperatures. However, this procedure cannot be used for cooling near room temperature as will be demonstrated in section 2.3. We introduce the method of adiabatic demagnetization here because it historically precedes any other magnetic cooling method, because it is an interesting appetizer and because it is still in use to this day as a way of achieving very low temperatures.

To cool using adiabatic demagnetization the system is first prepared [6]. A magnetic field is applied to a paramagnetic salt with dilute, *i.e.* weakly-interacting, spins, which is in contact with a He bath. When the salt and the bath are in thermal equilibrium, so that the temperature of the salt is a few
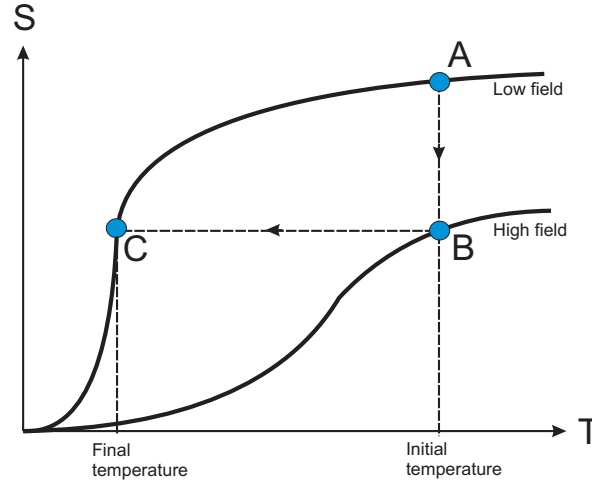
Figure 2.2: Entropy-temperature diagram showing cooling by adiabatic demagnetization. The system is first in state A, where it is in contact with a He bath. A magnetic field is applied, the total entropy is lowered and the system is in state B. Contact with the He bath is removed and the magnetic field is removed adiabatically causing an increase in magnetic entropy. Due to the adiabaticity of the process, this causes a decrease in lattice entropy and the system cools until state C is reached.

Kelvin, the contact between the bath and the salt is removed. The salt is now thermally isolated and adiabatic demagnetization can begin. The magnetic field is slowly removed and entropy is transferred from the lattice subsystem to the magnetic subsystem, cooling the salt, see Fig. 2.2.

Another way to describe adiabatic demagnetization is by considering the spin states and their occupation density as a magnetic field is removed adiabatically. For clarity, we consider a spin-$\frac{1}{2}$ system. The energy of the two magnetic states with spin-up and spin-down in a uniform magnetic field, B, is $\epsilon = \pm\mu B$, where μ is the magnetic moment, see Fig. 2.3. Thus, the occupation of the two states is given by $n_j = \exp(\mp\mu B/k_B T)$. As the magnetic field is applied, while the system and He bath are in contact, the occupation of the state with the lower energy, $-\mu B$, therefore grows at the expense of the state with the higher energy. However, when the system is isolated by removing contact with the bath, the occupation numbers can no longer change. As the magnetic field is removed the energy of the two states goes down, so that the temperature has to go down as well for $\epsilon/k_B T$ to remain constant.

The two-state model used here is a good approximation to the system of dilute spins in the salts used for adiabatic demagnetization as the requirement of the model is that the spins are practically non-interacting and experience
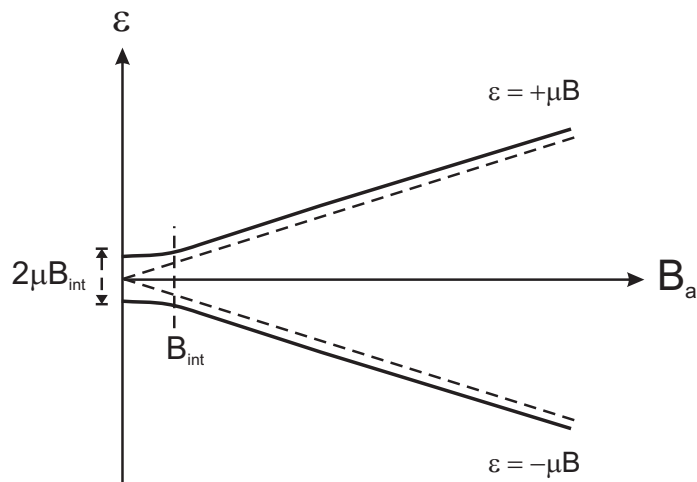
Figure 2.3: Energy levels of a two-state magnetic system as a function of applied magnetic field, B_a. The weak interactions between the dilute spins results in an effective field, B_{int}, which keeps the energy levels from becoming degenerate even when the applied field is zero.

a magnetic field that arises solely from the applied field. Indeed, the reason adiabatic magnetization fails to bring the system to zero kelvin is that as the temperature is lowered even the very weak interactions, such as dipole interactions, eventually become significant. When this happens the spins no longer disorder to as great an extent when the applied magnetic field is removed and the temperature difference between the initial and final temperature becomes smaller and smaller until it disappears.

By having a sample in thermal contact with the paramagnetic salt, adiabatic demagnetization can be used to cool samples to very low temperatures for experimental studies. By slowly reducing the strength of the applied magnetic field the temperature of the paramagnetic salt can be held at a constant temperature for hours, while measurements on the sample are performed. Once the field has been reduced to zero, the temperature can no longer be controlled via internal energy transfer to the spin subsystem and a new cycle of cooling will need to be established. This involves reapplying the magnetic field and thermally coupling the paramagnetic salt to the He bath once more.

2.3 Magnetic Cooling at Temperatures > 10 K

In the previous section we delved into the method of adiabatic demagnetization for cooling at very low temperatures and it was explained why the

method has a natural cooling limit. But what about magnetic cooling near temperatures such as 77.36 K, the boiling point of liquid N_2 [7], or near room temperature? In adiabatic demagnetization one utilizes the shift in occupation of magnetic states when going from zero to non-zero applied magnetic fields in a paramagnetic solid. To obtain a significant difference in occupation density between magnetic states, we should have $\epsilon/k_B T \geq 1$. Table 2.1 gives the magnetic fields required to obtain $\epsilon/k_B T \sim 1$ in a spin-$\frac{1}{2}$ system and from these values it is clear that the method of adiabatic demagnetization is not applicable at temperatures as high as room temperature or even at the boiling point of liquid N_2. Another difficulty which arises when the cooling

Temperature	$k_B T$	$k_B T/\mu$ ($\mu \sim \mu_B$)
2	2.76×10^{-23} J	~ 3 T
4	5.52×10^{-23} J	~ 6 T
77.36	1.07×10^{-21} J	~ 115 T
300	4.14×10^{-21} J	~ 446 T

Table 2.1: Magnetic fields required to obtain $\epsilon/k_B T \sim 1$.

temperature region is above ~ 10 K is the increasing heat capacity of the lattice, which acts to reduce ΔT_{ad}. However, all this does not mean that we cannot utilize the magnetocaloric effect for cooling at higher temperatures. In Fig. 2.4 is shown the magnetization, M, for Gd, a ferromagnetic material as a function of temperature, T, and applied magnetic field, $\mu_0 H_a$. From Eq. (2.9) we see that if we can achieve a large value of $\partial M/\partial T$ at both zero and non-zero applied field, we will obtain a large entropy difference between the two states, and this is exactly what can happen near magnetic phase transitions of non-dilute magnetic systems. Here, the thermal excitation of the system and the magnetic ordering are of approximate size and the application of a magnetic field can have a large effect on the magnetization.

In 1976 Brown published a paper [5] demonstrating the feasibility of room temperature magnetic refrigeration:

> *"Magnetic heat pumping can be made practical at room temperature by using a ferromagnetic material with a Curie point in or near the operating temperature range and an appropriate regenerative thermodynamic cycle." - G.V. Brown[5]*

Brown had constructed a magnetic refrigeration setup using the ferromagnetic rare-earth metal Gd and achieved a temperature span of 47 K. Gd becomes paramagnetic near 293 K, depending on the purity and microstructure
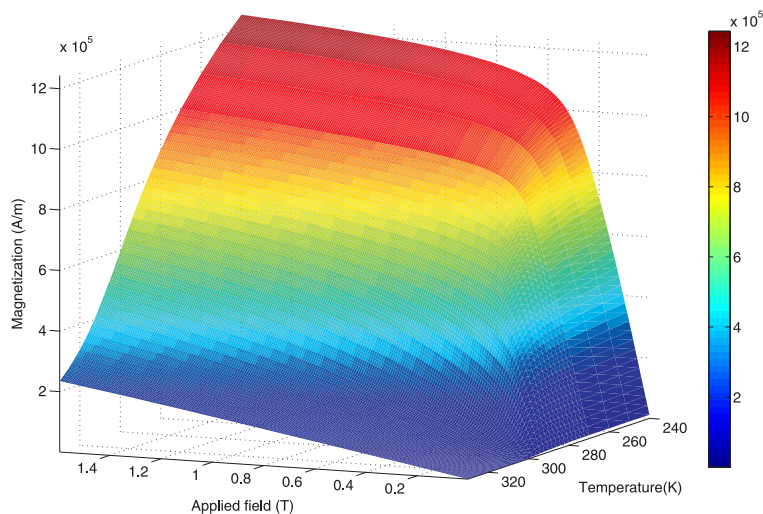
Figure 2.4: Magnetization, M, of a sample of Gd, which has a ferromagnetic transition, as a function of the applied magnetic field, $\mu_0 H_a$, and temperature, T.

of the sample [8, 9]. It is also a material with a large magnetization and little to no magnetic anisotropy. This makes the material very useful for magnetic cooling near room temperature. Brown applied a magnetic field of 7 T under adiabatic conditions and recorded a temperature change of 14 K at the Curie temperature. The temperature span of 47 K was achieved by the use of a regenerative cycle made possible by a simple linear design of his test device; a design, which still sees use today in test devices, where easy variation of different operative parameters is desirable [10]. An example of a basic linear design for a magnetic refrigeration device is shown in Fig. 2.5.

This device consists of a tube filled with a heat transfer fluid. A magnetocaloric material, which is shaped in a way so that it allows the heat transfer fluid to flow through it, is placed within the tube. In the device shown in Fig. 2.5 this is achieved by having the magnetocaloric material in the shape of plates, so that the heat transfer fluid can flow between the plates. A magnetic field is applied parallel to the plates. This can be achieved by *e.g.* turning on an electromagnet or moving the tube, so that the magnetocaloric material is positioned inside a permanent magnet. The latter is the case for the versatile test device located at Risø National Laboratory for Sustainable Energy [10, 11]. The sudden application of a magnetic field causes a temperature change in the magnetocaloric material as the field is applied fast enough that heat cannot be exchanged with the surroundings and the process becomes quasi-adiabatic. For a ferromagnetic refrigerant the field-application will cause an increase in the material temperature. The heat transfer fluid is
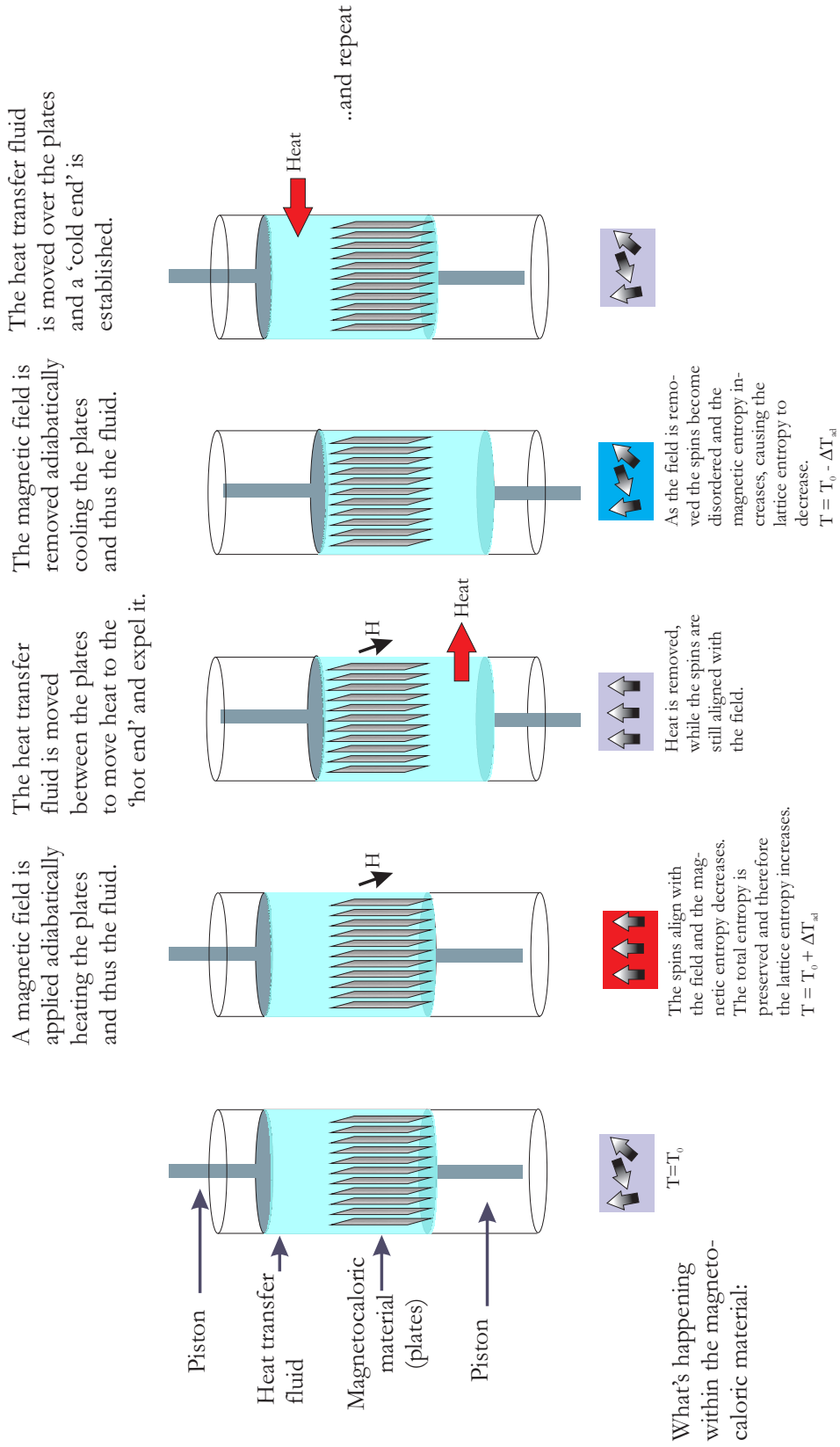
Figure 2.5: Sketch of the magnetic refrigeration cycle using an active magnetic regenerator.

then moved past the magnetic refrigerant and thus moves heat to what will become the hot end. As the applied magnetic field is turned off, the refrigerant material cools and when the heat transfer fluid is moved to the other end of the tube a cold end is established. In this way a temperature gradient is set up within the tube and a cooling cycle is achieved.

Using a 7 T applied magnetic field from an electromagnet, Gd plates as the magnetic refrigerant and a column filled with a mixture of water and antifreeze Brown was able to obtain a 47°C temperature difference between the hot and cold end, which were at 46°C and −1°C, respectively. It should be noted that there was no heat load on his refrigeration test device. Other designs for magnetic cooling devices have been developed *e.g.* a rotary design, where the magnetocaloric material is situated in a ring surrounding the magnet at the core. Rotation of either the magnet or the ring of magnetocaloric material will provide the change in applied magnetic field.

A great deal of research has been done during the last decade on magnetic refrigeration near room temperature and the number of publications on this topic is steadily increasing. In Fig. 2.6 is shown the result of a search done in ISI Web of Knowledge (*http://www.isiknowledge.com*). The search was done using the following search string: ("magnetic refrigeration" or "magnetic heat pumping" or "magnetic cooling" or magnetocaloric) and "room temperature" and the numbers were normalized by the results using the search string: magnetic. In this way, an attempt is made at stating the number of papers on magnetic cooling as a percentage of all papers dealing with magnetism. Many
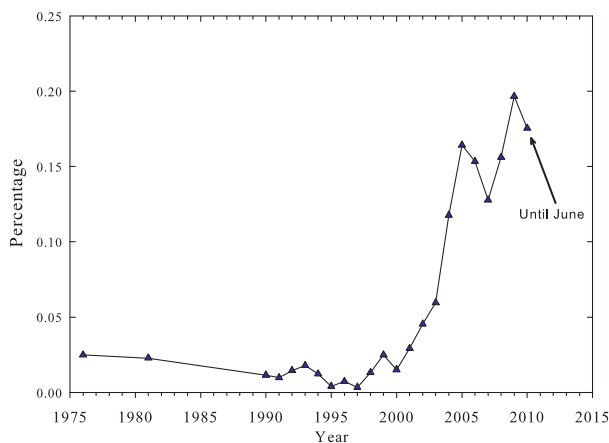
Figure 2.6: Result of search on number of publications dealing with room temperature magnetic refrigeration. The search was done using ISI Web of Knowledge and the search terms given in the text.

tasks still lie ahead on the road to the realization of a commercial magnetic refrigeration system at room temperature and an important one is finding suitable magnetocaloric materials. As will be made clear in the following chapter, several candidate magnetocaloric materials exist and each have their advantages and disadvantages.

Magnetocaloric Materials

In the following a review of selected magnetocaloric materials is presented. The materials discussed here are all among the more studied materials for room temperature magnetic refrigeration. From the onset it was a goal of this thesis work to get an overview of the known magnetocaloric materials, to determine the criteria with which to evaluate magnetocaloric materials and, if possible, to find new and hopefully better materials. The review presented here is far from exhaustive and the intent is to provide the unfamiliar reader with a small grasp of the materials research in room temperature magnetic refrigerants. At the end of the chapter a summary of the properties for each magnetocaloric material presented in the following is provided.

3.1 Criteria for Evaluating Magnetocaloric Materials

One can list the criteria for evaluation of room temperature magnetocaloric materials in different ways as some properties can be listed separately or together. In the following a list of criteria used here is provided and, as some of the criteria will seem obvious while others perhaps less so, additional information is also provided on each criterium. Examples of other listings of criteria can be found in refs. [12, 13].

Large ΔT_{ad} and a large ΔS_M
It should be clear from the theory of magnetic cooling given in chapter 2 that both the adiabatic temperature change, ΔT_{ad}, and the magnetic entropy change, ΔS_M, need to be large. ΔT_{ad} is a measure of the temperature change that occurs in the material as a magnetic field is applied, while ΔS_M is a measure of the heat that can be extracted during a cycle.

Little to no thermal or magnetic hysteresis
As hysteresis leads to energy losses, it is advantageous if both magnetic

and thermal hysteresis in the magnetic material is low or absent.

Temperature span needed: $40 - 50$ K

For a refrigeration setup near room temperature, the temperature span should be at least $40 - 50$ K, so that we can cool from $20 - 40$°C and down. If we wish for the cooling system to provide the common freezer temperature of -18°C, the temperature span may need to be even larger. Only Gd can provide this temperature span near room temperature without the use of a very large magnetic field. To meet the criterium the magnetic refrigerant should be effective within the temperature range for an applied field of $1.5 - 2$ T. One solution is to have materials where the transition temperature can be tuned by changes in the stoichiometry. In this way, a material series can provide a magnetocaloric effect over a larger temperature range.

Little to no thermal expansion/contraction

The importance of this criterium depends on how the magnetic refrigerant will be mounted in the refrigeration setup. If the refrigerant is in the shape of plates, which are held in place tightly, thermal expansion can be detrimental. In other refrigeration setups, *e.g.* one where the magnetic refrigerant is spherical in shape and packed in a bed, this criterium may or may not have relevance. Ref. [14] provides references for a variety of magnetic refrigeration devices.

Low fabrication costs

Low fabrication costs of the magnetic refrigerant is tied to the competition between the magnetic refrigeration system and the traditional vapor-compression system in use today. The latter has been through many phases of development already and sets a price standard, which new systems must be able to compete with.

Large-scale production

While not a necessary criterium early in the characterization of a magnetic refrigerant, the ability to produce the material in large quantities is a requirement for its use in a commercial refrigeration device.

Can be shaped

As mentioned above different devices for magnetic refrigeration may require different shapes of the refrigerant material.

Appropriate electrical resistivity to minimize eddy currents

Eddy currents occur as a response to changes in magnetic flux to create a magnetic field, which opposes the applied one. The eddy currents will result in unwanted heating of the material. In order to determine *a priori* whether eddy currents pose a problem in a given magnetic refrigeration device certain parameters, such as *e.g.* electrical conductivity and the rate of change of the applied magnetic field, is needed. Very little is

published on this topic and the work presented here also does not address the issue.

Appropriate thermal conductivity

In metals, the thermal conductivity, κ, is largely due to valence electrons and so is proportional to the electrical conductivity, σ, and temperature. This relationship is known as the Wiedemann-Franz law: $\kappa \propto \sigma \cdot T$. Therefore, this criterium and the previous one is in conflict. However, these criteria will also depend critically on the engineering aspects of the device. The thermal conductivity of Gd, which is $\sim$ 14 W/Km at 300 K [15], is known to be sufficient.

Low toxicity

There are obvious benefits environmentally in having a low toxicity of the magnetic refrigerant and this is also one of the selling points for magnetic refrigeration. A low toxicity will also mean a lower cost of production and, as discussed above, cost is an issue for new refrigeration systems in competition with the mature vapor-compression system.

Stability (low brittleness, solubility and corrosion)

A magnetic refrigerant failing to meet one or more of the stability requirements will have problems with functioning over many years as is necessary in a commercial refrigeration device. Again, the specifics of the device may determine the parameters, *e.g.* a brittle material may work well in the form of spheres, but will have problems when shaped as plates/sheets. It is naturally a problem, if the material degrades by dissolving in the cooling fluid. Corrosion is currently a problem for many of the room temperature magnetic refrigerants as they are metals, which may corrode in water and water is an excellent cooling fluid. To lessen this problem one can add anti-freeze with corrosion inhibitors, but the system will still need to be sealed very effectively. One can also try and coat the refrigerant although this may affect the heat transfer.

3.2 Gd

When Brown [5], as the first to do so, demonstrated that a magnetic cooling cycle is possible by utilizing the magnetic entropy change that can be accomplished by an applied field near the transition temperature of a ferromagnet, he used Gd. There are many reasons why Gd is interesting for magnetic cooling near room temperature and much research has since been done on Gd as a magnetocaloric material. For this historical reason and because it is the best magnetic refrigerant for room temperature use, Gd is today the benchmark against which all other possible magnetic refrigerants are compared. It is not expected that Gd will be used in commercial magnetic refrigeration devices,

but the material is still used in test devices [10, 16] due to its large magnetocaloric effect at room temperature and the ease with which samples can be obtained.

Gd crystallizes in the hexagonal close-packed structure and is trivalent as is common for rare-earth metals [17]. Gd^{3+} has electronic configuration $[Xe]4f^7$ and therefore a large spin angular momentum, $S = 7/2$, and zero orbital angular momentum, $L = 0$. Due to the lack of orbital angular momentum, there is no anisotropy from this source, as is otherwise the case for rare-earth metals, which, in contrast to transition metals, have unquenched orbital angular momenta. Above ~ 230 K the magnetic moments are parallel with the hexagonal c axis, whereas below this temperature a spin reorientation has taken place and the spins are at an angle with the c axis, though still collinear [18, 19]. This reorientation can be quenched by an applied magnetic field of > 2 T [20]. At around 293 K, depending on the sample purity [20], a second-order ferromagnetic-to-paramagnetic transition takes place. With a Curie temperature close to room temperature, little to no anisotropy and a large magnetization, Gd displays a large magnetic entropy change near room temperature. ΔT_{ad} is ~ 5 K for a change in applied magnetic field from 0 to 2 T [20].

In terms of the criteria for room temperature magnetic refrigerants, Gd has few shortcomings. For one thing, while Gd is easily obtained commercially in various shapes and forms, it is not cheap. Another disadvantage is that Gd tarnishes in water and a loosely adhering layer of oxide is formed that comes off in flakes exposing a new surface layer to oxidation. Thus, the stability is compromised in aqueous fluids.

3.3   Perovskite Manganites

In 1996 a number of articles were published on the magnetocaloric effect in perovskite manganites, see *e.g.* [21, 22]. A few years before, in 1994, attention had been drawn to these materials, when it was discovered that they exhibited colossal magnetoresistance near, but not at, their Curie temperature when in the form of high-purity thin films [23]. This inexplicable magnetic behavior of the perovskite manganites piqued the interest of those who came across it and prompted further studies. From the beginning it was believed that some of the perovskite manganites had great potential due to their significant ΔS_M - larger than that of Gd. However, due to the large number of non-magnetic ions present in the compounds they also have a substantial heat capacity, which accounts for the small ΔT_{ad} observed in these materials. This property, as well as a low heat transfer, leaves the perovskite manganites somewhat wanting. However, their many advantages as magnetic refrigerants

make them attractive for further study.

One feature of the perovskite structure is its high stability when doped. As the magnetic and electronic properties in perovskites are strongly coupled to the lattice an array of effects are observed in these materials. The structure has the form ABO_3, where A and B are cations of different sizes. The A-site atom is centrally placed and larger than the B-site atoms, which, ideally, are cubically arranged around the central atom and sit in octahedral coordination with the oxygen atoms, see Fig. 3.1. Most perovskites show displacement of atoms from the ideal cubic [24]. The perfectness of the perovskite structure due to the size of the atoms on the A- and B-sites can be crudely estimated by using what is known as Goldschmidt's tolerance factor [25] given by

$$t \equiv \frac{r_A + r_X}{\sqrt{2}(r_B + r_X)},$$ (3.1)

where r_A, r_B and r_X are the ionic radii for the A-site, B-site and oxygen atom, respectively. The formula characterizes the mismatch between the available space created by the network of the MnO_6 octahedra and the size of the central A-site ion. When this factor is different from one, the octahedra will be distorted. A caveat is that the formula assumes pure ionic bonding, so that the atoms can be thought of as hard spheres that follow maximum packing rules, which is never the case in reality. The perovskites may change crystal structure if doped, upon changes in temperature or during the application of a magnetic field. Examples of distorted perovskites are shown in Fig. 3.1.

The perovskite manganites studied for room temperature magnetic refrigeration have a rare-earth in the A-site. As most rare-earths prefer a valency of three, the Mn will likewise have valency three. Undoped rare-earth manganites, $RMnO_3$, are antiferromagnets due to the superexchange interaction between the Mn ions via the O ions. However, when the A-site is doped with an atom that has a preferred valency different from three, it is possible to change the interaction from antiferromagnetic to ferromagnetic. In *e.g.* $La_{1-x}Ca_xMnO_3$, the Mn will have either valency three or four and to elucidate this point the chemical formula may be written as $La_{1-x}^{3+}Ca_x^{2+}Mn_{1-x}^{3+}Mn_x^{4+}O_3$. In an octahedral complex the five d orbitals of Mn are split into two sets: the triply degenerate t_{2g} and the doubly degenerate e_g [26], see Fig. 3.2. In the perovskites Mn^{3+} has a single electron in the e_g orbital and this electron can become itinerant if the Mn spins all point in the same direction. This is achieved through the double-exchange mechanism, which was introduced by Zener [27, 28] to explain the ferromagnetic coupling in the doped perovskite manganites. Double-exchange is a form of superexchange, where two electrons are simultaneously exchanged as depicted in Fig. 3.2. As there is strong on-site Hunds coupling at the Mn site, *i.e.* the total spin S is the maximum allowed by the exclusion principle, the mechanism of double exchange is only allowed if the orientation of the spin is the same on the Mn^{3+} and Mn^{4+} sites and
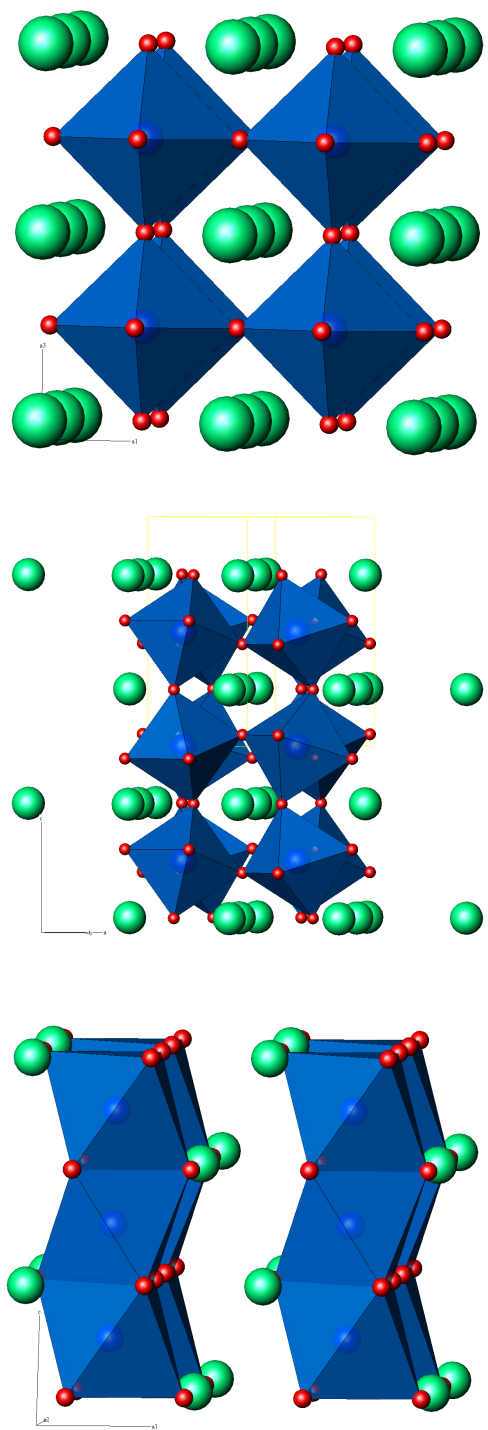
Figure 3.1: Perovskite structures with the central A-site atom shown in green, octahedra surrounding B-site atoms in blue and oxygen atoms in red. Top: Ideal cubic structure, $SrTiO_3$. Middle: Perovskite with $t = 0.81$, orthorhombic $GdFeO_3$. Bottom: Perovskite with $t = 1.13$, hexagonal $BaNiO_3$.
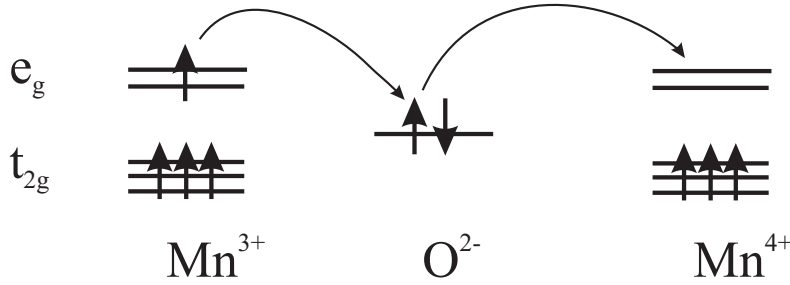
Figure 3.2: Double exchange mechanism depicted for the exchange of an electron between two d orbitals as it happens in mixed valency compounds with Mn^{3+}/Mn^{4+}. The energy levels of the Mn ions are split due to the octahedral coordination of the Mn ions.

an effective, though indirect, ferromagnetic coupling is created. This coupling will be dependent on the relative angle between the spins on neighboring sites [27] and in this way, the magnetization is affected by the degree of distortion of the Mn octahedra.

The perovskite manganites can be doped on both the A-site and B-site and many doped compounds have been studied for their magnetocaloric effect. As mentioned above, the A-site cation must be large and, as the ionic sizes increase towards the lower numbered groups and towards the higher numbered periods in the periodic table, the A-site usually contains alkali metals, alkaline earth metals, lanthanides, or poor metals. The B-site cation, however, usually contains a transition metal. In 1996 Phan and Yu published a review of the magnetocaloric effect in manganites [13]. In this review they list the results of ΔS_M measurements for 132 different samples of perovskite manganites with Curie temperatures ranging from 21.5 K for $Pr_{0.68}Ca_{0.32}MnO_3$ to 370 K for $La_{0.67}Sr_{0.33}MnO_3$. Upon examining this list it quickly becomes clear that the manganites cannot be compared so easily. For example, the Curie temperature of $La_{0.9}Pb_{0.1}MnO_3$ from two different publications are given as 235 K and 160 K [29, 30]. In both publications, the samples described were produced by sintering mixed powders and subsequent x-ray diffraction patterns showed that they were single-phase. Still, a difference in perhaps microstructure or oxygen content must account for the observed discrepancy in Curie temperatures. This example is not the only one of its kind and, in general, it is very difficult to compare manganites, especially as oxygen content is usually not determined.

A great advantage of the manganite perovskites is the ease with which the Curie temperature can be altered by doping. One of the larger ΔS_M among manganites is seen in $La_{1-x}Ca_xMnO_3$ for $0.20 \geq x \geq 0.33$ with Curie temperatures between 176 K and 276 K for increasing values of x. Unfortunately, when this series is doped to increase the Curie temperature further, the mag-

netic entropy change quickly drops off. The reason for this is the change in the order of the magnetic phase transition from first- to second-order. Due to the large heat capacity of the manganite perovskites their ΔT_{ad} is quite low. For example, Dinesen showed that while $La_{0.67}Ca_{0.33}MnO_{3\pm\delta}$ has a ΔS_M that is a third larger than that of Gd, ΔT_{ad} for the manganite is half that of Gd [32].

Hysteresis is often present in the manganite perovskites, which present with first-order phase transitions. In some cases, the hysteresis is large, in some small. Again, different publications have reported conflicting data. As an example, $La_{0.7}Ca_{0.3}MnO_3$ has been reported to have a thermal hysteresis of almost 20 K [33] or ~ 1 K [34]. In the case of $La_{1-x}Sr_xMnO_3$ the crystal structure is orthorhombic for $x \lesssim 0.17$ and rhombohedral for larger values of x. Asamitsu *et al.* showed that a single-crystal sample with $x = 0.17$ has a hysteretic field-induced transition between the two crystal structures [35].

A small thermal expansion at the transition temperature is present in some manganite perovskites, such as *e.g.* $La_{0.75}Ca_{0.25}MnO_3$, which shows a volume change of $\Delta V/V \sim 0.13\%$ [36].

Depending on the composition the manganite perovskites could have low fabrication costs as they can be easily manufactured by an array of production methods and usually a single phase material can be obtained by sintering an appropriate amount of time. This also bodes well for the possibility of large-scale production and the possibility of shaping the perovskite materials. The cheapness of fabrication could, however, be compromised if an expensive raw material, such as *e.g.* the more costly rare-earths, is included. The toxicity will naturally also depend on the actual composition used for a perovskite magnetic refrigerant.

An advantage of the manganite perovskites is their stability. As they are ceramics, they do not corrode and are not particularly brittle. The stability will, of course, depend on the exact composition, production method and shape of the perovskite sample.

As should be clear by now it is difficult to generalize, when it comes to the manganite perovskites. In the case of evaluating their electrical resistivity and thermal conductivity, the different compositions have highly varied properties. Some perovskites are metallic in nature, while others are insulators. For example, the thermal conductivity of the materials series $Ca_{1-x}La_xMnO_3$ decreases as x is increased. While the thermal conductivity of $CaMnO_3$ is between 5 and 11 W/mK in the temperature range between $50-200$ K, $La_{0.5}Ca_{0.5}MnO_3$ has a thermal conductivity between 1.5 and 2.6 W/mK in the temperature range $180-330$ K [37, 38].

In summary, the manganites are fascinating materials as they present with many interesting effects due to their complex interactions. Examples of aspects not expanded upon here, are the significant Jahn-Teller effect of the Mn^{3+} ion in octahedral coordination and the possible charge ordering of the Mn electrons that takes place in *e.g.* Nd$_{0.5}$Sr$_{0.5}$MnO$_3$ at 155 K, which results in a large ΔS_M [39, 40]. With so many favorable properties for magnetic refrigeration and such a variety of possible compounds, the manganite perovskites are attractive and continue to be the focus of research. It should also be noted that only the manganite perovskites have been the subject of extensive research into their magnetocaloric properties and it is possible that a better magnetic refrigerant could be found with the non-manganite perovskites.

3.4 Gd$_5$(Si,Ge)$_4$ Materials

In 1997 Pecharsky and Gschneidner presented to the world the giant magnetocaloric effect of Gd$_5$Si$_2$Ge$_2$ [41–43]. Gd$_5$Si$_4$ orders ferromagnetically at 336 K, while Gd$_5$Ge$_4$ is an antiferromagnet with a Néel temperature of ~ 125 K [42, 44]. However, in the intermediate range of Gd$_5$(Si$_x$Ge$_{1-x}$)$_4$ with $0.24 < x < 0.5$ the material has a coupled magnetostructural first-order phase transition, which can be induced by temperature, an applied magnetic field or pressure [42, 45, 46]. During the structural transition the material goes from an orthorhombic structure at low temperature to a monoclinic one at high temperature. The temperature region of the structural transition is broad and the two phases co-exist within it [47]. As the transition can also be induced by an applied magnetic field, a large temperature region exists within which the magnetization curves become s-shaped and show remanence-free hysteresis. In the intermediate range, the first-order transition occurs at $125 - 276$ K. However, the magnetic properties of the Gd$_5$(Si,Ge)$_4$ are highly dependent on the purity of the Gd and how the sample was produced [48]. For this reason, it can be difficult to compare different samples of Gd$_5$(Si,Ge)$_4$ even though they are thought to have the same stoichiometry.

The Gd$_5$(Si,Ge)$_4$ materials show a large ΔS_M and a ΔT_{ad} of ~ 7 K for a change in applied magnetic field from 0 to 2 T, which is larger than that found for Gd.

A problem for the Gd$_5$(Si,Ge)$_4$ compounds is their hysteresis. The first-order phase transition shows a large magnetic and thermal hysteresis [41]. The thermal hysteresis is ~ 10 K for Gd$_5$Si$_2$Ge$_2$.

A very large temperature span is achievable with the Gd$_5$(Si,Ge)$_4$ compounds. Although the highest transition temperature of the first-order magnetostructural transition is ~ 276 K, this range can be increased by alloying with

small amounts of Ga, which has the effect of increasing T_C without reducing the magnetocaloric properties much [49].

A volume change of 0.4% takes place for the magnetostructural phase transition as the volume is smaller in the orthorhombic ferromagnetic than in the monoclinic paramagnetic phase [50]. Such a small change in volume is thought not to pose a problem for the use of $Gd_5(Si,Ge)_4$ compounds in a magnetic refrigeration device

A disadvantage of $Gd_5(Si,Ge)_4$ compounds besides their hysteresis is the inclusion of expensive raw materials such as Gd and Ge. It was also thought that the production of $Gd_5(Si,Ge)_4$ materials requires Gd with extremely high purity [48]. However, a large-scale process for manufacturing $Gd_5(Si,Ge)_4$ compounds from commercial grade Gd was described and patented by Gschneidner *et al.* [51, 52]. With regards to the malleability of the materials, Gschneidner *et al.* classify it as a negative property of the material without providing details on the matter [52].

The thermal conductivity of $Gd_5Si_2Ge_2$ is half that of Gd [53], which may prove to be too low a value, whereas corrosion is believed not to be an issue for $Gd_5(Si,Ge)_4$ compounds [54].

3.5   Magnetic NaZn$_{13}$-Structured Compounds

The magnetocaloric effect of $R(TM,SM)_{13}$ compounds, where R is a rare-earth metal, TM is one or more transition metals and SM is one of the semi-metals Si or Al, was first published by Hu *et al.* [55, 56] and Zhang *et al.* [57] in 2000. At this time, results had been published on the magnetocaloric properties of $Gd_5Si_2Ge_2$ and perovskite manganites near room temperature. Hu *et. al* published results on $LaFe_{11.4}Si_{1.6}$, $LaFe_{10.98}Co_{0.22}Si_{1.8}$, $LaFe_{11.12}Co_{0.71}Al_{1.17}$ and $La(Fe_{0.98}Co_{0.02})_{11.7}Al_{1.3}$, while Zhang *et al.* published on $LaFe_{10.6}Si_{2.4}$. $LaFe_{13}$ does not exist due to the positive heat of formation between La and Fe, but small amounts of Co, Si or Al can stabilize the compounds, which form in the cubic NaZn$_{13}$-structure [58, 59] illustrated in Fig. 3.3. The unit cell contains 8 formula units, *i.e.* 112 atoms, with a large atom such as La or Na in the $8a$ positions (Wyckoff notation). The smaller atoms such as Zn, Fe, Co, Si, Al are located in one of two sites, either the $8b$ positions or the $96i$ positions. The atoms in the $96i$ positions form regular icosahedra[1] surrounding the $8b$ positions. Thus, for each formula unit of *e.g.* $LaCo_{13}$, one Co atom will sit in the center of a regular icosahedron made up of the other 12 Co atoms.

---

[1]A polyhedron having 20 faces and 12 vertices.
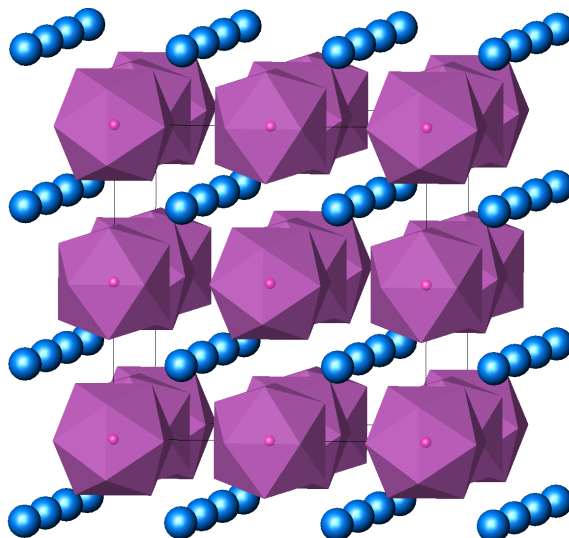
Figure 3.3: The cubic structure of NaZn$_{13}$. The large atoms (blue) sit interstitially in the 8a site between icosahedra of smaller atoms in the 96i site (purple), which surround a central smaller atom in the 8b site.

For all the magnetic NaZn$_{13}$-structured materials, the nature of their magnetization and their critical temperature is highly sensitive to the composition. Tables 3.1 and 3.2 provide a selection of magnetic NaZn$_{13}$-structured materials that demonstrates the variety of magnetic phases displayed by these compounds. A number of trends are clear, $e.g.$ when LaCo$_{13}$ is doped with Fe, Al or Si, the Curie temperature rapidly decreases. Replacing Co with Al leads to a drop in magnetic moment per 3d atom, whereas replacement by Fe leads to a rise [60].

As the La(Fe,Si)$_{13}$H$_y$ and La(Fe,Co,Si)$_{13}$ compounds are ferromagnets with Curie temperatures close to room temperature, these are the more promising of the NaZn$_{13}$-structured materials for room temperature magnetic refrigeration. Therefore, in the following we will consider only these compounds. The Al-containing compounds can also be made to have useful Curie temperatures, but the magnetization in these compounds is less than that of the Si-containing ones, which leads to smaller ΔS_M. In the case of the La(Fe,Si)$_{13}$H$_y$ materials, hydrogenation leads to increase in T_C, while maintaining both the first-order thermal-induced and first-order field-induced transition of La(Fe,Si)$_{13}$ [64].

ΔS_M for both the first-order La(Fe,Si)$_{13}$H$_y$ and second-order La(Fe,Co,Si)$_{13}$ compounds is larger than or comparable to that of Gd [64, 66]. The ferromagnetic NaZn$_{13}$-structured compounds can have quite sharp second-order

Compound	Type	Transition temperature [K]	Comments and Reference(s)
$LaCo_{13}$	FM	1290/1318	[60, 61][62]
$LaFe_xSi_{13-x}$ $10.5 \leq x \leq 11.5$	FM	$262 - 198$	Saturation moment decreases as Curie temperature increases [61].
$11.18 < x < 11.44$	FM	$207 - 195$	First-order itinerant-electron transition above T_C, which is induced by an applied magnetic field of about 1 T [63].
$LaFe_{11.44}Si_{1.56}$	FM	195	First-order phase transition [64].
$LaFe_{11.44}Si_{1.56}H_y$ $0.5 < y < 1.6$	FM	$233 - 323$	Hydrogen absorption leads to increase in T_C, while maintaining the first-order transition and a large magnetocaloric effect. [64].
$LaNi_{11}Si_2$	Pauli paramagnet		[61]

Table 3.1: Examples of $NaZn_{13}$-structured compounds and their varied magnetic properties. FM = ferromagnetic, AFM = antiferromagnetic.

Compound	Type	Transition temperature [K]	Comments and Reference(s)
LaFe$_x$Al$_{13-x}$ $5.98 \leq x \leq 8.06$	Mictomagnet	$T_f = 44.5$K ($x = 7.54$)	Also known as superparamagnets, mictomagnets contain ferro- or ferrimagnetically coupled domains that behave independently from one another and therefore mimic paramagnetism even though on a microscopic level they are ordered [65]. T_f is the freezing temperature. [65]
$8.06 < x \leq 11.18$	Soft FM	250 K for $x = 9.75$ and lower for the rest	[65]
$11.18 < x \leq 11.96$	AFM		
LaFe$_{11.9-x}$Co$_x$Si$_{1.1}$ $0.65 < x < 1.45$	FM	$255 - 346$	[66]
LaFe$_{10.98}$Co$_{0.22}$Si$_{1.8}$	FM	242	[55]
LaFe$_{11.12}$Co$_{0.71}$Al$_{1.17}$	FM	279	[55]
LaFe$_{11.47}$Co$_{0.23}$Al$_{1.3}$	FM	198	[56]
PrCo$_{13-x}$Si$_x$ $2.0 < x < 4.0$	FM	974-1060	[67]

Table 3.2: Examples of NaZn$_{13}$-structured compounds and their varied magnetic properties. FM = ferromagnetic, AFM = antiferromagnetic.

transitions from the ferromagnetic-to-paramagnetic state, which is surprising considering that the local environment of the Fe atoms is varying, which, as commented by Palstra *et al.*[61], one would expect to result in a distribution of exchange fields and therefore a phase transition that was smeared out. The La(Fe,Co,Si)$_{13}$ compounds, which generally have a smaller ΔS_M due to the magnetic phase transition being second-order, also have a smaller ΔT_{ad} than that of the La(Fe,Si)$_{13}$H$_y$ compounds. For a change in applied magnetic field from 0 to 2 T, LaFe$_{11.44}$Si$_{1.56}$H$_y$ compounds with $0 < y < 1.6$ have a ΔT_{ad} of ~ 6.5 K [68], while LaFe$_{11}$Co$_{0.9}$Si$_{1.1}$ shows a ΔT_{ad} of ~ 2 K [69].

A large magnetic hysteresis is seen during the magnetically induced first-order transition in the La(Fe,Si)$_{13}$H$_y$ materials produced by arc-melting [70]. In addition, a small thermal hysteresis of ~ 1 K is present in the same materials [71]. However, when hydrogenization is achieved by reactive milling it has been shown that the magnetic hysteresis in La(Fe,Si)$_{13}$H$_y$ is significantly reduced [72]. In the La(Fe,Co,Si)$_{13}$ compounds, which present with second-order phase transitions, no hysteresis, thermal or magnetic, is observed [66].

For much of the research on the La(Fe,Co,Si)$_{13}$ and the La(Fe,Si)$_{13}$H$_y$ compounds, the materials have been produced by arc-melting in an Ar atmosphere and subsequent heat treatment for 10 or more days [70, 73, 74]. However, reactive milling after arc-melting of La(Fe,Si)$_{13}$H$_y$ [72, 75] and powder metallurgy of La(Fe,Co,Si)$_{13}$ [66, 76] has shown that other production methods are available. In particular, the powder metallurgy method significantly reduces the production time and is well-suited for large-scale production. Further, it has been shown that it is possible to shape the La(Fe,Co,Si)$_{13}$ refrigerants as plates by using a decomposition and recombination process and conventional wire electrical discharge machining (EDM) [77].

The thermal conductivity of the La(Fe,Si)$_{13}$H$_y$ and La(Fe,Co,Si)$_{13}$ compounds is greater than that of Gd$_5$Si$_2$Ge$_2$, but comparable to that of Gd [53, 66, 68].

A disadvantage of the La(Fe,Co,Si)$_{13}$ and La(Fe,Si)$_{13}$H$_y$ compounds could be their volume contraction as the magnetic state is reduced [66, 78]. Whether the volume contraction poses a problem or not will depend on the actual magnetic refrigeration setup.

Another disadvantage of the La(Fe,Co,Si)$_{13}$ and the La(Fe,Si)$_{13}$H$_y$ compounds could be their brittleness and corrosiveness. As shown in section 5.3 corrosion is severe, when the materials are in contact with water and air. However, if the system can be sealed a solution of anti-freeze and water will work as cooling fluid without corroding the refrigerant. With regards to the brittleness, a 0.9 mm thick plate of La(Fe,Co,Si)$_{13}$ produced by powder metallurgy can be broken easily by hand.

It is worth mentioning that using pressure in conjunction with a magnetic field has been shown to lead to consecutive magnetic transitions in LaFe$_{11.57}$Si$_{1.43}$H$_{1.64}$ and an increase in ΔS_M [79]. Therefore, this may be a way of further improving the usefulness of the La(Fe,Si)$_{13}$H$_y$ compounds for room temperature magnetic refrigeration.

3.6 Summary

Properties of five much-studied magnetocaloric material groups for room temperature magnetic refrigeration have been presented. The findings are summarized in Table 3.3, which shows that all the materials have advantages and disadvantages. Although the five materials presented here far from constitute an exhaustive list of the candidate materials, no known material or material series stands out and it may be that an as yet unknown material will turn out to be the more suitable one for room temperature magnetic refrigeration.

	Gd	Gd$_5$(Si$_x$Ge$_{1-x}$)$_4$	Perovskite Manganites	La(Fe,Si)$_{13}$H$_y$	La(Fe,Co,Si)$_{13}$
Large ΔT_{ad}	+	+	-	+	-
Large ΔS_M	+	+	+	+	+
Lack of hysteresis	+	-	?	-/+	+
Temperature span	-	+	+	+	+
Thermal expansion	+	+	+	-	-
Fabrication costs	-	-	+	+	+
Large-scale production	+	+	?	+	+
Can be shaped	+	-	+	?	+
Electrical resistivity	?	?	?	?	?
Thermal conductivity	+	-	?	?	+
Toxicity	+	+	?	+	+
Stability	-	+	+	-	-

Table 3.3: Advantages and disadvantages of various room temperature magnetic refrigerants.

Chapter 4

Sample Characterization

In the following a brief description of a number of experimental methods that were used in the characterization of samples in the course of this thesis work is given. These include x-ray diffraction (XRD), vibrating sample magnetometry (VSM), Mössbauer spectroscopy, differential scanning calorimetry (DSC) and scanning electron microscopy (SEM). The listing is nearly ordered so that the participation of this author in the experiments using a given method is decreasing. In the case of XRD and VSM measurements preparation of the samples, handling and programming of the instrument and data analysis was all carried out by the author. When obtaining the Mössbauer spectra, the author helped preparing the sample and the instrumentation. The actual experiments were conducted by research technician H. Rasmussen, who supplied the data files. All subsequent analysis of the Mössbauer spectroscopy data was then done by this author. For DSC measurements, the sample was prepared by this author. The instrument responsible, C. Ancona-Torres, then prepared the instrumentation and handled it throughout the experiment. The transformation of the raw data into heat capacity data was also performed by C. Ancona-Torres. The act of this author was thereafter to interpret this data and correlate it with other obtained results. In the case of SEM, the sample was prepared by research technician J. S. Bang and the experiment performed by scientist M. Lundberg, who then supplied the mapping data. All subsequent analysis of the mapping data was then done by this author.

4.1   X-ray Diffraction (XRD)

X-ray diffraction (XRD) was used in this work to determine sample composition and lattice parameters. It is a non-destructive analysis that is performed by impinging photons with a wavelength in the range of $0.1 - 100$ Å on a sample and recording the intensity of the scattered photons. In the setup used for the analysis described in this thesis the so-called Bragg-Brentano configuration is used. In this configuration, the x-ray source and the detector are situated on the same circle with the sample surface being tangential to

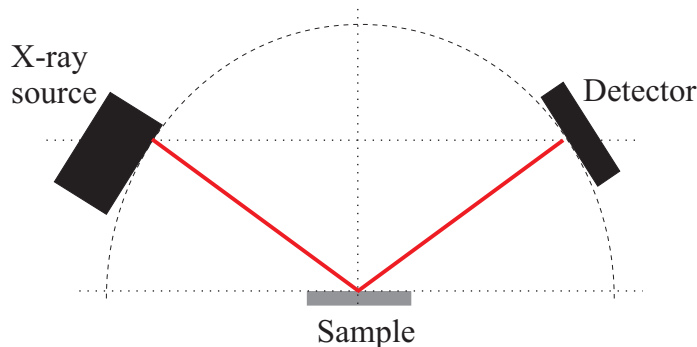the center of the circle, see Fig. 4.1. The in-house x-ray diffractometer is

Figure 4.1: Basic x-ray diffraction setup in Bragg-Brentano configuration.

a Bruker D8 Advance, which uses as its x-ray source Cu K_α radiation. In samples containing Fe, the use of Cu K_α x-rays will cause a large background of fluorescent radiation. This is due to the incoming x-rays being energetic enough to eject a photoelectron from the K-shell of the Fe atoms. As an electron from an L-shell falls into the vacancy in the K-shell, it emits its surplus energy as an x-ray photon with a wavelength of 1.937 Å [80]. The flourescent background from Fe atoms, can be eliminated by the use of a solid state detector, which analyzes the wavelength of the recorded photon and discards those which lie outside the set window. By setting the window closely around the Cu K_α wavelength of 1.542 Å, the pattern of a sample containing Fe is much improved, see Fig. 4.2.

After obtaining the patterns Rietveld refinement was used to analyze the data and extract the lattice parameters. For this analysis the software Fullprof was used [81].

4.1.1 X-ray Diffraction at Non-Ambient Temperatures

An option available with the in-house Bruker D8 Advance is recording patterns at non-ambient temperatures. For this purpose, the normal sample holder is replaced by a wide range temperature chamber. The chamber itself is evacuated using a BOC Edwards pump, which lowers the pressure to less than 1 mbar as required according to the included manual. Two Be windows in the chamber allow the x-rays to pass through them with only a small reduction in intensity, as Be is highly transparent to x-rays [82]. The sample is placed on a holder, which has both a heater and a cold finger in thermal contact with it. In this way the temperature can be regulated and even programmed, so that a series of measurements at different temperatures can be obtained.
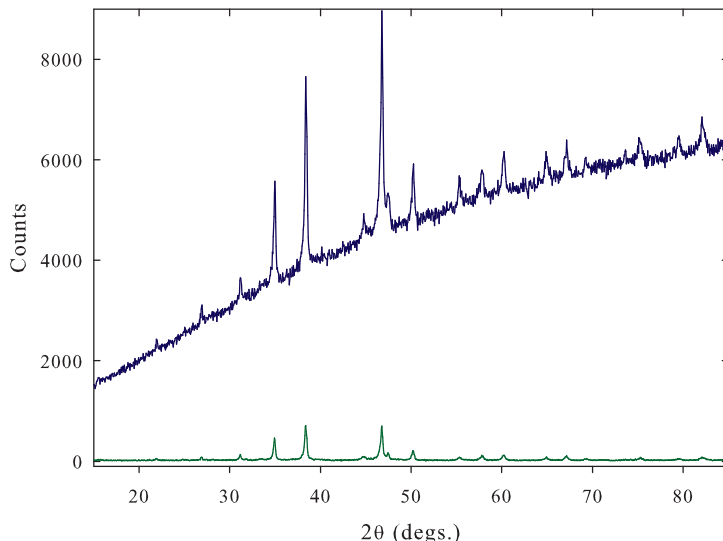
Figure 4.2: X-ray diffraction patterns of a sample of La(Fe,Co,Si)$_{13}$ (sample no. 4 in chapter 5) recorded using two different detectors: one, which does not distinguish the wavelength of incoming photons, and a solid state detector, which discards photons with a wavelength outside a set range. The two scans were recorded at room temperature with similar experimental parameters such as step size, divergence and scattering slits, and recording time at each step.

4.2 Vibrating Sample Magnetometer (VSM)

The in-house VSM is a LakeShore 7407, see Fig. 4.3, fitted with a low-temperature cryostat, which has a built-in heater so that a large temperature range can be achieved. In all measurements, the cryostat was cooled with liquid nitrogen allowing for stable temperatures between 80 and 450 K. Samples to be studied are mounted on a sample rod, which is positioned between the poles of an electromagnet capable of producing a field of $H_{max} = 1.59$ T at the sample position when the cryostat is mounted. Between the sample and the magnet poles are placed two pick-up coils. As the sample is driven up and down sinusoidally by a speaker head its magnetization will induce a voltage in the pick-up coils. This signal is then translated into a magnetization by the accompanying software.

Three types of experiments were conducted for the characterizations reported on in this thesis: hysteresis curves, magnetization as a function of temperature and sets of initial magnetization curves. For the hysteresis curves, an initial curve was also measured, so that the magnetization is recorded as the applied field is ramped in the following sequence: $0 \rightarrow H_{max} \rightarrow -H_{max} \rightarrow$
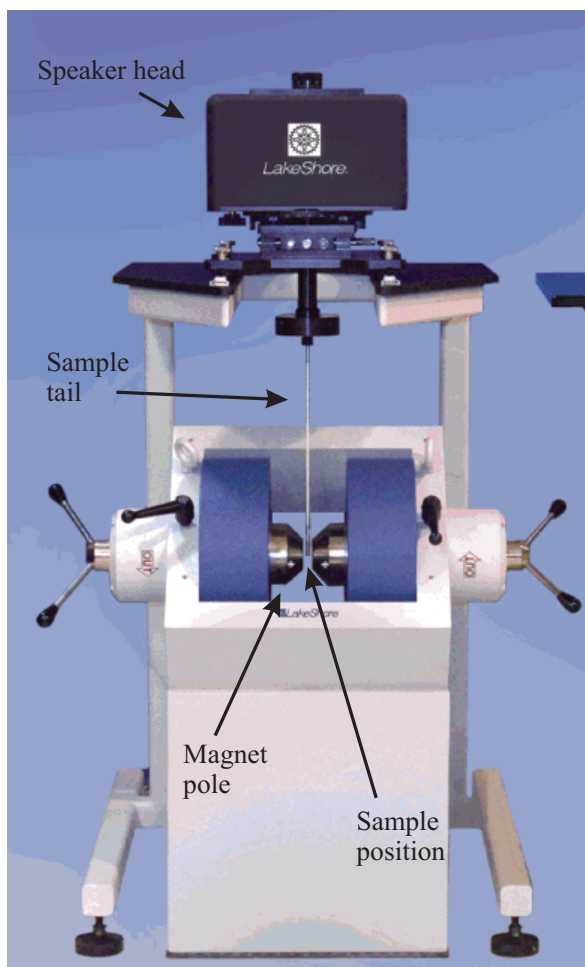
Figure 4.3: Photograph of the LakeShore 7400 series VSM (from http://lakeshore.com/).

H_{max}. The reason an initial curve was also measured is that the VSM software would otherwise ramp the applied field quickly to H_{max}, which could cause heating in the sample due to the magnetocaloric effect. For measurements of the magnetization as a function of temperature a start and end temperature is set as well as a temperature interval. Usually a low magnetic field, *e.g.* 0.01 T, is applied at the beginning of these measurements and this field is kept constant for the duration of the measurement. To indirectly determine ΔS_M a set of isothermal initial curves, where the applied field is ramped from $0 \rightarrow H_{max}$, while the temperature is kept constant, is required. From these one can calculate ΔS_M by numerical integration. This procedure is described in section 4.2.3, which deals with a Matlab program that was written by this author for the very purpose of calculating ΔS_M from sets of isothermal initial curves.

The initial curve and hysteresis data can be recorded in two ways, either in point-by-point or in continuous mode. In point-by-point mode, the VSM software ramps the field to fixed values specified by the maximum applied field and number of points. In this case, the sweep-rate is low enough that, for the materials studied here, heating of the sample does not occur due to the magnetocaloric effect. When dealing with continuous mode measurements, however, care must be taken not to cause heating in the sample as the field is then ramped with a constant sweep-rate, while the magnetization is measured at approximate intervals. This heating during continuous magnetization measurements is the topic of paper III included in part II and here it is shown how the heating of the sample during continuous measurements can lead to very different recordings of the magnetization than those intended. If ΔS_M is then calculated from these faulty magnetization data, wrong values are obtained.

4.2.1   Thermocouple Setup

Sample holders for the VSM are ready-made for specific samples, whether powder, bulk or thin-film. An original setup was made to mount an E-type thermocouple in-between a bulk sample and the sample rod for measuring the sample temperature during the magnetization measurement. The thermocouple wire was attached to a VSM sample rod using tape, while the junction was attached to the end of the sample rod using double-sided Scotch tape to which the sample was also attached, so that the thermocouple was sandwiched between the tape and sample, see Fig. 4.4. The type E Quick Connect thermocouple from Omega Engineering, Inc. was connected to a TC-08 thermocouple data logger from Pico Technology, which logged the temperature at chosen time intervals. This thermocouple setup was used during the magne-
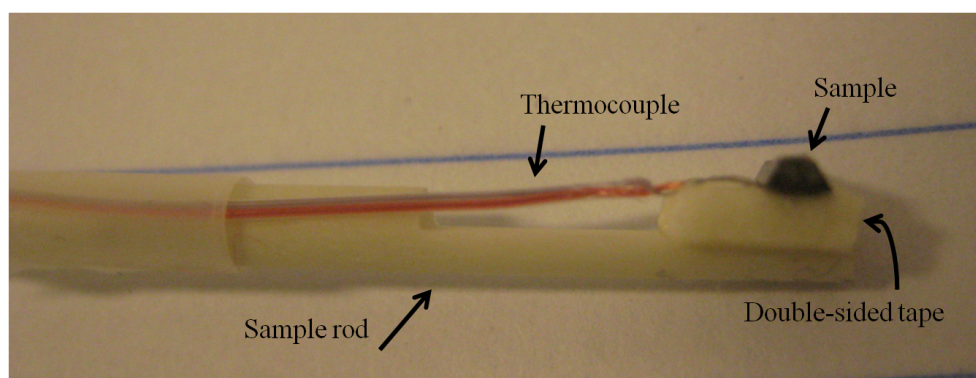

Figure 4.4: Thermocouple setup, where the thermocouple junction is sandwiched between double-sided tape and the sample.

tization measurements performed on the La(Fe,Co,Si)$_{13}$ samples, see chapter 5, and for the measurements presented in paper III.

4.2.2 Demagnetization

When a material of finite size is magnetized a so-called demagnetization field results from the distribution of surface charges [83]. This demagnetization field is, in general, directed opposite to the magnetization, hence the name. In the case of an ellipsoid the demagnetization field is uniform, something which is not true for any other finite shape [84]. If demagnetization is corrected for, one obtains the internal field, H_i, which is given by

$$H_i = H_a - N \cdot M, \tag{4.1}$$

where H_a is an applied field, M the magnetization and N the demagnetization factor. In the measurements performed on the La(Fe,Co,Si)$_{13}$ samples, see chapter 5, an approximate demagnetization factor was used to correct the raw data. The samples were all oblong in shape and the demagnetization factor of a rectangular cuboid as calculated by Aharoni [85] was used,

$$
\begin{aligned}
N \;=\; & \frac{1}{\pi}\left(\frac{b^2-c^2}{2bc}\ln\left(\frac{\sqrt{a^2+b^2+c^2}-a}{\sqrt{a^2+b^2+c^2}+a)}\right) + \frac{a^2-c^2}{2ac}\ln\left(\frac{\sqrt{a^2+b^2+c^2}-b}{\sqrt{a^2+b^2+c^2}+b}\right)\right. \\
& + \; \frac{b}{2c}\ln\left(\frac{\sqrt{a^2+b^2}+a}{\sqrt{a^2+b^2}-a}\right) + \frac{a}{2c}\ln\left(\frac{\sqrt{a^2+b^2}+b}{\sqrt{a^2+b^2}-b}\right) \\
& + \; \frac{c}{2a}\ln\left(\frac{\sqrt{b^2+c^2}-b}{\sqrt{b^2+c^2}+b}\right) + \frac{c}{2b}\ln\left(\frac{\sqrt{a^2+c^2}-a}{\sqrt{a^2+c^2}+a}\right) \\
& + \; 2\arctan\left(\frac{ab}{c\sqrt{a^2+b^2+c^2}}\right) + \frac{a^3+b^3-2c^3}{3abc} + \frac{a^2+b^2-2c^2}{3abc}\sqrt{a^2+b^2+c^2} \\
& + \; \frac{c}{ab}\left(\sqrt{a^2+c^2}+\sqrt{b^2+c^2}\right) - \left. \frac{(a^2+b^2)^{3/2}+(b^2+c^2)^{3/2}+(c^2+a^2)^{3/2}}{3abc}\right).
\end{aligned}
\tag{4.2}
$$

The dimensions of the cuboid is a, b, c and the magnetic field is applied along the $c-$axis. Due to the shape not being ellipsoid, the demagnetization field within the samples will not be uniform and the value of the internal field calculated is an average value [84]. The correction of the raw data was accomplished by a Matlab program, that was written for the calculation of the magnetic entropy change from sets of isothermal magnetization curves. This program is presented in the section following this one.

Ferromagnetic materials form domains, if possible, within which the magnetization is uniform, but between which the magnetization is at an angle. This allows the material to reduce its macroscopic magnetization and thereby

lower its energy [83]. When a magnetic field is applied, the domains having a magnetization in the direction of the field will grow, while the rest will diminish. Unless anisotropies or inhomogeneities are present, which can pin the magnetization to the new direction, the domains will reappear when the applied field is removed. If domain structure is present in the material, it will require a certain applied field, before the domains are all aligned. Before this field is reached, the internal field calculated using Eq. (4.1) will be negative if the macroscopic magnetization is used in place of M. To account for this phenomenon the data with $H_i < 0$ is removed in the Matlab program before the calculation of ΔS_M.

4.2.3 Description of Matlab Program for Analysis of Magnetization Data

A Matlab program was written to analyze recorded magnetization data and calculate ΔS_M from isothermal magnetization curves. Following is a description of the program and its outputs, while the source code can be found in appendix A.

The program reads an initialization file with sample information provided by the user. The initialization file is a simple text file with sample specific data and input on the internal fields at which the program shall extract the magnetization and calculate ΔS_M. An example of the input file is given in appendix A.2. After reading the sample information, the program reads the data files stored in the same directory as the initialization file. The demagnetization factor for a rectangular cuboid as given by Aharoni [85] is calculated and used to correct the data for demagnetization. Afterwards, the data for $H_i < 0$ are removed and the data is interpolated with a field step size of 5 mT. During execution, the program creates a number of figures. The first is a graph of the raw magnetization data, the data corrected for demagnetization and the interpolated magnetization data, see Fig. 4.5. The next step in the program is the calculation of ΔS_M, which is given by

$$\Delta S_M(T, \Delta H) = \mu_0 \int_{H_1}^{H_2} \left(\frac{\partial M}{\partial T} \right)_{p,H} dH \qquad (4.3)$$

as shown in chapter 2. To calculate ΔS_M we need as many data points in the space (M, T, H) as possible. As it is faster to vary the applied magnetic field, while keeping the temperature fixed, this is the preferred method for obtaining the magnetization data. If the data is recorded with sufficiently small intervals one can make use of the approximation

$$\Delta S_M(T_{av}, H_1 \rightarrow H_2) = \mu_0 \int_{H_1}^{H_2} \frac{M_{i+1} - M_i}{T_{i+1} - T_i} dH, \qquad (4.4)$$
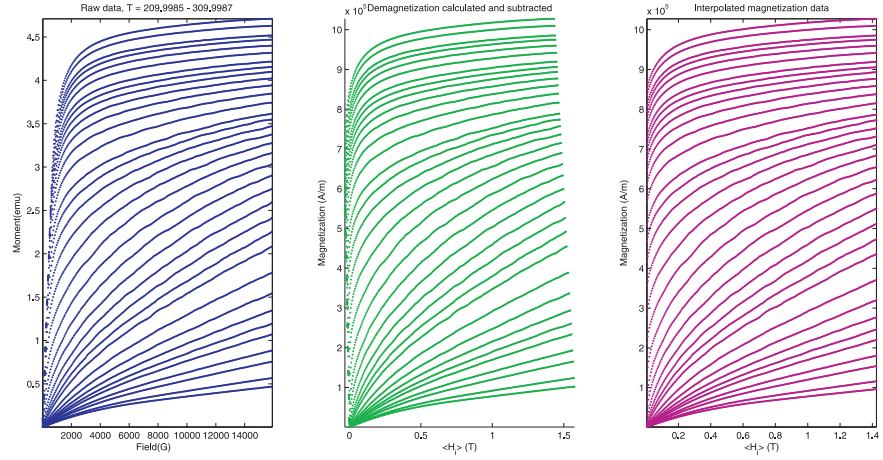
Figure 4.5: Figure output by Matlab program showing the raw magnetization data, the data corrected for demagnetization and the interpolated magnetization data for a sample of $La(Fe,Co,Si)_{13}$ (sample no. 2 in chapter 5).
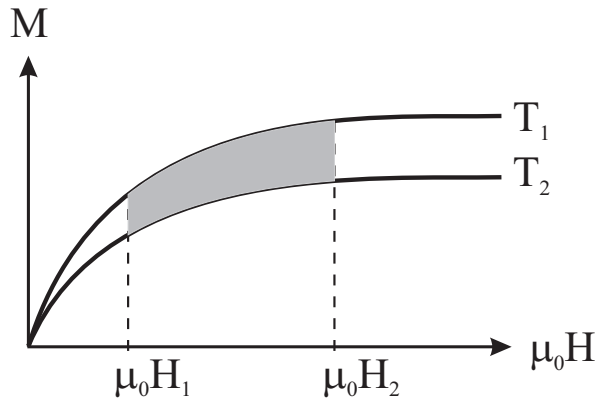
Figure 4.6: Two isothermal magnetization curves of a ferromagnetic material. The area shown in grey is the magnetic entropy change for the average temperature given by $T_{av} = \frac{T_2 + T_1}{2}$ and for a change in the magnetic field from H_1 to H_2. This area is calculated by numerical integration in the Matlab program.

where $T_{av} = \frac{T_{i+1} + T_i}{2}$. If we look at a plot of M versus H for different values of T, see Fig. 4.6, $\Delta S_M(T_{av}, H_1 \rightarrow H_2)$ is given by the area shown in grey. The Matlab program calculated this area using numerical integration. For this, the function `cumsimpson` written by D. C. Hanselman and shared on Matlab Central (http://www.mathworks.com/matlabcentral/) is used. The function is included in the source code in appendix A. Although one could calculate
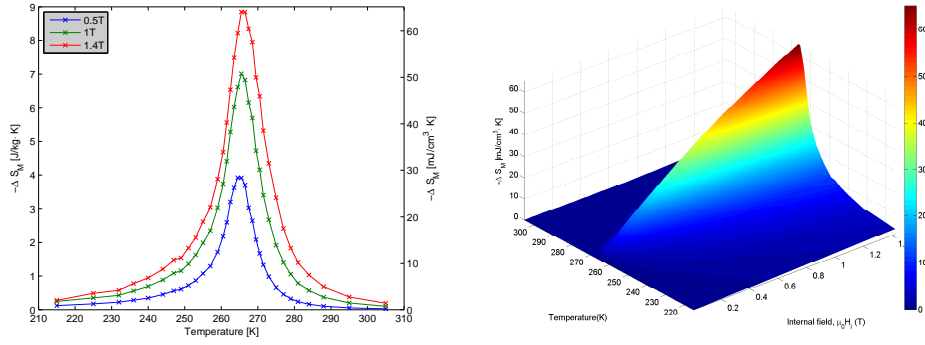
Figure 4.7: Plots generated by the Matlab program showing the calculated ΔS_M for a range of internal fields in 2D and 3D for a sample of La(Fe,Co,Si)$_{13}$ (sample no. 2 in chapter 5).
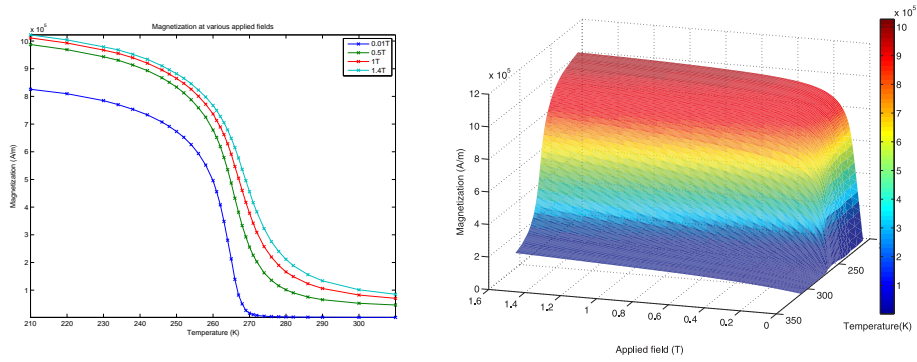
Figure 4.8: Plots generated by the Matlab program showing the magnetization for a range of applied magnetic fields in 2D and 3D for a sample of La(Fe,Co,Si)$_{13}$ (sample no. 2 in chapter 5).

ΔS_M for a change in the magnetic field from a non-zero value, the program only calculates from zero and up to the fields given in the initialization file. This calculation is done for internal fields and the output is two figures, a 2D and a 3D plot, see Fig. 4.7. The magnetization is also plotted in 2D and 3D for the applied fields supplied in the initialization file, see Fig. 4.8. Finally, the program creates a so-called Arrott plot for mean-field values of the critical exponents, *i.e.* an H/M versus M^2 plot, see Fig. 4.9. A description of the background of the Arrott plot will follow and introduce the critical exponents that characterize a continuous phase transition.

The Arrott plot is based on the Arrott-Noakes equation of state for ferro-
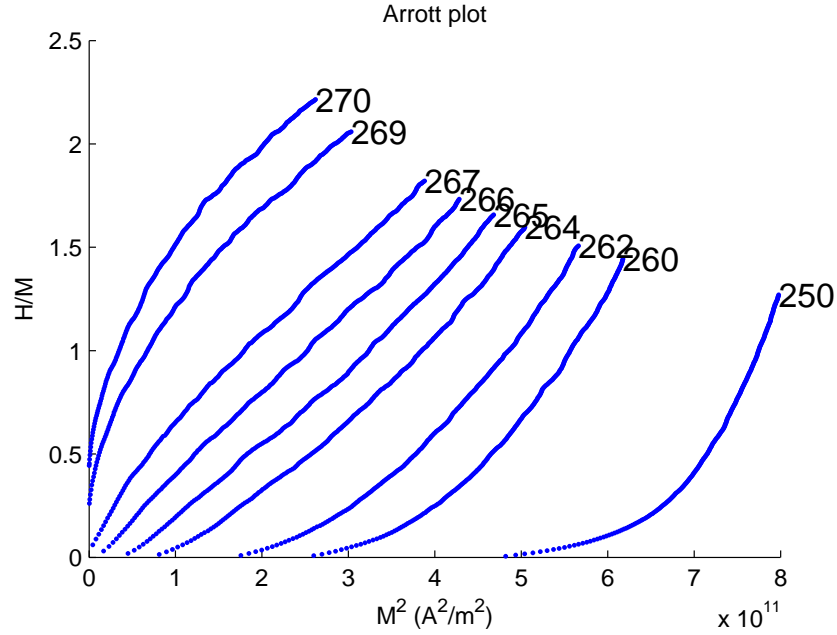
Figure 4.9: Arrott plot generated by the Matlab program for a sample of La(Fe,Co,Si)$_{13}$ (sample no. 2 in chapter 5).

magnetic materials [86]:

$$\left(\frac{H}{M}\right)^{\frac{1}{\gamma}} = \frac{T - T_C}{T_1} + \frac{T}{T_2}\left(\frac{M}{M_0}\right)^{\frac{1}{\beta}}, \qquad (4.5)$$

where M_0 is the spontaneous magnetization at the absolute zero of temperature, T_1 and T_2 are material specific values and γ and β are critical exponents. Near continuous phase transitions a number of physical quantities can be described by their critical exponents. The critical exponents depend on only three properties of the system:

- the dimensionality of the system, d

- the dimensionality of the order parameter, D

- the range of the interaction (short- or long-range)

Since these properties may be the same across a number of otherwise different systems, which will then have the same critical exponents, the exponents are said to be universal. The systems must have a continuous phase transition and be characterized by an order parameter, which is zero above the transition

and non-zero below. For magnetic systems the order parameter is the (sub-lattice) magnetization, M, and the critical exponents describe the behavior of the quantities shown in Table 4.1 near the magnetic transition temperature. The values of the critical exponents can be calculated theoretically and Table

Critical exponents for the disordered phase ($\tau > 0$)	
Susceptibility	$\chi \propto (T - T_c)^{-\gamma}$
Specific heat	$C \propto (T - T_c)^{-\alpha}$
Correlation length	$\xi \propto (T - T_c)^{-\nu}$

Critical exponents for the ordered phase ($\tau < 0$)	
Magnetization	$M \propto (T - T_c)^{\beta}$
Susceptibility	$\chi \propto (T - T_c)^{-\gamma'}$
Specific heat	$C \propto (T - T_c)^{-\alpha'}$
Correlation length	$\xi \propto (T - T_c)^{-\nu'}$

Critical exponents at the transition ($\tau = 0$)	
Equation of state	$M \propto H^{1/\delta}$

Table 4.1: Critical exponents for a magnetic system. The reduced temperature, τ, is given by $\frac{T_c}{T - T_c}$. The applied field, H, must be zero when determining the exponents save for δ.

4.2 lists values for the critical exponents for different dimensionalities of the system and order parameter. From Table 4.2, we find that for a system that

	2d-Ising ($D = 1$)	3d-Ising ($D = 1$)	3d-Heisenberg ($D = 3$)	Mean-field ($d \geq 4$)
α				
β	$^1/_8$	0.326	0.367	$^1/_2$
γ	$^7/_4$	1.2378(6)	1.388(3)	1
δ	15	4.78	4.78	3
ν				

Table 4.2: Theoretical values of critical exponents for various systems [83]. d is the dimensionality of the system and D the dimensionality of the order parameter, which in a magnetic system is the magnetization. Therefore, D is the dimensionality of the spins.

can be described using mean-field theory, *i.e.* one where the behavior can be described by an average or effective interaction between the spins, the values of γ and β are 1 and $^1/_2$, respectively. Using these values, the Arrott-Noakes equation takes on the form:

$$\left(\frac{H}{M}\right) \propto \left(\frac{M}{M_0}\right)^2 . \tag{4.6}$$

If the critical exponents are correct, the Arrott plot will result in straight lines for large values of M^2 at and near T_C. As Arrott describes it himself, rather figuratively,

> The coat does not fit everywhere, but it fits well in the shoulders, which means near the critical isotherm, giving a series of rather evenly spaced straight isotherms on a plot of $\left(\frac{M}{M_S}\right)^{\frac{1}{\beta}}$ against $\left(\frac{H}{M}\right)^{\frac{1}{\gamma}}$. The sleeves are too long and it looks bad near the axes.
> - A. S. Arrott in "Equations of State Along the Road to Arrott's Last Plot" [87]

From the description given it is clear that the Arrott plot can be used to determine the Curie temperature and critical exponents of a ferromagnetic material. In the output generated by the Matlab program, however, the assumption is that the system can be described using mean-field theory.

Finally, the program writes text output files, where the calculated data is arranged in columns for easy extraction, see examples in appendix A.3.

4.3 Direct Measurement of the Adiabatic Temperature Change

A device for directly measuring ΔT_{ad} was constructed by R. Bjørk at Risø DTU [88], see Fig. 4.10. The instrument has a pneumatic piston, which moves the sample in and out of a permanent magnet array. The magnet consists of two concentric cylindrical Hallbach arrays, which allows one to adjust the resulting field at the core of the assembly by rotating the two magnets in relation to each other, see *e.g.* [89]. A freezer, inside which the magnet and piston are placed, cools the whole setup before an experiment begins. After the initial cooling done by the freezer, its cooling is turned off and the internal temperature is increased by a 75 W light bulb and thermal diffusion. While the temperature is slowly increasing the sample is moved in and out of the magnet array. Attached to the sample is a type E Quick Connect thermocouple from Omega Engineering, Inc., which is connected to a TC-08 thermocouple data logger from Pico Technology that logs the temperature at chosen time intervals.

The raw data is the temperatures recorded by the thermocouple as a function of time. A Matlab program written by R. Bjørk extracts the sample temperature before and after the magnetic field is applied to the sample. From
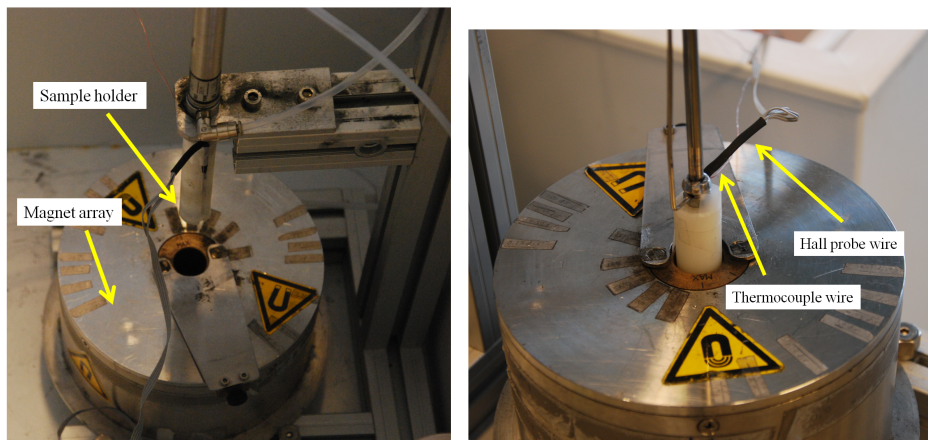
Figure 4.10: Home-made device for directly measuring ΔT_{ad}. Left: photograph showing the permanent magnet and the sample holder. Also seen is part of the pneumatic piston system, which will drive the sample positioned in the bottom of its holder into the magnetic field at the core of the permanent magnet. Right: photograph of the sample holder positioned within the core of the permanent magnet.

this, two curves of ΔT_{ad} as a function of temperature result, one for when the field is applied and one for when the field is removed. The two curves will differ as it makes a difference whether the field is applied or removed at a given temperature, as illustrated in Fig. 4.11 and described in the accompanying figure text.

4.4 Mössbauer Spectroscopy

Mössbauer spectroscopy was used in this thesis work to study a sample of $Gd_3Fe_5O_{12}$. The spectrometer used is located at the Mössbauer laboratory at DTU Physics and consists of a $^{57}Co/Rh$ source and a proportional counter in transmission geometry.

Mössbauer spectroscopy is a nuclear spectroscopy with an energy resolution high enough to resolve the hyperfine structure of nuclear levels. For ^{57}Fe Mössbauer spectroscopy the basic experimental setup consists of a ^{57}Co source, which can be moved back and forth, the sample to be studied and a γ-detector, see Fig. 4.12. ^{57}Co is unstable and decays to ^{57}Fe, which will be in an excited state. When the excited ^{57}Fe nucleus decays it does so by emission of a γ-photon. As the source is moved back and forth the emission line is Doppler shifted, so that a range of γ-photon energies is obtained. γ-photons are then directed at the sample and those transmitted through the sample are
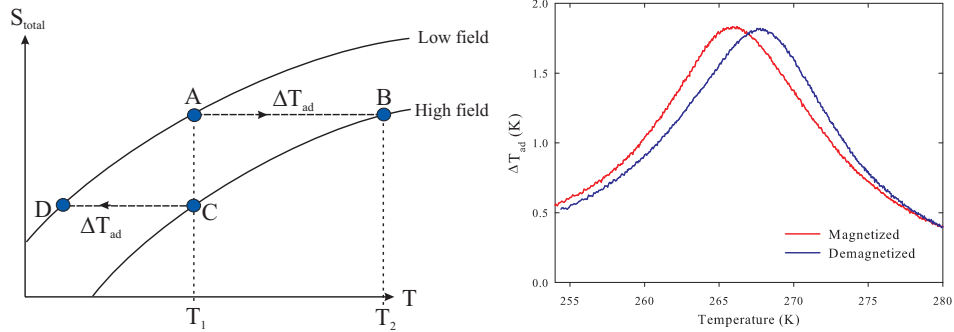
Figure 4.11: Left: Illustration of why two curves result from a direct measurement of the adiabatic temperature change, one for when the field is applied and one for when the field is removed. Starting from A and ending up at B, does not equal the route C→D. The two curves will be shifted by ΔT_{ad} as the same value of ΔT_{ad} will be obtained by removing the field at temperature T_2 as by applying it at the temperature T_1. Right: Direct measurement of ΔT_{ad} on a sample of La(Fe,Co,Si)$_{13}$ (sample no. 2 in chapter 5) for an applied/removed magnetic field of 1 T.

recorded in a detector. The resulting Mössbauer spectrum shows the absorption of γ-quanta as a function of the source velocity, see Fig. 4.12. The sample should contain enough ^{57}Fe to give a usable spectrum in a reasonable time, but not so much sample as to result in significant non-resonant absorption of the γ-quanta. The abundance of ^{57}Fe is $\sim 2\%$ of naturally occurring isotopes of Fe.

As the energies of the ^{57}Fe nuclear ground state and excited state will shift and split due to the effects of the nuclear environment, the Mössbauer spectrum can give information on *e.g.* valency, coordination and the effective magnetic induction at the nucleus. In ^{57}Fe Mössbauer spectroscopy the ground state has nuclear spin $I = \frac{1}{2}$ and therefore $2I + 1 = 2$ sublevels, while the excited state with a difference in energy from the ground state of 14.4 keV has $I = \frac{3}{2}$ and therefore four sublevels. Due to selection rules only six transitions between the sublevels are allowed. If a magnetic field is applied perpendicular to the $\gamma-$rays all six transitions are allowed, whereas a field applied parallel to the γ-rays results in only four transitions being allowed. The γ-quanta with an energy that matches the energy of a nuclear transition will be absorbed, see Fig. 4.13.

After obtaining the Mössbauer spectrum a fitting of the lines will give the values of three important quantities: the isomer shift, the quadrupole splitting and the magnetic hyperfine splitting. The isomer shift of the excited state relative to that of metallic Fe at room temperature is a measure of the
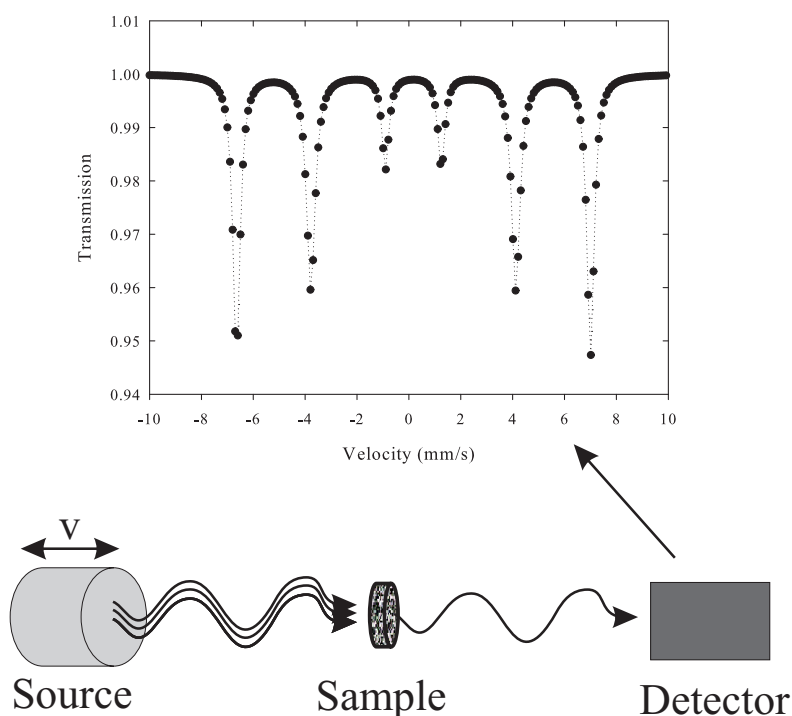
Figure 4.12: Basics of a Mössbauer spectroscopy setup.

density of s-electrons at the Fe-nucleus and gives information on the oxidation state and chemical bonding of the Fe-atom. The value of the isomer shift will indicate the valency of the Fe-atom and also indicate whether the Fe-atom is in a high-spin or low-spin state. If the ^{57}Fe nucleus is aspherical, its charge distribution can be described by a quadrupole moment, and it will be affected by the surrounding electrostatic field, which will cause a splitting of the excited state. This is the quadrupole splitting, which is proportional to the electric field gradient at the nucleus. The quadrupole splitting can be decomposed into two contributions, one from the crystal field, i.e. the lattice, and one from the $3d$ valence electrons of the Fe-atom. The size and temperature dependence of the quadrupole splitting will, in combination with the value of the isomer shift, reveal the valency and spin-state of the Fe-atom. Finally, an effective magnetic induction acting on the nucleus will cause a splitting of all sublevels and six lines will appear in the Mössbauer spectrum. The effective magnetic induction is given by

$$B = B_a + B_{orb} + B_D + B_C, \tag{4.7}$$

where B_a is an applied external magnetic induction, B_{orb} is the contribution from the electrons orbital momentum and B_D is a contribution from the moment of the spins outside the nucleus. Finally, B_C comes from the electron spin-density of the s-electrons at the nucleus and is the largest contribution

to B. Fig. 4.13 shows the shifting and splitting of the ^{57}Fe nuclear sublevels due to magnetic and quadrupole interactions.
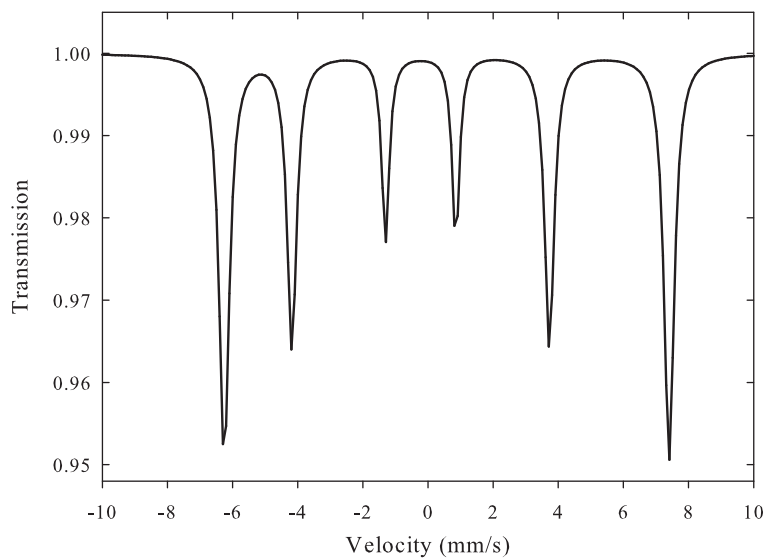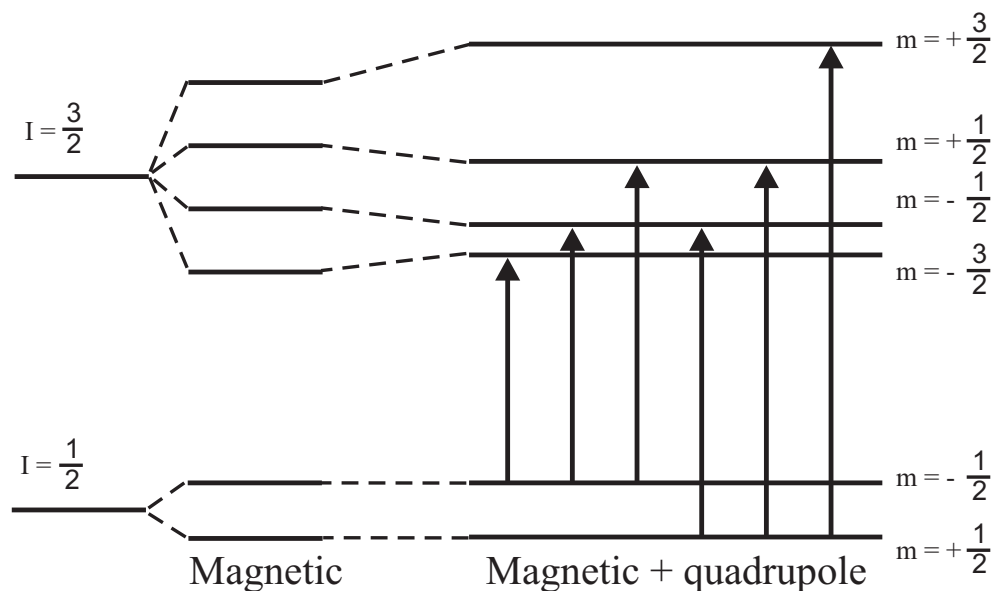

Figure 4.13: Effect of magnetic and quadrupole interactions on the subleves of the ^{57}Fe nucleus.

4.5 Differential Scanning Calorimetry (DSC)

The calorimetric data presented in this thesis were all obtained on a home-made DSC constructed by S. Jeppesen and a detailed description of the instrument can be found in ref. [90]. A DSC measures the thermal response of the sample to a uniform heat flow [91]. The sample is placed on a temperature sensor, which has two positions, see Fig. 4.14. One is called the sample position and the other the reference position. If the sample is placed inside a holder of some kind, an empty identical holder is placed in the reference position, so that the sole difference between the two is the sample to be studied. The heat flow sensor is situated inside the DSC unit surrounded by large amounts of heat shielding and a system for regulating the temperature of the sample chamber. During the measurement a uniform heat flow is supplied identically to the sample and reference positions, while the sensor measures the difference in temperature between the two. This is the differential heat
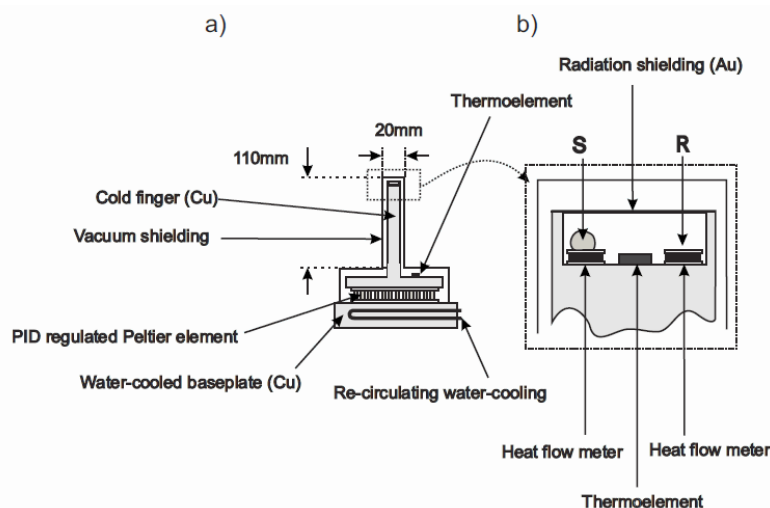
Figure 4.14: Schematic of the measuring unit of the home-made DSC (from [90], for details see reference). (a) The complete DSC unit and (b) a close-up of the sample holder.

flow signal. To calculate the heat capacity of the sample three DSC signals are required: (1) a baseline, which is obtained by having the sample position as well as the reference position empty, (2) a standard, such as sapphire (Al_2O_3) or Cu and (3) a sample. When these are at hand the heat capacity, c_p, of the sample can be calculated from the three equations for the heat flow changes:

$$\left(\frac{dq}{dt}\right)_{\text{empty}} = K \cdot m_i \cdot c_{p,i} \left(\frac{dT}{dt}\right), \tag{4.8}$$

$$\left(\frac{dq}{dt}\right)_{\text{standard}} = (m_i \cdot c_{p,i} + m_{\text{standard}} \cdot c_{p,\text{standard}}) \left(\frac{dT}{dt}\right), \tag{4.9}$$

51

$$\left(\frac{dq}{dt}\right)_{\text{sample}} = (m_i \cdot c_{p,i} + m_{\text{sample}} \cdot c_{p,\text{sample}}) \left(\frac{dT}{dt}\right). \qquad (4.10)$$

Here, $\frac{dq}{dt}$ is the heat flow signal and $\frac{dT}{dt}$ is the heating rate. The subscript i refers to the instrument. From the three equations, we find that

$$c_{p,sample}(T) = c_{p,\text{standard}}(T)\frac{m_{\text{standard}}}{m_{\text{sample}}} \cdot \frac{DSC_{\text{sample}}(T) - DSC_{\text{empty}}(T)}{DSC_{\text{standard}}(T) - DSC_{\text{empty}}(T)}. \qquad (4.11)$$

The magnet array described in section 4.3 can be used together with the home-made DSC, so that the heat capacity can be determined for different applied magnetic fields up to 1.5 T.

The heat capacity is ultimately a function of the free energy of the system. Therefore, in the case of magnetic materials, discernable changes in the heat capacity is often observed close to the phase transition temperature. In the case of a ferromagnetic-to-paramagnetic phase transition, applying a magnetic field will often broaden the transition and shift the transition temperature, see Fig. 4.15.
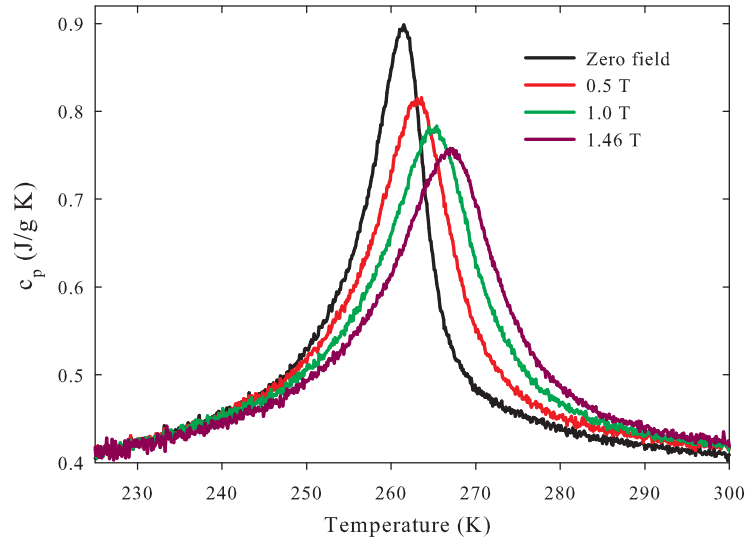

Figure 4.15: Heat capacity of La(Fe,Co,Si)$_{13}$ (sample no. 2 in chapter 5), which presents a ferromagnetic-to-paramagnetic phase transition. The heat capacity reflects the fact that the larger an applied magnetic field is, the broader the transition and the greater the shift in transition temperature will be.

From the heat capacity at constant applied field it is also possible to cal-

culate ΔS_M as the heat capacity at constant applied magnetic field, c_H, is given by

$$c_H = T \left(\frac{\partial S}{\partial T} \right)_H .$$ (4.12)

From this, we find that

$$S_H(T) = \int_0^T \frac{c_H}{T} dT$$ (4.13)

and so

$$\Delta S_M(T, H_1 \rightarrow H_2) = S_{H_2}(T) - S_{H_1}(T) = \int_0^T \frac{c_{H_2}}{T} dT - \int_0^T \frac{c_{H_1}}{T} dT.$$ (4.14)

The calculation of ΔS_M from heat capacity measurement thus require measurements from as close to absolute zero as possible. The home-made DSC used for the measurements presented in this thesis cannot cool the sample below ~ 220 K. However, one might make the assumption that away from the phase transition the heat capacity will be the same for zero and non-zero applied fields, but this procedure was not investigated.

4.6   Scanning Electron Microscopy (SEM)

The SEM measurements presented in this thesis were made on a Zeiss Supra 35 SEM. In an SEM an electron gun provides a beam of electrons, which is directed at the sample to be studied. A number of lenses help focus the beam, the size of the beam being the lower limit of the spatial resolution [92]. The electron beam is scanned across the surface of the sample in a raster pattern and, depending on the detector used, a number of imaging techniques are available. Using the backscattering detector one can record the electrons reflected by elastic scattering and an electron detector records the secondary electrons emitted after inelastic scattering. Backscattered electrons are better suited for obtaining contrast between areas with different elemental composition, while secondary electrons, which escape from a shallower depth, are better suited for giving depth to the image. Elemental analysis may be performed by measuring the x-rays resulting from ionization using energy dispersive spectroscopy (EDS). As the electrons strike the sample they interact with a volume close to the surface, the so-called interaction volume, see Fig. 4.16. The size of this volume depends on the energy of the electrons and sample specific properties such as density. Some advantages of SEM are resolutions of $1 - 10$ nm and a large depth of field, which means that a large portion of the image will appear sharp.

Electron beam

Secondary
electrons

Characteristic
x-rays

Backscattered
electrons

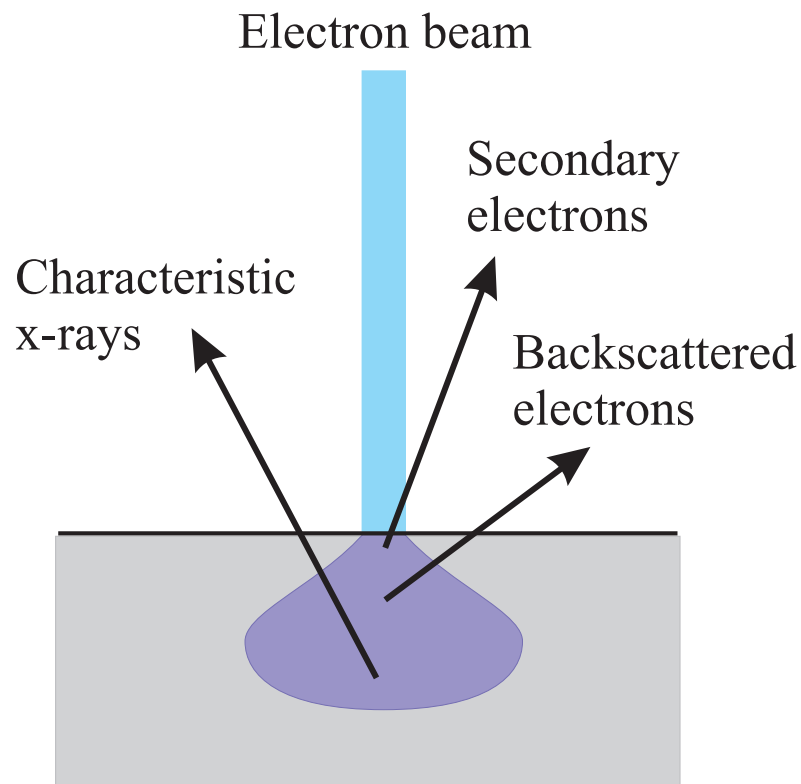Figure 4.16: Illustration of the interaction volume with the origin of the backscattered electrons, secondary electrons and characteristic x-rays indicated. Secondary electrons that can be detected escape from a depth of $1-10$ nm, while the backscattered electrons probe a larger information depth. The characteristic x-rays are excited in the volume, where the electron energy is larger than the required ionization energy [92].

Chapter 5

$La(Fe,Co)_{11.9}Si_{1.1}$ - a Room Temperature Magnetic Refrigerant

A general background to the $La(M,A)_{13}$ materials where M is one or more transition metals and A = Al or Si was provided in Section 3.5. In this chapter is presented some of the experimental work and analysis done on eight different compositions of $La(Fe,Co,Si)_{13}$ (LFCS). The majority of the work is published in paper I and II, while the analysis and results not included in these papers is provided below. The eight samples of LFCS were manufactured and supplied by Vacuumschmelze GmbH, a company that has a long history of manufacturing and handling of magnetic materials. Vacuumschmelze produced the LFCS samples using powder metallurgy and this manufacturing method makes industrial scale production feasible. Samples with similar compositions have been described previously, see *e.g.* [74, 93], however, the samples described in the cited works were all produced by arc-melting and subsequent heat treatment for weeks. This production method is not suitable for industrial scale production, which has counted against LFCS compounds in reviews on magnetic refrigerants, where different magnetocaloric materials are compared [12]. Also, plates of LFCS have not previously been manufactured and due to the brittleness of LFCS, cutting the as-prepared material into sheets is not a trivial task. Vacuumschmelze GmbH has overcome both obstacles by creating a manufacturing method for large-scale production and by demonstrating that they can deliver samples in the shape of regular plates.

In the following is first proffered information on the as-prepared samples delivered by Vacuumschmelze and their characteristics after being prepared for magnetization measurements. Following this, the results of a simple corrosion study is presented in section 5.3. The results of this study are interesting, but due to their unquantified nature, they were not published. An x-ray diffraction experiment at different temperatures in order to determine the lattice parameter was made and the result of the data analysis is given in section 5.4. Finally, in section 5.5 Arrott plots of seven LFCS samples are presented and discussed.

For a summary on the results of the extensive characterization done on the
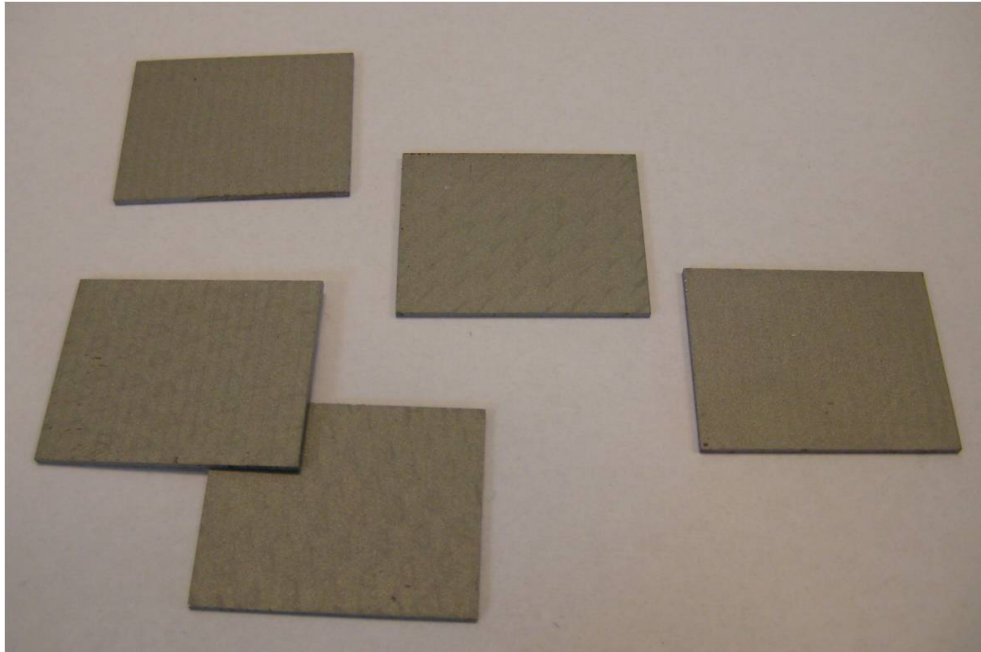
Figure 5.1: Plates measuring approximately 20 mm $\times$ 25 mm $\times$ 0.9 mm produced by Vacuumschmelze GmbH for the test machine at Risø DTU. Paper I deals with the characterization of one of these plates.

LFCS samples, the reader is referred to paper I and, in particular, paper II.

5.1 Description of As-prepared Samples

The plate described in paper I, was one of a set of plates, which were delivered by Vacuumschmelze GmbH for use in the test machine at Risø National Laboratory for Sustainable Energy [10, 11]. For this use, the characterization presented in paper I was necessary for the experiments with running the test machine. The plates measured approximately 20 mm $\times$ 25 mm $\times$ 0.9 mm and were regular in shape, see Fig. 5.1. The topic of paper II is the extensive characterization of a materials series of LFCS. For the materials series consisting of seven samples with varying stoichiometry, the as-prepared samples were die-pressed blocks measuring approximately 23 mm $\times$ 19 mm $\times$ 12.5 mm, see Fig. 5.2.

Figure 5.2: Blocks measuring approximately 23 mm $\times$ 19 mm $\times$ 12.5 mm produced by Vacuumschmelze GmbH. The blocks were cut into smaller pieces for experimental work, as discussed in section 5.2. The characterization of these seven samples is the subject of paper II.

Sample no.	Sample dimensions [mm]	Demagnetization factor, D_z	Maximum internal magnetic field
1	$0.78 \times 1.75 \times 4.44$	0.1089	1.45 T
2	$0.86 \times 1.80 \times 4.20$	0.1220	1.43 T
3	$0.71 \times 1.58 \times 3.44$	0.1254	1.43 T
4	$0.76 \times 2.21 \times 4.45$	0.1156	1.44 T
5	$1.02 \times 1.27 \times 4.09$	0.1191	1.43 T
6	$1.03 \times 1.57 \times 4.02$	0.1324	1.42 T
7	$0.96 \times 1.40 \times 4.20$	0.1175	1.44 T
Plate	$0.90 \times 2.00 \times 5.00$	0.1109	1.47 T

Table 5.1: Dimensions, demagnetization factor and maximum internal magnetic field for the eight LFCS samples measured on the in-house LakeShore VSM.

5.2 Preparation of Samples for Magnetization Measurements

The eight LFCS samples were cut into smaller pieces for magnetization measurements. The resulting sample pieces had an elongated shape and were mounted with the longest side parallel to the applied magnetic field direction. Dimensions are given in Table 5.1. A thermocouple was mounted in-between the sample piece and the holder as described in section 4.2.1. For the isothermal magnetization curves the maximum applied magnetic field was 1.59 T. Table 5.1 gives the sample dimensions, the demagnetization factor as calculated from Aharoni's formula for a rectangular cuboid [85] and the resulting maximum internal magnetic field, see section 4.2.2. The demagnetization factors are seen to be similar and the maximum internal field is around 1.44 T for all samples.

5.3 Corrosion Experiment

To examine how susceptible to corrosion the LFCS samples are two sets of simple experiments were conducted in collaboration with co-worker K. K. Nielsen. In the first experiment, a plate provided by Vacuumschmelze GmbH similar to that shown in Section 5.1 was broken into six smaller pieces, three of which were subsequently placed in demineralized water, ethanol and a commercial automotive antifreeze with added corrosion inhibitors, respectively. The remaining three pieces were coated in different ways, one with a lumocolor pen, one with a permanent marker and one with varnish, before being placed in demineralized water. In Table 5.2 is shown a series of images documenting

0 hours	2.5 hours	20 hours	67.5 hours	∼ 10 days
Demineralized water. No coating.				
Ethanol. No coating.				
Antifreeze. No coating.				
Demineralized water. Coating: Lumocolor pen (waterproof on most surfaces).				

Table 5.2: Visible corrosion of LFCS sample in stated liquids and coatings.

the corrosion of the six samples.

It is clear from the images presented in Tables 5.2 and 5.3, that LFCS has significant problems with corrosion and that this must be factored in, when designing a refrigeration device with LFCS as the magnetic refrigerant. In pure demineralized water the LFCS plate quickly tarnishes and after only 20 hours an oxide layer is flaking off. The sample placed in ethanol is faring better, however, the containers were not sealed off and so the ethanol evaporated after

0 hours	24.5 hours	47.5 hours
Coating: Waterproof marker. Demineralized water.		
Coating: Pink varnish. Demineralized water.		
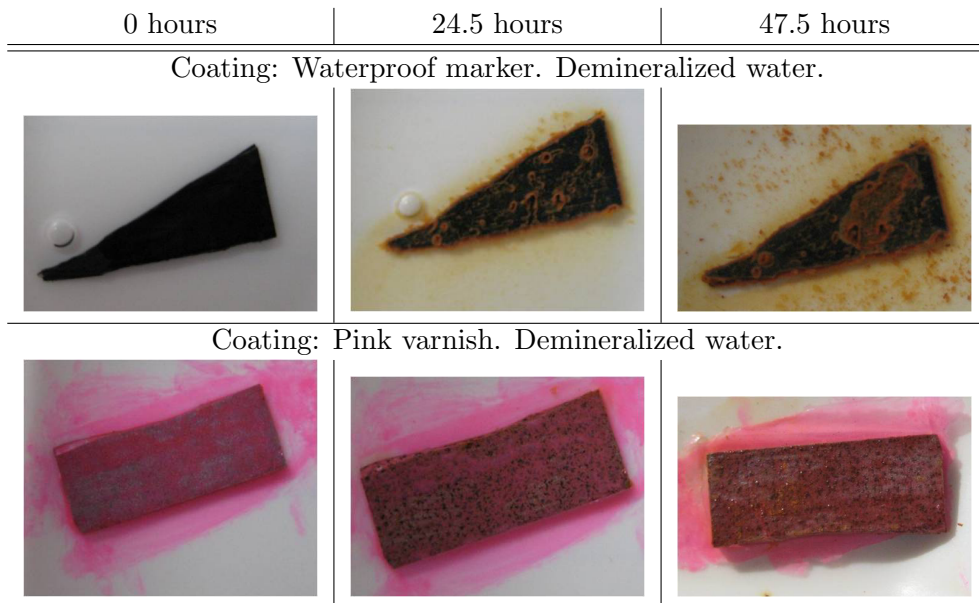
Table 5.3: Visible corrosion of LFCS sample in demineralized water and with different coatings applied. In the photograph on the far right of the sample coated in varnish, the sample has been turned over and therefore looks slightly different than in the other photographs.

a few hours. In antifreeze LFCS is clearly doing much better, but after about 10 days the sample has tarnished, which is surprising as the antifreeze is said to contain corrosion inhibitors. As this could possibly be due to oxygen from the air dissolving in the antifreeze, a second experiment with sealed containers was decided upon and described below. The various coatings also did not succeed in inhibiting the corrosion. The Lumocolor pen, which is *"waterproof on most surfaces"*, is apparently not waterproof on LFCS as a ring of dye was visible right after the plate had been put into the water. Neither was the black waterproof marker able to keep an LFCS plate from tarnishing. Finally, the pink varnish was very sticky and difficult to apply, which may have caused the layer to not be homogenous enough. The corrosion in the sample treated with varnish seems to be halted, but not prevented.

In the second set of experiments a similar plate of LFCS was again broken into pieces, which were placed in sealed containers with a mixture of antifreeze and water. Three solutions of water and/or antifreeze were made: 100% antifreeze, 50% antifreeze/50% water, and 25% antifreeze/75% water. In Fig. 5.3 (top) is shown the sealed container with an LFCS sample and a mixture of 25% antifreeze/75% water. After almost two years none of the three sample show any signs of oxidation, see Fig. 5.3 (bottom). This simple experiment providing unquantified information on the corrosion of LFCS samples in fluids, indicate that it may be possible to prevent the oxidation of LFCS in a cooling

fluid. However, in a refrigeration system, the sheets of LFCS will be in contact with other materials, which could also affect the rate of corrosion and so it is clear that this will be a challenge.

Figure 5.3: Top: Sealed container with LFCS sample and a 25% antifreeze/75% water mixture. Bottom: Untarnished sample after almost two years.

5.4   Lattice Parameter as a Function of Temperature

Using the experimental setup described in section 4.1.1 a series of x-ray patterns were recorded at different temperatures on LFCS sample no. 2. The sample piece was a plate with dimensions larger than the x-ray footprint. Thermal contact between sample and holder was improved by a thin layer of type H Apiezon grease. As LFCS sample no. 2 has a Curie temperature of about 266 K, the temperature range of the diffraction experiment was chosen to be $223 - 303$ K. The temperature was controlled by the accompanying Bruker software, which was programmed to record the patterns at increasing temperatures. After ramping the temperature, a wait time was always included, before the pattern was recorded, so that the sample temperature could stabilize. The resulting patterns are shown in Fig. 5.4. All patterns
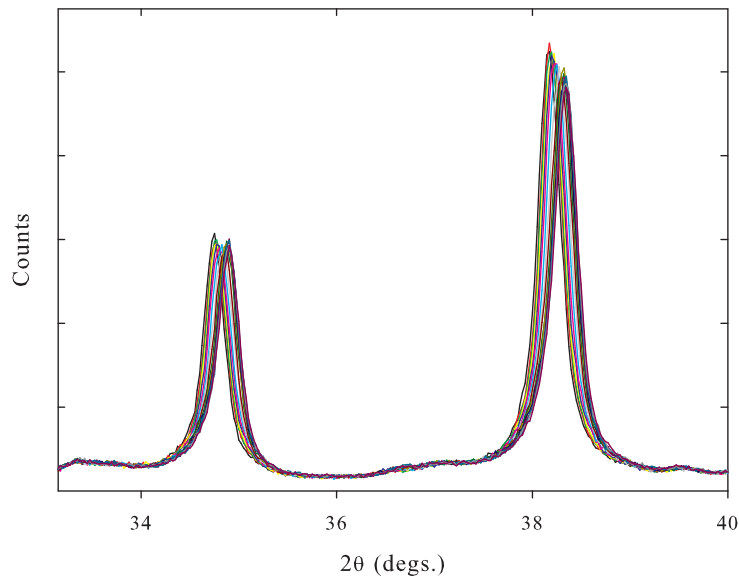
Figure 5.4: X-ray diffraction patterns of LFCS sample no. 2. The patterns were recorded at temperatures from $223 - 303$ K. As the temperature increases, the peaks move to higher scattering angles corresponding to a decrease in the cubic lattice parameter.

were obtained using a solid state detector and in the scattering angle range $33.15 < 2\theta < 40°$ degrees. The scattering angle range was chosen as it contains two peaks with large intensities, see Fig. 1 in paper I or Fig. 3 in paper II. To obtain a good Rietveld refinement fit of the peaks a fitting file, which had been used to fit a room temperature pattern with a greater scattering

angle range, was used as the starting point for the Rietveld refinement of the 303 K pattern. The new fitting file from the refinement of the 303 K pattern was then used as a starting point for fitting the pattern recorded at the second highest temperature and so forth. The resulting fits are shown in Fig. 5.6 on page 64. During these refinements only two parameters were fitted: scale and the cubic lattice parameter.

In this way the cubic lattice parameter as a function of sample temperature was obtained, see Fig. 5.5. This shows the volume change taking place as the magnetization of the sample decreases. X-ray diffraction patterns were
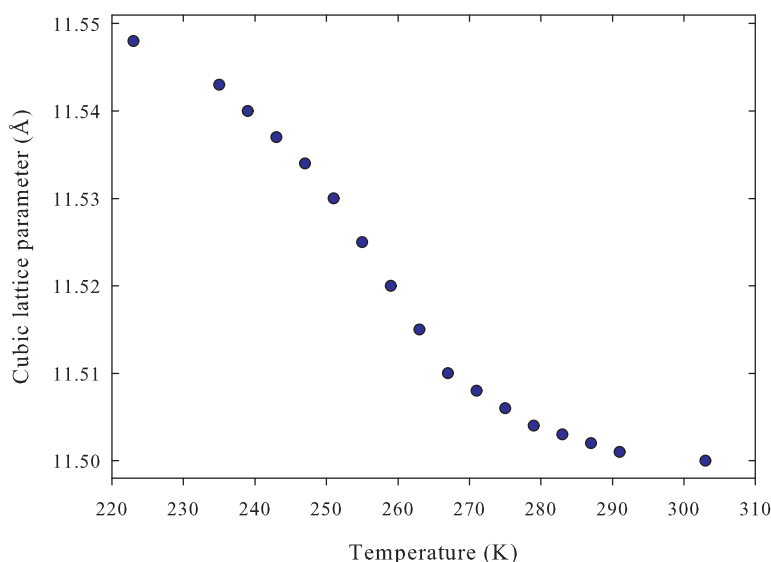
Figure 5.5: Cubic lattice parameter of LFCS sample no. 2 as a function of temperature determined from Rietveld refinement of x-ray diffraction patterns.

obtained for all seven LFCS samples at room temperature, see paper II. The cubic lattice parameter for sample no. 2 determined from the full Rietveld refinement of these diffraction scans is 11.498(1) Å, which corresponds well with the results from the scans done at varying temperatures, where we find a lattice parameter of 11.50 Å for the scan performed at 303 K. Unfortunately, at the time of the experiments no option for recording the temperature into a file existed. As the program ran during the night, the accuracy and stability of the temperature was not monitored. It was observed that even if the temperature deviated grossly from the requested one, the pattern would continue recording. Therefore, the obtained lattice parameters come with large uncertainties, although the smoothness of the decrease in volume as the magnetic transition temperature is crossed is compelling. It was decided to redo the ex-
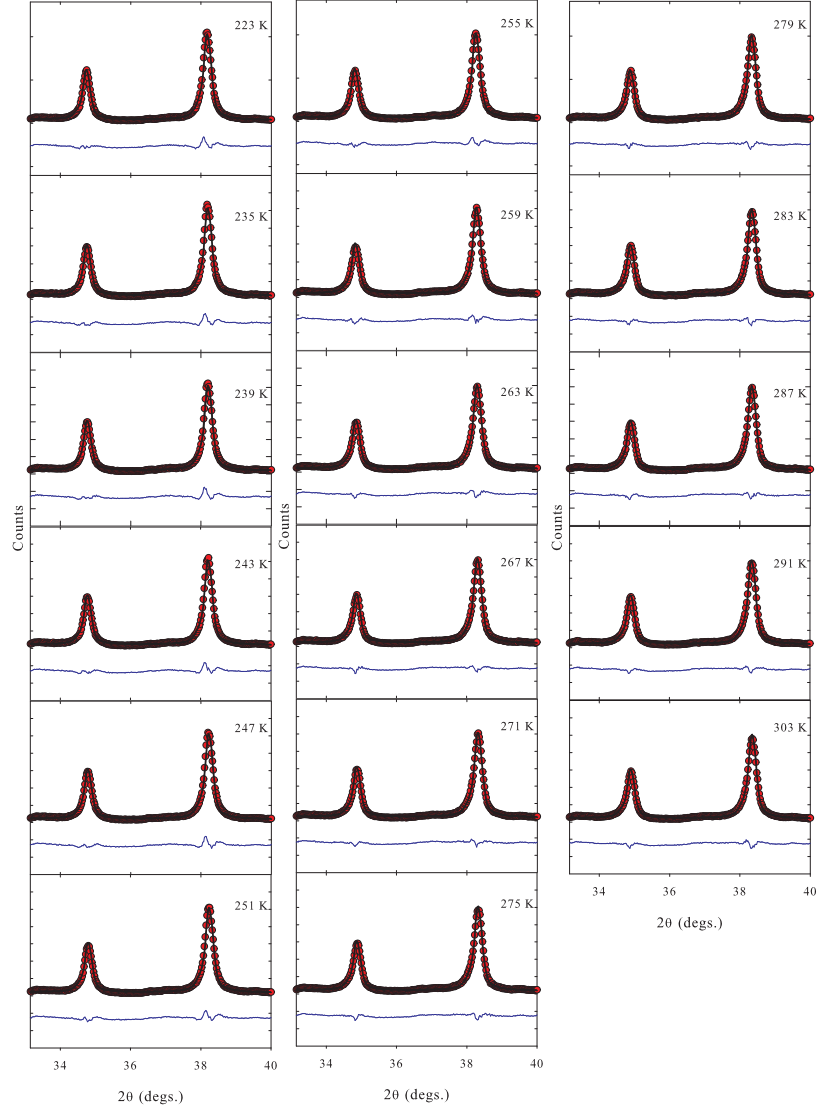
Figure 5.6: Fits of the 17 x-ray diffraction patterns on LFCS sample no. 2 obtained in the temperature range $223 - 303$ K.

periment and remove this uncertainty in sample temperature, an enterprise, which, unfortunately, could not be completed in time for the completion of this thesis. A determination of the lattice parameter as a function of temperature on a sample of LFCS with very similar stoichiometry was done by Hu *et al.* [73], who find similar values of the cubic lattice parameter although their values are lower throughout the temperature range.

Although the lattice contraction that takes place, when passing from the

ferromagnetic to the paramagnetic phase, does not appear to have been recorded in full, it will still be useful to calculate the volume change. We find that for an increase in temperature from 223 to 303 K, a volume contraction of 1.5% takes place in sample no. 2, which could be significant in a cooling device.

5.5 Arrott Plots

As described in section 4.2.3, the Arrott plot can be used to determine the critical exponents and Curie temperature of a ferromagnetic system. If the ferromagnet can be described using mean-field theory, the Arrott-Noakes equation will take the form

$$\left(\frac{H}{M}\right) \propto \left(\frac{M}{M_0}\right)^2 \tag{5.1}$$

and an Arrott plot, *i.e.* a plot of $\frac{H}{M}$ versus M^2, will result in straight lines for large values of M^2 near the Curie temperature, T_C. At T_C, an extrapolation of the straight line for large M^2 will pass through the origin. Figs. 5.7 and 5.8 show the Arrott plots of the seven LFCS samples constituting a materials series using mean-field values of the critical exponents.

We see that the seven samples are well described by mean-field theory as we obtain straight lines for large values of M^2. A straight line was fitted to the data near the Curie temperature as determined by other methods, see paper II for details. The table from paper II summarizing the determined Curie temperatures is reproduced in part in Table 5.4. The fits to the Arrott plots confirm the determined values of T_C.

Curie and peak temperatures [K]			
Sample no.	T_c determined from inflection point $(-\partial M/\partial T)$	T_c from linear fit of $1/\chi$	T_c from Landau coefficient, c_1, see paper II	Arrott plot
1	255(1)	256(1)	255(1)	$255-256$
2	266(1)	267(1)	265(1)	$266-267$
3	281(1)	282(1)	281(1)	$280-281$
4	292(1)	293(1)	292(1)	$292-294$
5	311(1)	312(1)	311(1)	$310-312$
6	327(1)	327(1)	327(1)	$326-328$
7	345(1)	347(1)	345(1)	$344-346$

Table 5.4: T_c determined from the inflection point $(-\partial M/\partial T)$, low-field susceptibility and the Landau coefficient compared with that determined from Arrott plots as described in the text.

(a) Sample no. 1

(b) Sample no. 2

(c) Sample no. 3

(d) Sample no. 4
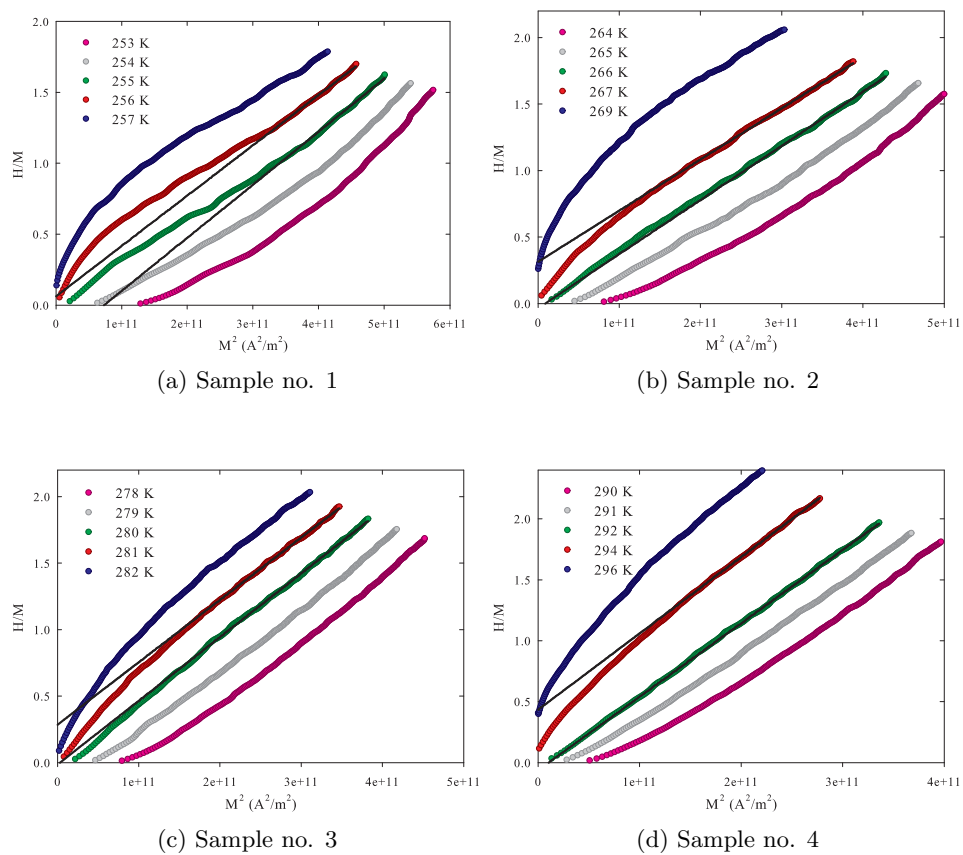
Figure 5.7: Arrott plots of LFCS samples no. $1 - 4$ for mean-field values of the critical exponents, *i.e.* $\gamma = 1$ and $\beta = {}^1\!/_2$. A straight line is fitted to data near the Curie temperatures for large values of M^2.

(a) Sample no. 5

(b) Sample no. 6

(c) Sample no. 7
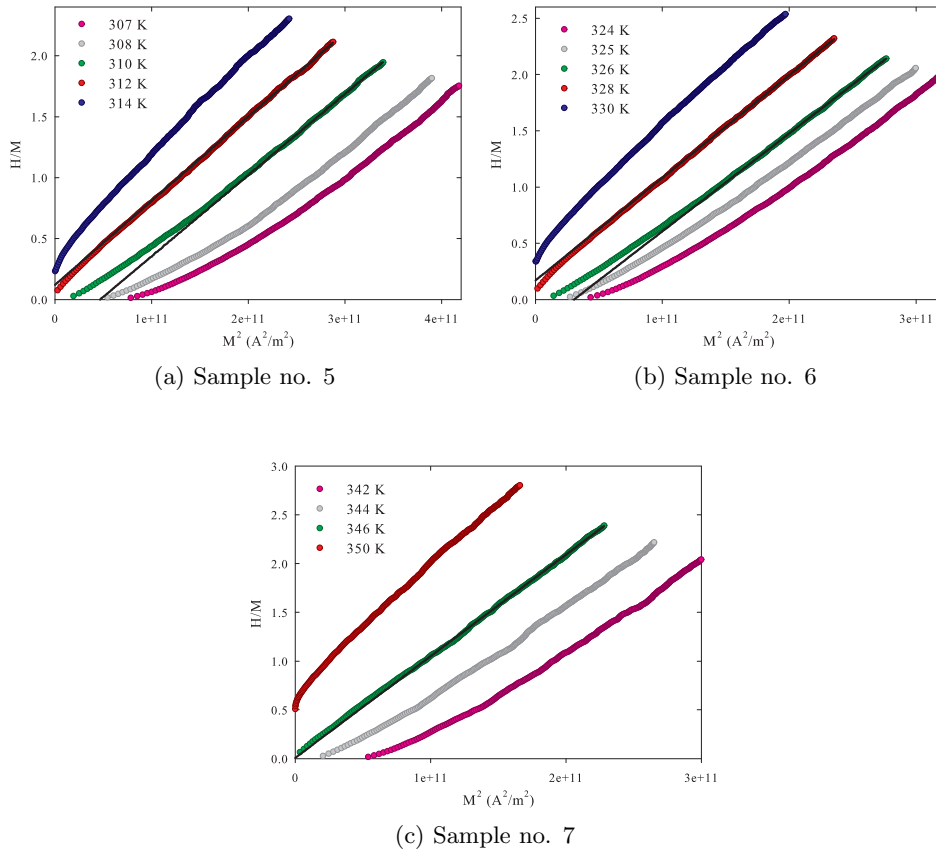
Figure 5.8: Arrott plots of LFCS samples no. $5-7$ for mean-field values of the critical exponents, *i.e.* $\gamma = 1$ and $\beta = {}^1/_2$. A straight line is fitted to data near the Curie temperatures for large values of M^2.

Chapter 6

Y_6(Fe,Mn)$_{23}$ - a Poor Magnetic Refrigerant

The idea of studying the magnetocaloric effect in $Y_6(Fe_{1-x}Mn_x)_{23}$ compounds came about after reading ref. [94], where it is shown that Curie temperatures near 300 K can be achieved by choosing $x \sim 0.15$ or $x \sim 0.8$. The Curie temperature and magnetic moment initially decreases with increasing x and then increases again for $x > 0.6$. A sample with nominal stoichiometry $Y_6(Fe_{0.84}Mn_{0.16})_{23}$ was prepared by a colleague using arc-melting in an Ar atmosphere. The ingots were turned over and re-melted a number of times for homogenization. An X-ray pattern was obtained on a Bruker D8 Advance Diffractometer using Cu K$_\alpha$ radiation and a solid state detector, which reduces the fluorescent background from Fe.

R_6(Fe,Mn)$_{23}$ stabilizes in the cubic Th$_6$Mn$_{23}$ structure, where the Mn/Fe has four non-equivalent crystallographic sites: (0.5, 0.5, 0.5), (0, 0.25, 0.25), (0.178, 0.178, 0.178) and (0.378, 0.378, 0.378) denoted in the following by their multiplicity and Wyckoff letters: $4b$, $24d$, $32f1$ and $32f2$. The rare-earth atoms form octahedrons around the transition metals in site $4b$, while most of the remaining Fe and Mn atoms form stellarquadrangula, i.e. tetrahedra capped with tetrahedra. These structures are drawn only for visualization; they do not reflect the chemical or magnetic relations between atoms, see Fig. 6.1.

An initial Rietveld refinement lead to the fit shown in Fig. 6.2. The intensities are clearly wrong. As the reason for this was not obvious, a Le Bail fit was made to confirm that the main phase is in the cubic Th$_6$Mn$_{23}$ structure and to ensure that all peaks were accounted for. A Le Bail fit contains all the information on the crystal structure, but no information on the atoms in the crystal [95]. The fitting program therefore tries to adjust the intensity to comply with the diffraction data. Crystallographica Search/Match was used to identify impurities in the sample and from this search MnO appears as a possible minor phase. However, as a caveat it should be pointed out that only one peak is fitted by MnO. The result of a Le Bail fit with the structure information for Y_6(Fe,Mn)$_{23}$ and MnO is shown in Fig. 6.3. It is clear from the Le Bail fit that the main phase is likely Y_6(Fe,Mn)$_{23}$.
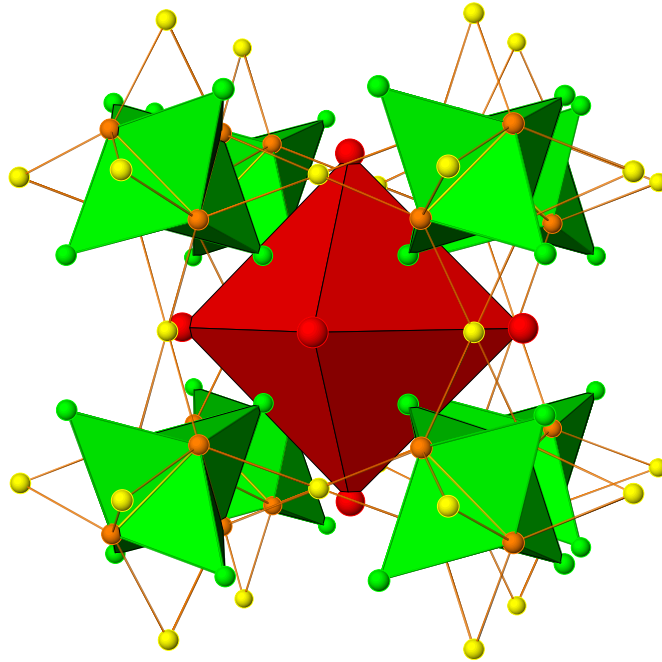
Figure 6.1: The crystal structure of Y_6(Fe,Mn)$_{23}$. The Fe/Mn in site $32f1$ are located within the octahedrons formed by Y (red), while the three remaining Fe/Mn sites, $4b$ (orange), $24d$ (yellow), $32f2$ (green), form stellarquadrangula.

A sample piece with dimensions 1 mm $\times$ 1.39 mm $\times$ 4.11 mm was cut using a table top Accutom 5 cutting machine and used for magnetization measurements. A sweep-rate of 0.02 T/s was used for the measurements and the calculated ΔS_M is shown in Fig. 6.4. The determined ΔS_M is too small for use in a magnetic refrigeration setup. In comparison, the ΔS_M of Gd at 295 K is $\sim$ 26 mJ/cm^{3}K for a change in applied magnetic field from 0 to 1 T.

An attempt was made at producing samples of Gd$_6$(Fe,Mn)$_{23}$, which would have Curie temperatures near 300 K, but x-ray patterns showed that the desired phases were not obtained. As the R$_6$(Fe,Mn)$_{23}$ are believed unsuitable for magnetic refrigeration due to the low magnetic entropy change that results from applying a field, no further attempts were made to produce additional samples.
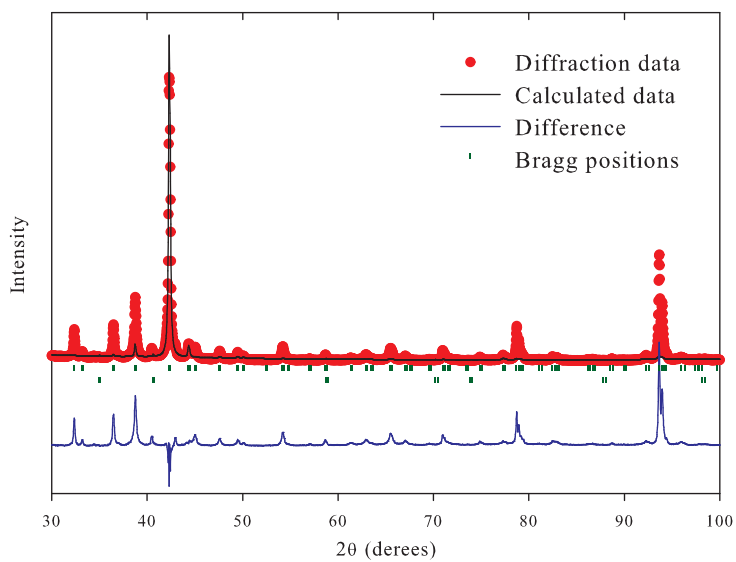
Figure 6.2: Initial Rietveld refinement of $Y_6(Fe_{0.84}Mn_{0.16})_{23}$ sample.
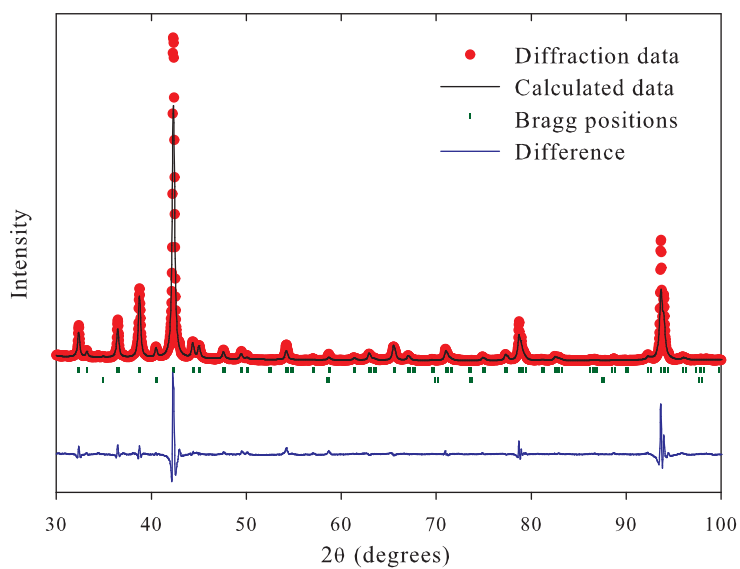
Figure 6.3: Le Bail refinement of $Y_6(Fe_{0.84}Mn_{0.16})_{23}$ sample.
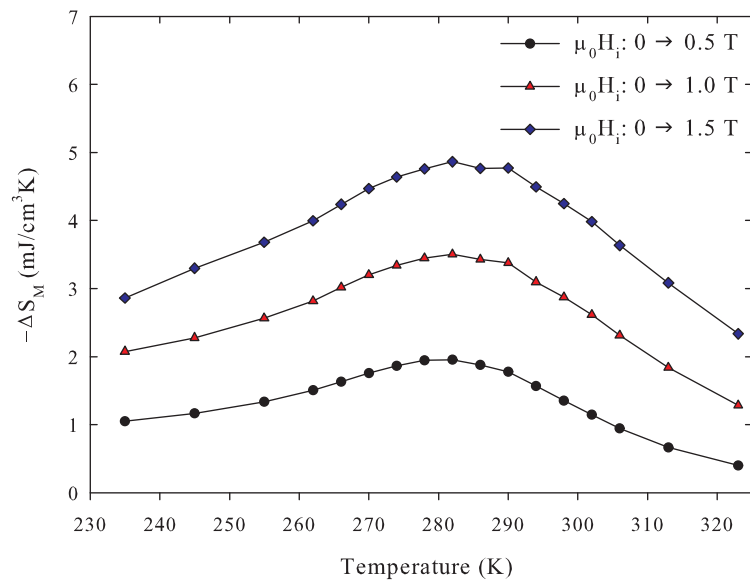
Figure 6.4: The volumetric magnetic entropy change, ΔS_M, as a function of temperature for a selection of internal fields, $\mu_0 H_i$.

Chapter 7

Magnetic Entropy Change and Spin Reversal in Gadolinium Iron Garnet, $Gd_3Fe_5O_{12}$.

7.1 Introduction and Motivation

While browsing through the series "Handbook of magnetic materials" [96], an 18-volume tome of knowledge on magnetic materials, the material $Gd_3Fe_5O_{12}$ (GdIG) caught the eye of this author. GdIG is a rare-earth iron garnet with a complex magnetic structure, where Fe atoms sit in two different crystallographic sites and their magnetic moments are antiferromagnetically coupled. As the number of Fe atoms in the two sites is unequal, there is an excess moment. The Gd magnetic moment is coupled antiferromagnetically to this excess Fe moment. The result is a characteristic magnetization versus temperature as shown in Fig. 7.1. At low temperatures the rare-earth (RE) moments order, but this order is soon lost to thermal fluctuations as the RE-RE coupling is weak. Therefore, at temperatures close to room temperature, the Gd moments can be thought of as paramagnetic moments sitting in an effective magnetic field generated by the ferrimagnetic Fe spins. Meanwhile, the Fe-Fe superexchange coupling is strong and the magnetization stemming from the Fe atoms does not change much until the Néel temperature of $\sim$562.5 K [97] is reached. The ordering of the rare-earth moments at low temperatures can provide a significant magnetocaloric effect and the rare-earth garnet $Gd_3Ga_5O_{12}$ was shown by Barclay and Steyert [98] to be an excellent refrigerant in the temperature range $2-20$ K. All iron garnets with a lanthanide in the RE position have a characteristic temperature, known as the compensation temperature, T_{comp}, where the sum of the sublattice magnetizations becomes zero. At temperatures above T_{comp} the Gd moment becomes smaller than the excess Fe moment and the Fe moment now dominates. This results in a reversal of the magnetic moments at T_{comp} if a magnetic field is applied, as it is the resultant moment, which aligns with an applied magnetic field.

After reading Phan *et al.* [99] where the magnetocaloric effect in bulk and nanostructured GdIG were compared, but only for temperatures below T_{comp} this author decided to examine what happens with the magnetic entropy near
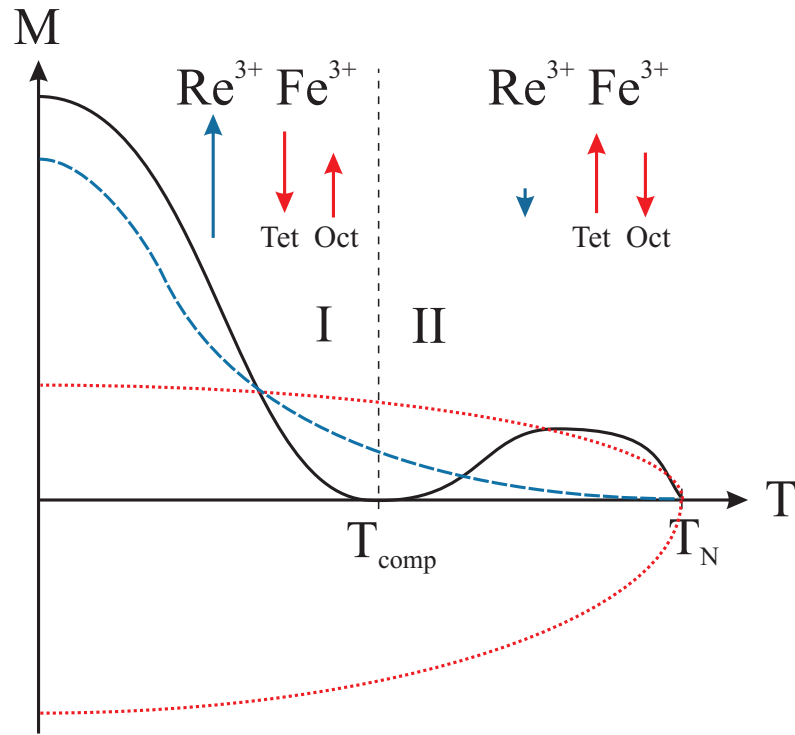
Figure 7.1: Magnetization versus temperature of a rare-earth iron garnet for a small applied magnetic field. The total magnetization (black) is a sum of the magnetization of the rare-earth (RE) sublattice (blue, dashed) and the Fe sublattices (red, dotted). In region I the RE^{3+} moment dominates, whereas in region II the ferrimagnetic Fe^{3+} moment dominates. At the temperature T_{comp}, the moments cancel and the magnetization is zero.

the compensation temperature. For this purpose, a sample of GdIG was made and characterized using x-ray powder diffraction, magnetometry, calorimetry and ^{57}Fe Mössbauer spectroscopy.

A number of papers dealing with the magnetocaloric effect in GdIG from $\sim 75-600$ K have been published by Belov *et al.* [100–102]. Their results show the same behavior of the magnetic entropy change as indirectly determined by us. Of importance are the results we present obtained from the Mössbauer spectra at applied magnetic fields, which provide a direct measurement of the spin reversal at the compensation temperature.
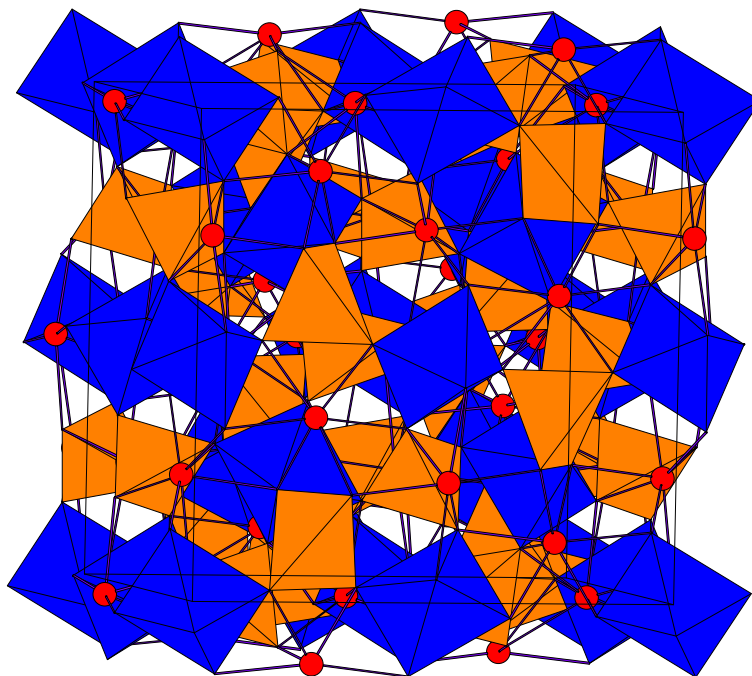
Figure 7.2: Cubic unit cell of GdIG showing the Fe^{3+} tetrahedra (orange), Fe^{3+} octahedra (blue) and Gd^{3+} atoms (red). Oxygen is present at the polyhedral vertices. The tilting of the polyhedra is apparent.

7.2 Background on $Gd_3Fe_5O_{12}$

GdIG crystallizes in a cubic structure and the magnetic moments order preferentially along the [111] axis for temperatures between 4.2 K and the Néel temperature [97]. The chemical formula of GdIG can be written in long form as ${Gd^{3+}}_3(Fe^{3+})_2[Fe^{3+}]_3O_{12}^{-2}$, where {} refers to dodecahedral, () to octahedral and [] to tetrahedral coordination with the oxygen lattice [103, 104]. The polyhedra are tilted with respect to the unit cell axes, see Fig. 7.2. Gd^{3+} has electronic configuration $[Xe]4f^7$, while that of Fe^{3+} is $[Ar]3d^5$, which means that both have a large magnetic moment and both are in an S-state, *i.e.* their orbital angular momentum is zero. The magnetic moments on the two Fe^{3+} sites are coupled strongly and antiferromagnetically. However, since there are three tetrahedrally coordinated Fe atoms for every two octahedrally coordinated Fe atoms, the result is a ferrimagnetic Fe moment. The Gd moments are coupled weakly and also antiferromagnetically to the ferrimagnetic Fe moment, so that the couplings between the three sublattices result in a total

magnetization given by [105]

$$\bar{M}_{\text{total}} = \bar{M}_{\text{Gd}} - \bar{M}_{\text{(Fe,tet)}} + \bar{M}_{\text{(Fe,oct)}}. \tag{7.1}$$

The magnetization of GdIG as a function of temperature follows the sketch shown in Fig. 7.1 for iron garnets. At low temperatures, in region I, the Gd moment dominates. As the Gd-Gd coupling is almost negligible, it is the Gd-Fe coupling, which aligns the Gd spins resulting in a slow decrease of the Gd magnetization as the temperature is increased. Near room temperature the Gd^{3+} spins are essentially disordered spins, *i.e.* paramagnetic spins, in an effective magnetic field from the ferrimagnetic Fe spins. At T_{comp} the total magnetization is zero as the moments on the three sublattices cancel. T_{comp} is sample dependent probably due to impurities, *e.g.* the presence of other rare earths or other magnetic phases, but appears around $286 - 290$ K [106, 107]. Above T_{comp} the ferrimagnetic Fe moment dominates until the temperature reaches the Néel temperature of the system, $\sim$562.5 K [97].

Due to the strong coupling between the Fe atoms, canting of the magnetic moments only happens in extremely high fields ($\gtrsim 100$ T) except when close to T_{comp} in temperature [108]. When passing through T_{comp} with a magnetic field applied, the sublattice spin reorientation happens in a finite temperature interval, *i.e.* an angled phase exists. Bernasconi and Kuse [108] find that the slope of the phase boundary between the collinear and angled phases is ± 1 K/T, see Fig. 7.3.

As the magnetic moments cancel at T_{comp} the energy cannot be reduced by having magnetic domains and the individual grains will become single domain if not for local defects. This was directly observed and reported by Mee [109] for single crystals of GdIG. When a magnetic field is applied at temperatures near T_{comp} the spins become canted and the magnetic moments may no longer cancel completely. The existence of the canted phase results in saturation of the magnetocaloric effect as an applied field will no longer change the magnetic entropy of the rare-earth sublattice, which is responsible for the magnetocaloric effect in GdIG below the Néel temperature. This saturation of the magnetocaloric effect has also been used to determine the phase boundary between the collinear and canted phases [102]. The transition between the collinear and angled phases causes a symmetry breaking of rotational invariance, *i.e.* the crystal is no longer invariant to rotation about an axis. As the spin canting will develop continuously, the phase transition is of second-order.

7.3 Sample Preparation

The GdIG sample was prepared by solid state synthesis of powders of Gd$_2$O$_3$ (99.9 %) and Fe$_2$O$_3$ (99.9 %). The powders were mixed in a 3:5 molar ratio
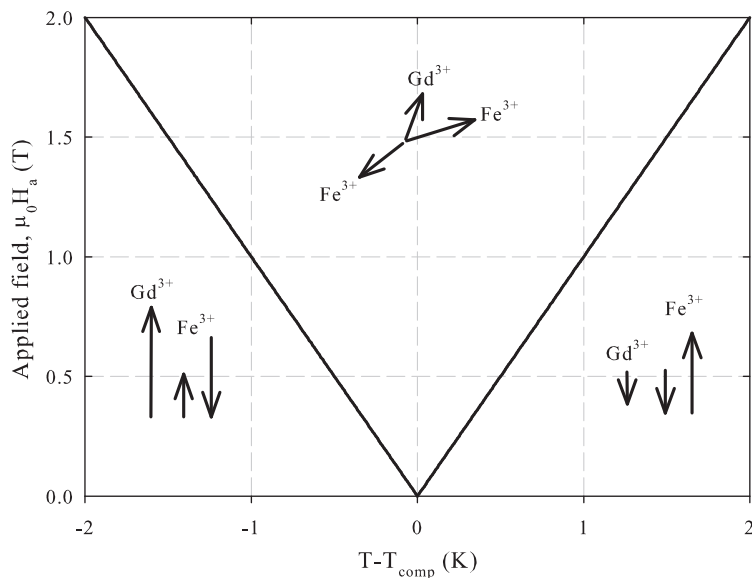
Figure 7.3: Phase diagram for GdIG from values of the phase boundary slope determined experimentally by Bernasconi and Kuse [108]. The phase boundaries separate collinear and angled phases.

and pressed into a pellet, which was then pressed isostatically and sintered in air for 35 hours at 1400°C. This changed the sample color from reddish brown to a dark green. The sintered pellet was crushed to a powder using an agate mortar and pestle.

7.4 X-ray Powder Diffraction

The sample was examined by x-ray powder diffraction using an in-house Bruker D8 Advance diffractometer and Cu K_α radiation. To avoid the fluorescent background scattering from Fe an energy dispersive solid state (Sol-X) detector was used. Variable slits were used when recording the x-ray diffraction data and the recorded intensity was corrected for by using the formula

$$I_{\text{corrected}} = \frac{I_{\text{(variable slit)}}}{\sin \theta}.$$ (7.2)

FullProf [81] was used for Rietveld refinement of the corrected x-ray spectrum, see Fig. 7.4. From the refinement of the XRD spectrum it was found that the main phase in the sample is GdIG. Four peaks from an impurity phase, which is present in small amounts, are seen at low scattering angles, see inset
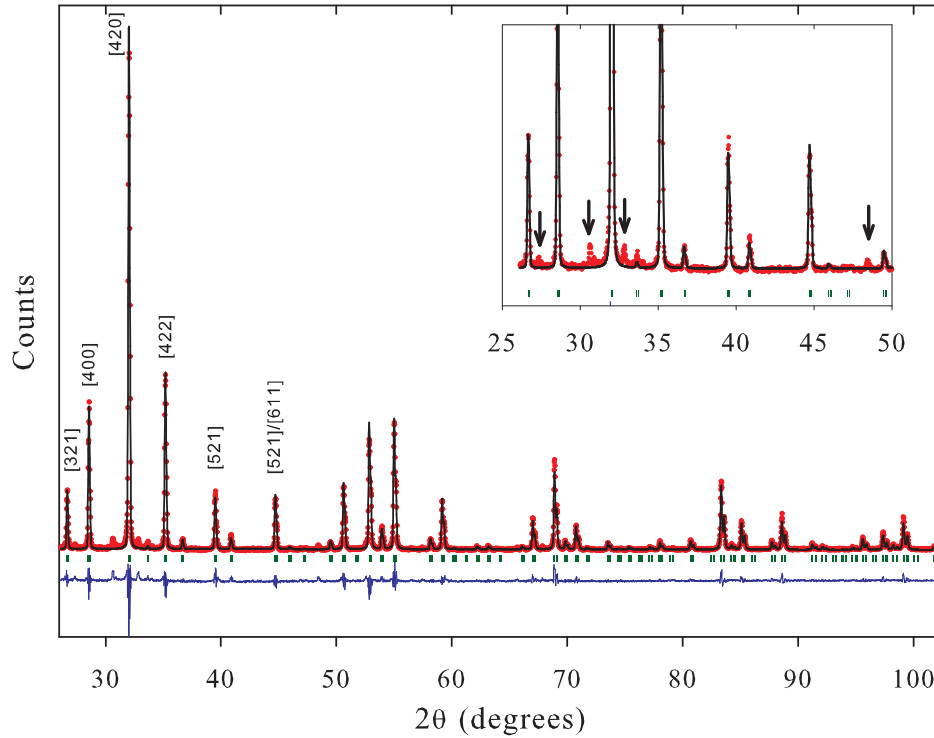
Figure 7.4: Rietveld refinement of x-ray powder diffraction on GdIG sample. Inset: Low scattering angles. Four peaks from an unidentified impurity are marked by arrows.

of Fig. 7.4. Although the spectrum was analyzed using Crystallographica Search/Match the impurity could not be identified. Without an identification of the impurity it is not possible to calculate its weight %. However, it is clear from the relative intensities that GdIG is the main phase. The cubic lattice parameter of GdIG determined from the Rietveld refinement is given in Table 7.1 and is seen to correspond well with that from literature.

ICSD code	Compound	Space group	Unit-cell parameters [Å]	
			Determined	From literature [103]
15456	$Gd_3Fe_5O_{12}$	Ia3d	a, b, c = 12.474	a, b, c = 12.470

Table 7.1: Room temperature cubic lattice parameter for GdIG sample compared to published value.
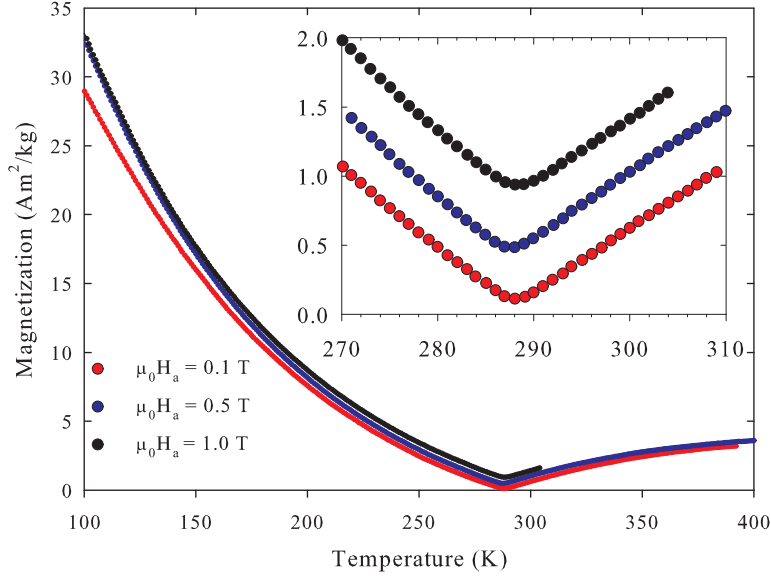
Figure 7.5: The magnetization of GdIG for a selection of applied magnetic fields. Inset: The magnetization near T_{comp}.

7.5 Magnetometry

For magnetization measurements the in-house LakeShore 7407 Vibrating Sample Magnetometer (VSM) was used. Isothermal magnetization measurements as a function of field were made as continuous measurements at a sweep rate of 0.01 T/s and for applied magnetic fields up to $\mu_0 H_a = 1.6$ T. Magnetization measurements as a function of temperature at various applied magnetic fields were made as point-by-point measurements in steps of 1 K and with a measurement time of 5 s/point.

In Fig. 7.5 is shown the magnetization of GdIG for a range of applied magnetic fields. The recorded magnetization as a function of temperature acts as expected when compared with Fig. 7.1. For temperatures below T_{comp} the magnetization slowly decreases as the Gd^{3+} spins, which are weakly coupled to the ferrimagnetic Fe^{3+} spins, lose their order due to the increasing thermal fluctuations. At T_{comp}, dM/dT is zero for all applied magnetic fields, but the magnetization is non-zero as the essentially paramagnetic Gd^{3+} moments are affected by the applied magnetic field. Canting of the spins cannot account for the non-zero magnetization, as the effect will be very small for the applied fields here. In plots of magnetization versus applied magnetic field, see Fig. 7.6, the low-field data show a quick rise in magnetization due to domain wall
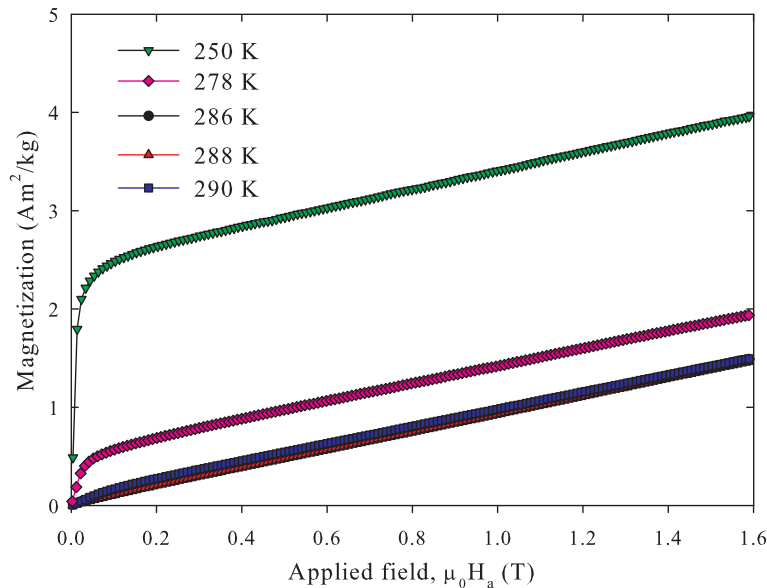
Figure 7.6: Magnetization of GdIG as a function of applied magnetic field.

movement. At applied magnetic fields larger than $\sim$0.1 T the magnetization increases linearly and the magnetization here is due to the Gd^{3+} spins. As the grains can more easily become single domain near T_{comp} when a field is applied the magnetization increases linearly without the initial sharp increase originating from magnetic domains, see Fig. 7.7. From the magnetization data in Fig. 7.6 it is also clear that the magnetization of GdIG does not saturate for applied magnetic fields up to $\mu_0H_a = 1.6$ T at the shown temperatures.

Hysteresis curves near T_{comp}, see Fig. 7.8 and Fig. 7.9, show that a hysteresis exists for small applied magnetic fields, $\mu_0H_a < 0.20$ T. The resultant hysteresis curves are a combination of two processes: (1) a paramagnetic, *i.e.* linearly increasing, response from Gd^{3+} and (2) a hysteretic curve originating with the strongly coupled ferrimagnetic Fe sublattice due to domain structure. As T_{comp} is approached in temperature from above or below, the coercivity increases as shown by Mee [109] for GdIG and by Uemura et al. for DyIG [110], while it disappears at T_{comp}, which results in two peaks in the coercivity when plotted against temperature. At low temperatures, where the Gd moments dominate, GdIG has a large total magnetic moment and is therefore rich in domain structure. This allows for easy displacement of domain walls and, as seen in the measurement at 100 K shown in the inset of Fig. 7.9, very little coercivity. Close to T_{comp} the GdIG grains can more easily become single domain and the temperature at which this happens will depend on the grain size. In a temperature range around T_{comp} then, the magnetization as a function of field is due to rotation of a single domain and in polycrystalline
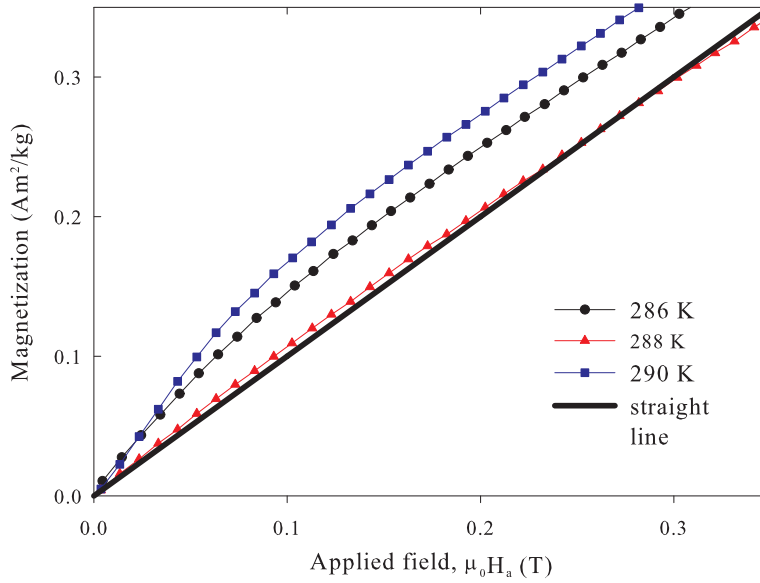
Figure 7.7: Magnetization of GdIG as a function of applied magnetic field at a temperatures close to T_{comp}. Near T_{comp} the magnetization as a function of applied field becomes increasingly linear. Also shown is a straight line with $M = a\mu_0 H_a$, where $a = 1 Am^2/kgT$.

or powder samples this can result in hysteresis as the grains are randomly oriented and the field is applied at an angle to the preferred orientation of the moments [110].

From isothermal magnetization curves we can calculate the change in magnetic entropy as a magnetic field is applied using Eq. (4.4). In this way, the magnetic entropy change of GdIG was calculated for temperatures near T_{comp}, see Fig. 7.10. Below T_{comp}, ΔS_M is negative as the Gd spins are ordered parallel to the applied magnetic field. Thus, when the applied field is increased, the magnetic entropy of the Gd spins is decreased. Above T_{comp}, the Gd spins are oriented anti-parallel to the applied magnetic field. The applied field does not affect the magnetization of the strongly coupled Fe magnetic moments much, but does reduce the effective field acting on the Gd spins. Therefore, the applied magnetic field has the effect of increasing the magnetic entropy of the Gd spins [100]. The lines between the entropy points in Fig. 7.10 calculated from the magnetization data all meet at the same point for which ΔS_M is zero. Without more calculated points we cannot determine the compensation temperature for our sample of GdIG from this data with any great accuracy, however, we know that it must be between 287 and 289 K.
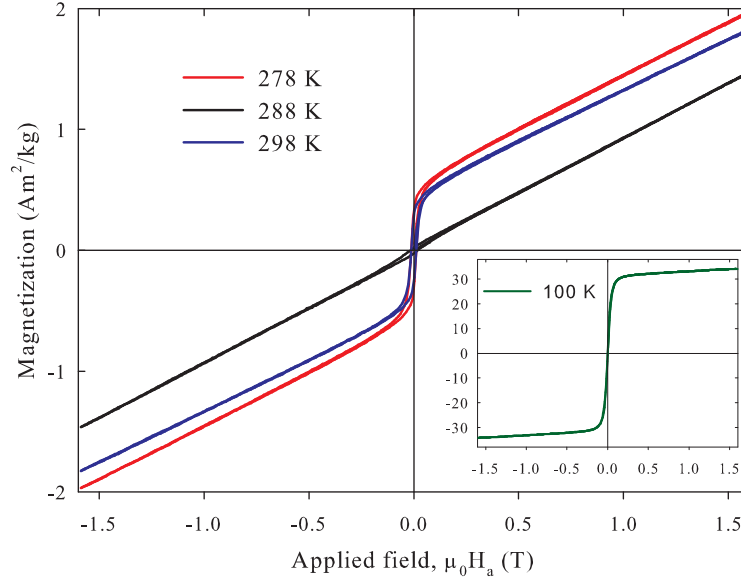
Figure 7.8: Hysteresis curves for GdIG recorded at temperatures below, near and above T_{comp} at applied fields up to $\mu_0 H_a = 1.6$ T. Inset: Hysteresis curve recorded at 100 K.

7.6 Calorimetry

Using a novel Differential Scanning Calorimeter (DSC) [90] the heat capacity was determined near T_{comp} for a range of applied magnetic fields, see Fig. 7.11. These measurements were made on a piece cut from the GdIG pellet before it was powdered. For zero or a low applied magnetic field of 0.01 T no change is seen in the heat capacity near T_{comp}. However, for applied magnetic fields of $\mu_0 H_a = 0.5$ or 1.0 T a small peak is clearly visible in the heat capacity near T_{comp}. The presence of a peak in the heat capacity indicates that a phase transition is taking place. However, we see only a single peak, not two as would be expected from the calculated phase diagram. Also, the appearance of a peak is a signature of first-order rather than second-order transitions, where a jump in the heat capacity is expected. However, these jumps in heat capacity often resemble peaks and the features in the determined heat capacities are not very clear, which could be the reason for this discrepancy. Kamilov and Shakhshaev investigated the heat capacity in a sample of GdIG at zero field and for an applied magnetic field of $\mu_0 H_a = 2.05$ T and found two clear peaks 4.2 K apart in the applied field data [111]. However, in their published data it appears that these peaks are also present in the zero-field measurement and appear at the same temperatures as in the applied-field
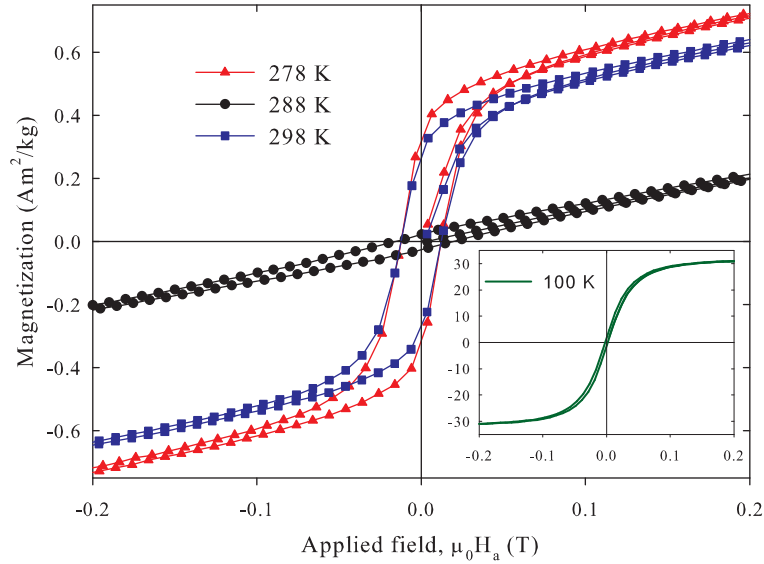
Figure 7.9: Close-up of the recorded hysteresis curves for GdIG. The curves were recorded at temperatures below, near and above T_{comp}. Inset: Close-up of hysteresis curve recorded at 100 K.
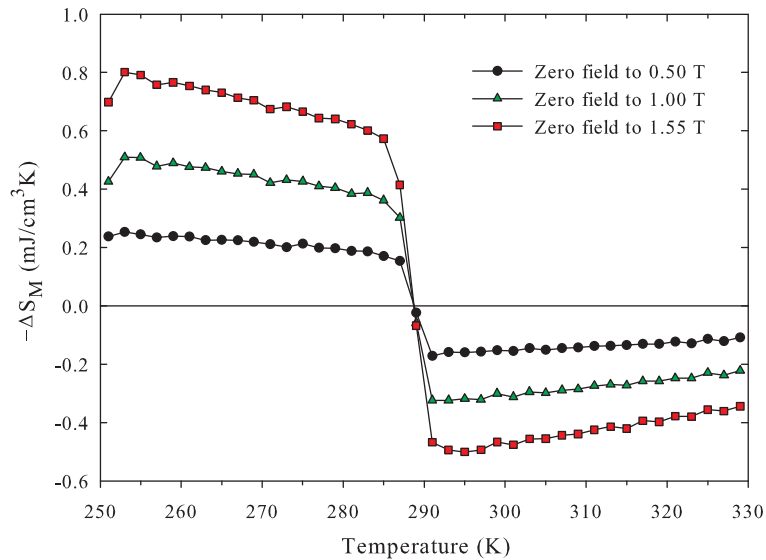
Figure 7.10: Magnetic entropy change, ΔS_M, for GdIG near T_{comp} for a change in applied magnetic field from zero field to $\mu_0 H_a = 0.5$, 1.0 and 1.5 T.
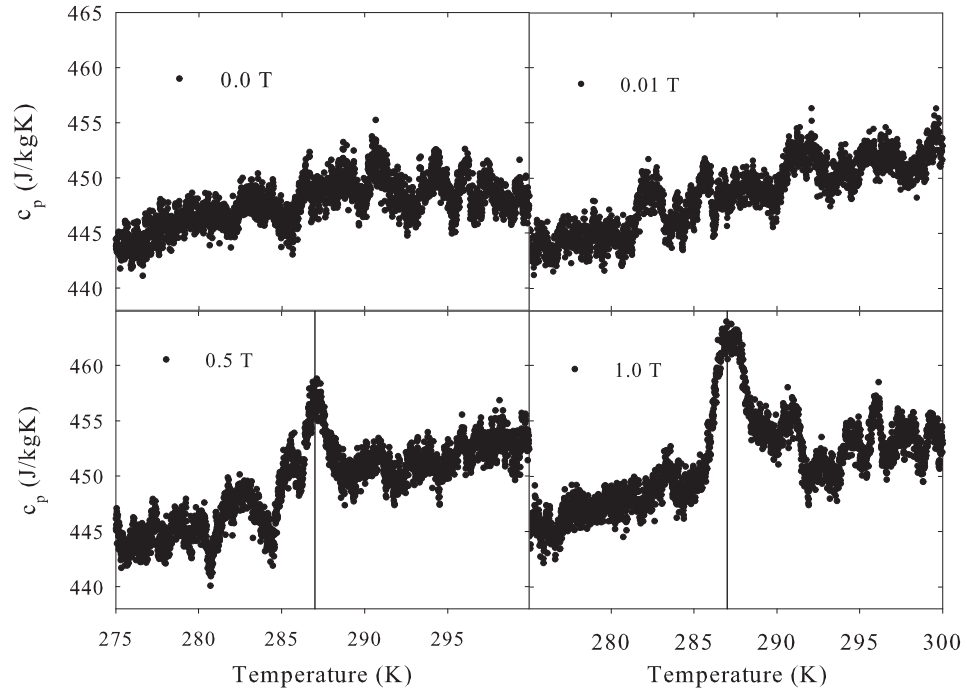
Figure 7.11: Heat capacity of GdIG near T_{comp} for a range of applied magnetic fields, $\mu_0 H_a$. The vertical lines in the plots of heat capacity for applied magnetic fields of $\mu_0 H_a = 0.5$ and 1.0 T are at 287 K.

measurement, which makes one question their origin.

7.7 Mössbauer Spectroscopy

The Mössbauer spectra were obtained using conventional constant acceleration Mössbauer spectrometers with sources of ^{57}Co in a Rh matrix. Spectra at different temperatures were obtained using a temperature-controlled liquid nitrogen cryostat. The spectrometers were calibrated with α-Fe foil at room temperature.

The information obtained from ^{57}Fe Mössbauer spectra on GdIG is the splitting and shifts of the nuclear levels of the ^{57}Fe in the Fe^{3+} sites. Due to the tilting of the Fe^{3+} tetra- and octahedra in GdIG, there are seven non-equivalent Fe sites, three tetrahedral and four octahedral ones [112]. This means that seven sextets are present in each spectrum. However, it is not

possible to fit so many sextets and obtain consistent and comparable values, so in the following only one sextet is fitted for the octahedral site and one for the tetrahedral site. Nine Mössbauer spectra on the sample of GdIG were recorded: at zero applied magnetic field, at 0.3 T and at 0.6 T for temperatures of 276, 286 and 296 K, see Fig. 7.12, Fig. 7.13 and Fig. 7.14. In the measurements the magnetic field was applied perpendicular to the direction of the γ-photons. The spectra were all fitted using the program mfit with line pairs having area, width and intensities equal and no constraints were put on the area ratios. The area ratios were not constrained as we are fitting only two sextets instead of seven, as mentioned above. This means that the area ratios from fitting only two sextets do not provide us with useful information.

In the Mössbauer spectra recorded at 276 K a small shoulder on line 6 in the sextet from the octahedral sites is seen, which could be due to a magnetic impurity containing Fe. As the lines shift with temperature and magnetic field, the shoulder on line 6 of the sextet for the octahedral site is not visible in the majority of the spectra. For this reason, and because the shoulder on line 6 could well be due to the existence of four octahedral sites, no separate sextet was fitted for it.

The determined values of the isomer shift and quadrupole interaction for the two fitted sextets are shown in Fig. 7.15 and Fig. 7.16. As expected due to their different coordination, the two Fe sites have different isomer shifts. For Fe^{3+} in a high-spin configuration, the typical values of the isomer shift are 0.2 - 0.6 mm/s relative to metallic Fe at room temperature [113]. Although the Fe in the tetrahedral site has isomer shifts of $\sim$0.17 mm/s, the value is not significantly lower than those typical for the high-spin state. The quadrupole splitting of the two Fe sites, shown in Fig. 7.16, is close to zero for both sites and at all temperatures and fields. As expected for Fe^{3+} in a high-spin state, there is no apparent temperature dependence of the quadrupole splitting.

Affecting the energy of the nuclear levels is also the magnetic induction acting on the magnetic moment of the Fe nuclei. The size of this induction is a sum of contributions as given by Eq. (4.7). Fig. 7.17 and Fig. 7.18 show the determined hyperfine fields for the two Fe sites. For zero applied magnetic field, the hyperfine field at both sites decreases as the temperature is increased due to thermal fluctuations reducing the magnetization, as expected. In Table 7.2, we compare the determined isomer shift, quadrupole splitting and hyperfine fields with values found in literature. Only the values determined for zero applied field are compared as, to the best of our knowledge, no values for applied magnetic fields exist in literature to compare with. In the applied-field data, we see the evidence of spin reversal as the temperature is changed from below to above T_{comp}. In region I, see Fig. 7.1, the Fe magnetic moment in the octahedral site is oriented parallel to the total magnetic moment, while the moment in the tetrahedral site is oriented anti-parallel to it. As the magnetic field at the nucleus is anti-parallel to the magnetic moment, the hyperfine field

Figure 7.12: Mössbauer spectra of GdIG sample recorded at 276 K and for various magnetic fields applied perpendicular to the γ-photons. The red line is the fit to the octahedral site, while the blue line is the fit to the tetrahedral site.

Figure 7.13: Mössbauer spectra of GdIG sample recorded at 286 K and for various magnetic fields applied perpendicular to the γ-photons. The red line is the fit to the octahedral site, while the blue line is the fit to the tetrahedral site.

Figure 7.14: Mössbauer spectra of GdIG sample recorded at 296 K and for various magnetic fields applied perpendicular to the γ-photons. The red line is the fit to the octahedral site, while the blue line is the fit to the tetrahedral site.

Figure 7.15: Determined isomer shifts for the two Fe sites in the nine Mössbauer spectra.
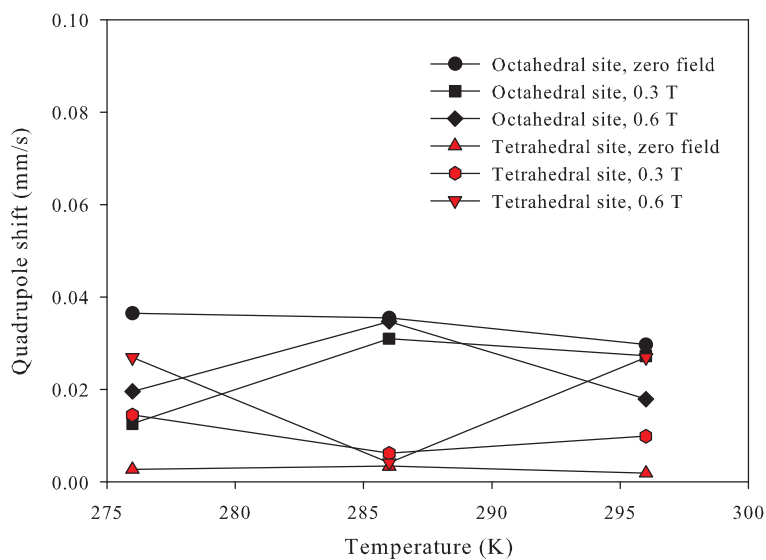
Figure 7.16: The quadrupole shifts for the two Fe sites in the nine Mössbauer spectra.
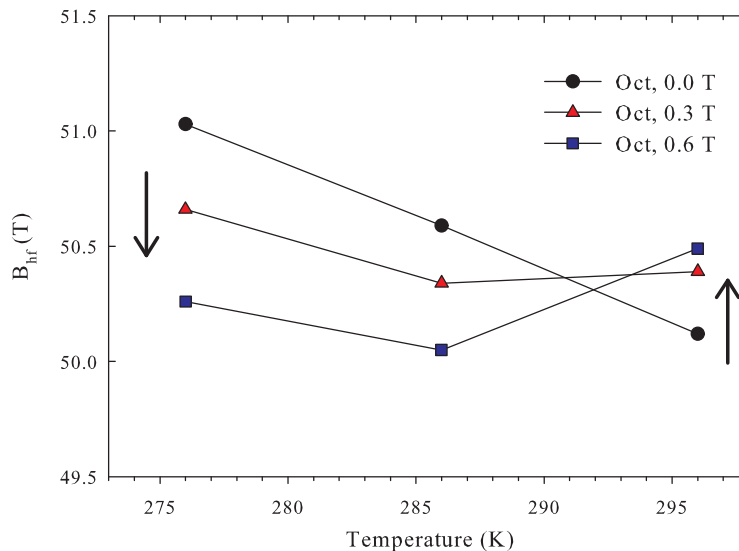
Figure 7.17: Hyperfine magnetic induction, B_{hf}, for the octahedrally coordinated Fe sites in GdIG.

	Isomer shift		Quadrupole shift		Hyperfine fields	
	Oct	Tet	Oct	Tet	Oct	Tet
GdIG sample	0.39	0.17	0.03	0.00	50.1	40.9
Literature [114]	0.39	0.18	0.04	0.00	49.4	40.5

Table 7.2: Values of the isomer shift, quadrupole shift and hyperfine fields determined for the two Fe sites in the GdIG sample at 296 K and with no applied magnetic field. The determined values are compared with ones found in literature for room temperature.

affecting the Fe nuclei in the octahedral sites is anti-parallel to the applied magnetic field, while that affecting the Fe nuclei in the tetrahedral sites is parallel to the applied field. As we apply a magnetic field, this results in a decrease (increase) in the moments, which are anti-parallel (parallel) to the applied field. Above T_{comp}, in region II, the spins have reversed, so that the applied field now causes an increase in the hyperfine field at the octahedral sites and a decrease in the field at the tetrahedral sites. Thus, the determined hyperfine fields at the two Fe-sites in GdIG is a direct way of measuring the reversal of the spins at T_{comp}.
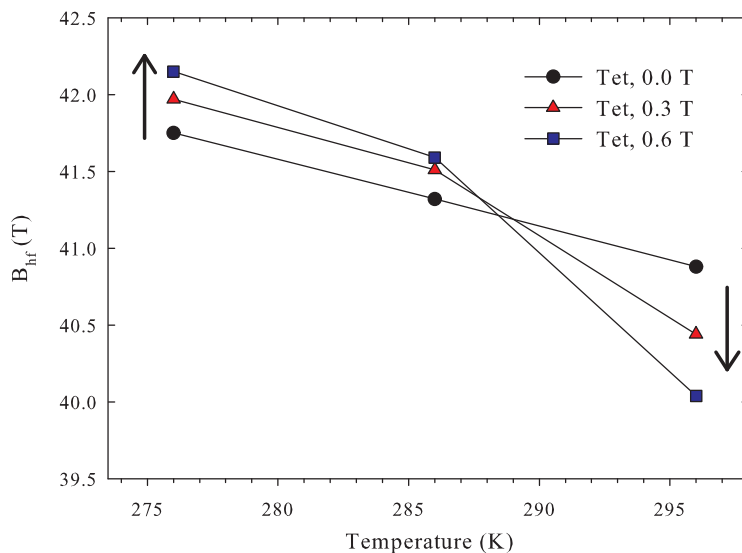
Figure 7.18: Hyperfine magnetic induction, B_{hf}, for the tetrahedrally coordinated Fe sites in GdIG.

7.8 Conclusions

GdIG is an interesting and complex magnetic system with its three magnetic sublattices. X-ray powder diffraction, magnetometry, calorimetry and Mössbauer spectroscopy were performed near the compensation temperature in a sample of GdIG. From the Mössbauer measurements recorded with a magnetic field applied perpendicular to the direction of propagation of the γ-photons, we have determined the effect of the field on the Fe magnetic moments. This provides a direct measurement of the reversal of the magnetic moments as T_{comp} is passed in temperature. The complexity of the three-sublattice system makes it possible for the magnetic entropy to change sign at T_{comp}. Our heat capacity measurements show a peak developing as the applied magnetic field is increased, but no conclusions can be drawn from the heat capacity data, which are, unfortunately, of poor quality. As a magnetic refrigerant the system is only of interest at low temperatures.

Chapter 8

Summary and Outlook

This thesis presented the work that was done to characterize a number of magnetic materials within the framework of magnetic refrigeration. Three very different magnetic materials were characterized, La(Fe,Co,Si)$_{13}$ (LFCS), Y$_6$(Fe,Mn)$_{23}$ (YFM) and Gd$_3$Fe$_5$O$_{12}$ (GdIG).

Results on an extensive characterization of eight LFCS samples produced by powder metallurgy have been presented and compared with reported measurements on samples produced by methods not suitable for large scale production. Also, as the material is a candidate for magnetic refrigeration, the LFCS samples were compared with the benchmark material Gd and evaluated on a number of criteria for magnetic refrigerants. The LFCS samples are found to have many characteristics making them suitable as magnetic refrigerants. The materials have a T_C temperature span of 90 K and a magnetic entropy change, ΔS_M is larger than or comparable to that of Gd. For a change in applied field from 0 to 1 T, the LFCS materials have $\Delta S_{M,\max} = 24 - 62$ mJ/cm^{3}K, while that of Gd is ~ 26 mJ/cm^{3}K. The materials series La(Fe$_{1-x}$Co$_x$)$_{11.9}$Si$_{1.1}$ with $0.055 < x < 0.122$ shows no hysteresis, magnetic or thermal, while a small thermal hysteresis of ~ 2 K is seen in the plate of La(Fe$_{0.851}$Co$_{0.066}$Si$_{0.083}$)$_{13}$. Two of the LFCS samples had their thermal conductivity, κ, measured and within the temperature span os $310 - 370$ K, it was found that $\kappa = 7.4 - 8.25$ W/Km, which is slightly smaller than the $10 - 12$ W/Km of Gd within the same temperature interval. The addition of a production method suitable for industrial use, which produces samples with the advantageous properties for magnetic refrigeration intact, enhances the outlook for these materials as magnetic refrigerants. A study on the corrosion of the LFCS samples demonstrated that this is an issue, which must be taken into consideration, if these materials are to be used in a refrigeration setup, where a cooling fluid in employed. The thermal expansion of the samples was studied using x-ray diffraction and a volume contraction of 1.5% in the temperature interval $223 - 303$ K was found, which could be significant in a refrigeration device. The brittleness of LFCS samples is also an issue, which needs to be addressed.

A single sample of YFM was studied using x-ray diffraction and magne-

tometry. From the magnetometry data, the magnetic entropy change was calculated and found to be too small for use in a magnetic refrigeration setup. It is possible that replacing the transition metals could lead to a better material as this would change the magnetic interactions.

Lastly, a sample of GdIG was characterized. It was found that the magnetic entropy change near the compensation temperature of ~ 288 K is very small, while it is zero at the compensation temperature itself. Therefore, the material is not suited for room temperature magnetic refrigeration. Mössbauer spectroscopy measurements allowed for a direct view of the spin reversal that takes place at the compensation temperature.

All the known magnetocaloric materials have advantages and disadvantages in the framework of magnetic refrigeration and it is possible that an as yet unknown material may be the answer. It is the opinion of this author that the progress towards a commercial room temperature magnetic refrigeration system is progressing slowly. A permanent magnet using Nd-Fe-B can only produce a magnetic field of $1.5 - 2$ T without becoming too big and heavy for a home or industrial refrigeration setup. With the available magnetic refrigerants, this magnetic field is insufficient to produce the magnetic entropy and adiabatic temperature changes needed. Therefore, it will be necessary to either increase the field available or find better magnetic refrigerants. With the promise of a cleaner and more efficient refrigeration system, it is desirable that the research be continued.

Appendix A

Matlab Program

A.1 Source Code

```matlab
1  function DeltaS_demag(PathName,IniFileName)
2  % DeltaS_demag(PathName,IniFileName)
3  % loads data files from VSM and calculates DeltaS
4  % A rectangular prism sample is assumed and dimensions
5  % are read from .ini file, so that demagnetization can be calculated and
6  % subtracted from applied fields to obtain internal fields.
7  %
8  % After internal fields are calculated, data for H_i<0 are removed and the
9  % magnetization data is interpolated to create a dataset with a step size
10 % of 0.005 T = 5 mT.
11 %
12 % PathName and IniFileName are optional.
13 % PathName can contain a path, where the data and .ini file is stored.
14 % If no path is given a window for selecting an .ini file is opened.
15 % If no IniFileName is given, the program assumes it is inifile.ini.
16 %
17 % Output is placed in a directory called Outputdir and consists of .pngs of
18 % graphs and text files with the calculated values.
19 %
20 % CAVEAT: The magnetization is extracted from the initial curves at a
21 % chosen number of fields given in the .ini file, plotted as a function of
22 % temperature and written as output. Depending on step-size of the
23 % initialcurves and whether the curves were measured using the continuous
24 % or point-by-point mode these results may deviate to some degree from a
25 % properly done magnetization versus temperature curve.
26 %
27 % BRH June 2010
28
29 %!! Do not make changes in the following
30 %% ---------------.ini file is read ---------------------
31 % If no arguments are given a browse window opens
32 if nargin<1
33     [IniFileName,PathName] = uigetfile('*.ini','Select the .ini file');
34 end
35 % If only the path is given, the name of the .ini file is assumed to be
36 % inifile.ini
37 if nargin<2
```

```
38         IniFileName='inifile.ini';
39    end
40    % If the path given does not end with a backslash one is appended
41    if PathName(length(PathName))≠'\'
42         PathName=cell2mat({[PathName,'\']});
43    end
44
45    % .ini file is opened and read
46    FileName={PathName,num2str(IniFileName)};
47    FileName=cell2mat(FileName);
48    fid=fopen(FileName);
49    if fid==-1
50         fprintf('Input file (inifile.ini) not found\n')
51         return
52    end
53    fgetl(fid);
54    data=textscan(fid, '%s', 'delimiter', '\n','commentStyle', '//');
55    fclose(fid);
56    data=data{1};
57
58    % The parameters from the .ini file are extracted
59    name=data(1);
60    composition=data(2);
61    m_gram=str2double(data(3));
62    density=str2double(data(4));
63    molarmass=str2double(data(5));
64    EntropyFieldstemp=cell2mat(data(6));
65    MagFieldstemp=cell2mat(data(7));
66    ArrottTempstemp=cell2mat(data(8));
67    a=str2double(data(9));
68    b=str2double(data(10));
69    c=str2double(data(11));
70    EntropyFields=cell2mat(textscan(EntropyFieldstemp,'%n','delimiter', ' '))';
71    MagFields=cell2mat(textscan(MagFieldstemp,'%n','delimiter', ' '))';
72    ArrottTemps=cell2mat(textscan(ArrottTempstemp,'%n','delimiter', ' '))';
73
74    %% ----------------- Filenames in directory determined --------------------
75    predir=cd; % current dir is saved, so that we can change back to this later
76    cd(PathName)
77
78    % Preallocation
79    filename=[];DIR=dir;fileindex_dat=[];fileindex_txt=[];outdir=0;
80
81    for i=3:length(DIR)
82         filename{i-2}=DIR(i,:).name;
83    end
84    m=1;k=1;
85    for i=1:length(filename)
86         answ1=findstr(filename{i},'dat');
87         answ2=findstr(filename{i},'txt');
88         answ3=findstr(filename{i},'Outputdir');
89         if answ1
90             fileindex_dat(m)=i;m=m+1;
91         elseif answ2
92             if findstr(filename{i},'Log')
```

```
 93              continue
 94          else
 95              fileindex_txt(k)=i;k=k+1;
 96          end
 97      elseif answ3
 98          outdir=1;
 99      end
100  end
101  cd(predir);
102  test1=length(fileindex_dat);test2=length(fileindex_txt);
103  if test1≠test2
104      fprintf('# of .dat files is not equal to the # of .txt files \n');
105      fprintf('(excluding files containing ''Log'')\n');
106      return
107  end
108  number=length(fileindex_dat);
109
110  %% -------------------- Data is read from .txt and .dat files ---------------
111  fprintf('Working...\n')
112
113  for r=1:number
114      filenames(r,:)={PathName,filename{fileindex_txt(r)}};
115
116      % Data is read from .txt files:
117      [vsm_matrix(:,:,r),datastr(:,:,r),dferror]=...
118          vsmdata(cell2mat(filenames(r,:)));
119      if dferror==1,
120          fprintf('File not found: %s \n',cell2mat(filenames(r,:)))
121          beep
122          return
123      end
124      if dferror==2
125          fprintf('File ended unexpectedly: %s \n',cell2mat(filenames(r,:)))
126          beep
127      end
128      filenames2(r,:)={PathName,filename{fileindex_dat(r)}};
129
130      % We determine the average temperature for the scan from the temperature
131      % data in the .dat file:
132      [temperature(r,:),dferror]=vsmdata2(cell2mat(filenames2(r,:)));
133      if dferror==1
134          fprintf('File not found: %s \n',cell2mat(filenames(r,:)))
135          beep
136          return
137      end
138      if dferror==2
139          fprintf('File ended unexpectedly: %s \n',cell2mat(filenames(r,:)))
140          beep
141      end
142  end
143  fclose all;
144
145  % Data is sorted according to temperature
146  [temperature,IX] = sort(temperature);
147  vsm_matrix(:,:,:)=vsm_matrix(:,:,IX);
```

```matlab
148  number=length(temperature);
149
150  %--------------- Preallocation (speeds up execution)---------------------
151  Z=zeros(length(EntropyFields),number);T=zeros(1,number);
152  Mag=zeros(1,number); AvT=zeros(1,number-1);T_interval=zeros(1,number-1);
153  DeltaS=zeros(length(EntropyFields),number-1);
154  peak_kg=zeros(1,length(EntropyFields));
155  peak_mol=zeros(1,length(EntropyFields));
156  peak_mJcm3=zeros(1,length(EntropyFields));
157  cv=zeros(1,number);arrottcheck=0;
158  legendtexttemp=cell(1,length(EntropyFields));
159  legendtext=cell(1,length(EntropyFields));
160  legendtexttemp2=cell(1,length(MagFields));
161  legendtext2=cell(1,length(MagFields));
162  arrottx=zeros(1,length(ArrottTemps));
163  arrotty=zeros(1,length(ArrottTemps));
164  ArrottTempsFound=zeros(1,length(ArrottTemps));
165  %% ------------------- Initialization of figures -----------------------
166  FigureNames={'Raw data', 'Delta S', 'Magnetization','Arrottplot',...
167      'Gridplot of magnetization','Gridplot of Delta S'};
168  FigurePositions={'[0 280 1486 692]','[8 348 610 481]',...
169      '[801 266 876 645]','[488 69 495 353]','[789 204 873 697]',...
170      '[21 127 1165 839]'};
171  FigureDesignations={'fig1','fig2','fig3','fig4','fig5','fig6'};
172  FigureMax=size(FigureNames,2);
173  handl=zeros(1,FigureMax);
174  for k=1:FigureMax
175      ExeString=cell2mat({FigureDesignations{k},'=findobj(''Name'','''',...
176          FigureNames{k},''');'});
177      eval(ExeString);
178      if isempty(eval(FigureDesignations{k}));
179          ExeString=cell2mat({FigureDesignations{k},'=figure(''Name'','''',...
180              FigureNames{k},''',''position'',',FigurePositions{k},');'});
181          eval(ExeString);
182      end
183      ExeString=cell2mat({'figure(',FigureDesignations{k},')'});
184      eval(ExeString);clf;
185      handl(k)=gcf;
186  end
187  %% ----------- Extract raw VSM data and calculate area under curves -------
188  count=1;
189  mu0=4*pi*1E-7;
190
191  % Demagnetization calculated for rectangular prism (Aharoni, 1998)
192  Dz=1/pi*((b^2-c^2)/(2*b*c)*log((sqrt(a^2+b^2+c^2)-a)/(sqrt(a^2+b^2+c^2)+a))+...
193      (a^2-c^2)/(2*a*c)*log((sqrt(a^2+b^2+c^2)-b)/(sqrt(a^2+b^2+c^2)+b))+...
194      b/(2*c)*log((sqrt(a^2+b^2)+a)/(sqrt(a^2+b^2)-a))+...
195      a/(2*c)*log((sqrt(a^2+b^2)+b)/(sqrt(a^2+b^2)-b))+...
196      c/(2*a)*log((sqrt(b^2+c^2)-b)/(sqrt(b^2+c^2)+b))+...
197      c/(2*b)*log((sqrt(a^2+c^2)-a)/(sqrt(a^2+c^2)+a))+...
198      2*atan((a*b)/(c*sqrt(a^2+b^2+c^2)))+(a^3+b^3-2*c^3)/(3*a*b*c)+...
199      (a^2+b^2-2*c^2)/(3*a*b*c)*sqrt(a^2+b^2+c^2)+...
200      c/(a*b)*(sqrt(a^2+c^2)+sqrt(b^2+c^2))-...
201      ((a^2+b^2).^(3/2)+(b^2+c^2).^(3/2)+(c^2+a^2).^(3/2))/(3*a*b*c));
202
```

98

```matlab
203    for m=1:number
204        data=[vsm_matrix(:,1,m) vsm_matrix(:,2,m)];
205        if m==1 % Preallocation
206            Happlied_Oe=zeros(number,length(data(:,1)));
207            Happlied_Am=zeros(number,length(data(:,1)));
208            Happlied_T=zeros(number,length(data(:,1)));
209            Hdemag=zeros(number,length(data(:,1)));
210            Hinternal_T1=zeros(number,length(data(:,1)));
211            M_emu=zeros(number,length(data(:,2)));
212            M_Am1=zeros(number,length(data(:,2)));
213        end
214        Happlied_Oe(m,:)=abs(data(:,1));                  % G
215        Happlied_Am(m,:)=Happlied_Oe(m,:)*1E3/(4*pi);     % A/m
216        Happlied_T(m,:)=Happlied_Am(m,:)*mu0;             % T
217        M_emu(m,:)=abs(data(:,2));                        % emu
218        M_Am1(m,:)=M_emu(m,:)/m_gram*density*1E3;         % A/m
219
220        % Internal fields calculated from demagnetization factor, data plotted
221        Hdemag(m,:)=Dz*M_Am1(m,:);
222        Hinternal_T1(m,:)=(Happlied_Am(m,:)-Hdemag(m,:))*mu0;
223
224        figure(fig1)
225        subplot(1,3,2);hold on
226        plot(Hinternal_T1(m,:),M_Am1(m,:),'.g');
227        xlabel('<H_i> (T)');ylabel('Magnetization (A/m)')
228        title('Demagnetization calculated and subtracted')
229        axis tight
230
231        % Data for Hinternal<0 removed. The data is then interpolated.
232        if m==1
233            Hinternal_T_temp=Hinternal_T1(m,Hinternal_T1(m,:)>0);
234            HintMaxRounded1=...
235                round(Hinternal_T_temp(length(Hinternal_T_temp))*100)/100;
236            % Hinternal_T with step size 0.005T:
237            Hinternal_T(m,:)=0.005:0.005:HintMaxRounded1-0.005;
238            M_Am_temp=M_Am1(m,Hinternal_T1(m,:)>=0);
239            % Magnetization interpolated:
240            M_Am(m,:)=interp1(Hinternal_T_temp,M_Am_temp,Hinternal_T(m,:));
241        else
242            Hinternal_T_temp=Hinternal_T1(m,Hinternal_T1(m,:)>0);
243            HintMaxRounded=...
244                round(Hinternal_T_temp(length(Hinternal_T_temp))*100)/100;
245            % Hinternal_T with step size 0.005T
246            Hinternal_T_temp2=0.005:0.005:HintMaxRounded;
247            M_Am_temp=M_Am1(m,Hinternal_T1(m,:)>=0);
248            % Magnetization interpolated
249            M_Am_temp2=interp1(Hinternal_T_temp,M_Am_temp,Hinternal_T_temp2);
250            M_Am(m,:)=M_Am_temp2(1:length(Hinternal_T(1,:)));
251            Hinternal_T(m,:)=Hinternal_T_temp2(1:length(Hinternal_T(1,:)));
252        end
253        for j=1:length(M_Am(m,:))
254            if isnan(M_Am(m,j))
255                M_Am(m,j)=0;
256            end
257        end
```

```
258
259      % Magnetic moment at internal fields given in .ini file extracted
260      for n=1:length(MagFields)
261          [i,cv(m)]=searchclosest(Happlied_T(m,:),MagFields(n));
262          Mag(n,m)=M_Am1(m,i);
263      end
264
265      % Area under magnetization curve cumulated for each data point (T*A/m)
266      X(m,:)=cumsimpson(Hinternal_T(m,:),M_Am(m,:));
267
268      for i=1:length(EntropyFields)
269          mask=Hinternal_T(m,:)≤EntropyFields(i);
270          Hmask=Hinternal_T(m,:).*mask;
271          % Area up to first, second etc. internal field (T*A/m):
272          Z(i,m)=X(m,Hmask==max(Hmask));
273      end
274
275      Hinternal_Am(m,:)=Hinternal_T(m,:)./mu0;   %Internal field (A/m)
276
277      % Values for Arrott plot extracted (internal field used)
278      if size(ArrottTemps,2)≠0
279          if ArrottTemps(count)-0.5<temperature(m,:)&&...
280                  ArrottTemps(count)+0.5>temperature(m,:)
281              arrottcheck=1;
282              arrottxplot(count,:)=(M_Am(m,:)).^2;
283              arrottyplot(count,:)=Hinternal_Am(m,:)./M_Am(m,:);
284              % Extract x-position for figure text:
285              arrottx(count)=max(arrottxplot(count,:));
286              % Extract y-position for figure text:
287              arrotty(count)=max(arrottyplot(count,:));
288              % The temperatures found for writing in file later
289              ArrottTempsFound(count)=ArrottTemps(count);
290              if count≠length(ArrottTemps)
291                  count=count+1;
292              end
293          end
294      end
295
296      T(m)=temperature(m,:);
297  end
298  %% --------- Plots of raw data, interpolated data and Arrott plot ---------
299  % Plot of raw data
300  figure(fig1)
301  subplot(1,3,1)
302  plot(Happlied_T*10000,M_emu,'.b');
303  xlabel(datastr(1,:,m));ylabel(datastr(2,:,m));
304  title(['Raw data, T = ' num2str(temperature(1,:)) ...
305      ' - ' num2str(temperature(number,:))]);
306  axis tight
307
308  % Plot of interpolated magnetization versus temperature
309  subplot(1,3,3)
310  plot(Hinternal_T,M_Am,'.m');
311  xlabel('<H_i> (T)');ylabel('Magnetization (A/m)')
312  title('Interpolated magnetization data')
```

```matlab
313  axis tight
314
315  % If values for Arrott plot exists, plot
316  if count>1
317      figure(fig4);
318      hold on;plot(arrottxplot,arrottyplot,'.b');
319      xlabel('M^2 (A^2/m^2)');ylabel('H/M');
320      title('Arrott plot');
321      for k=1:length(arrottx)
322          text(arrottx(k),arrotty(k),num2str(ArrottTemps(k)),'FontSize',14)
323      end
324  end
325
326  %% ------------------- Calculation of DeltaS ----------------------------
327  for k=1:number-1
328      AvT(k)=(T(k)+T(k+1))/2;          % Average temp. of curves defining area
329      T_interval(k)=abs(T(k)-T(k+1)); % Temperature interval between curves
330      for l=1:length(EntropyFields)
331          % Unit of DeltaS: (T*A/m)/(g/cm^3*K) = 10^-3 J/kg*K
332          DeltaS(l,k)=(Z(l,k)-Z(l,k+1))/T_interval(k)/density;
333      end
334  end
335  DeltaS_kg=DeltaS*1E-3;               % J/kg*K
336  DeltaS_mol=DeltaS*molarmass*1E-6;   % J/g*K * g/mol = J/mol*K
337  DeltaS_mJcm3=DeltaS_kg*density;     % mJ/cm^3*K = 10^3 (T*A/m)/K
338
339  peak_x=AvT(find(DeltaS_kg(1,:)==max(DeltaS_kg(1,:))));
340  for k=1:length(EntropyFields)
341      peak_kg(k)=max(DeltaS_kg(k,:));
342      peak_mol(k)=max(DeltaS_mol(k,:));
343      peak_mJcm3(k)=max(DeltaS_mJcm3(k,:));
344  end
345
346  %% ----------------- Plot DeltaS in two sets of units -------------------
347
348  % Plot DeltaS for selected fields
349  figure(fig2);
350  ratio=density;
351  [ax, h]=plot2axes(AvT,DeltaS_kg','YScale', ratio);
352  set(h,'LineStyle','-');set(h,'Marker','x')
353  set(get(ax(1), 'ylabel'), 'string', '-\Delta S_M [J/kg\cdot K]');
354  set(get(ax(2), 'ylabel'), 'string', '-\Delta S_M [mJ/cm^3\cdot K]');
355  xlabel('Temperature [K]');
356  for i=1:length(EntropyFields)
357      legendtexttemp{i}={num2str(EntropyFields(i)),'T'};
358      legendtext{i}=cell2mat(legendtexttemp{i});
359  end
360  legend(legendtext(:),'Location','NorthWest')
361
362  % Gridplot of Delta S (internal fields)
363  figure(fig6)
364  for k=1:length(Hinternal_T)
365      for h=1:number-1
366          T_interval=abs(T(h)-T(h+1)); % Temperature interval between curves
367          DSmesh(h,k)=abs((X(h,k)-X(h+1,k)))./T_interval*1E-3;
```

```matlab
368            %Units of DSmesh: T *A/m /K = 10^3 mJ/cm^3.K
369            hmesh(h,:)=Hinternal_T(h,:);
370       end
371  end
372  AvTcat=AvT';
373  surf(hmesh,AvTcat,DSmesh,'EdgeColor','none','FaceColor','interp')
374  axis tight
375  colorbar('FontSize',14)
376  lighting phong
377  xlabel('Internal field, \mu_0H_i (T)','FontSize',14);
378  ylabel('Temperature(K)','FontSize',14);
379  zlabel('-\Delta S_M [mJ/cm^3\cdot K]','FontSize',14)
380  view([-40 40])
381  grid on
382  set(gca,'FontSize',14)
383
384  %% ----------------- Plot magnetization vs temperature ------------------
385
386  % 2D plot of magnetization (NOT internal fields)
387  figure(fig3)
388  plot(T,Mag,'-x')
389  xlabel('Temperature (K)');ylabel('Magnetization (A/m)')
390  title('Magnetization at various applied fields');
391  axis tight
392  for i=1:length(MagFields)
393      legendtexttemp2{i}={num2str(MagFields(i)),'T'};
394      legendtext2{i}=cell2mat(legendtexttemp2{i});
395  end
396  legend(legendtext2(:),'Location','NorthEast')
397
398  % Gridplot of magnetization (NOT internal fields)
399  figure(fig5)
400  for h=1:number
401      mmesh(h,:)=abs(vsm_matrix(:,2,h))/m_gram*density*1E3;
402      % Units of mmesh: A/m = 10^-3 emu/cm^3
403      hmesh2(h,:)=abs(vsm_matrix(:,1,h))/10000;
404  end
405  surf(hmesh2,temperature,mmesh,'EdgeColor','none')
406  axis tight
407  colorbar('FontSize',14)
408  lighting phong
409  xlabel('Applied field (T)','FontSize',14);
410  ylabel('Temperature(K)','FontSize',14);
411  zlabel('Magnetization (A/m)','FontSize',14)
412  view([-162 22])
413  grid on
414  set(gca,'FontSize',14)
415
416  %% ----------------- Write output files and pngs -------------------------
417  if ¬outdir
418      cd(PathName);
419      mkdir('Outputdir');
420  end
421  name=cell2mat(name);composition=cell2mat(composition);
422
```

```matlab
423  % Data for Arrott plot at chosen temperatures written to file
424  if arrottcheck
425      sizearrott=size(arrottxplot);
426      n=1;
427      Writearrott=zeros(sizearrott(1),sizearrott(2)+1);
428      for i=1:size(arrottxplot,1)
429          Writearrott(i+(n-1),:)=[ArrottTempsFound(i),arrottxplot(i,:)];
430          Writearrott(i+n,:)=[ArrottTempsFound(i),arrottyplot(i,:)];
431          n=n+1;
432      end
433      Writearrott=Writearrott';
434      Filename2={PathName,'Outputdir\',name,'_Arrott.out'};
435      Filename2=cell2mat(Filename2);
436      dlmwrite(Filename2,Writearrott, 'delimiter', '\t');
437  end
438
439  % Data for DeltaS at chosen fields written to files
440  WriteDS=[AvT;DeltaS_kg];WriteDS=WriteDS';
441  Filename2={PathName,'Outputdir\',name,'_DeltaS_kg.out'};
442  Filename2=cell2mat(Filename2);
443  extEntropyFields=[0,EntropyFields];
444  DSwrite_kg=[extEntropyFields;WriteDS];
445  dlmwrite(Filename2,DSwrite_kg, 'delimiter', '\t');
446
447  WriteDS=[AvT;DeltaS_mol];WriteDS=WriteDS';
448  Filename2={PathName,'Outputdir\',name,'_DeltaS_mol.out'};
449  Filename2=cell2mat(Filename2);
450  extEntropyFields=[0,EntropyFields];
451  DSwrite_mol=[extEntropyFields;WriteDS];
452  dlmwrite(Filename2,DSwrite_mol, 'delimiter', '\t');
453
454  WriteDS=[AvT;DeltaS_mJcm3];WriteDS=WriteDS';
455  Filename2={PathName,'Outputdir\',name,'_DeltaS_mJcm3.out'};
456  Filename2=cell2mat(Filename2);
457  extEntropyFields=[0,EntropyFields];
458  DSwrite_mJ=[extEntropyFields;WriteDS];
459  dlmwrite(Filename2,DSwrite_mJ, 'delimiter', '\t');
460
461  % Gridplot data for DeltaS written to files
462  Filename2={PathName,'Outputdir\',name,'_DSmesh.out'};
463  Filename2=cell2mat(Filename2);
464  dlmwrite(Filename2,DSmesh, 'delimiter', '\t');
465  WriteDS=hmesh;
466  Filename2={PathName,'Outputdir\',name,'_hmesh.out'};
467  Filename2=cell2mat(Filename2);
468  dlmwrite(Filename2,WriteDS', 'delimiter', '\t');
469  Filename2={PathName,'Outputdir\',name,'_AvTcat.out'};
470  Filename2=cell2mat(Filename2);
471  dlmwrite(Filename2,AvTcat, 'delimiter', '\t');
472
473  % Magnetization at chosen fields written to file
474  Writemag=[T;Mag];Writemag=Writemag';
475  Filename2={PathName,'Outputdir\',name,'_Magnetization.out'};
476  Filename2=cell2mat(Filename2);
477  extMagFields=[0,MagFields];
```

```
478  MagFieldswrite=[extMagFields;Writemag];
479  dlmwrite(Filename2,MagFieldswrite, 'delimiter', '\t');
480
481  % Main output file
482  Filename2={PathName,'Outputdir\',name,'_output.out'};
483  Filename2=cell2mat(Filename2);
484  [n, s] = weekday(now);
485  fid = fopen(Filename2, 'wt');
486  fprintf(fid, 'Main output file for Matlab program DeltaS\n\n');
487  fprintf(fid, 'The run was executed on %s %s \n\n', s, datestr(now));
488  fprintf(fid, 'The input file contained the following information:\n');
489  fprintf(fid, 'Name:            %s\n', name);
490  fprintf(fid, 'Composition:     %s\n', composition);
491  fprintf(fid, 'Sample weight:   %6.6f g\n',m_gram);
492  fprintf(fid, 'Sample density:  %6.4f g/cm^3\n',density);
493  fprintf(fid, 'Sample molarmass: %6.4f g/mol\n',molarmass);
494  fprintf(fid, 'Sample dimensions:%6.2f x %6.2f x %6.2f mm\n\n',a,b,c);
495  fprintf(fid, 'Using Aharonis formula the demagnetization is: %6.4f \n\n',Dz);
496  fprintf(fid, 'The Max. internal applied field is %2.2f T\n\n',HintMaxRounded1);
497  fprintf(fid, 'The entropy change was calculated at the following fields:\n');
498  fprintf(fid, '%6.2f T\n', EntropyFields);
499  fprintf(fid, '\n The magnetization was extracted at the following fields:\n');
500  fprintf(fid, '%6.2f T\n', MagFields);
501  fprintf(fid,...
502      '\nPeak in DeltaS_M (determined for max field) is at %6.2f K\n\n',peak_x);
503  fprintf(fid, 'Values of maxima in DeltaS_M:\n');
504  fprintf(fid, 'Applied field        J/kg.K                 J/mol.K\n');
505  for i=1:length(EntropyFields)
506      fprintf(fid, '%6.2f          %6.4f           %6.4f          %6.4f\n',...
507          EntropyFields(i), peak_kg(i), peak_mol(i), peak_mJcm3(i));
508  end
509  fclose(fid);
510
511  % ------- Figures saved as .pngs -------
512  for i=1:length(handl)
513      FigFileName={'RawData','DeltaS','Magnetization','Arrottplot',...
514          'Magnetization gridplot','DeltaS gridplot'};
515      FigFilePath={PathName,'Outputdir\',FigFileName{i}};
516      saveas(handl(i),cell2mat(FigFilePath),'png');
517  end
518  fprintf('Done! \n')
519  cd(predir)
520  end %DeltaS_demag
521
522  %-------------------------------------------------------------------------
523  function [data,datastr,dferror]=vsmdata(file)
524  %-------------------------------------------------------------------------
525  % function [data,datastr]=dscdata(file)
526  %
527  % MATLAB function to load VSM .txt file, returning
528  % the applied field and magnetic moment with headings 'datastr'
529  %
530  % BRH: 31.5.07
531  % Made by altering Tascom load file written by
532  % DFM: 27.4.97
```

```matlab
533  %
534  %----- Open VSM data file
535  data=[]; datastr=[];dferror=0;
536
537  fid=fopen(file,'r');
538  if (fid <0)
539      dferror=1;
540      return;
541  end
542
543  %----- Read through data file
544  test='zzzz';data=[];datastr=[];
545
546  while strncmp(test,'***DATA***',10)==0
547      dataline=fgetl(fid);
548      if ¬isempty(dataline)
549          if dataline==-1, dferror=2; return, end
550      end
551      [test,remain]=strtok(dataline);
552      if (length(test)==10),test=dataline; end
553  end
554  fgetl(fid); %skip line
555
556  %----- Create column headers
557  dataline=fgetl(fid);
558  while ¬isempty(dataline)
559      [column_lab,dataline]=strtok(dataline);
560      datastr=strvcat(datastr,column_lab);
561  end
562
563  %----- Read data
564  while(1)
565      dataline=fgetl(fid);
566      if isempty(dataline),
567          return
568      elseif ¬isempty(dataline)
569          a=sscanf(dataline,'%f'); data=[data; a'];
570      end
571  end
572
573  fclose(fid)
574  return
575  end %vsmdata
576
577  function [temperature,dferror]=vsmdata2(file)
578  %
579  % function [data,datastr]=dscdata(file)
580  %
581  % MATLAB function to load VSM .dat file, returning
582  % the temperature
583  %
584  % BRH: 31.5.07
585  % Made by altering Tascom load file written by
586  % DFM: 27.4.97
587  %
```

105

```matlab
588  %----- Open VSM data file
589
590  temperature=[];dferror=0;
591  fid=fopen(file,'r');
592  if (fid <0)
593      dferror=1;
594      return;
595  end
596
597  %----- Read number of points
598  test='zzzz';
599  while strncmp(test,'Points',6)==0
600      dataline=fgetl(fid);
601      [test,remain]=strtok(dataline);
602      m=str2double(remain);
603  end
604
605  %----- Read through data file
606  while strncmp(test,'Temperature ',12)==0
607      dataline=fgetl(fid);
608      if ¬isempty(dataline)
609      if dataline==-1, dferror=1; return, end
610      end
611      [test,remain]=strtok(dataline);
612      test=dataline;
613  end
614
615  %----- Read data
616  temperaturedata=zeros(m,1);m=1;
617  while strncmp(test,'Angle ',6)==0
618      dataline=fgetl(fid);
619      test=dataline;
620      temperaturedata(m)=str2double(dataline);
621      m=m+1;
622  end
623  temperaturedata(length(temperaturedata))=[];
624  temperature=sum(temperaturedata)/length(temperaturedata);
625
626  fclose(fid);
627  return
628  end %vsmdata2
629
630  %-------------------------------------------------------------------------
631  function z=cumsimpson(x,y)
632  %CUMSIMPSON Cumulative Simpson Numerical Integration.
633  % Z=CUMSIMPSON(Y) computes an approximation of the cumulative integral of Y
634  % using a Simpson rule with unit spacing between the data points in Y. To
635  % compute the integral for spacing different from one, multiply Z by the
636  % spacing increment. When Y is a matrix, the cumulative integral is
637  % computed over each column of Y.
638  %
639  % Z=CUMSIMPSON(X,Y) computes the integral with respect to the data in
640  % vector X. X need NOT be EQUALLY spaced but must have the same number of
641  % elements as Y. When Y is a matrix, Y must have as many rows as X has
642  % elements.
```

```matlab
643  %
644  % Z has the same dimensions as Y.
645  %
646  % See also CUMSUM, CUMTRAPZ, QUAD, QUADV.
647
648  % D.C. Hanselman, University of Maine, Orono, ME 04469
649  % MasteringMatlab@yahoo.com
650  % Mastering MATLAB 7
651  % 2005-09-30, 2006-02-21
652
653  if nargin<2
654      y=x;
655      [ry,cy]=size(y);
656      if ry==1
657          x=1:cy;
658      else
659          x=1:ry;
660      end
661  elseif nargin==2
662      [ry,cy]=size(y);
663  else
664      error('One or Two Inputs Are Required.')
665  end
666  if ndims(y)≠2
667      error('N-dimensional Data is Not Supported.')
668  end
669  if min(size(x))>1
670      error('X Must be a Vector.')
671  end
672  x=x(:);    % make x a column
673  if ry==1 % y is a row vector, make it a column
674      yisrow=true;
675      y=y.';
676      ry=cy;
677      cy=1;
678  else
679      yisrow=false;
680  end
681  if length(x)≠ry
682      error('Length of X Must Match Length of Y or Rows of Matrix Y.')
683  end
684  if length(x)<3
685      error('At Least 3 Data Points are Required.')
686  end
687  dx=repmat(diff(x),1,cy);
688  dy=diff(y);
689
690  dx1=dx(1:end-1,:);
691  dx2=dx(2:end,:);
692  dxs=dx1+dx2;
693  dy1=dy(1:end-1,:);
694  dy2=dy(2:end,:);
695
696  a=(dy2./(dx2.*dxs) - dy1./(dx1.*dxs))/3;
697  b=(dy2.*dx1./(dx2.*dxs) + dy1.*dx2./(dx1.*dxs))/2;
```

```matlab
698  c=y(2:end-1,:);
699
700  i1=((a.*dx1-b).*dx1+c).*dx1; % left half integral
701  i2=((a.*dx2+b).*dx2+c).*dx2; % right half integral
702
703  z=zeros(ry,cy);               % pure cumlative Simpson
704  z(2:2:end-1,:)=i1(1:2:end,:);
705  z(3:2:end,:)=i2(1:2:end,:);
706  z(end,:)=i2(end,:);
707  z=cumsum(z);
708
709  % z=[zeros(1,cy);...           % original algorithm here has ¬2X error
710  %    cumsum([i1(1,:); (i1(2:end,:)+i2(1:end-1,:))/2; i2(end,:)])];
711
712  if yisrow
713      z=z.';
714  end
715  end %cumsimpson
716  %-------------------------------------------------------------------------
717  function [ax, h] = plot2axes(varargin)
718  %-------------------------------------------------------------------------
719  %PLOT2AXES Graphs one set of data with two sets of axes
720  %
721  %   PLOT2AXES(X, Y, 'Option1', 'Value1', ...) plots X versus Y with secondary
722  %   axes.  The following options are accepted [default values]:
723  %
724  %      XLoc ['top']: location of secondary X-axis
725  %      YLoc ['right']: location of secondary Y-axis
726  %      XScale [1]: scaling factor for secondary X-axis (scalar)
727  %      YScale [1]: scaling factor for secondary Y-axis (scalar)
728  %
729  %                   XScale and YScale can also be a character string
730  %                   describing the relationship between the 2 axes, such as
731  %                   the equation relating Celsius and Fahrenheit: '5/9*(x-32)'
732  %
733  %         Note: PLOT2AXES only works when the relationship is linear.
734  %               Non-linearly related axes (e.g. 1/x, x^2, etc) do not work.
735  %
736  %      XLim [NaN NaN] : XLim in the primary axes (secondary is adjusted
737  %                       accordingly). The default is naturally selected by
738  %                       the plotting function.
739  %      YLim [NaN NaN] : YLim in the primary axes (secondary is adjusted
740  %                       accordingly). The default is naturally selected by
741  %                       the plotting function.
742  %
743  %   PLOT2AXES(@FUN, ...) uses the plotting function @FUN instead of PLOT to
744  %   produce the plot.  @FUN should be a function handle to a plotting
745  %   function, e.g. @plot, @semilogx, @semilogy, @loglog ,@stem, etc. that
746  %   accepts the syntax H = FUN(...).  Optional arguments accepted by these
747  %   plotting functions are also allowed (e.g. PLOT2AXES(X, Y, 'r*', ...))
748  %
749  %   [AX, H] = PLOT2AXES(...) returns the handles of the primary and
750  %   secondary axes (in that order) in AX, and the handles of the graphic
751  %   objects in H.
752  %
```

```
753  %    The actual data is plotted in the primary axes.  The primary axes lie
754  %    on top of the secondary axes.  After the execution of this function,
755  %    the primary axes become the current axes.  If the next plot replaces
756  %    the axes, the secondary axes are automatically deleted.
757  %
758  %    When you zoom in or out using the toolbar, it would only zoom the
759  %    primary axes, so you should click on the 'Fix Axes' menu at the top of
760  %    the figure to re-adjust the secondary axes limits.
761  %
762  %    PLOT2AXES('FixAxes') fixes the secondary limits of all figures created
763  %    using plot2axes.
764  %
765  %    Example 1:
766  %      x = 0:.1:1;
767  %      y = x.^2 + 0.1*randn(size(x));
768  %      [ax, h] = plot2axes(x, y, 'ro', 'YScale', 25.4);
769  %      title('Length vs Time');
770  %      set(get(ax(1), 'ylabel'), 'string', 'inch');
771  %      set(get(ax(2), 'ylabel'), 'string', 'millimeter');
772  %      xlabel('time (sec)');
773  %
774  %    Example 2:
775  %      [ax, h] = plot2axes(x, y, 'ro', 'YScale', '5/9*(x-32)');
776  %      set(get(ax(1), 'ylabel'), 'string', 'Fahrenheit');
777  %      set(get(ax(2), 'ylabel'), 'string', 'Celcius');
778  %
779  % VERSIONS:
780  %   v1.0 - first version
781  %   v1.1 - added option to specify X and Y limits
782  %   v1.2 - remove tick labels for secondary axes if no scaling factors are
783  %          specified. Also, fixed bug in matching the scaling type (linear
784  %          or log).
785  %   v1.3 - added the 'Fix Axes' menu for adjusting the secondary axes limits
786  %          after zooming.
787  %   v1.4 - added the option for specifying an equation for XScale and YScale
788  %          (June 2005)
789  %   v1.5 - fixed problem plotting on uipanel, where the parent of the axes
790  %          is not a figure. (Feb 2006)
791  %
792
793  % Jiro Doke (Inspired by ideas from Art Kuo, Univ of Michigan)
794  % March 2005
795  %
796
797  if nargin < 1
798    error('Not enough input arguments');
799  end
800
801  if nargin == 1 && strcmpi(varargin{1}, 'FixAxes')
802    figsH = findobj('Type', 'figure');
803    if ¬isempty(figsH)
804      for iFig = 1:length(figsH)
805        p2a = getappdata(figsH(iFig), 'p2a');
806        FixAxes([], [], p2a);
807      end
```

```
808     end
809     return;
810   end
811
812   % Default options
813   options{1} = 'top';        % XLoc
814   options{2} = 'right';      % YLoc
815   options{3} = 1;            % XScale
816   options{4} = 1;            % YScale
817   options{5} = [NaN NaN];    % XLim
818   options{6} = [NaN NaN];    % YLim
819
820   opts = {'XLoc', ...
821       'YLoc', ...
822       'XScale', ...
823       'YScale', ...
824       'XLim', ...
825       'YLim'};
826
827   var = varargin;
828
829   % Check to see if the first argument is a function handle
830   if isa(var{1}, 'function_handle');
831     func  = var{1};
832     var(1) = '';
833   else
834     func = @plot;
835   end
836
837   % Parse through input arguments for options
838   try
839     removeID = [];
840     for iVar = 1:length(var)
841       if ischar(var{iVar})
842         id = strmatch(lower(var{iVar}), lower(opts), 'exact');
843         if ¬isempty(id)
844           options{id} = var{iVar + 1};
845           removeID = [removeID, iVar, iVar + 1];
846         end
847       end
848     end
849   catch
850     error('Error parsing options.\n%s\n', lasterr);
851   end
852
853   % Verify options
854   if ¬ismember(lower(options{1}), {'top', 'bottom'}) || ...
855       ¬ismember(lower(options{2}), {'right', 'left'}) || ...
856       ¬(isnumeric(options{5}) && length(options{5}) == 2) || ...
857       ¬(isnumeric(options{6}) && length(options{6}) == 2)
858     error('Bad options');
859   end
860
861   var(removeID) = '';
862
```

```matlab
863  % Determine the axes to plot
864  ax1 = newplot;
865  nextplot = get(ax1, 'NextPlot');
866
867  figH = gcf;
868
869  % Plot data
870  try
871    h = feval(func, var{:});
872  catch
873    error('Failed to plot\n%s\n', lasterr);
874  end
875
876  set(ax1, 'Box', 'off', 'Color', 'none');
877
878  % Create secondary axes on top of primary axes
879  ax2 = axes(...
880    'Position', get(ax1, 'Position'), ...
881    'Box'      , 'off', ...
882    'Parent'   , get(ax1, 'Parent'));
883
884  %-------------------------------------------------------------------------
885  % Apply options
886  %-------------------------------------------------------------------------
887  if strcmpi(options{1}, 'top') % XLoc
888    set(ax1, 'XAxisLocation', 'bottom');
889    set(ax2, 'XAxisLocation', 'top');
890  else
891    set(ax1, 'XAxisLocation', 'top');
892    set(ax2, 'XAxisLocation', 'bottom');
893  end
894
895  if strcmpi(options{2}, 'right') % YLoc
896    set(ax1, 'YAxisLocation', 'left');
897    set(ax2, 'YAxisLocation', 'right');
898  else
899    set(ax1, 'YAxisLocation', 'right');
900    set(ax2, 'YAxisLocation', 'left');
901  end
902
903  if ¬all(isnan(options{5}))  % XLim
904    set(ax1, 'XLim', options{5});
905  end
906  if ¬all(isnan(options{6}))  % YLim
907    set(ax1, 'YLim', options{6});
908  end
909
910  if ischar(options{3}) % for functional relationship
911    tmp = inline(options{3});
912    set(ax2, 'XLim', tmp(get(ax1, 'XLim')));
913  else
914    set(ax2, 'XLim', get(ax1, 'XLim') * options{3})
915  end
916  if ischar(options{4})
917    tmp = inline(options{4});
```

```matlab
918    set(ax2, 'YLim', tmp(get(ax1, 'YLim')));
919  else
920    set(ax2, 'YLim', get(ax1, 'YLim') * options{4})
921  end
922
923  set(ax2, 'XScale', get(ax1, 'XScale'), ...
924    'YScale', get(ax1, 'YScale'));
925
926  if options{3} == 1 % if there is no scaling, remove tick labels
927    set(ax2, 'XTickLabel', '');
928  end
929  if options{4} == 1 % if there is no scaling, remove tick labels
930    set(ax2, 'YTickLabel', '');
931  end
932
933  %-------------------------------------------------------------------------
934  % Create DeleteProxy objects (an invisible text object) so that the other
935  % axes will be deleted properly.  <inspired by PLOTYY>
936  %-------------------------------------------------------------------------
937  DeleteProxy(1) = text(...
938    'Parent'          , ax1, ...
939    'Visible'         , 'off', ...
940    'HandleVisibility', 'off');
941  DeleteProxy(2) = text(...
942    'Parent'          , ax2, ...
943    'Visible'         , 'off', ...
944    'HandleVisibility', 'off', ...
945    'UserData'        , DeleteProxy(1));
946  set(DeleteProxy(1), ...
947    'UserData'        , DeleteProxy(2));
948
949  set(DeleteProxy, ...
950    'DeleteFcn'       , @DelFcn);
951
952  %-------------------------------------------------------------------------
953  % Switch the order of axes, so that the secondary axes are under the
954  % primary axes, and that the primary axes become the current axes.
955  %-------------------------------------------------------------------------
956  % get list of figure children. ax1 and ax2 must exist in this list
957  ch = get(get(ax1, 'Parent'), 'Children');
958  i1 = find(ch == ax1);        % find where ax1 is
959  i2 = find(ch == ax2);        % find where ax2 is
960  ch([i1, i2]) = [ax2; ax1];  % swap ax1 and ax2
961
962  % assign the new list of children and set current axes to primary
963  set(get(ax1, 'Parent'), 'Children', ch);
964  set(figH, 'CurrentAxes', ax1);
965
966  % Restore NextPlot property (just in case it was modified)
967  set([ax1, ax2], 'NextPlot', nextplot);
968
969  % Store axes information
970  p2a = getappdata(figH, 'p2a');
971  if isempty(p2a)
972    p2a = {};
```

```matlab
973 end
974 p2a = [p2a;{ax1, ax2, options{3}, options{4}}];
975 setappdata(figH, 'p2a', p2a);
976
977 % Create 'Fix Axes' button for adjusting the secondary axes limits after
978 % zooming
979 hMenu = findobj(figH, 'Type', 'uimenu', 'Label', 'Fix Axes');
980 if strcmpi(get(figH, 'Menubar'), 'figure') && ...
981     (isempty(hMenu) || ¬ishandle(hMenu))
982   uimenu(...
983     'Parent'  , figH, ...
984     'Label'   , 'Fix Axes', ...
985     'Callback', @FixAxes);
986 end
987
988 if nargout
989   ax = [ax1, ax2];
990 end
991 end %plot2Axes
992 %-------------------------------------------------------------------------
993 % DelFcn - automatically delete both axes
994 %-------------------------------------------------------------------------
995 function DelFcn(obj, edata)
996
997 try
998   set(get(obj, 'UserData'), ...
999     'DeleteFcn', 'try;delete(get(gcbo, ''UserData''));end');
1000   set(obj, 'UserData', ...
1001     get(get(obj, 'UserData'), 'Parent'));
1002   delete(get(obj,'UserData'));
1003 end
1004 end %DelFcn
1005 %-------------------------------------------------------------------------
1006 % FixAxes - fix the scaling of the axes
1007 %-------------------------------------------------------------------------
1008 function FixAxes(obj, edata, p2a)
1009
1010 if nargin < 3
1011   p2a = getappdata(get(obj, 'Parent'), 'p2a');
1012 end
1013
1014 if ¬isempty(p2a)
1015   for iAx = 1:size(p2a, 1)
1016     if ishandle(p2a{iAx, 1}) && ishandle(p2a{iAx, 2})
1017       if ischar(p2a{iAx, 3})
1018         tmp = inline(p2a{iAx, 3});
1019         set(p2a{iAx, 2}, 'XLim', tmp(get(p2a{iAx, 1}, 'XLim')));
1020       else
1021         set(p2a{iAx, 2}, 'XLim', p2a{iAx, 3} * get(p2a{iAx, 1}, 'XLim'));
1022       end
1023       if ischar(p2a{iAx, 4})
1024         tmp = inline(p2a{iAx, 4});
1025         set(p2a{iAx, 2}, 'YLim', tmp(get(p2a{iAx, 1}, 'YLim')));
1026       else
1027         set(p2a{iAx, 2}, 'YLim', p2a{iAx, 4} * get(p2a{iAx, 1}, 'YLim'));
```

```
1028         end
1029       end
1030     end
1031   end
1032   end %FixAxes
1033   %--------------------------------------------------------------------------
1034   function [i,cv] = searchclosest(x,v)
1035   %--------------------------------------------------------------------------
1036   % % Search value 'v' in sorted vector 'x' and find index and value
1037   % % with respect to vector x that is equal or closest to 'v'.
1038   % %
1039   % % If more than one value is equal then anyone can be returned
1040   % % (this is property of binary search).
1041   % % If more than one value is closest then first occurred is returned
1042   % % (this is property of linear search).
1043   % %
1044   % %
1045   % % Algorithm
1046   % % First binary search is used to find v in x. If not found
1047   % % then range obtained by binary search is searched linearly
1048   % % to find the closest value.
1049   % %
1050   % % INPUT:
1051   % % x: vector of numeric values,
1052   % % x should already be sorted in ascending order
1053   % %    (e.g. 2,7,20,...120)
1054   % % v: numeric value to be search in x
1055   % %
1056   % % OUTPUT:
1057   % % i: index of v with respect to x.
1058   % % cv: value that is equal or closest to v in x
1059   clear i;
1060   from=1;
1061   to=length(x);
1062
1063   % % Phase 1: Binary Search
1064   while from≤to
1065       mid = round((from + to)/2);
1066       diff = x(mid)-v;
1067       if diff==0
1068           i=mid;
1069           cv=v;
1070           return
1071       elseif diff<0      % x(mid) < v
1072           from=mid+1;
1073       else               % x(mid) > v
1074           to=mid-1;
1075       end
1076   end
1077
1078   % % Phase 2: Linear Search
1079   % % Remember Bineary search could not find the value in x
1080   % % Therefore from > to. Search range is to:from
1081   y=x(to:from);            %vector to be searced for closest value
1082   [ignore,mini]=min(abs(y-v));
```

```
1083  cv=y(mini);
1084  % % cv: closest value
1085  % % mini: local index of minium (closest) value with respect to y
1086
1087  % % find global index of closest value with respect to x
1088  i=to+mini-1;
1089
1090  % % -----------------------------------------
1091  % % This program or any other program(s) supplied with it does not provide any
1092  % % warranty direct or implied.
1093  % % This program is free to use/share for non-commerical purpose only.
1094  % % Kindly reference the author.
1095  % % Thanking you.
1096  % % @ Copyright M Khan
1097  % % Email: mak2000sw@yahoo.com
1098  % % http://www.geocities.com/mak2000sw/
1099  end %searchclosest
```

A.2 Input File for Matlab Program

```
//Sample name:
LaFeCoSi2
//composition:
La(Fe_{0.857}Co_{0.058},Si_{0.085})_{13}
//Mass of sample in grams:
0.03319
//Density of sample in grams/cm^3:
7.24
//Molar mass of sample in g/mol:
836.702
//Fields in Tesla at which DeltaS will be calculated:
0.5 1 1.4
//Fields in Tesla at which the magnetization is extracted and plotted:
0.01 0.5 1 1.4
//Temperatures for Arrott plot:
264 265 266 267 269
//Dimension, a, of sample in mm if rectangular prism (field is along c-axis)
1.80
//Dimension, b, of sample in mm if rectangular prism (field is along c-axis)
0.86
//Dimension, c, of sample in mm if rectangular prism (field is along c-axis)
4.20
```

A.3 Examples of Output Files from Matlab Program

A.3.1 Main Output File

```
Main output file for Matlab program DeltaS

The run was executed on Fri 09-Jul-2010 10:18:51

The input file contained the following information:
Name:           LaFeCoSi1
Composition:    La(Fe_{0.865}Co_{0.05},Si_{0.085})_{13}
Sample weight:  0.029540 g
Sample density: 7.2400 g/cm^3
Sample molarmass: 836.3623 g/mol
Sample dimensions:  0.78 x   1.75 x   4.44 mm


Using Aharonis formula the demagnetization is: 0.0963


The Max. internal applied field is 1.46 T


The entropy change was calculated at the following fields:
  0.50 T
  1.00 T
  1.40 T


 The magnetization was extracted at the following fields:
  0.01 T
  0.01 T
  0.50 T
  1.00 T
  1.40 T


Peak in DeltaS_M (determined for max field) is at 254.49 K

Values of maxima in DeltaS_M:
Applied field        J/kg.K                 J/mol.K
  0.50          5.1198        4.2820           37.0673
  1.00          8.5400        7.1425           61.8294
  1.40         10.6798        8.9322           77.3219
```

A.3.2 ΔS_M in mJ/cm^3K Output File

```
0 0.5 1 1.4
204.99 1.0104 2.0392 2.3264
214.99 1.2685 2.5346 3.5147
221.99 1.5974 3.1735 4.3823
225.99 1.8793 3.7072 5.0753
230 2.2773 4.4601 6.0929
233.99 2.8682 5.5477 7.5115
236.99 3.5192 6.6534 8.9892
239 4.0583 7.7661 10.388
241 4.866 9.098 12.048
243 5.8167 10.926 14.445
244.99 7.3625 13.259 17.333
247 9.4749 16.873 21.787
249 13.15 22.855 28.935
250.5 18.08 29.882 37.386
251.5 23.043 37.153 45.541
252.5 28.174 44.787 54.047
253.49 34.877 54.703 65.847
254.49 37.067 60.971 73.355
255.5 35.201 61.829 77.322
256.5 27.608 57.136 74.594
257.5 21.75 49.282 69.157
258.5 15.877 41.412 61.94
259.5 12.56 32.58 52.225
260.5 9.553 26.653 43.817
261.5 7.3006 21.825 36.721
263 5.4253 16.249 28.142
265 3.7262 11.537 21.118
266.99 2.5721 8.4237 15.02
269 1.8049 6.1812 11.305
271 1.4055 4.8402 8.7087
274 0.94784 3.3924 6.2166
277.99 0.60007 2.2255 4.1428
284.99 0.33731 1.2559 2.3823
295 0.17018 0.64512 1.2265
```

Bibliography

[1]   J. T. Tuoriniemi, K. K. Nummila, R. T. Vuorinen, O. V. Lounasmaa, A. Metz, K. Siemensmeyer, M. Steiner, K. Lefmann, K. N. Clausen, and F. B. Rasmussen, "Neutron Experiments on Antiferromagnetic Nuclear-Order in Silver at Picokelvin Temperatures," Phys. Rev. Lett. **75**(20), 3744–3747 (1995).

[2]   P. Debye, "Einige Bemerkungen zur Magnetisierung bei Tiefer Temperatur," Ann. Phys. **81**, 1154–1160 (1926).

[3]   W. F. Giauque, "A Thermodynamic Treatment of Certain Magnetic Effects. A Proposed Method of Producing Temperatures Considerably Below 1° Absolute," J. Am. Chem. Soc. **49**, 1864–1870 (1927).

[4]   W. F. Giauque and C. W. Clark, "The Conditions for Producing Temperatures Below 1° Absolute by Demagnetization of $Gd_2(SO_4)_3 \cdot 8H_2O$ Temperature-Magnetic Field Isentropics," J. Am. Chem. Soc. **54**, 3135–3142 (1932).

[5]   G. V. Brown, "Magnetic Heat Pumping Near Room Temperature," J. Appl. Phys. **47**, 3673–3680 (1976).

[6]   C. G. B. Garrett, *Magnetic Cooling* (Harvard University Press, 1954).

[7]   *CRC Handbook of Chemistry and Physics*, 89th ed., edited by D. R. Lide (CRC, 2008-2009).

[8]   G. Urbain, P. Weiss, and F. Trombe, "Un nouveau métal ferromagnétique, le gadolinium," Compt. Rend. **200**, 2132–2134 (1935).

[9]   M. Griffel, R. E. Skochdopole, and F. H. Spedding, "The Heat Capacity Of Gadolinium From 15 To 355°K," Phys. Rev. **93**(4), 657–663 (1954).

[10] C. R. H. Bahl, T. F. Petersen, N. Pryds, and A. Smith, "A Versatile Magnetic Refrigeration Test Device," Rev. Sci. Instrum. **79**, 093906 (2008).

[11] K. Engelbrecht, J. B. Jensen, C. R. H. Bahl, and N. Pryds, "Experiments on a Modular Magnetic Refrigeration Device," Conference Proceedings

of the 3rd International Conference on Magnetic Refrigeration at Room Temperature, Des Moines, USA,431–436 (2009).

[12] K. A. Gschneidner, Jr. and V. K. Pecharsky, "Thirty years of near room temperature magnetic cooling: Where we are today and future prospects," Int. J. Refrig. **31**, 945–961 (2008).

[13] M. H. Phan and S. C. Yu, "Review of the Magnetocaloric Effect in Manganite Materials," J. Magn. Magn. Mater. **308**, 325–340 (2007).

[14] H. Auracher and P. Egolf, "Magnetic Refrigeration at Room Temperature," Special Issue of Int. J. Refrig. **29**, 1235–1238 (2006).

[15] S. Arajs and R. V. Colvin, "Thermal Conductivity and Lorenz Function of Gadolinium between 5 and 310 K," J. Appl. Phys. **35**(3), 1043–1044 (1964).

[16] A. Rowe, A. Tura, J. Dikeos, and R. Chahine, "Near Room Temperature Magnetic Refrigeration," Proceedings of the International Green Energy Conference, (2005).

[17] P. Strange, A. Svane, W. M. Temmerman, Z. Szotek, and H. Winter, "Understanding the Valency of Rare Earths from First-Principles Theory," Nature **399**, 756–758 (1999).

[18] J. W. Cable and E. A. Wollan, "Neutron Diffraction Study of Magnetic Behavior of Gadolinium," Phys. Rev. **165**(2), 733–734 (1968).

[19] S. N. Kaul and S. Srinath, "Gadolinium: A Helical Antiferromagnet or a Collinear Ferromagnet," Phys. Rev. B **62**(2), 1114–1117 (2000).

[20] S. Dankov, A. M. Tishin, V. K. Pecharsky, and K. A. Gschneidner, Jr., "Magnetic Phase Transition and the Magnetothermal Properties of Gadolinium," Phys. Rev. B **57**(6), 3478–3490 (1998).

[21] X. X. Zhang, J. Tejada, Y. Xin, G. F. Sun, K. W. Wong, and X. Bohigas, "Magnetocaloric Effect in $La_{0.67}Ca_{0.33}MnO_\delta$ and $La_{0.60}Y_{0.07}Ca_{0.33}MnO_\delta$ Bulk Materials," Phys. Rev. Lett. **69**(23), 3596–3598 (1996).

[22] D. Morelli, A. Mance, J. Mantese, and A. Micheli, "Magnetocaloric Properties of Doped Lanthanum Manganite Films," J. Appl. Phys. **79**(1), 373–375 (1996).

[23] M. McCormack, S. Jin, T. H. Tiefel, R. M. Fleming, J. M. Phillips, and R. Ramesh, "Very Large Magnetoresistance in Perovskite-Like La-Ca-Mn-O Thin-Films," Appl. Phys. Lett. **64**(22), 3045–3047 (1994).

[24] M. Johnsson and P. Lemmens, "Crystallography and Chemistry of Perovskites," arXiv:cond-mat/0506606, (2005).

[25] A. S. Bhalla, R. Guo, and R. Roy, "The Perovskite Structure - a Review of its Role in Ceramic Science and Technology," Mat. Res. Innovat. **4**, 3–26 (2000).

[26] F. A. Cotton, *Chemical Applications of Group Theory*, 3rd ed. ed. (John Wiley & Sons, 1990).

[27] C. Zener, "Interaction Between the d-Shells in the Transition Metals," Phys. Rev. **81**(3), 440–444 (1951).

[28] C. Zener, "Interaction Between the d-Shells in the Transition Metals. 2. Ferromagnetic Compounds of Manganese with Perovskite Structure," Phys. Rev. **82**(3), 403–405 (1951).

[29] N. Chau, H. N. Nhat, N. H. Luong, D. L. Minh, N. D. Tho, and N. N. Chau, "Structure, Magnetic, Magnetocaloric and Magnetoresistance Properties of $La_{1-x}Pb_xMnO_3$ Perovskite," Physica B **327**, 270–278 (2003).

[30] S. G. Min, K. S. Kim, S. C. Yu, H. S. Suh, and S. W. Lee, "Magnetocaloric Properties of $La_{1-x}Pb_xMnO_3$ ($x = 0.1, 0.2, 0.3$) Compounds," IEEE Trans. Magn. **41**(10), 2760–2762 (2005).

[31] Z. Guo, J. Zhang, H. Huang, W. Ding, and Y. Du, "Large Magnetic Entropy Change in $La_{0.75}Ca_{0.25}MnO_3$," Appl. Phys. Lett. **70**(7), 904–905 (1997).

[32] A. R. Dinesen, S. Linderoth, and S. Mørup, "Direct and Indirect Measurement of the Magnetocaloric Effect in $La_{0.67}Ca_{0.33-x}Sr_xMnO_{3\pm\delta}$ ($x \in [0; 0.33]$)," J. Phys.: Condens. Matter **17**, 6257–6269 (2005).

[33] J. C. Debnath, R. Zeng, J. H. Kim, and S. X. Dou, "Giant Magnetic Entropy Change in Colossal Magnetoresistance in $La_{0.7}Ca_{0.3}MnO_3$ Material in Low Field," J. Appl. Phys. **107**, 09A916 (2010).

[34] A. N. Ulyanov, J. S. Kim, G. M. Shin, Y. M. Kang, and S. I. Yoo, "Giant Magnetic Entropy Change in $La_{0.7}Ca_{0.3}MnO_3$ in Low Magnetic Field," J. Phys. D: Appl. Phys. **40**, 123–126 (2007).

[35] A. Asamitsu, Y. Moritomo, R. Kumai, Y. Tomioka, and Y. Tokura, "Magnetostructural Phase Transitions in $La_{1-x}Sr_xMnO_3$ with Controlled Carrier Density," Phys. Rev. B **54**(3), 1716 –1723 (1996).

[36] P. G. Radaelli, D. E. Cox, M. Marezio, S. W. Cheong, P. E. Schiffer, and A. P. Ramirez, "Simultaneous Structural, Magnetic, and Electronic-Transitions in $La_{1-x}Ca_xMnO_3$ with $x = 0.25$ and 0.50," Phys. Rev. Lett. **75**(24), 4488–4491 (1995).

[37] J. L. Cohn, Heat Conduction and Charge Ordering in Perovskite Manganites, Nickelates and Cuprates, arXiv:cond-mat/0003047, 2000.

[38] J. L. Cohn and J. Neumeier, "Heat Conduction and Magnetic Phase Behavior in Electron-Doped $Ca_{1-x}La_xMnO_3$ ($0 \leq x \leq 0.2$)," Phys. Rev. B. **66**, 100404 (2002).

[39] M. Coey, "Condensed-Matter Physics: Charge-Ordering in Oxides," Nature **430**, 155–157 (2004).

[40] P. Sande, L. E. Hueso, D. R. Miguéns, J. Rivas, F. Rivadulla, and M. A. López-Quintela, "Large Magnetocaloric Effect in Manganites with Charge Order," Appl. Phys. Lett. **79**(13), 2040–2042 (2001).

[41] V. K. Pecharsky and K. A. Gschneidner, Jr, "Giant Magnetocaloric Effect in $Gd_5(Si_2Ge_2)$," Phys. Rev. Lett. **78**(23), 4494–4497 (1997).

[42] V. K. Pecharsky and K. A. Gschneidner, Jr, "Tunable Magnetic Regenerator Alloys with a Giant Magnetocaloric Effect for Magnetic Refrigeration from $\sim$20 to $\sim$290 K," Appl. Rev. Lett. **70**(24), 3299–3301 (1997).

[43] J. Glanz, "Materials Science - Making a Bigger Chill with Magnets," Science **279**(5359), 2045 (1997).

[44] F. Holtzbgerg, R. J. Gambino, and T. R. McGuire, "New Ferromagnetic 5:4 Compounds in Rare Earth Silicon and Germanium Systems," J. Phys. Chem. Solids **28**, 2283–2289 (1967).

[45] L. Morellon, P. A. Algarabel, M. R. Ibarra, J. Blasco, B. García-Landa, Z. Arnold, and F. Albertini, "Magnetic-Field-Induced Structural Phase Transition in $Gd_5(Si_{1.8}Ge_{2.2})$," Phys. Rev. B **58**(22), R14721 (1998).

[46] L. Morellon, Z. Arnold, P. A. Algarabel, C. Magen, M. R. Ibarra, and Y. Skorokhod, "Pressure Effects in the Giant Magnetocaloric Compounds $Gd_5(Si_xGe_{1-x})_4$," J. Phys. Condens. Matter **16**, 1623–1630 (2004).

[47] J. D. Moore, K. Morrison, G. K. Perkins, D. L. Schlagel, K. A. G. T.A. Lograsso, V. K. Pecharsky, and L. F. Cohen, "Metamagnetism Seeded by Nanostructural Features of Single-Crystalline $Gd_5Si_2Ge_2$," Adv. Mater. **21**(37), 3780–3783 (2009).

[48] A. O. Pecharsky, K. A. Gschneidner, Jr, and V. K. Pecharsky, "The Giant Magnetocaloric Effect of Optimally Prepared $Gd_5Si_2Ge_2$," J. Appl. Phys. **93**(8), 4722–4728 (2003).

[49] V. K. Pecharsky and K. A. Gschneidner, Jr, "Effect of Alloying on the Giant Magnetocaloric Effect of $Gd_5(Si_2Ge_2)$," J. Magn. Magn. Mater **167**, L179–L184 (1997).

[50] E. Brück, "Developments in Magnetocaloric Refrigeration," J. Phys. D: Appl. Phys. **38**, R381–R391 (2005).

[51] K. A. Gschneidner, Jr., A. O. Pecharsky, and V. K. Pecharsky, US Patent 6,589,366, (2003).

[52] K. A. Gschneidner, Jr., V. K. Pecharsky, and A. O. Tsokol, "Recent Developments in Magnetocaloric Materials," Rep. Prog. Phys. **68**, 1479–1539 (2005).

[53] S. Fujieda, Y. Hasegawa, A. Fujita, and K. Fukamichi, "Thermal Transport Properties of Magnetic Refrigerants $La(Fe_xSi_{1-x})_{13}$ and their Hydrides, and $Gd_5Si_2Ge_2$ and MnAs," J. Appl. Phys. **95**(5), 2429–2431 (2004).

[54] K. A. Gschneidner, Jr., V. K. Pecharsky, A. O. Pecharsky, and C. B. Zimm, "Recent Developments in Magnetic Refrigeration," Mater. Sci. Forum **69**, 315–317 (1999).

[55] F. X. Hu, B. G. Shen, J. R. Sun, and X. X. Zhang, "Great Magnetic Entropy Change in $La(Fe, M)_{13}$ (M = Si, Al) with Co Doping," Chinese Physics **9**(7), 550–553 (2000).

[56] F. X. Hu, B. G. Shen, J. R. S. Z. H. Cheng, and X. X. Zhang, "Magnetic Entropy Change in $La(Fe_{0.98}Co_{0.02})_{11.7}Al_{1.3}$," J. Phys.: Condens. Matter **12**, L691–L696 (2000).

[57] X. X. Zhang, G. H. Wen, F. W. Wang, W. H. Wang, C. H. Yu, and G. H. Wu, "Magnetic Entropy Change in Fe-based Compound $LaFe_{10.6}Si_{2.4}$," Appl. Phys. Lett. **77**(19), 3072–3074 (2000).

[58] K. Buschow, "Intermetallic Compounds of Rare-earth and 3d Transition Metals," Rep. Prog. Phys. **40**, 1179–1256 (1977).

[59] D. Shoemaker, R. E. Marsh, F. J. Ewing, and L. Pauling, "Interatomic Distances and Atomic Valences in $NaZn_{13}$," Acta Cryst. **5**, 637–644 (1952).

[60] H. Ido, J. C. Sohn, F. Pourarian, S. F. Cheng, and W. E. Wallace, "Magnetic Properties of $LaCo_{13}$-Based Systems," J. Appl. Phys. **67**, 4978–4980 (1990).

[61] T. T. M. Palstra, J. A. Mydosh, G. J. Nieuwenhuys, A. M. van der Kraan, and K. H. J. Buschow, "Study of the Critical Behaviour of the Magnetization and Electrical Resistivity in Cubic $La(Fe,Si)_{13}$ Compounds," J. Magn. Magn. Mater. **36**, 290–296 (1983).

[62] W. A. J. J. Velge and K. H. J. Buschow, "Magnetic and Crystallographic Properties of Some Rare Earth Cobalt Compounds with $CaZn_5$ Structure," J. Appl. Phys. **39**(3), 1717–1720 (1968).

[63] A. Fujita, Y. Akamatsu, and K. Fukamichi, "Itinerant-electron Meta-magnetic Transition in La(Fe$_x$Si$_{1-x}$)$_{13}$ Intermetallic Compounds," J. Appl. Phys. **85**(8), 4756–4758 (1999).

[64] A. Fujita, S. Fujieda, Y. Hasegawa, and K. Fukamichi, "Itinerant-electron Metamagnetic Transition and Large Magnetocaloric Effects in La(Fe$_x$Si$_{1-x}$)$_{13}$ Compounds and their Hydrides," Phys. Rev. B **67**, 104416 (2003).

[65] T. T. M. Palstra, G. J. Nieuwenhuys, J. A. Mydosh, and K. H. J. Buschow, "Magnetic Properties of Cubic La(Fe$_x$Al$_{1-x}$)$_{13}$ Intermetallic Compounds," J. Appl. Phys. **55**(6), 2367–2369 (1984).

[66] B. R. Hansen, L. Theil Kuhn, C. R. H. Bahl, M. Lundberg, and C. Ancona-Torres, "Properties of Magnetocaloric La(Fe,Co,Si)$_{13}$ Produced by Powder Metallurgy," *Accepted by J. Magn. Magn. Mater.*, (2010).

[67] W. H. Tang, J. K. Liang, G. H. Rao, and F. M. Yang, "Metamagnetic Transition in PrCo$_{13-x}$Si$_x$," J. Appl. Phys. **79**(10), (1996).

[68] K. Fukamichi, A. Fujita, and S. Fujieda, "Large Magnetocaloric Effects and Thermal Transport Properties of La(Fe,Si)$_{13}$ and their Hydrides," J. Alloy Compd. **408-412**, 307–312 (2006).

[69] M. Balli, D. Fruchart, O. Sari, D. Gignoux, J. H. Huang, J. Hu, and P. W. Egolf, "Direct Measurement of the Magnetocaloric Effect on La(Fe$_{13-x-y}$Co$_y$)Si$_x$ Compounds Near Room Temperature," J. Appl. Phys. **106**(2), 023902 (2009).

[70] A. Fujita and K. Fukamichi, "Control of Large Magnetocaloric Effects in Metamagnetic La(Fe$_x$Si$_{1-x}$)$_{13}$ Compounds by Hydrogenation," J. Alloys Compd. **404-406**, 554–558 (2005).

[71] S. Fujieda, A. Fujita, and K. Fukamichi, "Large Magnetocaloric Effects in NaZn$_{13}$-type La(Fe$_x$Si$_{1-x}$)$_{13}$ Compounds and their Hydrides Composed of Icosahedral Clusters," Sci. Technol. Adv. Mater. **4**, 339–346 (2003).

[72] K. Mandal, D. Pal, O. Gutfleisch, P. Kerschl, and K.-H. Müller, "Magnetocaloric Effect in Reactively-Milled LaFe$_{11.57}$Si$_{1.43}$H$_y$ Intermetallic Compounds," J. Appl. Phys. **102**(5), 053906 (2007).

[73] F. X. Hu, J. Gao, X. L. Qian, M. Ilyn, A. M. Tishin, J. R. Sun, and B. G. Shen, "Magnetocaloric Effect in Itinerant Electron Metamagnetic Systems La(Fe$_{1-x}$Co$_x$)$_{11.9}$Si$_{1.1}$," J. Appl. Phys. **97**, 10M303 (2005).

[74] M. Balli, D. Fruchart, and D. Gignoux, "Optimization of La(Fe, Co)$_{13-x}$Si$_x$ Based Compounds for Magnetic Refrigeration," J. Phys.: Condens. Matter **29**, 236230 (2007).

[75] J. Lyubina, O. Gutfleisch, M. D. Kuz'min, and M. Richter, "La(Fe,Si)$_{13}$-based Magnetic Refrigerants Obtained by Novel Processing Routes," J. Magn. Magn. Mater. **320**, 2252–2258 (2008).

[76] M. Katter, V. Zellmann, G. W. Reppel, and K. Uestuener, "Magnetocaloric Properties of La(Fe,Co,Si)$_{13}$ Bulk Material Prepared by Powder Metallurgy," IEEE Trans. Magn. **44**, 3044–3047 (2008).

[77] M. Katter, V. Zellmann, G. W. Reppel, and K. Uestuener, "Magnetocaloric and Mechanical Properties of Reactively Sintered La(Fe,Co,Si)$_{13}$," Conference Proceedings of the 3rd International Conference on Magnetic Refrigeration at Room Temperature, Des Moines, USA,83–88 (2009).

[78] S. Fujieda, A. Fujita, K. Fukamichi, Y. Yamazaki, and Y. Iijima, "Giant Isotropic Magnetostriction of Itinerant-Electron Metamagnetic La(Fe$_{0.88}$Si$_{0.12}$)$_{13}$H$_y$ Compounds," Appl. Phys. Let. **79**(5), 653–655 (2001).

[79] J. Lyubina, K. Nenkov, L. Schultz, and O. Gutfleisch, "Multiple Metamagnetic Transitions in the Magnetic Refrigerant La(Fe,Si)$_{13}$H$_x$," Phys. Rev. Lett. **101**, 177203 (2008).

[80] J. C. Taylor and I. Hinczak, *Rietveld Made Easy* (Sietronics Pty Limited, 2006).

[81] J. Rodríguez-Carvajal, "Recent Advances in Magnetic Structure Determination by Neutron Powder Diffraction," Physica B **192**, 55–69 (1993).

[82] H. P. Klug, "Beryllium Windows for X-Ray Tubes," Rev. Sci. Instrum. **12**, 155–156 (1941).

[83] S. Blundell, *Magnetism in Condensed Matter* (Oxford University Press, 2001).

[84] A. Aharoni, *Introduction to the Theory of Ferromagnetism* (Oxford Science Publications, 2007).

[85] A. Aharoni, "Demagnetizing Factors for Rectangular Ferromagnetic Prisms," J. Appl. Phys. **83**(6), 3432–3434 (1998).

[86] A. Arrott and J. E. Noakes, "Approximate Equation of State for Nickel Near its Critical Temperature," Phys. Rev. Lett. **19**(14), 786–789 (1967).

[87] A. S. Arrott, "Equations of State Along the Road to Arrott's Last Plot," J. Magn. Magn. Mater **322**(9-12), 1047–1051 (2009).

[88] R. Bjørk, C. R. H. Bahl, and M. Katter, "Magnetocaloric Properties of LaFe$_{13-x-y}$Co$_x$Si$_y$ and Commercial Grade Gd," *submitted*, (2010).

[89] T. R. Ní Mhíocháin, D. Weaire, S. M. McMurry, and J. M. D. Coey, "Analysis of Torque in Nested Magnetic Cylinders," J. Appl. Phys. **86**(11), 6412–6424 (1999).

[90] S. Jeppesen, S. Linderoth, N. Pryds, L. Theil Kuhn, and J. Buch Jensen, "Indirect Measurement of the Magnetocaloric Effect Using a Novel Differential Scanning Calorimeter with Magnetic Field," Rev. Sci. Instrum. **79**(8), 083901 (2008).

[91] *Springer Handbook of Materials Measurement Methods*, edited by L. S. Horst Czichos, Tetsuya Saito (Springer, 2006).

[92] L. Reimer, *Image Formation in Low-Voltage Scanning Electron Microscopy* (SPIE Optical Engineering Press, 1993).

[93] E. Passamani, C. Larica, J. Proveti, A. Takeuchi, A. Gomes, and L. Ghivelder, "Magnetic and Magnetocaloric Properties of $La(Fe,Co)_{11.4}SP_{1.6}$ Compounds (SP = Al or Si)," J. Magn. Magn. Mater. **312**, 65–71 (2007).

[94] G. Hilscher, N. Buis, and J. J. M. Franse, "The Transition from Ferromagnetism to Paramagnetism in $Ti(Fe_{1-x}Co_x)$, $Y_6(Fe_{1-x}Mn_x)_{23}$ and the Effect of Pressure," Physica **91B**, 170–177 (1977).

[95] A. Le Bail, H. Duroy, and J. L. Fourquet, "Ab-initio Structure Determination of $LiSbWO_6$ by X-ray Powder Diffraction," Mat. Res. Bull. **23**(3), 447–452 (1988).

[96] *Handbook of Magnetic Materials*, edited by K. Buschow (Elsevier Science, 2007), Vol. 17.

[97] D. C. Cook and J. Li, "Mössbauer Effect Study of Gadolinium Iron Garnet," Hyp. Int. **28**, 495–498 (1986).

[98] J. Barclay and W. Steyert, "Materials for magnetic refrigeration between 2 K and 20 K," Cryogenics **22**(2), 73–80 (1982).

[99] M. H. Phan, M. B. Morales, C. N. Chinnasamy, B. Latha, V. G. Harris, and H. Srikanth, "Magnetocaloric Effect in Bulk and Nanostructured $Gd_3Fe_5O_{12}$ Materials," J. Phys. D: Appl. Phys. **42**, 115007 (2009).

[100] K. P. Belov, E. V. Talalaeva, L. A. Chernikova, and V. I. Ivanovskii, "Anomalous Sign of the Magnetocaloric Effect in Ferrites in the Region of the Compensation Point," JETP Letters-USSR **7**(11), 331–334 (1968).

[101] K. P. Belov, E. V. Talalaeva, L. A. Chernikova, V. I. Ivanovskii, and T. V. Kudryavtesva, "Magnetocaloric Effect in Rare-Earth Iron Garnets," JETP Letters-USSR **9**, 416–418 (1969).

[102] K. P. Belov, L. A. Chernikova, E. V. Talalaeva, R. Z. Levitin, T. V. Kudryavtseva, S. Amadesi, and V. I. Ivanovskii, "Induced Noncollinear Magnetic Structure in Rare-Earth Ferrite-Garnets," Soviet Physics JETP-USSR **31**(6), 1035–1037 (1970).

[103] J. Weidenborner, "Least Squares Refinement of Structure of Gadolinium-Iron Garnet, $Gd_3Fe_2Fe_3O_{12}$," Acta Cryst. **14**(10), 1051–1056 (1961).

[104] J. M. D. Coey, "Mössbauer Spectra of Mixed Crystals; Diamagnetically Substituted Yttrium Iron Garnet in the Critical Region," Phys. Rev. B. **6**(9), 3240–3253 (1972).

[105] R. Pauthenet, "Spontaneous Magnetization of Some Garnet Ferrites and the Aluminum Substituted Garnet Ferrites," J. Appl. Phys. **29**(3), 253–255 (1958).

[106] R. Pauthenet, "Proprietes Magnetiques des Ferrites de Gadolinium," Compt. Rend., Paris **242**(15), 1859–1862 (1956).

[107] S. Geller, J. P. Remeika, R. C. Sherwood, H. J. Williams, and G. P. Espinosa, "Magnetic Study of the Heavier Rare-Earth Iron Garnets," Phys. Rev. **137**, 1034–1038 (1965).

[108] J. Bernasconi and D. Kuse, "Canted Spin Phase in Gadolinium Iron Garnet," Phys. Rev. B. **3**(3), 811–815 (1971).

[109] C. D. Mee, "The Magnetization Mechanism in Single-Crystal Garnet Slabs Near the Compensation Temperature," IBM J. Res. Dev. **11**, 468–476 (1967).

[110] M. Uemura, T. Yamagishi, S. Ebisu, S. Chikazawa, and S. Nagata, "A Double Peak in the Coercive Force Near the Compensation Temperature in the Rare Earth Iron Garnets," Phil. Mag. **88**(2), 209–228 (2008).

[111] I. K. Kamilov and G. M. Shakhshaev, "Influence of Magnetic Field on the Specific Heat on Gadolinium Iron Garnet in the Vicinity of the Magnetic Compensation Point," JETP Letters-USSR **15**(8), 339–341 (1972).

[112] C. Alff and G. K. Wertheim, "Hyperfine Structure of ^{57}Fe in Yttrium-Iron Garnet from the Mössbauer Effect," Phys. Rev. **122**(5), 1414–1417 (1961).

[113] S. Mørup, Mössbauer Spectroscopy and its Applications in Materials Science, Course notes, 2004.

[114] S. C. Zanatta, L. F. Cótica, A. Paesano, Jr., S. N. de Medeiros, J. B. M. da Cunha, and B. Hallouche, "Mechanosynthesis of Gadolinium Iron Garnet," J. Am. Ceram. Soc. **88**, 3316–3321 (2005).

Part II

Papers

Paper I: Characterization Study of a Plate of the Magnetocaloric Material La(Fe,Co,Si)$_{13}$

CHARACTERIZATION STUDY OF A PLATE OF THE MAGNETO-CALORIC MATERIAL La(Fe,Co,Si)$_{13}$

B.R. HANSEN [a], M. KATTER [b], L. THEIL KUHN [a], C.R.H. BAHL [a], A. SMITH [a], and C. ANCONA-TORRES [a]

[a] Fuel Cells and Solid State Chemistry Division,
Risø National Laboratory for Sustainable Energy,
Technical University of Denmark,
4000 Roskilde, Denmark,
E-mail: britt.hansen@risoe.dk
[b] Vacuumschmelze GmbH & Co. KG, 63450 Hanau, Germany

ABSTRACT

A sample of magnetocaloric material with nominal composition La(Fe$_{0.851}$Co$_{0.066}$Si$_{0.083}$)$_{13}$ is shown to present a ferromagnetic-to-paramagnetic transition with a Curie temperature of T_C = 278.7 K. Isothermal magnetization curves were used to determine the volumetric magnetic entropy change, ΔS_M(mJ/cm^{3}K). The values thus found are compared to those of Gd and found to be almost twice as large for a given field. Hysteresis curves and thermomagnetic data show that a slight thermal hysteresis of 2 K is present, while no magnetic hysteresis exists in this material. Therefore, we show that several of the disadvantages previously associated with NaZn$_{13}$-structured materials are not present in La(Fe,Co,Si)$_{13}$ materials produced by powder metallurgy.

1. INTRODUCTION

A number of magnetocaloric materials series are currently being studied for the purpose of magnetic refrigeration near room temperature, where the material will play the role of refrigerant. One such series is La(Fe,Co,Si)$_{13}$ (see e.g. Liu and Altounian 2003, Ilyn et al. 2005), which has the NaZn$_{13}$ structure. Other material series with the same structure are e.g. La(Fe,Si)$_{13}$ and La(Fe,Al)$_{13}$. These materials display a variety of magnetic states and transitions. La(Fe,Si)$_{13}$ shows a first-order ferromagnetic transition and a field-induced itinerant-electron magnetic transition (Fujieda et al. 2002, Fujita et al. 2001, Palstra et al. 1983), whereas La(Fe$_x$Al$_{1-x}$)$_{13}$ for x > 0.86 is an antiferromagnet (Palstra et al. 1985). This variety has made the NaZn$_{13}$-structured materials interesting, some of them for magnetic refrigeration. The disadvantages of the magnetocaloric NaZn$_{13}$-structured materials, when compared to the benchmark material Gd, have been fabrication, shape processing, size of the adiabatic temperature change (ΔT_{ad}), hysteresis, corrosion and brittleness (Gschneidner et al. 2008). In this paper, we present the results of a characterization study on a sheet of La(Fe,Co,Si)$_{13}$, which was fabricated using a powder metallurgical production route that can be utilized for large scale production (Katter et al. 2008).

2. SAMPLE PREPARATION

The sample was prepared by Vacuumschmelze GmbH using a novel production method significantly reducing the preparation time compared to arc-melting and subsequent heat treatment, the standard method for obtaining bulk samples of La(Fe,Co,Si)$_{13}$. Initially, commercial powders of elemental Fe and Si were mixed with coarse powders of LaH$_x$ as well as various La-Fe-Co-Si master alloys. The mixture was milled in kg quantities in a jet mill under inert gas to a particle size of <5 μm as measured by a Fisher Sub-Sieve Sizer (FSSS). The powders, which were shown by the sieve analysis to contain particles < 32 μm, were then compacted in a die with an applied pressure of about 400 MPa (4 t/cm^2). Following this, the green parts were sintered at temperatures between 1333 K and 1433 K for 4 to 8 hours under inert conditions. The sample composition was determined by the manufacturer using X-ray Fluorescence Analysis (XFA) and the density was measured using the Archimedes principle to find a value of 6.98 g/cm^3. According to the TDR (Thermally induced Decomposition and Recombination) process (Katter et al. 2009) the sintered die-pressed blocks were heat treated at about 1073 K to decompose the La(Fe,Co,Si)$_{13}$ phase and improve their

machinability. This allowed the sample to be cut to the required shape (a plate) by conventional wire Electrical Discharge Machining (EDM). The sample was then rehomogenized at about 1323 K to recombine the La(Fe,Co,Si)$_{13}$ phase. The prepared sample was a plate measuring $20 \times 25 \times 0.9$ mm, which was subsequently cut using a table top cut-off machine into smaller samples suitable for experiments.

3. EXPERIMENTAL

X-ray diffractograms were obtained on a Bruker D8 Advance Diffractometer using Cu K$_\alpha$ radiation. Rietveld refinement of the experimental data allowed for the determination of phases and lattice constants using the program FullProf (Rodriguez-Carvajal 1993). Magnetization measurements were carried out using a LakeShore 7407 Vibrating Sample Magnetometer (VSM). Isothermal magnetization measurements as a function of field were made at a ramp rate of 30 Oe/s, a rate low enough to cause only minor heating ($\sim$ 0.2 K) in the sample during application of the field, in applied fields up to $\mu_0 H = 1.6$ T. Magnetization measurements as a function of temperature at low applied fields of 85 Oe were made as point-by-point measurements in steps of 1 K and with a measurement time of 4 s/point. Calorimetric data in applied fields up to 1 T were obtained using a novel Differential Scanning Calorimeter (DSC) (Jeppesen et al. 2008).

4. RESULTS

The X-ray diffraction pattern confirms that the main phase in the prepared sample has crystallized in a cubic NaZn$_{13}$ structure. A nominal composition of the sample, La(Fe$_{0.851}$Co$_{0.066}$Si$_{0.083}$)$_{13}$, was determined beforehand by the manufacturer of the sample using XFA. However, two cubic phases were identified in the sample: La(Fe,Co,Si)$_{13}$ (space group: *Fm3c*) and α-Fe(Co,Si) (*Im3m*). Surprisingly, no peaks corresponding to LaFeSi (*P4/nmm*) are present. The information extracted from the X-ray diffraction analysis is given in Table 1. In addition to the two identified phases, peaks are seen at low scattering angles, which could not be identified, see Fig. 1. The unidentified phase(s) is/are considered to be present in small quantities. As no knowledge of the crystallite sizes was at hand, the microstructural analysis leading to the stated weight percentages did not take into account the possibility of differing absorption contrast factors (Brindley coefficients).

Table 1. Data for phases identified in sample from X-ray diffraction and subsequent Rietveld refinement.

	This paper	Comparison value	Reference
La(Fe,Co,Si)$_{13}$			
Lattice parameter	11.506 Å	~11.50 Å	(Hu et al. 2005)
Weight percentage	95 (2)		
α-Fe(Co,Si)			
Lattice parameter	2.869 Å	2.8604(5) Å	(Basinski et al. 1955)
Weight percentage	5.1 (3)		

Because impurities are present in the sample and the composition was determined using XFA, the actual composition of the La(Fe,Co,Si)$_{13}$ phase is known to differ slightly from the nominal one. The lattice parameters determined for the two cubic phases at room temperature are in good agreement with previously published values (Hu et al. 2005, Basinski et al. 1955). α-Fe is ferromagnetic with a transition temperature of 1043 K (Tauer and Weiss 1955) and could therefore interact magnetically with the other phases via exchange or dipole interaction. However, we consider this effect of the α-Fe phase negligible.

Thermomagnetic data recorded in an applied field of 85 Oe are presented in Fig. 2. The data was recorded for both increasing and decreasing temperature, and for increasing temperature both field-cooled (FC) and zero-field-cooled (ZFC) data is shown. The magnetization in the ferromagnetic state is slightly higher after field-cooling, but the paramagnetic-to-ferromagnetic transition follows closely that of the zero-field-cooled one. The experimental data shows that a small thermal hysteresis of 2 K is present and that the sample orders at a higher temperature upon cooling.
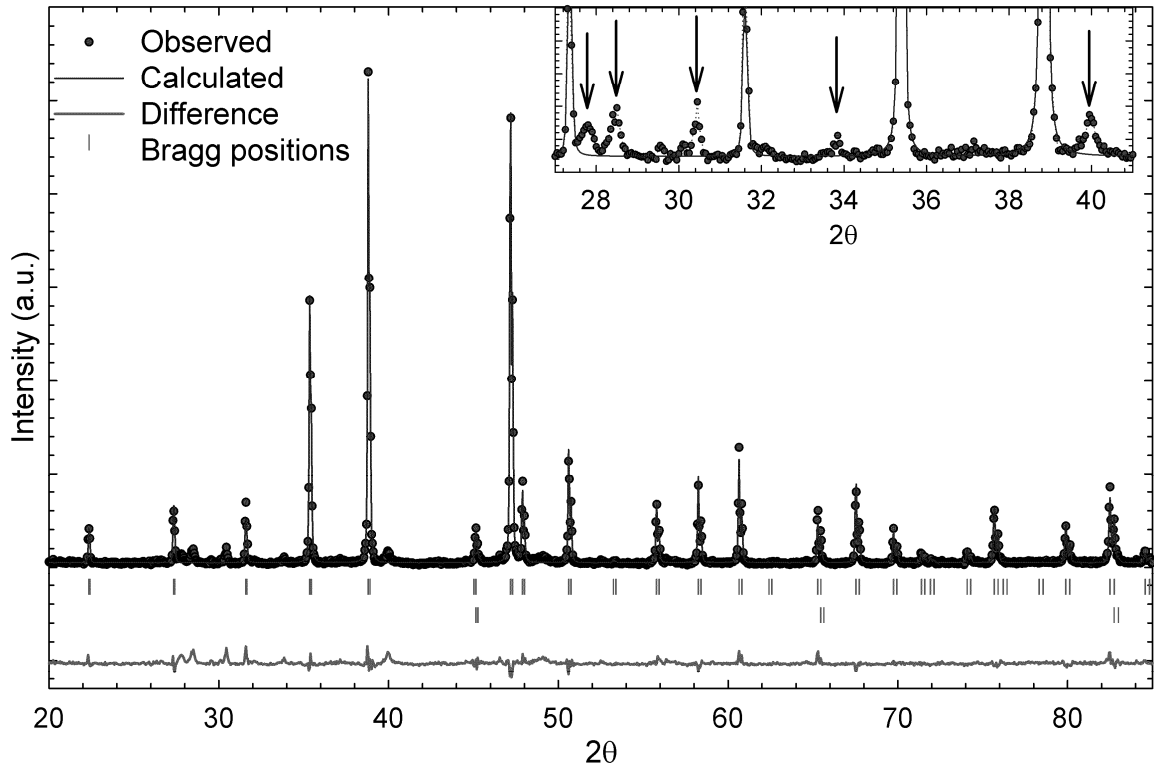
Figure 1. X-ray diffractogram of the La(Fe,Co,Si)$_{13}$ sample at room temperature. The inset shows unidentified peaks at low scattering angles.

Using the formula for the demagnetization in a rectangular prism (Aharoni 1998), the average internal fields were calculated. The low-field susceptibility, χ, at an internal field of 150 Oe was extracted from the isothermal initial curves recorded with increasing temperature and is shown in Fig. 2 for temperatures above that of the magnetic transition. In the paramagnetic phase, the susceptibility was fitted to the Curie-Weiss formula,

$$\chi \propto \frac{C}{T - T_c} \ . \tag{1}$$

By fitting the susceptibility for $T \geq 280$ K to Eq. (1) we find $T_C = 278.7$ K.
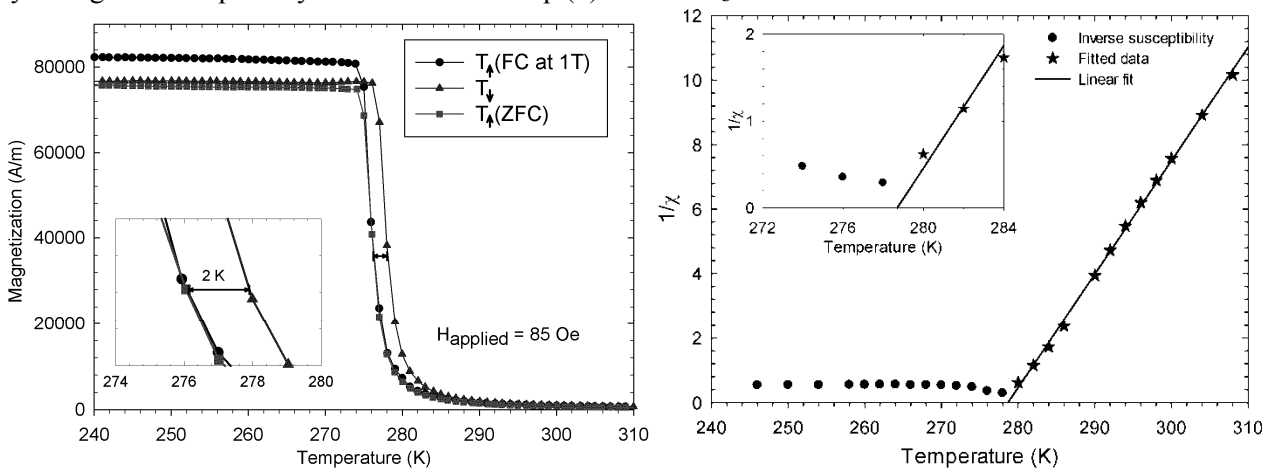
Figure 2. (left) Magnetization as a function of temperature recorded with an applied field of 85 Oe. A thermal hysteresis of 2 K is apparent and shown in more detail in the inset. (right) Magnetic susceptibility as a function of temperature. From the fit a Curie temperature of 278.7 K is found.

The magnetic entropy change, $\Delta S_M(T, \Delta H)$, was calculated using the equation,

$$\Delta S_M(T, \Delta H) = \mu_0 \int_0^H \left(\frac{\partial M}{\partial T} \right)_{H,p} dH, \qquad (2)$$

where T and H are the temperature and the magnetic field, respectively. Fig. 3 shows the calculated ΔS_M as a function of temperature for a selection of internal fields as well as a mesh plot of the magnetic entropy change for all recorded temperatures and internal fields. In Table 2 selected values of ΔS_M are given in different units, compared to the results from two different Gd samples. One Gd sample is a commercial grade Gd, while the purity of the other is unknown. As values of magnetic entropy change given in papers are usually for applied fields and not internal fields, both are given to aid in comparing the values.

Table 2. Selection of maximum values of magnetic entropy changes, ΔS_M, determined from isothermal magnetization measurements for a selection of applied and internal magnetic fields.

Applied field, $\mu_0 H$ (T)	0.75	1.00	1.25	1.50
La(Fe,Co,Si)$_{13}$ sample under study				
$\Delta S_{M,max}$(mJ/cm$^3\cdot$K)	34.3	43.5	52.3	60.3
$\Delta S_{M,max}$(J/mol$\cdot$K)	4.0	5.2	6.3	7.2
$\Delta S_{M,max}$(J/kg$\cdot$K)	4.9	6.2	7.2	8.2
Gd (own reference sample, commercial grade)				
$\Delta S_{M,max}$(mJ/cm$^3\cdot$K)	17.3	22.4	26.9	31.2
$\Delta S_{M,max}$(J/mol$\cdot$K)	0.3	0.4	0.5	0.6
$\Delta S_{M,max}$(J/kg$\cdot$K)	2.2	2.8	3.4	3.9
Gd (Gschneidner et al 2000)				
$\Delta S_{M,max}$(mJ/cm$^3\cdot$K)	-	23.7	-	33.1
Internal field, $\mu_0 H_i$ (T)	**0.75**	**1.00**	**1.25/1.20**	**1.46**
La(Fe,Co,Si)$_{13}$ sample under study				
$\Delta S_{M,max}$(mJ/cm$^3\cdot$K)	36.4	45.8	54.6	61.2
$\Delta S_{M,max}$(J/mol$\cdot$K)	4.4	5.5	6.5	7.3
$\Delta S_{M,max}$(J/kg$\cdot$K)	5.2	6.6	7.8	8.7
Gd (own reference sample, commercial grade)				
$\Delta S_{M,max}$(mJ/cm$^3\cdot$K)	21.2	25.3	29.4	-
$\Delta S_{M,max}$(J/mol$\cdot$K)	0.4	0.5	0.6	-
$\Delta S_{M,max}$(J/kg$\cdot$K)	2.7	3.3	3.7	-

In the figures, we present ΔS_M in volumetric units as it is desirable for the purpose of magnetic refrigeration to have the largest entropy change in the smallest volume. From the data presented we see that the sample of La(Fe,Co,Si)$_{13}$ has a higher maximum value of volumetric entropy change than that of the benchmark material Gd. It is well known that when the material series of La(Fe,Co,Si)$_{13}$ is doped to increase the transition temperature, the magnetic entropy change decreases (Hu et al. 2005). However, ΔS_M would not be expected to be halved for a shift in temperature of 20 K. The values of the gravimetric magnetic entropy change, ΔS_M (J/kgK), for our sample with nominal composition La(Fe$_{0.851}$Co$_{0.066}$Si$_{0.083}$)$_{13}$ compares well with previously published values (Hu et al 2005) for La(Fe$_{0.860}$Co$_{0.055}$Si$_{0.085}$)$_{13}$.
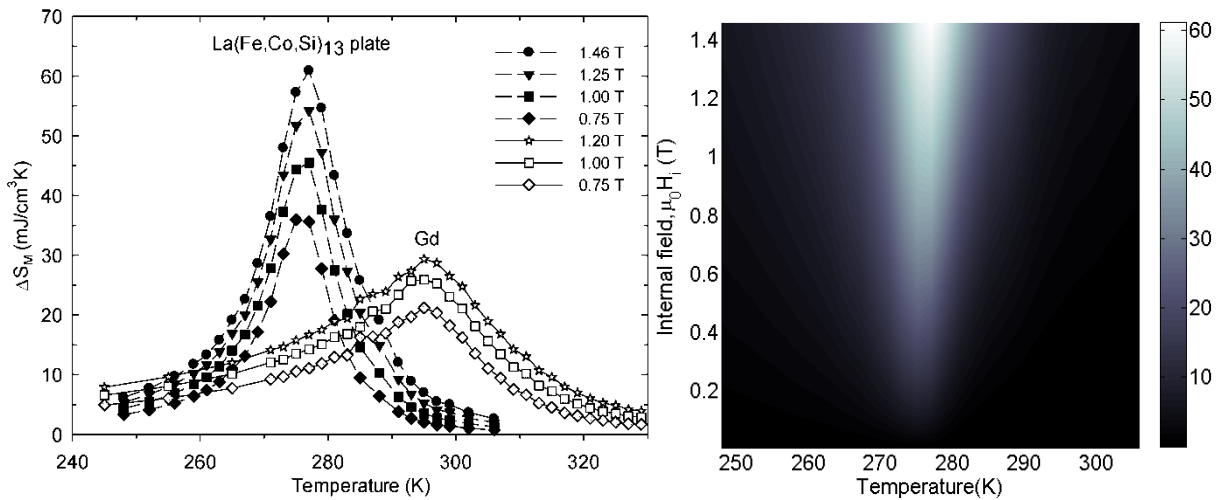
Figure 3. (left) The volumetric magnetic entropy change, ΔS_M, as a function of temperature for a selection of internal fields, $\mu_0 H_i$. Values for a sample of the benchmark material Gd is shown for comparison with that of the La(Fe,Co,Si)$_{13}$ sample. (right) The volumetric magnetic entropy change, ΔS_M (mJ/cm^{3}K) for all internal fields and temperatures. The data was plotted using an interpolating function.

Hysteresis curves near the transition temperature show no magnetic hysteresis, see inset of Fig. 4. A slight opening of the curve is seen in the data recorded near the transition temperature due to heating of the sample (~0.1 K) when the magnetic field is ramped for the measurements, i.e. due to the magnetocaloric effect itself.
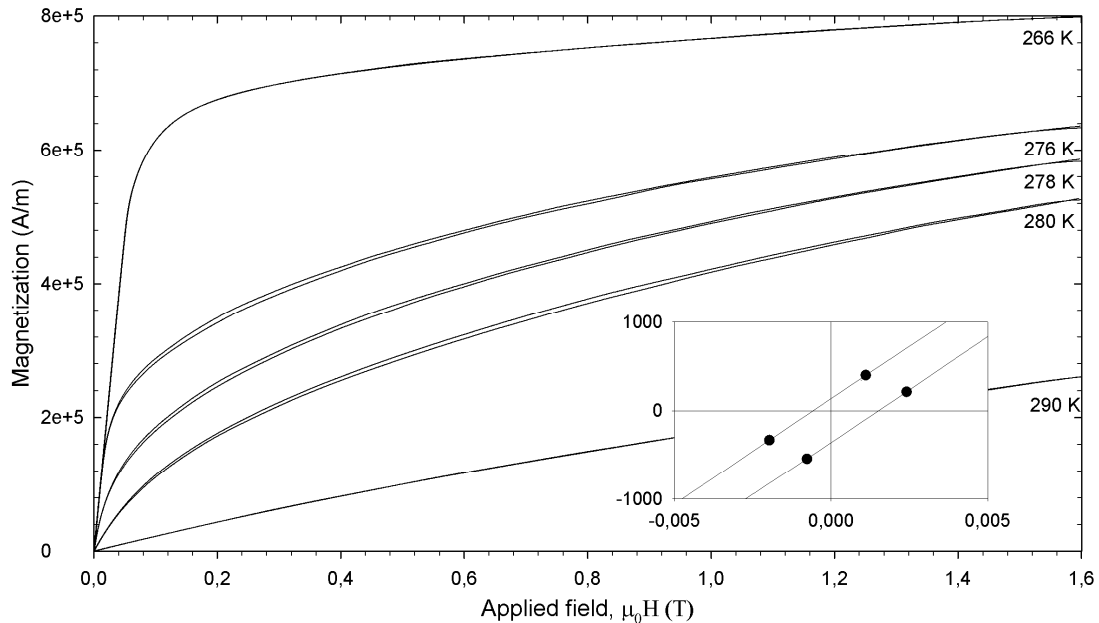
Figure 4. Hysteresis curves recorded at temperatures around that of the magnetic transition. Curves recorded near the transition temperature show a slight opening due to the magnetocaloric effect. Data near the origin is shown in the inset and from this it is clear that no magnetic hysteresis is present in the sample.

The heat capacity, c_p, of the sample was calculated from DSC measurements in a series of applied magnetic fields, see Fig. 5. With increasing applied field the peak in c_p shifts to higher temperatures and broadens. In future work this data will be used to calculate the adiabatic temperature change, ΔT_{ad}.
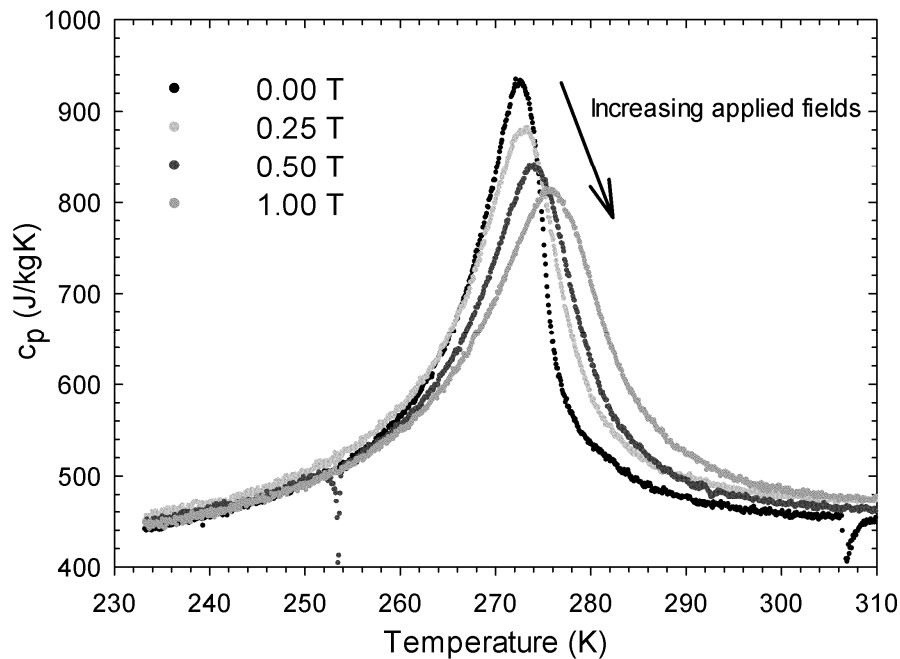
Figure 5. Heat capacity at constant pressure, c_p, in different applied fields, $\mu_0 H$. The two "spikes" observed in the data are purely instrumental.

5. CONCLUSIONS

In summary, we find that the magnetocaloric plate studied here with nominal composition La(Fe$_{0.851}$Co$_{0.066}$Si$_{0.083}$)$_{13}$ presents a ferromagnetic-to-paramagnetic transition and a large volumetric magnetic entropy change upon application of a magnetic field. Several of the problems in using the NaZn$_{13}$-structured materials as magnetic refrigerants have been shown to have been resolved. Fabrication and preparation are resolved in that the production method of powder metallurgy has been shown to result in a plate with only small amounts of impurities. With regards to hysteresis, only a small thermal hysteresis is present in the material and no magnetic hysteresis. Issues not addressed in this paper are those of corrosion and brittleness, but we would like to add comments to these. The material does corrode quickly in pure water, but we have found that corrosion is slowed drastically by using an admixture of water and anti-freeze. Brittleness, however, is an issue, which should be addressed if the material series of La(Fe,Co,Si)$_{13}$ is to be used commercially as magnetic refrigerants.

6. ACKNOWLEDGEMENTS

REFERENCES

1. Liu, X.B., and Altounian, Z., 2003, Effect of Co content on magnetic entropy change and structure of La(Fe$_{1-x}$Co$_x$)$_{11.4}$Si$_{1.6}$, *J. Magn. Magn. Mater.*, 264: 209-213.
2. Ilyn, M., Tishin, A.M., Hu, F.X., Gao, J., Sun, J.R., and Shen, B.G., 2005, Magnetocaloric properties of the LaFe$_{11.7}$Si$_{1.3}$ and LaFe$_{11.2}$Co$_{0.7}$Si$_{1.1}$ systems, *J. Magn. Magn. Mater.*, 290-291: 712-714.
3. Fujieda, S., Fujita, A., and Fukamichi, K., 2002, Large Magnetocaloric effect in La(Fe$_x$Si$_{1-x}$)$_{13}$ itinerant-electron metamagnetic compounds, *Appl. Phys. Lett.*, 81(7): 1276-1278.
4. Fujita, A., Fujieda, S., Fukamichi, K., Mitamura, H., and Goto, T., 2001, Itinerant-electron metamagnetic transition and large magnetovolume effects in La(Fe$_x$Si$_{1-x}$)$_{13}$ compounds, *Phys. Rev. B*, 65: 014410.
5. Palstra, T.T.M., Mydosh, J.A., Nieuwenhuys, G.J., van der Kraan, A.M., and Buschow, K.H.J., 1983, Study of the critical behaviour of the magnetization and electrical resistivity in cubic La(Fe,Si)$_{13}$ compounds, *J. Magn. Magn. Mater.*, 36: 290-296.

6. Palstra, T.T.M., Nieuwenhuys, G.J., Mydosh, J.A., and Buschow, K.H.J., 1985, Mictomagnetic, Ferromagnetic, And Antiferromagnetic Transitions In La(Fe$_x$Al$_{1-x}$)$_{13}$ Intermetallic Compounds, *Phys. Rev. B*, 31(7): 4622-4632.
7. Gschneidner, K.A. and Pecharsky, V.K., 2008, Thirty years of near room temperature magnetic cooling: Where we are today and future prospects, *Int. J. Refrig.*, 31: 945-961.
8. Katter, M., Zellmann, V., Repper, G., and Uestuener, K., Magnetocaloric and Mechanical Properties of Reactively Sintered La(Fe,Co,Si)$_{13}$, *Proc. of the Thermag III conference* (submitted), 2009.
9. Rodriguez-Carvajal, J., 1993, Recent advances in magnetic structure determination by neutron powder diffraction, *Physica B*, 192: 55.
10. Jeppesen, S., Linderoth, S., Pryds, N.,Theil Kuhn, L., and Buch Jensen, J., 2008, Indirect measurement of the magnetocaloric effect using a novel differential scanning calorimeter with magnetic field, *Rev. Sci. Instrum.*, 79(8): 083901.
11. Hu, F.X., Gao, J., Qian, X.L., Max llyn, Tishin, A.M., Sun, J.R., and Shen, B.G., 2005, Magnetocaloric effect in itinerant electron metamagnetic systems La(Fe$_{1-x}$Co$_x$)$_{11.9}$Si$_{1.1}$, *J. Appl. Phys.*, 97: 10M303.
12. Basinski, Z.S., Hume-Rothery, W., and Sutton, A., 1955, The lattice expansion of iron, *Proc. Roy. Soc. A*, 229(1179): 459.
13. Tauer, K.J. and Weiss, R.J., 1955, Magnetic Second-Order Transitions, *Phys. Rev.*, 100(4): 1223-1224.
14. Aharoni, A., 1998, Demagnetizing factors for rectangular ferromagnetic prisms, *J. Appl. Phys.*, 83(6): 3432.
15. Gschneidner, K. and Pecharsky, V.K., 2000, Magnetocaloric Materials, *Annu. Rev. Mater. Sci.*, 30: 387.
16. Katter M., Zellmann V., Reppel G.W., and Uestuener K., 2008, Magnetocaloric properties of La(Fe,Co,Si)$_{13}$ bulk material prepared by Powder Metallurgy, *IEEE Trans. Magn.* 44: 3044-3047.

Paper II: Properties of Magnetocaloric La(Fe,Co,Si)$_{13}$
Produced by Powder Metallurgy
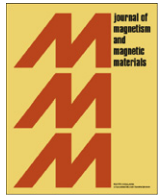
Properties of magnetocaloric La(Fe,Co,Si)$_{13}$ produced by powder metallurgy

Britt Rosendahl Hansen [a,*], L. Theil Kuhn [a], C.R.H. Bahl [a], M. Lundberg [a], C. Ancona-Torres [a], M. Katter [b]

[a] Fuel Cells and Solid State Chemistry Division, Risø National Laboratory for Sustainable Energy, Technical University of Denmark, DK-4000 Roskilde, Denmark
[b] Vacuumschmelze GmbH & Co. KG, Hanau, Germany

ARTICLE INFO

ABSTRACT

We present a comprehensive study of the magnetocaloric materials series La(Fe$_{1-x}$Co$_x$)$_{11.9}$Si$_{1.1}$ with $0.055 < x < 0.122$. The ferromagnetic samples were manufactured using a novel powder metallurgy process by which industrial scale production is feasible. This new production method makes the materials more attractive as magnetic refrigerants for room temperature magnetic refrigeration. The Curie temperature of the compounds can be easily tuned by altering the Co content and all samples have little magnetic anisotropy and present a second-order magnetic transition so that thermal and magnetic hysteresis is absent. For all seven samples, we have calculated the magnetic entropy change, ΔS_M, from initial curve measurements and measured the adiabatic temperature change, ΔT_{ad}, directly. In addition, for two of the samples, we determined the heat capacity as a function of applied magnetic field and the thermal conductivity. Where relevant, the results are compared with those of Gd, the benchmark material for room temperature magnetic refrigeration.

© 2010 Elsevier B.V. All rights reserved.

1. Introduction

In the last two decades scientists have shown a growing interest in magnetic refrigeration, a cooling method which utilizes the magnetocaloric effect. The effect arises as a result of entropy conservation and coupling between spin and lattice degrees of freedom. When a magnetic field is applied adiabatically to a spin system, the spin entropy may increase or decrease and to conserve the total entropy, the lattice entropy decreases or increases correspondingly resulting in a temperature change. For a change in applied magnetic field from H_1 to H_2 the isothermal magnetic entropy change, ΔS_M, is given by [1]

$$\Delta S_M(T,H_1 \to H_2) = \mu_0 \int_{H_1}^{H_2} \left(\frac{\partial M}{\partial T}\right)_{p,H} dH. \qquad (1)$$

Similarly, the adiabatic temperature change, ΔT_{ad}, which is the resulting change in sample temperature due to a change in applied magnetic field under adiabatic conditions, is given by [1]

$$\Delta T_{ad}(T,H_1 \to H_2) = -\mu_0 \int_{H_1}^{H_2} \frac{T}{c_p} \left(\frac{\partial M}{\partial T}\right)_{p,H} dH. \qquad (2)$$

The magnetocaloric effect has for almost a hundred years been used for cooling to very low temperatures via adiabatic demagnetization of atomic or nuclear spins [2–4]. Our interest here, however, concerns magnetic refrigeration near room temperature,

which was first demonstrated by Brown [5]. We see from Eqs. (1) and (2) that ΔS_M and ΔT_{ad} will peak close to a ferromagnetic-to-paramagnetic phase transition, as $\partial M/\partial T$ peaks here and the magnetic entropy change is an integral over the function $\partial M/\partial T$ at different applied magnetic fields.

We report on seven samples of La(Fe,Co,Si)$_{13}$, which were manufactured using powder metallurgy. The parent compound is LaCo$_{13}$ as the compound LaFe$_{13}$ has a positive heat of formation and so does not exist. However, La(Fe$_x$Si$_{1-x}$)$_{13}$ exists for $0.81 \leq x \leq 0.88$ [6] and La(Co$_{1-x}$Fe$_x$)$_{13}$ for $x \leq 0.6$ [6,7]. In general, replacing Co with Fe and/or Si leads to a reduction in the Curie temperature such that the transition temperature of LaCo$_{13}$ is ~ 1290 K [8] whereas we find transition temperatures from 255 to 345 K in our samples. La(Fe,Co,Si)$_{13}$ (LFCS) samples have previously mainly been produced using arc-melting and subsequent heat treatment in an oven for several weeks. This time-consuming production method has been counted against the materials in terms of suitability as magnetic refrigerants [9]. As we show in the following, powder metallurgy solves the problem of production thus making LFCS more suitable as a magnetic refrigerant. Conditions for suitability as a magnetic refrigerant at room temperature besides large $|\Delta S_M|$ and ΔT_{ad} are low raw material costs, the possibility of large-scale production and shaping, tunability of the transition temperature, a lack of hysteresis effects, toxicity, corrosion and brittleness. We present here a comprehensive study of a series of seven LFCS samples with $0.055 < x < 0.122$ and will, in the conclusions of this paper, reflect on the over-all suitability of LFCS materials as magnetic refrigerants.

* Corresponding author.
  E-mail address: broh@risoe.dtu.dk (B. Rosendahl Hansen).

2. Sample preparation

The samples were prepared by Vacuumschmelze GmbH using a novel powder metallurgy production method [10], which significantly reduces the preparation time compared to arc-melting and subsequent heat treatment, the standard method for obtaining bulk samples of La(Fe,Co,Si)$_{13}$. Initially, commercial powders of elemental Fe and Si were mixed with coarse powders of LaH$_x$ as well as various La–Fe–Co–Si master alloys. The mixture was milled in kilogram quantities in a jet mill under inert gas to a particle size of $<5\,\mu$m as measured by a Fisher sub-sieve sizer. The powders, which were shown by the sieve analysis to not contain particles $>32\,\mu$m, were then compacted in a die with an applied pressure of about 400 MPa (4 t/cm^2). Following this, the green parts were sintered at temperatures between 1333 and 1433 K for 4–8 h under inert conditions. The sample compositions were determined by the manufacturer using X-ray fluorescence analysis (XFA) and the densities were measured using the Archimedes principle. The as-prepared die-pressed blocks measuring approximately $23 \times 19 \times 12.5$ mm were subsequently cut into smaller pieces for experimental work. Table 1 presents an overview of the samples with information on the nominal compositions and densities determined by the manufacturer, Vacuumschmelze GmbH.

3. Experimental details

The microstructure of one sample was examined using a Zeiss Supra 35 scanning electron microscope (SEM) equipped with an thermo energy dispersive spectroscopy (EDS) system. The sample was coated with Au and measured in vacuum with a primary electron beam energy of 15 keV. For the analysis of the EDS data the program Noran System Six 2.2 from Thermo Scientific was used. X-ray diffraction data on all seven samples were obtained on a Bruker D8 Advance Diffractometer using Cu K$_\alpha$ radiation. To avoid the fluorescent background scattering an energy dispersive solid state detector (Sol-X) was used. Subsequent Rietveld refinement combined with the EDS data obtained from the SEM analysis allowed for the determination of phases and lattice constants using the program FullProf [11]. Magnetization measurements were carried out using a LakeShore 7407 Vibrating Sample Magnetometer (VSM). Isothermal magnetization measurements as a function of applied magnetic field, $\mu_0 H_a$, were made at a sweep-rate of 3 mT/s, a rate low enough to cause only minor heating in the samples during the sweep, in applied magnetic fields up to $\mu_0 H_a = 1.6$ T. The rate was chosen by comparing measurements at different ramp rates close to T_c [12]. In-between the isothermal initial curve measurements, the temperature was ramped to above T_c, so that any effect of the applied magnetic field was removed. Magnetization

measurements as a function of temperature at low applied fields of $\mu_0 H_a = 0.01$ T were made as point-by-point measurements in steps of 1 K and with a measurement time of 4 s/point. Calorimetric data in applied magnetic fields up to $\mu_0 H_a = 1.46$ T were obtained on two of the samples using a novel Differential Scanning Calorimeter (DSC) [13]. The thermal diffusivity was determined using a Netzsch LFA 457 MicroFlash and used in conjunction with the heat capacity to calculate the thermal conductivity. A direct measurement of the adiabatic temperature change, ΔT_{ad}, was made using a custom built instrument described in Ref. [14].

4. Structural analysis

LFCS stabilizes in the cubic NaZn$_{13}$-type structure [15], see Fig. 1. X-ray diffraction on the seven samples recorded at room temperature show that the main phase in all samples has the cubic NaZn$_{13}$ structure. In addition, four minor impurity phases were identified in the X-ray diffraction spectra. The identification of the minor phases was advanced by EDS mapping on sample no. 2. Two common impurities in samples of LFCS are ferromagnetic α−Fe, which has a Curie temperature of 1043 K [16], and LaFeSi, which is a Pauli paramagnet [17]. These impurities were also found in our samples and are the more prominent ones in weight percentage of the four impurity phases. The area of interest shown in Fig. 2a was submitted to EDS mapping and the linescans displayed in Fig. 2b–d were extracted from the EDS map data. From the extracted linescans, we find that the large, dark areas seen in the integral image contain mostly Fe and these areas are therefore identified as α−Fe, the structure of which could also contain small amounts of Co and Si. The smaller, dendritic areas containing La, Fe, and Si are identified as LaFeSi. Finally, we identified areas in the EDS integral image which contained mostly La and O. In fitting the X-ray diffraction data seven of the impurity peaks at low scattering angles were consistent with the presence of La(OH)$_3$. It is unclear from literature whether La(OH)$_3$ may be

Table 1
Nominal composition and density of the seven LFCS samples as determined by XFA and using the Archimedes principle.

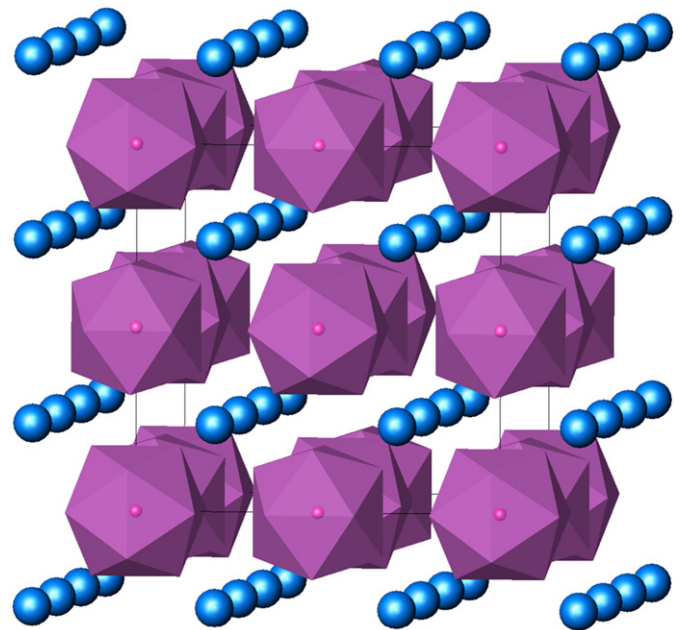| Sample no.	Nominal composition	Density, ρ (g/cm^3)
1	La(Fe$_{0.945}$Co$_{0.055}$)$_{11.9}$Si$_{1.1}$ = LaFe$_{11.25}$Co$_{0.65}$Si$_{1.1}$	7.24
2	La(Fe$_{0.936}$Co$_{0.064}$)$_{11.9}$Si$_{1.1}$ = LaFe$_{11.14}$Co$_{0.76}$Si$_{1.1}$	7.24
3	La(Fe$_{0.929}$Co$_{0.071}$)$_{11.9}$Si$_{1.1}$ = LaFe$_{11.05}$Co$_{0.85}$Si$_{1.1}$	7.24
4	La(Fe$_{0.918}$Co$_{0.082}$)$_{11.9}$Si$_{1.1}$ = LaFe$_{10.92}$Co$_{0.98}$Si$_{1.1}$	7.24
5	La(Fe$_{0.905}$Co$_{0.095}$)$_{11.9}$Si$_{1.1}$ = LaFe$_{10.77}$Co$_{1.13}$Si$_{1.1}$	7.21
6	La(Fe$_{0.892}$Co$_{0.108}$)$_{11.9}$Si$_{1.1}$ = LaFe$_{10.61}$Co$_{1.29}$Si$_{1.1}$	7.20
7	La(Fe$_{0.878}$Co$_{0.122}$)$_{11.9}$Si$_{1.1}$ = LaFe$_{10.45}$Co$_{1.45}$Si$_{1.1}$	7.21

Fig. 1. The cubic structure of La(Fe,Co,Si)$_{13}$. The La atoms (blue) sit interstitially between icosahedra of Fe, Co and Si (purple), which surround a central Fe/Co/Si atom. (For interpretation of the references to color in this figure legend, the reader is referred to the web version of this article.)
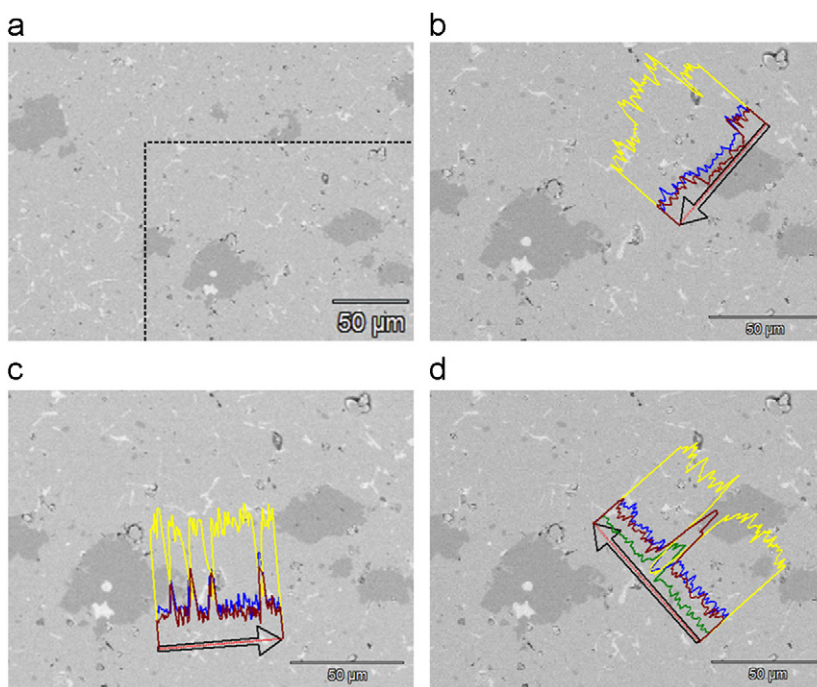
Fig. 2. Integral image and linescans extracted from the EDS mapping on sample no. 2. In all linescans the element content is given as follows: Fe (yellow), La (Red), Si (Blue) and O (Green). (a) Integral image. The dotted line shows the area displayed in the linescan images. (b) Linescan through dark areas in the micrograph containing mostly Fe. These grains are identified as the impurity α−Fe. (c) Linescan through bright and dendritic area. The Fe content goes down, while the amount of La and Si increases. These areas are identified as LaFeSi. (d) Linescan through area showing higher oxygen content. These areas do not contain Fe, however, the La content increases significantly. From X-ray diffraction these regions are identified as La(OH)$_3$. (For interpretation of the references to color in this figure legend, the reader is referred to the web version of this article.)

formed from the treatment of the LaH$_x$ powders and other precursors, but this appears to be the case here. Finally, in sample no. 5 a distinct peak is seen at $2\theta \sim 30°$, see Fig. 3, which is consistent with magnetite, Fe$_3$O$_4$, or the isostructural maghemite, γ-Fe$_2$O$_3$. This peak is not present in the other six samples. From Rietveld refinement we find particle sizes for all phases of $0.2−0.4\,\mu$m, which does not seem reasonable from the narrowness of the X-ray peaks and so the XRD peaks are probably broadened due to anisotropic strain in the particles and/or inhomogeneity in the sample compositions.

The Rietveld refinement of sample no. 5 is shown in Fig. 3 and the findings of the refinements on the seven X-ray diffraction spectra are presented in Tables 2 and 3. The determined lattice parameters correspond to published values [18,19] on similar samples. The lattice parameters determined at ambient temperatures are difficult to compare with those of other samples for three reasons: (1) An uncertainty in the actual composition of the LFCS phase often exists due to separation of elements into impurity phases, (2) a magnetovolume effect is displayed by LFCS compounds [18,19], whereby the lattice parameter increases, when entering the magnetic phase, and (3) the magnetic properties of the LFCS compounds depend critically on the Fe, Co and Si content. In the case of our seven samples, a trend of increasing lattice parameter with increasing Co content is observed. At ambient temperatures, where the XRD spectra were recorded, samples no. 1–3 are in the paramagnetic phase, sample no. 4 is close to its magnetic phase transition, whereas samples no. 5–7 are in the ferromagnetic phase, see Fig. 10. As the ion radius of Co is slightly smaller than that of Fe, we would expect to see a slight decrease in the lattice constant through the material series as the Co content is increased. Then, as the lattice constant is larger in the magnetic phase due to magnetovolume effects, we should see a shift to larger lattice
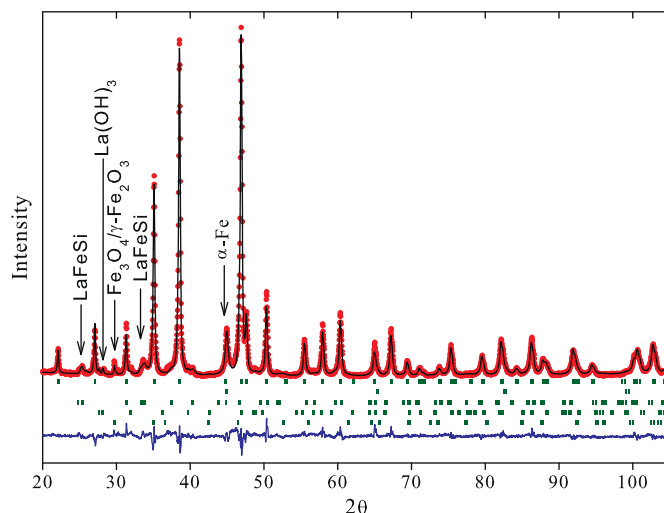

Fig. 3. Rietveld refinement of X-ray diffraction pattern for sample no. 5. Arrows mark the more prominent impurity peaks.

constants for samples no. 5–7. For the materials in the magnetic phase, the increase in Co content leads to a reduction in the magnetic moment, which should cause an additional reduction in lattice constant as the magnetovolume effect becomes smaller. Instead, as mentioned above, we see an increase in the lattice constant throughout the series. The reason for this discrepancy between theory and experiment is believed to be the broadness of the temperature range within which the lattice contraction takes place. This contraction is due to magnetovolume effects and so takes place during the magnetic phase transition.

Table 2
Lattice parameters of the LFCS phase determined from X-ray diffraction on the seven samples at ambient temperatures.

Sample no.	LFCS lattice parameter (Å)	
1	11.495(1)	
2	11.498(1)	
3	11.512(1)	
4	11.509(1)	
5	11.523(1)	
6	11.541(1)	
7	11.556(1)	
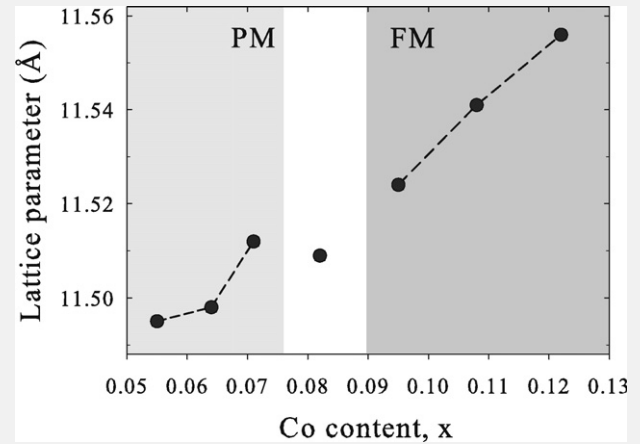
Table 3
Weight percentages of all phases identified in the seven LFCS samples by refinement of the X-ray diffraction spectra.

Sample no.	LFCS	α−Fe	LaFeSi	La(OH)$_3$	Fe$_3$O$_4$/γ−FeO$_3$
1	89.7(5)	5.0(1)	3.5(2)	1.7(1)	
2	88.0(5)	5.9(1)	4.5(2)	1.6(1)	
3	88.2(5)	6.5(1)	4.1(2)	1.1(1)	
4	87.9(5)	6.2(1)	4.4(2)	1.4(1)	
5	87.9(6)	6.5(1)	4.5(2)	0.8(1)	0.27(2)
6	87.2(5)	6.8(2)	4.8(2)	1.1(1)	
7	85.8(5)	8.8(1)	3.9(2)	1.4(1)	

5. Magnetic and thermal properties

Due to the highly symmetric environment of the Fe and Co magnetic moments in the cubic LFCS structure, see Fig. 1, very little magnetic anisotropy is observed [20]. For this reason, the LFCS compounds with their potentially large magnetization, depending on the Fe-content, are soft magnetic materials and cannot be used as permanent magnets. Attempts have been made at disrupting the cubic structure thereby creating anisotropy by doping with various elements, while hoping to retain the advantageous magnetic properties [21,22]. For magnetic refrigeration, however, the high permeability of the LFCS compounds make them suitable as refrigerants. The seven samples present a second-order magnetic phase transition at the Curie temperature. This can be concluded from magnetization and calorimetric data, which show no magnetic or thermal hysteresis as well as from a Landau fit to the isothermal magnetization data. In Fig. 4 we show magnetization versus temperature curves for sample no. 1. No thermal hysteresis is seen and so the field-cooled, zero field-cooled and decreasing temperature data all lie on top of each other. The inset of Fig. 4 shows a hysteresis curve for sample no. 6 recorded near its Curie temperature. Again, no hysteresis, this time magnetic, is seen. Magnetization curves obtained for the other LFCS samples showed the same lack of hysteresis. We also looked for evidence of hysteresis in the heat capacity measurements. Fig. 5 shows the heat capacity for two of the seven samples recorded at zero applied field and with an applied magnetic field of $\mu_0 H_a = 1.46\,T$. An applied field will move the
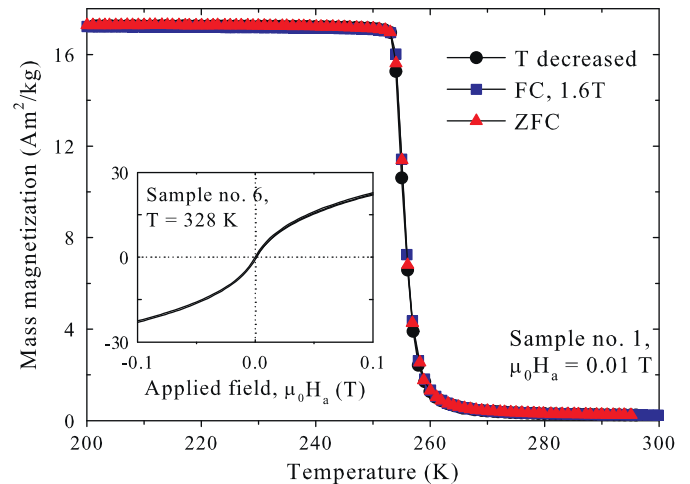

Fig. 4. Field cooled (FC), zero field cooled (ZFC) and decreasing temperature magnetization curves for sample no. 1. No thermal hysteresis is evident. Inset: Hysteresis curve for sample no. 6 recorded near its Curie temperature. No magnetic hysteresis is apparent.

magnetic transition to higher temperatures and broaden the transition and hence the heat capacity peak moves up in temperature and broadens. The heat capacity data was recorded for both increasing and decreasing temperatures and no difference between the data sets indicative of a hysteretic transition is seen. Finally, to examine the nature of the magnetic phase transition in our materials, we fitted isothermal magnetization data for all seven samples to obtain the Landau coefficients, c_1, c_2 and c_3. These coefficients can be defined by writing the thermodynamic potential, $\phi(M,T)$, as [27]

$$\phi(M,T) = \phi_0 + \tfrac{1}{2}c_1 M^2 + \tfrac{1}{4}c_2 M^4 + \tfrac{1}{6}c_3 M^6 - \mu_0 H M \qquad (3)$$

$$= \phi_0 + \tfrac{1}{2}a(T-T_0)M^2 + \tfrac{1}{4}c_2 M^4 + \tfrac{1}{6}c_3 M^6 - \mu_0 H M, \qquad (4)$$

where T_0 is a critical temperature. To have a first-order transition, we must have c_2 negative and c_3 positive as this can produce a minimum of $\phi(M,T)$, which first appears at a non-zero value of M. It is to this value of M that the system will make a discontinuous
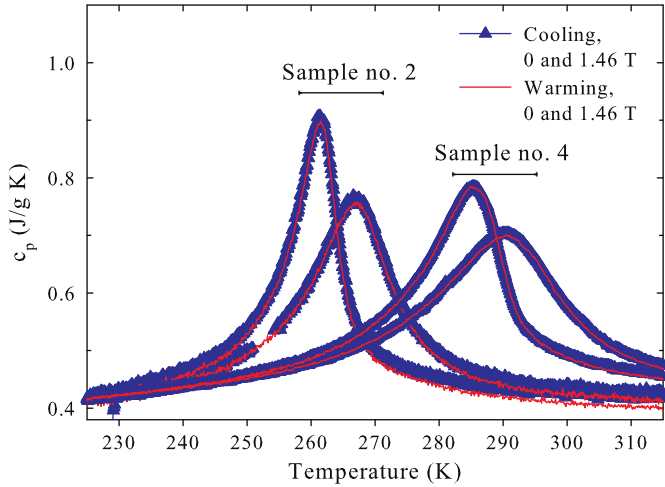
Fig. 5. Heat capacity of samples no. 2 and 4 recorded at zero field and with an applied magnetic field of $\mu_0 H_a = 1.46\,T$. The data were recorded for both heating and cooling of the sample. No difference between the heating and cooling data is seen indicating a second-order phase transition.

jump. In contrast, for a second-order transition the minimum, which exists for $T < T_c$, starts at $M=0$ and moves continuously to non-zero values of M as the temperature is decreased. If, however, c_2 is positive at T_c then we cannot have a first-order phase transition, but must have a second-order one, if any. In the case of a second-order transition, $T_0=T_c$, which means that $c_1=0$ at T_c. In order to obtain the Landau coefficients near the phase transition temperature, we make use of the fact that this occurs at a minimum in $\phi(M,T)$ with respect to the order parameter M. Therefore, we find

$$\frac{\partial \phi(M,T)}{\partial M} = c_1 M + c_2 M^3 + c_3 M^5 - \mu_0 H = 0 \qquad (5)$$

$$\Rightarrow \frac{H}{M} = c_1 + c_2 M^2 + c_3 M^4. \qquad (6)$$

By fitting Eq. (6) to isothermal magnetization data near the phase transition data, see Fig. 6, we can determine the Landau coefficients. Before fitting our data to obtain the Landau coefficients, we corrected for demagnetization. The samples were all in the shape of a rectangular parallelepiped and the formula for demagnetization of a rectangular ferromagnetic prism given by Aharoni [23] was used. In this way, the magnetic field given in Fig. 6 is the internal magnetic field. In Fig. 7 is shown the determined values of the Landau coefficient c_2 for all seven samples at temperatures close to their Curie temperatures. From Fig. 7, we see that for all seven samples, c_2 is greater than zero and, as indicated by the lack of hysteresis, the samples present with a second-order magnetic phase transition. In Fig. 8 we show the first Landau coefficient as determined by the fit and from these values we extract a value of the phase transition temperature, T_c, as this occurs for $c_1=0$. This value of T_c is extracted by fitting a straight line to the two data points on either side of $c_1=0$. The values of T_c so determined are presented in Table 4 along with values determined by the inflection point of the magnetization and by fitting the low-field susceptibility as described in the following.

The Curie temperatures of the seven samples were determined in three ways: (1) from the differential of low-field magnetization versus temperature data, (2) from the low-field inverse susceptibility and (3) from the temperature at which the first Landau coefficient is zero. The low-field magnetization versus temperature curve was recorded with an applied magnetic field of $\mu_0 H_a = 10\,mT$ and the magnetization was then differentiated with
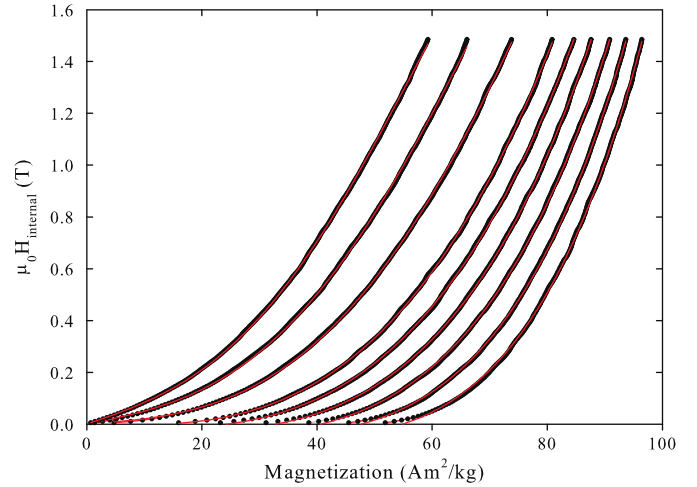

Fig. 6. Magnetization of sample no. 4 at temperatures from 287 to 298 K. The solid lines are the fits to Eq. (3).
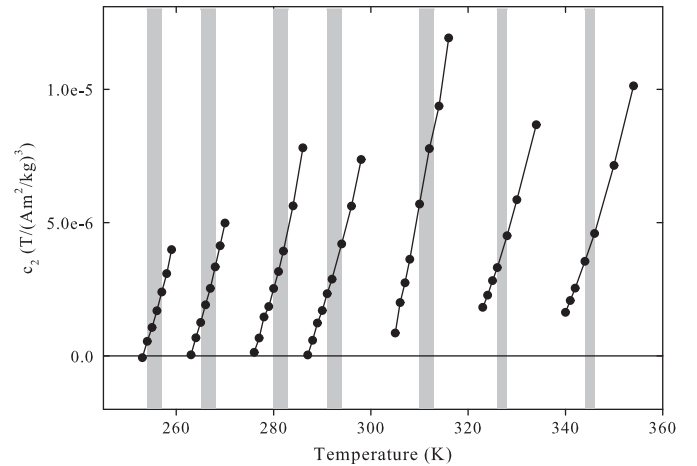

Fig. 7. Temperature dependence of the determined Landau coefficient c_2 for all seven samples. The gray area represents the range within which the Curie temperature must lie according to the values determined from the inflection point $(-\partial M/\partial T)$ and the low-field susceptibility, see Table 4.
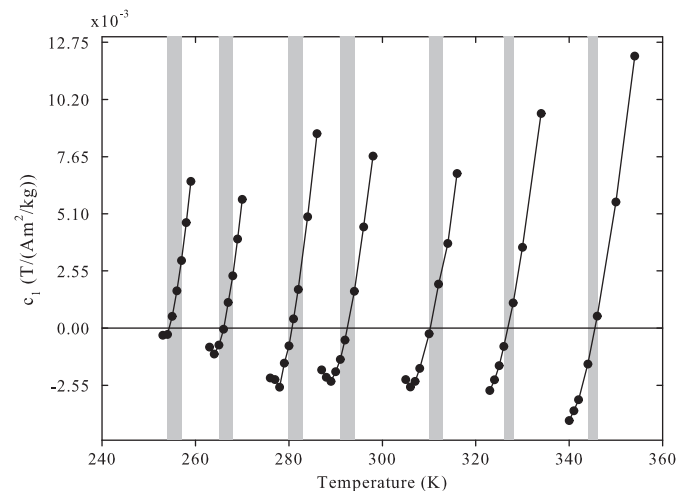

Fig. 8. Temperature dependence of the determined Landau coefficient c_1 for all seven samples. As described in the text c_1 is zero at T_c and the temperatures at which, this happens are given in Table 4. The gray area represents the range within which the Curie temperature must lie according to the values determined from the inflection point $(-\partial M/\partial T)$ and the low-field susceptibility.

Table 4
T_c determined from the inflection point ($-\partial M/\partial T$) and low-field susceptibility compared with the peak in ΔS_M calculated from VSM measurements and ΔT_{ad} from direct measurements.

Sample no.	T_c determined from inflection point ($-\partial M/\partial T$)	T_c from linear fit of $1/\chi$	T_c from Landau coefficient, c_1	ΔS_M peak	ΔT_{ad} peak (direct measurement)
Curie and peak temperatures (K)					
1	255(1)	256(1)	255(1)	255(1)	
2	266(1)	267(1)	265(1)	266(1)	266(1)
3	281(1)	282(1)	281(1)	280(1)	
4	292(1)	293(1)	292(1)	291(2)	291(1)
5	311(1)	312(1)	311(1)	309(2)	
6	327(1)	327(1)	327(1)	324(3)	
7	345(1)	347(1)	345(1)	341(3)	

respect to temperature. The temperature at which $-\partial M/\partial T$ peaked was taken as the transition temperature. As the data was recorded in 1 K steps, the uncertainty is given accordingly. The low-field inverse susceptibility was determined from the isothermal magnetization versus field curves for an average applied field of ~ 8 mT. A straight line was fitted to the data in the temperature region above the transition temperature, where the data is linear, see Fig. 9.

The Curie temperatures determined this way are given in Table 4, where they are compared to that determined from the inflection point of the magnetization and the maxima in the experimentally determined values of ΔS_M and ΔT_{ad}. Fig. 10 shows the almost linear relationship between the Curie temperature and the Co content in the seven LFCS samples.

For magnetic refrigeration the magnetic entropy change, ΔS_M, given by Eq. (1) is a measure of the amount of heat that can be extracted from the magnetic refrigerant. ΔS_M can be calculated from magnetization versus field curves by numerical integration and the expression:

$$\Delta S_M\left(T+\frac{\delta T}{2}, H_1 \to H_2\right)$$
$$\simeq \frac{\mu_0}{\delta T}\left[\int_{H_1}^{H_2} M(T+\delta T, H)\, dH - \int_{H_1}^{H_2} M(T, H)\, dH\right]. \quad (7)$$

Before calculating the magnetic entropy change from the recorded initial curves, we corrected for demagnetization as described above when determining the Landau coefficients. In this way, the magnetic entropy can be given as a function of internal field rather than applied field, which should make it easier to compare the values of the magnetic entropy change for different samples and materials. For the same reason, we give the magnetic entropy change in units of volume rather than mass, as this makes it easier to compare materials for use in an actual magnetic refrigeration setup, as suggested by Gschneidner et al. [24]. Fig. 11 shows the volumetric magnetic entropy change of the seven samples for a change in internal field of $\mu_0 H_i = 1.0$ and 1.4 T. When plotting the reduced magnetization versus reduced temperature, see Fig. 12, the magnetic transition is seen to be equally sharp for all seven materials. However, the magnetic moment in the magnetic phase is reduced with increasing Co content resulting in a smaller $\partial M/\partial T$ and therefore a smaller magnetic entropy change. The scaling of the reduced magnetization curves in the seven samples means that all the samples with their varying Co content have the same critical-point exponents and therefore no changes occur in the magnetic structure or characteristics such as e.g. anisotropy through the materials series. Sample no. 4 has a Curie temperature close to that of the commercial grade Gd and a comparison of the volumetric magnetic entropy change of the two for an internal field of $\mu_0 H_i = 1.0$ T is shown in the inset of Fig. 11.
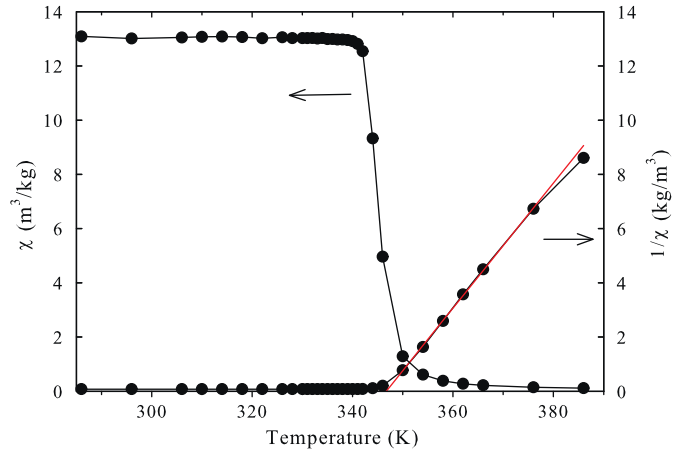

Fig. 9. Low-field (~ 8 mT) susceptibility and inverse susceptibility of sample no. 7. The low-field inverse susceptibility was fitted with a straight line to determine the Curie temperature.
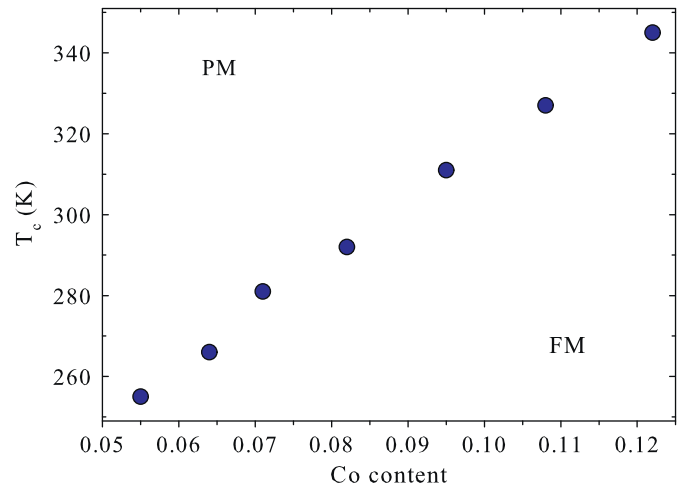

Fig. 10. The Curie temperature as a function of Co content using the values given in Table 4 determined from the inflection point. An almost linear relationship between the two is evident. The error bars are smaller than the symbols.

We see that sample no. 4 has a larger magnetic entropy change than Gd. However, due to the larger heat capacity of the LFCS samples their adiabatic temperature change, ΔT_{ad}, is less and it may be more difficult to build up a temperature difference in a magnetic refrigeration setup when using these materials rather than Gd. ΔT_{ad} can be calculated from the isothermal magnetization curves just as ΔS_M was. However, this requires additional knowledge of the heat capacity, $c_{p,H}$, for each value of
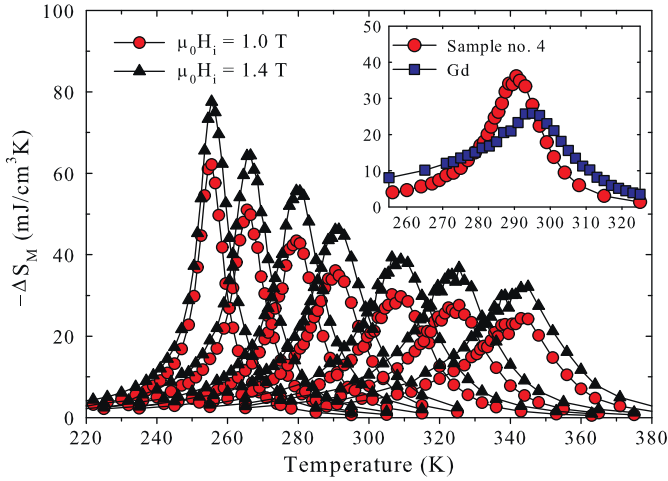
Fig. 11. The volumetric magnetic entropy change, ΔS_M, as a function of temperature for the seven samples of La(Fe,Co,Si)$_{13}$ for a change in internal field of $\mu_0 H_i = 1.0$ and $1.4\,T$. Inset: Volumetric magnetic entropy change of sample no. 4 compared to that of commercial grade Gd. Both are calculated for a change in internal field of $\mu_0 H_i = 1.0\,T$.
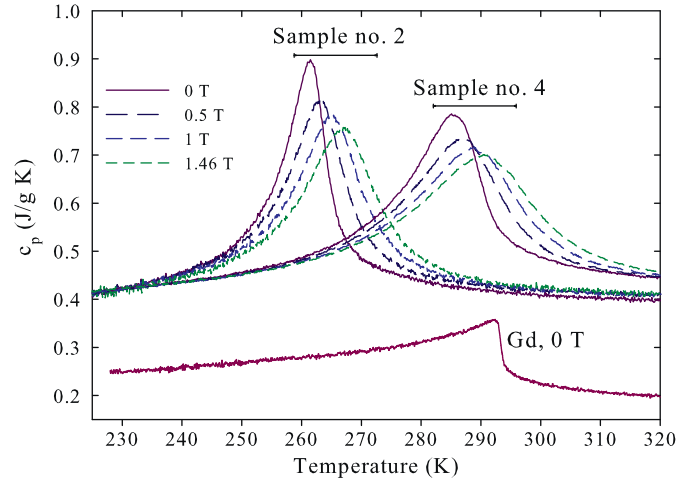

Fig. 13. Heat capacity of samples no. 2 and 4 recorded at zero-field and for applied magnetic fields of $\mu_0 H_a = 0.5$, 1.0 and $1.46\,T$. Also shown is the zero-field heat capacity of the benchmark material Gd.
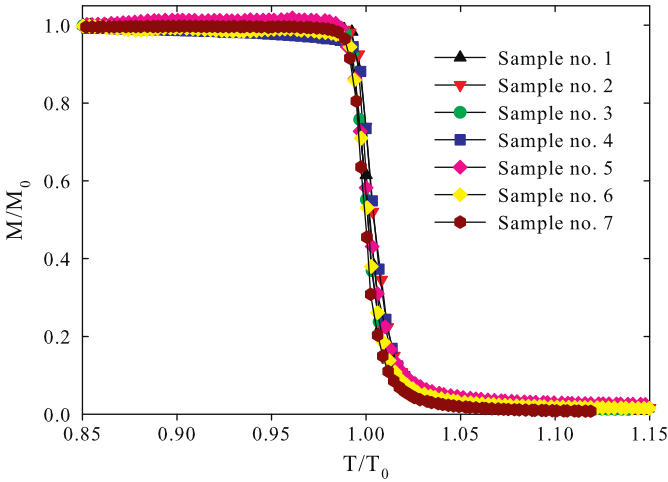
Fig. 12. Reduced magnetization versus reduced temperature of the seven samples for an applied magnetic field of $\mu_0 H_i = 0.01\,T$. The magnetization curves for all seven samples collapse and the samples all have the same critical point exponents.
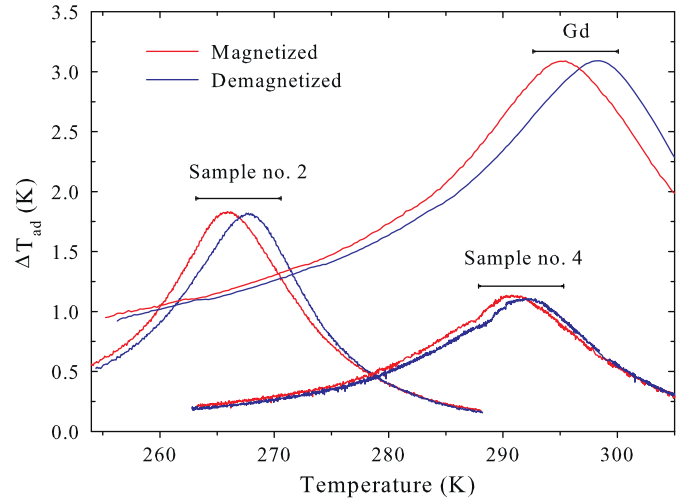

Fig. 14. Direct measurements of the adiabatic temperature changes, ΔT_{ad}, of samples no. 2 and 4 for an applied magnetic field of $\mu_0 H_a = 1.0\,T$ compared to that of commercial grade Gd.

the applied magnetic field. We recorded $c_{p,H}$ for a range of applied magnetic fields on samples no. 2 and 4, see Fig. 13. The $c_{p,H}$ data shows the larger heat capacity of LFCS when compared to Gd and the development in peak shape and value of the heat capacity as the applied magnetic field is increased. We also measured the adiabatic temperature change, ΔT_{ad}, of two of the seven samples directly, see Fig. 14. This was done using a custom built instrument described by Bjørk et al. [14]. Our results of the direct measurement of ΔT_{ad} are comparable to published values on LFCS samples with similar stoichiometry produced by arc-melting [25,18]. For magnetic refrigeration the temperature change achieved by the application of a magnetic field under adiabatic conditions is important for the build-up of a temperature difference between the hot and cold heat exchangers in the cooling system. The larger the ΔT_{ad}, the easier it is to achieve a temperature difference, whereas a small ΔT_{ad} of less than say 1 K will have more difficulty in building up a temperature difference as heat losses cannot be avoided. Many magnetocaloric materials with a ΔS_M larger than the benchmark material Gd have been found. However, as is clear from Eq. (2), the heat capacity of the magnetic refrigerant material, which so

far has always been larger for these materials than for Gd, acts to reduce ΔT_{ad}.

The thermal diffusivity, α, was measured for samples no. 2 and 6 just above room temperature and used to calculate the thermal conductivity, λ, see Fig. 15, using the equation

$$\lambda(T) = \alpha(T) \cdot \rho \cdot c_p(T). \tag{8}$$

For a magnetic refrigeration system the thermal conductivity plays an important role. At the temperature range where the thermal diffusivity was measured, sample no. 2 is paramagnetic, whereas sample no. 6 goes through its magnetic phase transition. This, however, is not apparent from the calculated $\lambda(T)$, which, as expected, slowly increases with temperature within the temperature range of $\sim 315{-}370\,K$. The values correspond well with previously published values [26] on LaFe$_{11.44}$Si$_{1.56}$ and LaFe$_{11.44}$Si$_{1.56}$H$_{1.0}$ and these materials also do not show any large change in $\lambda(T)$ near their magnetic phase transition. The addition of Co then does not change $\lambda(T)$ significantly and, as shown in Ref. [26], the thermal conductivity of LFCS is comparable to that of Gd near room temperature.
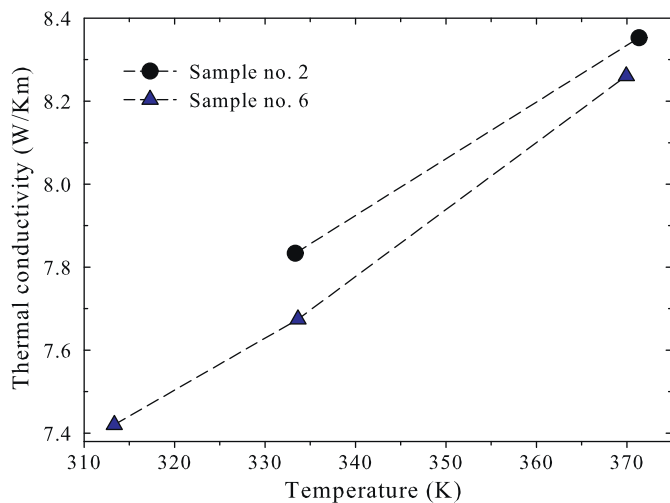
Fig. 15. Thermal conductivity of samples no. 2 and 6. The lines are guides to the eye.

6. Conclusion

As stated in the introduction conditions for suitability as a magnetic refrigerant include a large $|\Delta S_M|$ and ΔT_{ad}, low raw material costs, the possibility of large-scale production and shaping, tunability of the transition temperature, lack of hysteresis effects, toxicity, corrosion and brittleness. We have shown here that a material series of LFCS compounds that spans the room temperature regime by changing the Fe/Co ratio has a $|\Delta S_M|$ higher than or comparable to that of the benchmark material Gd. Due to the higher specific heat of the LFCS compounds their ΔT_{ad} is lower, but should be large enough to work in a magnetic refrigeration system. The materials series presented here was produced by powder metallurgy, which is a method that can be used in production on an industrial scale and the LFCS samples have a low toxicity. As the materials present a pure second-order magnetic phase transition with no anisotropy present, hysteresis is absent. The compounds can easily be tuned in Curie temperature to cover the room temperature regime and unlike many samples of La(Fe,Si)$_{13}$ there is very little thermal expansion during the magnetic phase transition. We also showed that the materials have a high thermal conductivity near room temperature, which leaves corrosion and brittleness as future challenges for the use of LFCS as magnetic refrigerants. Corrosion may be impeded by refraining from using pure water as a cooling fluid, but rather a mixture of water and anti-freeze, as well as a polymer coating. Further studies on ways to strengthen the materials, e.g. by an improved sintering are pertinent. In conclusion, the LFCS compounds are promising magnetic refrigerants with few disadvantages when compared to the criteria for suitability as a magnetic refrigerant operating at room temperature.

References

[1] A.M. Tishin, Y.I. Spichkin, The Magnetocaloric Effect and its Applications, IOP Publ. LTD, Bristol, UK, 2003.
[2] P. Debye, Einige Bemerkungen zur magnetisierung bei tiefer temperatur, Ann. Phys. 81 (1926) 1154.
[3] W.F. Giauque, A thermodynamic treatment of certain magnetic effects. A proposed method of producing temperatures considerably below 1° absolute, J. Am. Chem. Soc. 49 (1927) 1864.
[4] N. Kurti, F.N.H. Robinson, F. Simon, D.A. Spohr, Nuclear cooling, Nature 178 (1956) 450.
[5] G.V. Brown, Magnetic heat pumping near room temperature, J. Appl. Phys. 47 (1976) 3673.
[6] T.T.M. Palstra, J.A. Mydosh, G.J. Nieuwenhuys, A.M. Van der Kraan, K.H.J. Buschow, Study of the critical behavior of the magnetization and electrical resistivity in cubic La(Fe,Si)$_{13}$ compounds, J. Magn. Magn. Mater. 36 (1983) 290.
[7] H. Ido, J.C. Sohn, F. Pourarian, S.F. Cheng, W.E. Wallace, Magnetic properties of LaCo$_{13}$-based systems, J. Appl. Phys. 67 (1990) 4978.
[8] W.A.J.J. Velge, K.H.J. Buschow, Magnetic and crystallographic properties of some rare earth cobalt compounds with CaZn$_5$ structure, J. Appl. Phys. 39 (3) (1968) 1717.
[9] K.A. Gschneidner Jr., V.K. Pecharsky, Thirty years of near room temperature magnetic cooling: where we are today and future prospects, Int. J. Refrig. 31 (2008) 945.
[10] M. Katter, V. Zellmann, G.W. Reppel, K. Uestuener, Magnetocaloric properties of La(Fe,Co,Si)$_{13}$ bulk material prepared by powder metallurgy, IEEE Trans. Magn. 44 (2008) 3044.
[11] J. Rodriguez-Carvajal, Recent advances in magnetic structure determination by neutron powder diffraction, Physica B 192 (1993) 55.
[12] B.R. Hansen, C.R.H. Bahl, L. Theil Kuhn, A. Smith, K.A. Gschneidner Jr., V.K. Pecharsky, submitted for publication.
[13] S. Jeppesen, S. Linderoth, N. Pryds, L. Theil Kuhn, J. Buch Jensen, Indirect measurement of the magnetocaloric effect using a novel differential scanning calorimeter with magnetic field, Rev. Sci. Instrum. 79 (8) (2008) 083901.
[14] R. Bjørk, C.R.H. Bahl, M. Katter, Magnetocaloric properties of LaFe$_{13-x-y}$Co$_x$Si$_y$ and commercial grade Gd, submitted for publication.
[15] K.H.J. Buschow, W.A.J.J. Velge, Phase relations and intermetallic compounds in the lanthanum–cobalt system, J. Less-Common Metals 13 (1) (1967) 11.
[16] D. Lide, CRC Handbook of Chemistry and Physics, Internet Version, ninth ed., CRC Press, 2010.
[17] R. Welter, G. Venturini, B. Malaman, Magnetic properties of RFeSi (R=La–Sm, Gd–Dy) from susceptibility measurements and neutron diffraction studies, J. Alloys Compds. 189 (1992) 49.
[18] F.X. Hu, J. Gao, X.L. Qian, M. Ilyn, A.M. Tishin, J.R. Sun, B.G. Shen, Magnetocaloric effect in itinerant electron metamagnetic systems La(Fe$_{1-x}$Co$_x$)$_{11.9}$Si$_{1.1}$, J. Appl. Phys. 97 (2005) 10M303.
[19] F. Wang, A. Kurbakov, G.-J. Wang, F.-X. Hu, B.-G. Shen, Z.-H. Cheng, Strong interplay between structure and magnetism in LaFe$_{11.3}$Co$_{0.6}$Si$_{1.1}$: a neutron diffraction study, Physica B 385 (2006) 343.
[20] G.H. Rao, Magnetism in R–T intermetallic compounds with NaZn$_{13}$-type or its derivative structure, J. Magn. Magn. Mater. 139 (1995) 204.
[21] Y.V. Shcherbakova, G.V. Ivanova, Magnetic properties of novel LaFe$_{13-x}$Ga$_x$C compounds, J. Magn. Magn. Mater. 279 (2004) 69.
[22] M.Q. Huang, W.E. Wallace, R.T. Obermyer, S. Simizua, S.G. Sankar, Magnetic and structural characteristics PrCo$_{13-x}$Si$_x$ of alloys and their nitrides, J. Magn. Magn. Mater. 151 (1–2) (1995) 150.
[23] A. Aharoni, Demagnetizing factors for rectangular ferromagnetic prisms, J. Appl. Phys. 83 (6) (1998) 3432.
[24] K.A. Gschneidner Jr., V.K. Pecharsky, A.O. Tsokol, Recent developments in magnetocaloric materials, Rep. Prog. Phys. 68 (2005) 1479.
[25] M. Balli, D. Fruchart, O. Sari, D. Gignoux, J.H. Huang, J. Hu, P.W. Egolf, Direct measurement of the magnetocaloric effect on La(Fe$_{13-x-y}$Co$_y$)Si$_x$ compounds near room temperature, J. Appl. Phys. 106 (2009) 023902.
[26] S. Fujieda, Y. Hasegawa, A. Fujita, K. Fukamichi, Thermal transport properties of magnetic refrigerants La(Fe$_x$Si$_{1-x}$)$_{13}$ and their hydrides and Gd$_5$Si$_2$Ge$_2$ and MnAs, J. Appl. Phys. 95 (5) (2004) 2429.
[27] L.D. Landau, E.M. Lifshitz, Statistical Physics Part 1, third ed., Pergamon Press, 1989.

Paper III: Consequences of the Magnetocaloric Effect on Magnetometry Measurements

Consequences of the magnetocaloric effect on magnetometry measurements

B. R. Hansen,[1,a)] C. R. H. Bahl,[1] L. Theil Kuhn,[1] A. Smith,[1] K. A. Gschneidner, Jr.,[2] and V. K. Pecharsky[2]

[1]*Fuel Cells and Solid State Chemistry Division, Risø National Laboratory for Sustainable Energy, Technical University of Denmark, Frederiksborgvej 399, DK-4000 Roskilde, Denmark*
[2]*The Ames Laboratory, U.S. Department of Energy, Iowa State University, Ames, Iowa 50011-3020, USA and Department of Materials Science and Engineering, Iowa State University, Ames, Iowa 50011-2300, USA*

Magnetization curves recorded at high sweep-rates on magnetic materials near a phase transition temperature can be affected by temperature changes in the material due to the magnetocaloric effect. This change in the sample temperature is a result of the quasiadiabatic conditions that can occur under such conditions and we demonstrate its effects on magnetization curves of two magnetocaloric materials, La(Fe$_{0.945}$Co$_{0.055}$)$_{11.9}$Si$_{1.1}$ and Gd$_5$Si$_2$Ge$_2$. We show how a quantity calculated from isothermal magnetization curves, the magnetic entropy change, ΔS_M, is affected by the erroneous data. As ΔS_M is a measure of the magnetocaloric effect, the discrepancies demonstrated here are more severe close to a peak in ΔS_M, which is precisely the quantity that is of interest and reported on in the literature from possibly erroneous magnetization data. We also demonstrate how, through simple measurements and without a direct measurement of the sample temperature, one can determine an appropriate sweep-rate of the magnetic field. © *2010 American Institute of Physics*. [doi:10.1063/1.3466977]

I. INTRODUCTION

The magnetocaloric effect is a result of coupling between spin and lattice degrees of freedom and entropy conservation. When the application or removal of a magnetic field causes a change in magnetic entropy this, under adiabatic conditions, causes a change in temperature. The effect can be used to study magnetic phase transitions, see e.g.,[1] or as a method of cooling at any temperature, where a significant change in magnetic entropy can be induced. For instance, to achieve millikelvin temperatures one can use the method of adiabatic demagnetization,[2,3] while magnetic refrigeration at room temperature makes use of the criticality inherent in magnetic phase transitions.[4] Currently, research in magnetic materials with phase transitions near room-temperature is prolific[5] and in evaluating magnetocaloric materials an important parameter is the magnetic entropy change, ΔS_M. For a change in magnetic field from H_1 to H_2 this is given by

$$\Delta S_M(T, H_1 \rightarrow H_2) = \mu_0 \int_{H_1}^{H_2} \left(\frac{\partial M}{\partial T} \right)_{p,H} dH. \quad (1)$$

As the applied field can be more easily ramped than the temperature, one usually opts for obtaining the set of temperature, magnetization, and magnetic field data, (T, M, H), needed for calculation of ΔS_M by recording the magnetization as a function of applied field at a fixed temperature. From these isothermal magnetization curves, ΔS_M can be calculated by numerical integration.

As we show in the following, quasiadiabatic conditions can occur during high sweep-rates of the magnetic field in experiments even while the sample is in contact with a He or N gas and lead to significant sample heating due to the magnetocaloric effect. In this case, magnetization curves recorded during the sweep are nonisothermal and this has consequences for anyone performing measurements on magnetic materials. A lot of exciting research in the area of magnetocaloric materials is being published and the matter of the magnetocaloric effect interfering with the very measurements done to quantify it is fundamental to this research. When examining publications by often-cited groups in the field, e.g.,[6–9] in which ΔS_M is calculated from magnetization curves one finds that none of them clarify what was done to ensure that measurements were isothermal and there is no mention of the magnetic-field sweep-rates used. While several of the measurements reported in the cited works were done on a superconducting quantum interference device (SQUID) magnetometer, where it is more common to have waiting periods to ensure equilibrium, it would still be pertinent to include such information when describing the experiment. In a recent paper Moore *et al.*[10] discussed the significance of the magnetic-field sweep-rate on what they called "extrinsic magnetic hysteresis." Interestingly, although they compare the effect of different sweep-rates, they do not specify the sweep-rate used in obtaining the magnetization data for the calculation of ΔS_M in their paper.

We examine the effect of high sweep-rates on the magnetization curves of La(Fe$_{0.945}$Co$_{0.055}$)$_{11.9}$Si$_{1.1}$ (LFCS) and Gd$_5$Si$_2$Ge$_2$. The two materials are interesting because both belong to widely studied magnetocaloric material families and one, LFCS, shows a second-order magnetic phase tran-
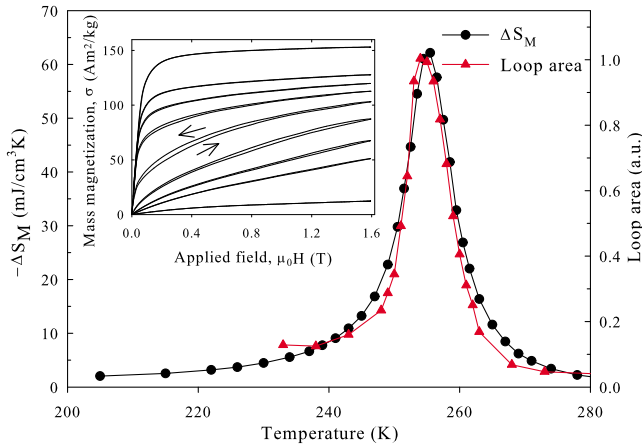
a)Electronic mail: broh@risoe.dtu.dk.

108, 043923-1

FIG. 1. (Color online) Magnetic entropy change, ΔS_M, of LFCS for an internal field change from zero to 1 T from magnetization data recorded at a sweep-rate of 2 mT/s compared to the area of magnetization loops recorded at a sweep-rate of 6.66 mT/s of which a selection is shown in the inset. The loop area is given in arbitrary units as it is an artifact.

sition at 255(1) K,[11] while the other, $Gd_5Si_2Ge_2$, shows a first-order magnetostructural phase transition with large hysteresis at ~272 K.[12] Both materials have a coercivity field, H_c, close to zero as can be seen in the inset of Fig. 1 and in Fig. 2 for LFCS and $Gd_5Si_2Ge_2$, respectively. This means that no significant magnetic viscosity is present in these materials, which is also consistent with the materials being soft magnetically, as a lag in the magnetization would cause an apparent $H_c \neq 0$.

II. EXPERIMENTAL DETAILS

The preparation of the samples is described elsewhere.[11–13] All magnetization measurements were performed on a Lake Shore 7407 vibrating sample magnetometer (VSM), which had been calibrated using a pure Ni sphere. When calculating the magnetic entropy change from recorded initial curves we corrected for demagnetization. Demagnetization is in general ignored, but it can have a significant effect. The samples were all approximately in the shape
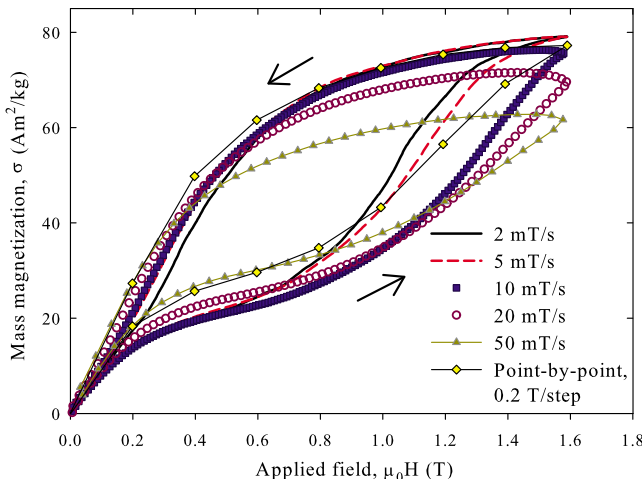

FIG. 2. (Color online) Magnetization loops of $Gd_5Si_2Ge_2$ recorded at different magnetic-field sweep-rates and with an initial sample temperature of 270 K.

of a rectangular parallelepiped and the formula for the average demagnetization factor of a rectangular ferromagnetic prism given by Aharoni[14] was used to correct the data. In this way, the magnetic entropy can be given as a function of average internal field rather than applied field, which should make it easier to compare the values of the magnetic entropy change of different samples and materials. In the raw magnetization data presented here demagnetization was not corrected for. Thermocouple measurements were performed with an E-type thermocouple attached to a VSM sample rod using double-sided Scotch tape to which the sample was attached, so that the thermocouple was sandwiched between the tape and sample.

III. RESULTS AND DISCUSSION

In a magnetometer with a cryostat setup the sample temperature during a measurement is equilibrated with that of the cryostat through thermal diffusion. The magnetization measurements are done continuously during a sweep of the magnetic field or as point-by-point measurements, where the field is ramped to a specific value before a measurement is done. In either case, quasiadiabatic conditions during the application of the magnetic field may cause heating or cooling in the sample and if so, the magnetization measurements will not be isothermal.

A. LFCS: the case of a second order material

LFCS presents a purely magnetic phase transition between a ferromagnetic and paramagnetic state and due to its high symmetry, there is negligible magnetic anisotropy. The heating/cooling of a simple ferromagnet such as LFCS due to quasiadiabatic conditions as the magnetic field is ramped up/down will result in a lower/higher magnetization, respectively, and the magnetization loop will open up. In the inset of Fig. 1, we show a selection of magnetization loops, where the magnetic field is ramped up then down. The curves were measured at a continuous magnetic-field sweep-rate of 6.66 mT/s up to an applied magnetic field of almost 1.6 T. To demonstrate that the opening of the magnetization loops is due to the magnetocaloric effect, we plot ΔS_M, calculated from data recorded at a lower sweep-rate of 2 mT/s together with the area of the loops, see Fig. 1. The two have nearly the same peak temperature and shape confirming that the magnetocaloric effect is causing the open magnetization loops.

B. $Gd_5Si_2Ge_2$: the case of a first order material

For a sample with a first-order phase transition such as $Gd_5Si_2Ge_2$ the situation is more complex. This is especially true if large hystereses are present as in $Gd_5Si_2Ge_2$. The sample used in this paper has a second-order purely magnetic ferromagnetic-to-paramagnetic phase transition with a Curie temperature of ~304 K and a ferromagnetic-to-ferromagnetic structural first-order transition temperature between 260 and 270 K depending on the applied magnetic field and whether the temperature is increased or decreased. During the structural transition the material goes from an orthorhombic structure at low temperature to a monoclinic

one at high temperature and it is this transition, which has a large magnetocaloric effect associated with it.[15] The temperature region of the structural transition is broad and the two phases coexist within it.[16] As the transition can also be induced by an applied magnetic field, a large temperature region exists within which the magnetization curves become s-shaped and show remanence-free hysteresis. In this case the open loops are inherent to the material and cannot be made to disappear by changing the sweep-rate of the applied field, see Fig. 2, as shown later for the case of the open loops in LFCS, where the cause is the magnetocaloric effect.

The appearance of the loops at different sweep-rates for $Gd_5Si_2Ge_2$ is more difficult to explain due to the complexity of the magnetization in the material. However, the remanence-free hysteresis loops should still be identical for different sweep-rates if no significant heating takes place during the ramping of the applied magnetic field. Indeed, when a magnetization curve of $Gd_5Si_2Ge_2$ was done with a sweep-rate of 1 mT/s and an initial temperature of 270 K (not shown) this was found to be almost identical to the curve measured with a sweep-rate of 2 mT/s. The magnetization loop recorded in point-by-point mode and with a step size of 0.2 T also results in heating of $Gd_5Si_2Ge_2$ due to the fast ramping of the magnetic field between the measurements. Later, a point-by-point measurement done on LFCS is shown with a step size of only 0.02 T (Fig. 5), which resulted in no significant heating in this material. A suitable step size for point-by-point magnetization measurements on the two materials was not determined and would depend on the magnetometer used as the time between measurement points is the crucial parameter. We note here, that in addition to the magnetocaloric effect, the behavior of the magnetization loops in first order phase transition materials may be further complicated by time dependence of the magnetization, especially in the phase separated region.[17,18]

In LFCS the magnetization loops simply open up due to the magnetocaloric effect, but in $Gd_5Si_2Ge_2$ the appearance of the loops at different sweep-rates is more complex. Initially, the magnetization recorded for the fast sweep-rate is lower as seen in LFCS, which is consistent with the increase in temperature. However, in $Gd_5Si_2Ge_2$ as the sample enters the region of the magnetic-field induced phase transition, the increase in temperature means that the sample leaves this region at a higher field than it would have, had the initial temperature been maintained.[16] Therefore, the magnetization curves cross as a higher field is required to cross the first-order transition region.

C. Effect on calculated magnetic entropy change

To obtain the magnetic entropy change, ΔS_M, one customarily records a series of magnetization curves at different temperatures and numerically integrates according to Eq. (1). The larger the magnetocaloric effect and sweep-rate of the applied field, the larger the discrepancy of the magnetization recorded compared to the intended isothermal one. In the inset of Fig. 3 we show a selection of magnetization curves for $Gd_5Si_2Ge_2$ recorded at initial sample temperatures near the structural transition and at different sweep-rates. It is
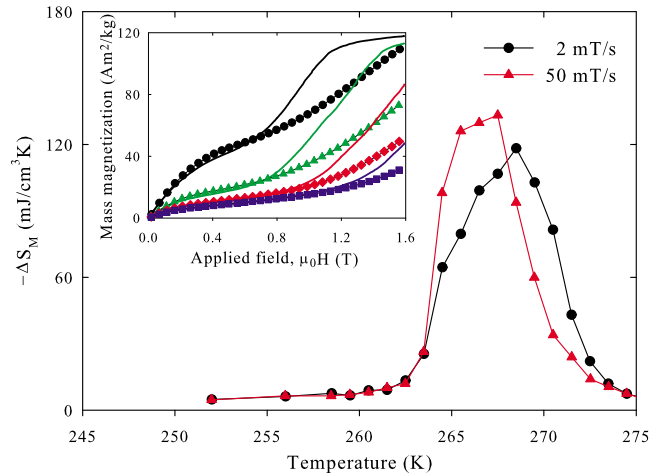

FIG. 3. (Color online) ΔS_M for a change of internal magnetic field from zero to 1 T calculated from two sets of magnetization data with different sweep-rates. Inset: initial curves of $Gd_5Si_2Ge_2$ recorded with sweep-rates of 2 mT/s (lines) and 50 mT/s (symbols) at initial sample temperatures of 268, 270, 272, and 274 K.

clear that for a material with as large a magnetocaloric effect as $Gd_5Si_2Ge_2$, one can obtain values far from the intrinsic ones. It should be noted that the absolute values of the magnetization in Fig. 3 do not match those of Fig. 2 as differently shaped samples were used for the measurements and their demagnetization was notably different. From the magnetization curves with sweep-rates of 2 and 50 mT/s, we calculated the magnetic entropy change, ΔS_M. Looking at the curves in the inset of Fig. 3, we expect to find that ΔS_M, which is proportional to the area between the magnetization curves, will be larger for some temperatures and smaller for others when comparing the two sweep-rates. This is indeed what we find as shown in Fig. 3. We see that the slow sweep-rate of 2 mT/s, which gives the correct value of the magnetic entropy change, has a smaller and broader peak than the one calculated from the data recorded with a fast sweep-rate of 50 mT/s. The highest value of 130 mJ/cm^3 K corresponds to 17.3 J/kgK and so is comparable in size to previously published values,[12] though a direct comparison is not possible as the values normally presented in papers are for applied and not internal magnetic fields.

D. Direct measurement of sample temperature

The temperature increase due to the ramping of the magnetic field was measured directly. Due to the heat exchange occurring in the setup, the temperature measured in this manner cannot be said to be the adiabatic temperature change, ΔT_{ad}. However, we are easily able to record the large temperature change in $Gd_5Si_2Ge_2$ due to high sweep-rates of the applied magnetic field as shown in Fig. 4, where the thermocouple data from two measurements with different sweep-rates are presented.

The temperature rise detected by the thermocouple during the continuous magnetization measurement with a sweep-rate of 50 mT/s is severe and even the very slow sweep-rate of only 2 mT/s appears to cause a slight temperature increase in the sample during the ramp again emphasizing the need for consideration when performing such mea-
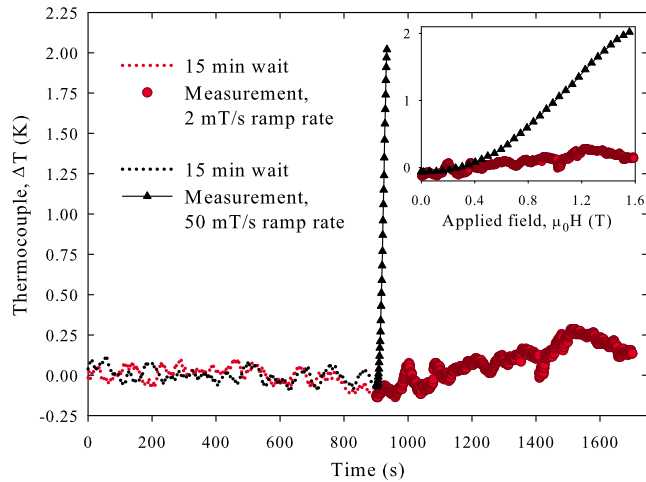
FIG. 4. (Color online) Thermocouple data recorded during magnetization measurements on $Gd_5Si_2Ge_2$ for an initial sample temperature of 270 K and a magnetic-field sweep-rate of 2 mT/s (circles) and 50 mT/s (triangles). The zero of the thermocouple data is the average of the temperature recorded during the 15 min wait prior to the measurement run. Inset: thermocouple data as a function of the applied magnetic field.
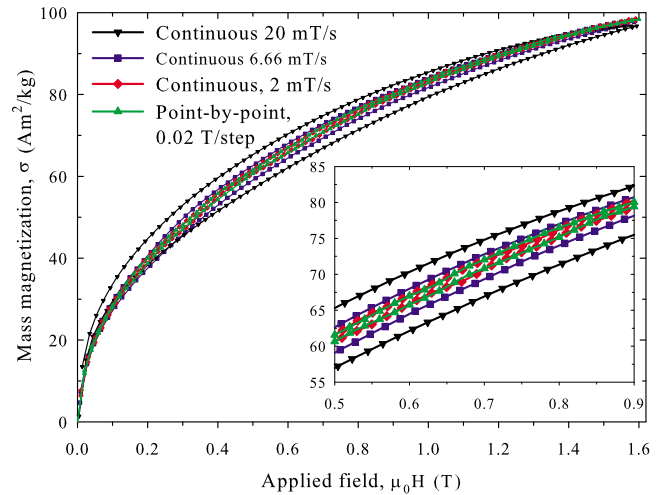

FIG. 5. (Color online) The effect of different sweep-rates on the magnetization of LFCS for an initial sample temperature of 255 K. In this case, the point-by-point measurement, where the magnetometer changes the applied field in discrete steps and waits after each field change shows no effect of heating as the sample has time to equilibrate with the cryostat.

surements. Thermal diffusion in our setup was a slow process. When the magnetic field was ramped at the higher rate of ~84 mT/s and at an initial sample temperature of 270 K the thermocouple registered a temperature increase of 2.8 K and equilibration took almost a minute.

E. Ensuring isothermal measurements

By using a sufficiently low magnetic-field sweep-rate in experiments the magnetization will not be affected by changes in sample temperature due to the magnetocaloric effect. One way of determining whether heating occurs is, of course, by measuring the sample temperature directly. However, the same can be achieved simply by measuring a series of loops near the Curie temperature, where the magnetocaloric effect is the largest. A suitable sweep-rate has been found, when a reduction in sweep-rate does not change the magnetization measured. In Fig. 5 we show magnetization loops for LFCS at different sweep-rates and at an initial temperature of 255 K, which is near the Curie temperature.

As expected, the loop closes as the sweep-rate is reduced. In Fig. 5 a magnetization loop for a point-by-point measurement, where the magnetometer changes the applied field in discrete steps and waits after each field change is also shown. The point-by-point data nearly overlap those of the slowest continuous data and therefore no significant sample heating occurs during the measurement.

IV. CONCLUSIONS

In conclusion, we have demonstrated that care must be taken when planning magnetization measurements on materials near temperatures where they show a large magnetocaloric effect. The change in sample temperature during ramping of the magnetic field is visible both in magnetization data and in data from a thermocouple attached close to the sample. By recording magnetization loops at different

sweep-rates a suitable one can be chosen, one which does not result in significant heating of the sample during the measurement.

[1]V. S. Zapf, D. Zocco, B. R. Hansen, M. Jaime, N. Harrison, C. D. Batista, M. Kenzelmann, C. Niedermayer, A. Lacerda, and A. Paduan-Filho, Phys. Rev. Lett. **96**, 077204 (2006).
[2]W. Giauque, J. Am. Chem. Soc. **49**, 1864 (1927).
[3]P. Debye, Ann. Phys. (N.Y.) **386**, 1154 (1926).
[4]A. M. Tishin and Y. I. Spichkin, *The Magnetocaloric Effect and its Applications*, (IOP, Bristol, UK, 2003).
[5]K. A. Gschneidner, Jr., V. K. Pecharsky, and A. O. Tsokol, Rep. Prog. Phys. **68**, 1479 (2005).
[6]V. Provenzano, A. J. Shapiro, and R. D. Shull, Nature (London) **429**, 853 (2004).
[7]J. Lyubina, K. Nenkov, L. Schultz, and O. Gutfleisch, Phys. Rev. Lett. **101**, 177203 (2008).
[8]O. Tegus, E. Brück, K. H. J. Buschow, and F. R. de Boer, Nature (London) **415**, 150 (2002).
[9]J. Marcos, A. Planes, L. Mañosa, F. Casanova, X. Batlle, A. Labarta, and B. Martínez, Phys. Rev. B **66**, 224413 (2002).
[10]J. D. Moore, K. Morrison, K. G. Sandeman, M. Katter, and L. F. Cohen, Appl. Phys. Lett. **95**, 252504 (2009).
[11]B. R. Hansen, L. Theil Kuhn, C. R. H. Bahl, M. Lundberg, C. Ancona-Torres, and M. Katter, J. Magn. Magn. Mater. **322**, 3447 (2010).
[12]A. O. Pecharsky, K. A. Gschneidner, Jr., and V. K. Pecharsky, J. Appl. Phys. **93**, 4722 (2003).
[13]M. Katter, V. Zellmann, G. W. Reppel, and K. Uestuener, IEEE Trans. Magn. **44**, 3044 (2008).

[14]A. Aharoni, J. Appl. Phys. **83**, 3432 (1998).

[15]V. K. Pecharsky and K. A. Gschneidner, Jr., Pure Appl. Chem. **79**, 1383 (2007).

[16]J. D. Moore, K. Morrison, G. K. Perkins, D. L. Schlagel, T. A. Lograsso, K. A. Gschneidner, Jr., V. K. Pecharsky, and L. F. Cohen, Adv. Mater.

(Weinheim, Ger.) **21**, 3780 (2009).

[17]E. M. Levin, K. A. Gschneidner, Jr., and V. K. Pecharsky, Phys. Rev. B **65**, 214427 (2002).

[18]Z. W. Ouyang, V. K. Pecharsky, K. A. Gschneidner, Jr., D. L. Schlagel, and T. A. Lograsso, Phys. Rev. B **76**, 134406 (2007).

Paper IV: Direct Measurement of the Spin Reversal in $Gd_3Fe_5O_{12}$ at the Compensation Point using Mössbauer Spectroscopy

Direct measurement of the spin reversal in $Gd_3Fe_5O_{12}$ at the compensation point using Mössbauer spectroscopy

B.R. Hansen,[*] L. Theil Kuhn, and C.R.H. Bahl

Fuel Cells and Solid State Chemistry Division, Risø National Laboratory for Sustainable Energy,
Technical University of Denmark, DK-4000 Roskilde, Denmark

C. Frandsen and S. Mørup

Department of Physics, Technical University of Denmark, Bldg. 307, DK-2800 Kgs. Lyngby, Denmark
(Dated: July 20, 2010)

We have performed ^{57}Fe Mössbauer spectroscopy measurements at zero and two non-zero applied magnetic fields on a powder sample of GdIG and directly observed the spin reversal of the Fe sublattices at the compensation temperature. This is achieved by the applied field defining a direction of the Fe spins, so that the spin reversal is apparent from the values of the hyperfine fields extracted from the Mössbauer spectra. The sample was characterized using x-ray powder diffraction and magnetometry and the compensation temperature, where $dM/dT = 0$, was found to be 288±1 K .

PACS numbers: 75.30.Sg

I. INTRODUCTION

Gadolinium Iron Garnet (GdIG), $Gd_3Fe_5O_{12}$, which crystallizes in a cubic structure, has three magnetic sublattices: Gd^{3+}, Fe^{3+} in a tetragonal environment and Fe^{3+} in an octahedral environment. The three sublattices couple in a complex manner making for interesting magnetic properties. ^{57}Fe Mössbauer spectroscopy is well-suited for studying the magnetic properties of Fe-containing materials and we present here the result of a Mössbauer study on a powder sample of GdIG near what is known as the compensation temperature, where the magnetic moments on the three sublattices cancel each other out. The Mössbauer measurements were performed both with and without an applied magnetic field and this will give a direct measurement of the spin reversal that happens at the compensation point, when a magnetic field is applied. Due to the large thermal neutron cross section of Gd, neutron scattering studies are difficult and Mössbauer spectroscopy can provide information on the magnetism in GdIG, which is otherwise hard to get.

The chemical formula of GdIG can be written as $\{Gd^{3+}\}_3(Fe^{3+})_2[Fe^{3+}]_3O_{12}^{2-}$, where $\{\}$ refers to dodecahedral, $()$ to octahedral and $[]$ to tetrahedral coordination with the oxygen lattice[12], see Fig. 1. Gd^{3+} and Fe^{3+} both have a large magnetic moment and are in an S-state, i.e. their orbital angular momentum is zero. The magnetic moments on the two Fe^{3+} sites are coupled strongly and antiferromagnetically. However, since there are three tetrahedrally coordinated Fe atoms for every two octahedrally coordinated ones, the result is a ferrimagnetic Fe moment. The Gd moments are coupled weakly and also antiferromagnetically to the total Fe moment, so that the couplings between the three sublattices result in a total magnetization given by[3]

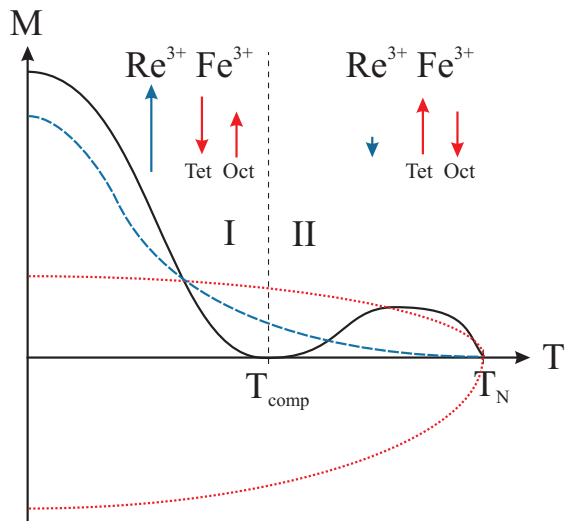$$M_{total} = M_{Gd} - M_{(Fe,tet)} + M_{(Fe,oct)} \qquad (1)$$

FIG. 1: Magnetization versus temperature of a rare-earth iron garnet for a small applied magnetic field. The total magnetization (black) is a sum of the magnetization of the rare-earth (RE) sublattice (blue, dashed) and the Fe sublattices (red, dotted). In region I the RE3+ moment dominates, whereas in region II the ferrimagnetic Fe3+ moment dominates. At the temperature T_{comp}, the moments cancel and the magnetization is zero.

The magnetization of GdIG as a function of temperature is illustrated in Fig. 1. At low temperatures, in region I, the Gd moment dominates and decreases slowly with temperatures due to the coupling to the Fe-sublattice. The Gd-Gd coupling is almost negligible and so it is the Gd-Fe coupling, which aligns the Gd spins. At room temperature the Gd^{3+} spins are essentially disordered, i.e. paramagnetic, spins in an effective magnetic field from the ferrimagnetic Fe spins. At the so-called compensation temperature, T_comp, the total magnetization is zero as the moments on the three sublattices cancel

each other out. T_{comp} is sample dependent due to impurities, e.g. the presence of other rare earths or other magnetic phases, but appears around 286 - 290 K[4,5]. Above T_{comp} the ferrimagnetic Fe moment dominates until the temperature reaches the Néel temperature of the system, $\sim$562.5 K[6]. It has been calculated that canting of the spins should occur when a magnetic field is applied. However, due to the strong coupling between the Fe atoms, canting of the magnetic moments only happens in extremely high fields except when close to T_{comp} in temperature[7]. When passing through T_{comp} with a magnetic field applied, the sublattice spin reorientation happens in a finite temperature interval, i.e. an angled phase exists. Bernasconi and Kuse[7] find that the slope of the phase boundary between the collinear and angled phases is $\sim \pm$ 1 K/T. In GdIG the magnetic moments order preferentially along the cubic [111] axis for temperatures between 4.2 K and the Néel temperature[6]. As the magnetic moments cancel at T_{comp} the energy cannot be reduced by having magnetic domains and the particles become single domain. This was directly observed and reported by Mee[8]. When a magnetic field is applied at temperatures near T_{comp} the spins become canted and the magnetic moments may no longer cancel completely. The existence of the canted phase results in saturation of the magnetocaloric effect, i.e. the heating or cooling that occurs in a magnetic material when a magnetic field is applied adiabatically. This happens because an applied field will no longer change the magnetic entropy of the rare-earth sublattice, which is responsible for the magnetocaloric effect in GdIG below the Néel temperature. The saturation of the magnetocaloric effect has also been used to determine the phase boundary between the collinear and canted phases[9]. The transition between the collinear and angled phases causes a symmetry breaking of rotational invariance, i.e. the crystal is no longer invariant to rotation about an axis. As the spin canting will develop continuously, the phase transition is of second-order. At T_{comp} and with no applied field, there is no symmetry breaking, which means that either the transition here is of first order or there is no phase transition[10]. In the following, we use Mössbauer spectroscopy to obtain values of the hyperfine fields affecting the Fe nuclei at temperatures around T_{comp}. By applying a magnetic field, the magnetic moments will order along the field direction and, as the octahedral and tetrahedral sites will be distinguishable, the reversal of the spins at T_{comp} can be observed directly.

II. EXPERIMENTAL DETAILS

The GdIG sample was prepared by solid state synthesis of powders of Gd_2O_3 (99.9%) and Fe_2O_3 (99.9%). The powders were mixed in a 3:5 molar ratio and pressed into a pellet, which was then pressed isostatically and sintered in air for 35 hours at 1400°C, which changed the sample color from reddish brown to a dark green. The sintered
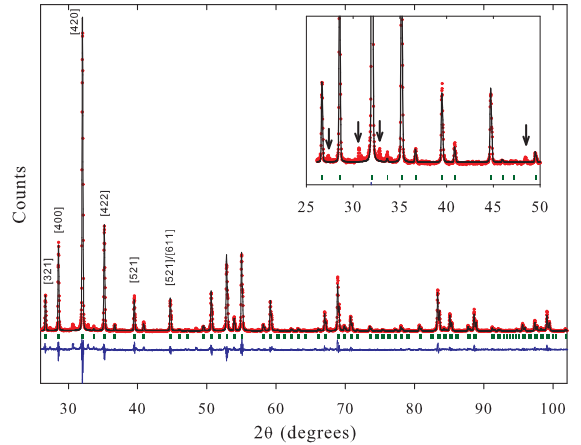

FIG. 2: Rietveld refinement of x-ray powder diffraction on GdIG sample. Inset: Low scattering angles. Four peaks from an unidentified impurity are marked by arrows.

pellet was crushed to a powder using an agate mortar and pestle. The sample was examined by Cu K_α x-ray powder diffraction using an in-house Bruker D8 Advance diffractometer. To avoid the fluorescent background scattering from Fe an energy dispersive solid state (Sol-X) detector was used. Variable slits were used when recording the x-ray diffraction data and the recorded intensity was corrected using the formula

$$I_{\text{corrected}} = \frac{I_{\text{variable slit}}}{\sin \theta}. \qquad (2)$$

FullProf[11] was used for Rietveld refinement of the corrected x-ray spectrum. For magnetization measurements a LakeShore 7407 Vibrating Sample Magnetometer (VSM) was used. The measurements of the magnetization as a function of temperature at various applied magnetic fields were made as point-by-point measurements in steps of 1 K and with a measurement time of 5 s/point. Mössbauer studies were performed using a conventional constant acceleration drive and an ^{57}Co:Rh source. The isomer shifts are given relative to that of iron at room temperature. A magnetic field was applied perpendicular to the direction of the γ-photons for some of the measurements. All Mössbauer spectra were all fitted with line pairs having area, width and intensities equal

III. RESULTS AND DISCUSSION

From the refinement of the XRD spectrum it was found that the main phase in the sample is GdIG. The presence of one or more impurities in small quantities is evident from four peaks at low scattering angles, which could not be identified, see Fig. 2.

In Fig. 3 is shown the recorded magnetization of GdIG for a range of applied magnetic fields. The magnetization
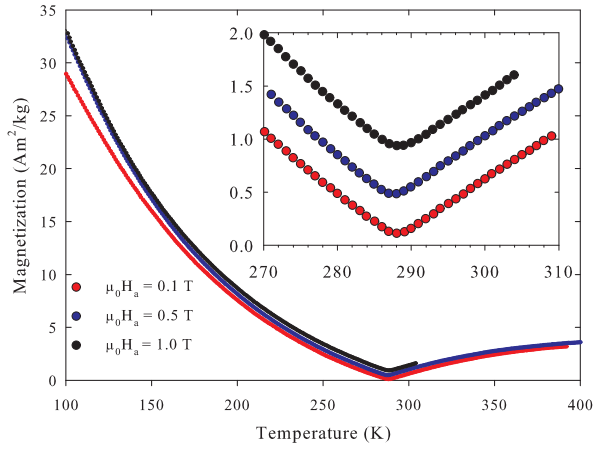
FIG. 3: The magnetization of GdIG for a selection of applied magnetic fields. Inset: The magnetization near T_{comp}.

as a function of temperature acts as expected when comparing with Fig. 1. For temperatures below T_{comp} the magnetization slowly decreases as the Gd^{3+} spins, which are weakly coupled to the ferrimagnetic Fe^{3+} spins, lose their order due to the increasing thermal fluctuations. At T_{comp}, dM/dT is zero for all applied magnetic fields, but the magnetization is non-zero as the essentially paramagnetic Gd^{3+} moments are affected by the applied magnetic field. By taking as the compensation temperature the point in the magnetization data where $dM/dT = 0$, we find $T_{comp} = 288 \pm 1$ K.

From ^{57}Fe Mössbauer spectra on GdIG we obtain the splitting and shifts of the nuclear levels of the ^{57}Fe in the Fe^{3+} sites. Due to the tilting of the Fe^{3+} tetra- and octahedra in GdIG, there are seven non-equivalent Fe sites, three tetrahedral and four octahedral ones[12]. This means that seven sextets are present in each spectrum. However, it is not possible to fit this many sextets and obtain consistent and comparable values, so in the following only one sextet is fitted for the octahedral site and one for the tetrahedral site. Nine Mössbauer spectra were recorded: at zero applied magnetic field, at 0.3 T and at 0.6 T for a temperature near T_{comp} and at $\sim T_{comp} \pm 10$ K, see Figs. 4, 5 and 6. In the three Mössbauer spectra recorded at 276 K a small shoulder at line 6 in the sextet from the octahedral sites could be due to the impurity $GdFeO_3$. This impurity would also be seen as a sextet in the Mössbauer spectrum, but the remaining five lines would overlap with those of the octahedral site and so a possible sextet caused by $GdFeO_3$ is difficult to fit. As the lines shift with temperature and magnetic field, the extra line seen near line 6 for the octahedral site is not visible in the majority of the spectra. For this reason, and because the shoulder at line 6 could well be due to the existence of four octahedral sites, no separate sextet was fitted for $GdFeO_3$.

The determined values of the isomer shift and quadrupole interaction for the two fitted sextets are given in Table I. As expected due to their different coordina-
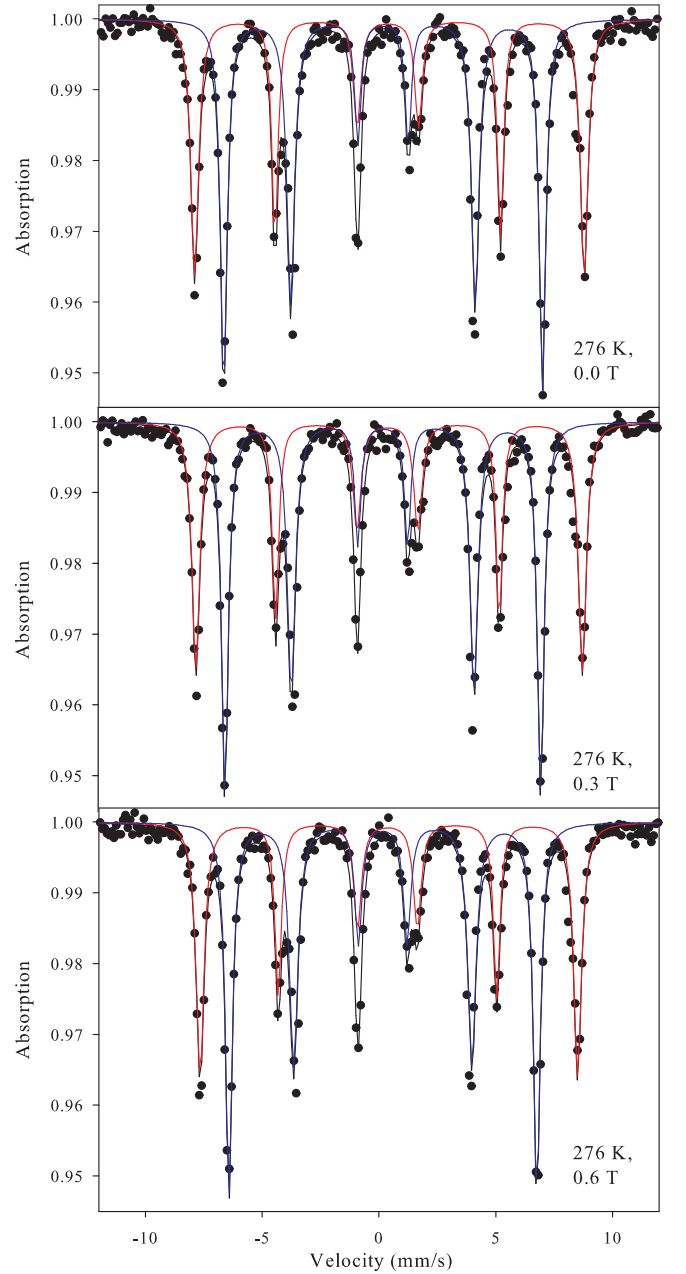

FIG. 4: Mössbauer spectra of GdIG sample recorded at 276 K and for various magnetic fields applied perpendicular to the γ-photons. The red line is the fit to the octahedral site, while the blue line is the fit to the tetrahedral site.

tion, the two Fe sites have different isomer shifts. For Fe^{3+} in a high-spin configuration, the typical values of the isomer shift are 0.2 - 0.6 mm/s relative to metallic Fe at room temperature. Although the Fe in the tetrahedral site has isomer shifts of ~ 0.17 mm/s, which could indicate an Fe^{3+} low-spin state where the typical values of the isomer shift are -0.1 - 0.4 mm/s, the value is not significantly lower than those typical for the high-spin state. The quadrupole splitting of the two Fe sites, shown in Fig. ??, is close to zero for both sites and at all
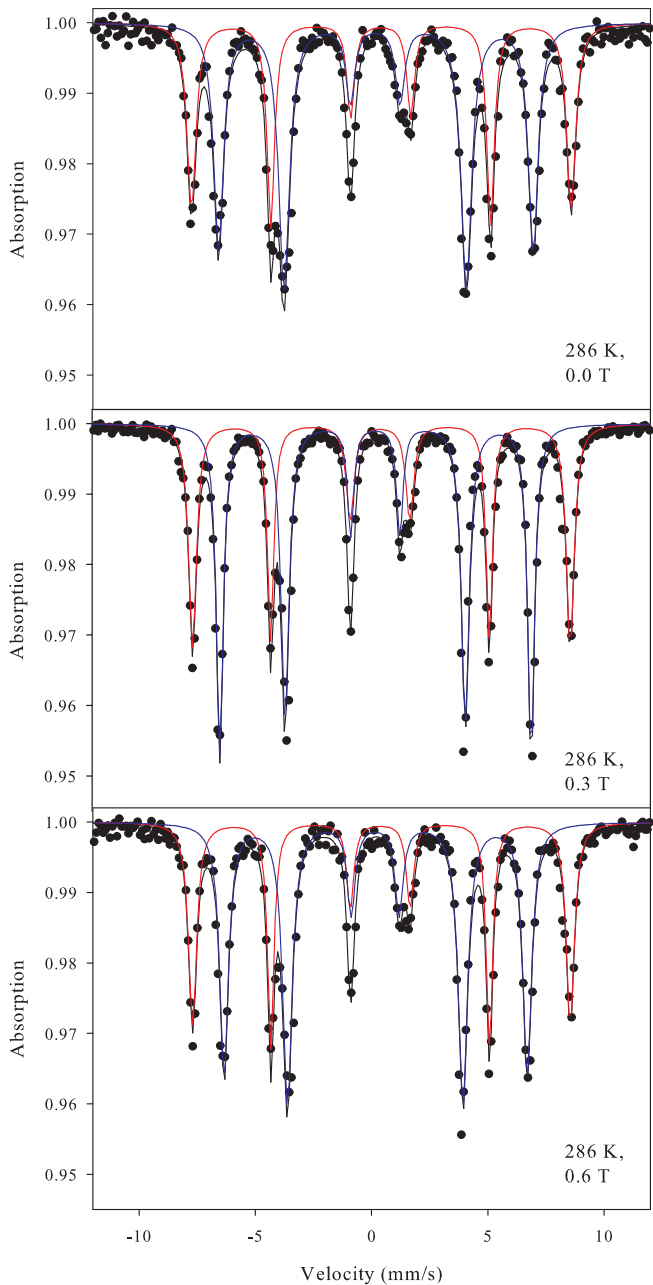
FIG. 5: Mössbauer spectra of GdIG sample recorded at 286 K and for various magnetic fields applied perpendicular to the γ-photons. The red line is the fit to the octahedral site, while the blue line is the fit to the tetrahedral site.

FIG. 6: Mössbauer spectra of GdIG sample recorded at 296 K and for various magnetic fields applied perpendicular to the γ-photons. The red line is the fit to the octahedral site, while the blue line is the fit to the tetrahedral site.

temperatures and fields. With no apparent temperature dependence of the quadrupole splitting, the Fe atoms are likely to be in an Fe^{2+} low-spin state or in an Fe^{3+} high-spin state. As we know, that the Fe atoms have a valence of three in GdIG, this is consistent with Fe^{3+} atoms in a high-spin state. The determined hyperfine magnetic induction for the two Fe sites is shown in Figs. 7 and 8.

For zero applied magnetic field, the hyperfine field at both sites decreases as the temperature is increased due to thermal fluctuations reducing the magnetization. In
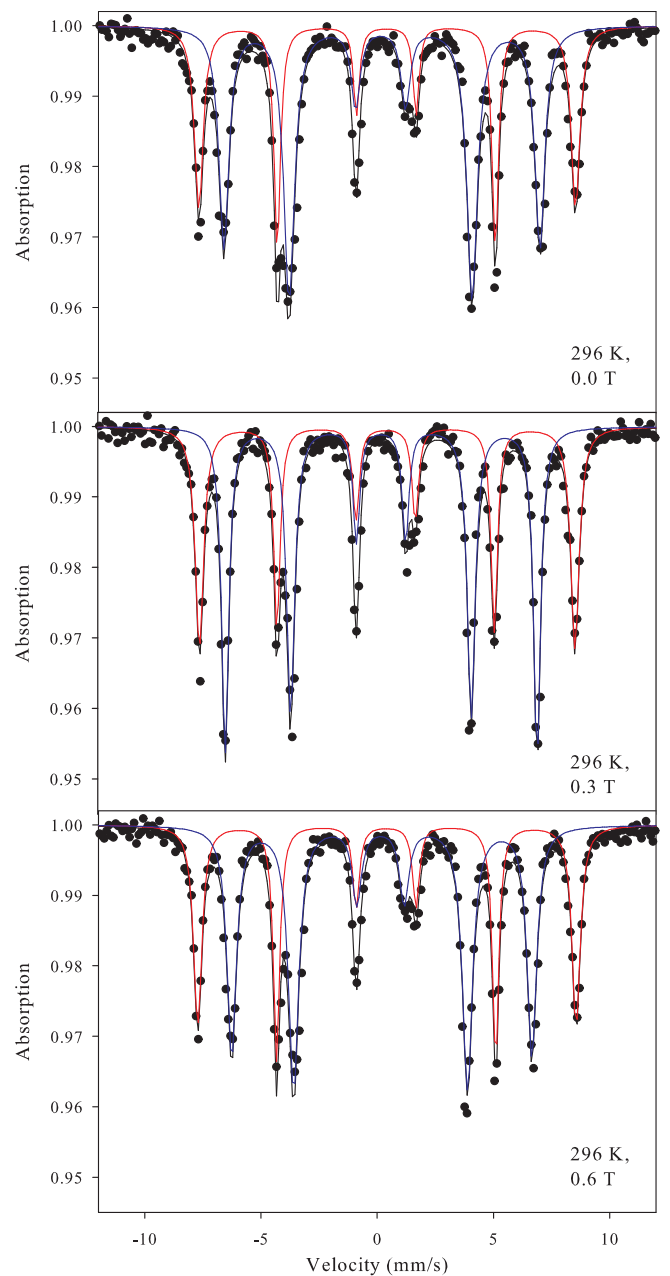
Table I, we compare the isomer shift, quadrupole splitting and hyperfine fields with values found in literature. Only the values determined for zero applied field are compared as, to the best of our knowledge, no values for applied magnetic fields exist to compare with.

In the applied-field data, we see the evidence of spin reversal as the temperature is changed from below to above T_{comp}. In region I, see Fig. 1, the Fe magnetic moment in the octahedral site is oriented parallel to the total magnetic moment, while the moment in the tetrahedral site
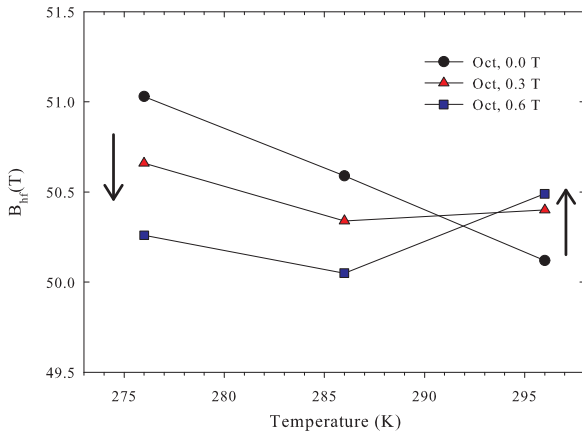
FIG. 7: Hyperfine magnetic induction, B_{hf}, for the octahedrally coordinated Fe sites in GdIG.
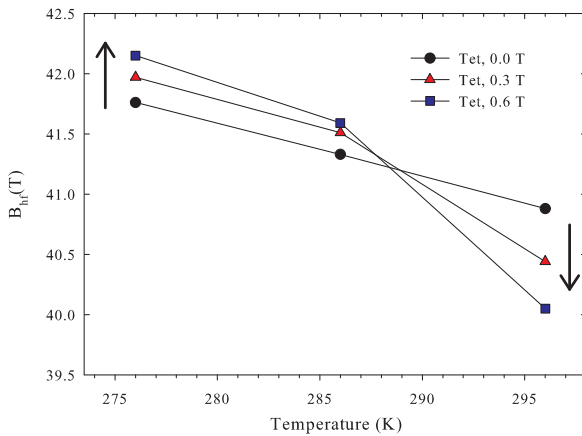

FIG. 8: Hyperfine magnetic induction, B_{hf}, for the tetrahedrally coordinated Fe sites in GdIG

at T_{comp} using Mössbauer spectroscopy.

	Isomer shift		Quadrupole splitting		Hyperfine fields	
	Oct.	Tet.	Oct.	Tet.	Oct.	Tet.
276 K, 0.0 T	0.41	0.18	0.04	0.00	51.0	41.8
276 K, 0.3 T	0.41	0.17	0.01	0.01	50.7	42.0
276 K, 0.6 T	0.41	0.17	0.02	0.03	50.3	42.2
286 K, 0.0 T	0.40	0.17	0.04	0.00	50.6	41.3
286 K, 0.3 T	0.40	0.17	0.03	0.00	50.3	41.5
286 K, 0.6 T	0.41	0.18	0.03	0.00	50.1	41.6
Ref. 13:						
RT, 0.0 T	0.39	0.18	0.04	0.00	49.4	40.5
296 K, 0.0 T	0.39	0.17	0.03	0.00	50.1	40.9
296 K, 0.3 T	0.40	0.17	0.02	0.00	50.4	40.4
296 K, 0.6 T	0.40	0.17	0.00	0.03	50.5	40.0

TABLE I: Values of the isomer shift, quadrupole splitting and hyperfine fields determined for the two Fe sites in the GdIG sample. The determined values are compared with ones found in literature for room temperature.

IV.   CONCLUSIONS

We performed Mössbauer spectroscopy near the compensation temperature of GdIG. The isomer shifts, quadrupole splitting and hyperfine fields determined from fits of the zero-field measurements close to room temperature are comparable to those reported in literature. From the Mössbauer measurements recorded with a magnetic field applied perpendicular to the direction of the γ-photons, we observe directly the reversal at T_{comp} of the magnetic moments in GdIG under an applied magnetic field. The compensation temperature of the sample was found to be 288 ± 1 K.

V.   ACKNOWLEDGEMENTS

is oriented anti-parallel to it. As the magnetic field at the nucleus is anti-parallel to the magnetic moment, the hyperfine field affecting the Fe nuclei in the octahedral sites is anti-parallel to the applied magnetic field, while that affecting the Fe nuclei in the tetrahedral sites is parallel to the applied field. As we apply a magnetic field, this results in a decrease (increase) in the moments, which are anti-parallel (parallel) to the applied field. Above T_{comp}, in region II, the spins have reversed, so that the applied field now causes an increase in the hyperfine field at the octahedral sites and a decrease in the field at the tetrahedral sites. Thus, by applying a magnetic field and thereby defining a direction of the magnetic moments in GdIG, we were able to directly record the spin reversal

* Electronic address: `broh@risoe.dtu.dk`
[1] J. Weidenborner, Acta Cryst. **14**, 1051 (1961).
[2] J. M. D. Coey, Phys. Rev. B. **6**, 3240 (1972).
[3] R. Pauthenet, J. Appl. Phys. **29**, 1958 (1958).
[4] R. Pauthenet, Compt. Rend., Paris **242**, 1956 (1956).
[5] S. Geller, J. P. Remeika, R. C. Sherwood, H. J. Williams, and G. P. Espinosa, Phys. Rev. **137**, 1034 (1965).
[6] D. C. Cook and J. Li, Hyp. Int. **28**, 495 (1986).

[7] J. Bernasconi and D. Kuse, Phys. Rev. B. **3**, 811 (1971).

[8] C. D. Mee, IBM J. Res. Dev. **11**, 468 (1967).

[9] K. P. Belov, L. A. Chernikova, E. V. Talalaeva, R. Z. Levitin, T. V. Kudryavtseva, S. Amadesi, and V. I. Ivanovskii, Soviet Physics JETP-USSR **31**, 1035 (1970).

[10] M. Guillot, F. Tchéou, A. Marchand, P. Feldmann, and R. Lagnier, Z. Phys. B. - Condensed Matter **44**, 53 (1981).

[11] J. Rodríguez-Carvajal, Physica B **192**, 55 (1993).

[12] C. Alff and G. K. Wertheim, Phys. Rev. **122**, 1414 (1961).

[13] S. C. Zanatta, L. F. Cótica, A. Paesano, Jr., J. B. M. d. S. N. de Medeiros, and B. Hallouche, J. Am. Ceram. Soc. **88**, 3316 (2005).

Risø DTU is the National Laboratory for Sustainable Energy. Our research focuses on development of energy technologies and systems with minimal effect on climate, and contributes to innovation, education and policy. Risø has large experimental facilities and interdisciplinary research environments, and includes the national centre for nuclear technologies.